

# **A LIDAR-compatible Approach to Remote Sensing of Water Temperature using Raman Spectroscopy**

By

**Andréa de Lima Ribeiro**

This thesis is submitted to Macquarie University  
for the degree of Doctor of Philosophy

Department of Physics and Astronomy

October 2018



**MACQUARIE**  
**University**  
SYDNEY • AUSTRALIA

FACULTY OF SCIENCE AND ENGINEERING





# Declaration

This thesis is submitted in fulfilment of the requirements of the degree of Doctor of Philosophy at Macquarie University and has not been submitted for a higher degree at any other university or institution. I certify that to the best of my knowledge, all sources used and assistance received in the preparation of this thesis have been acknowledged.

---

Andréa de Lima Ribeiro  
October 2018





# ACKNOWLEDGEMENTS

I couldn't start these acknowledgments in any other way but thanking my PhD supervisor Prof. Helen Pask. I have no words to express the gratitude I have for you believing in me when even I doubted myself. You were always there to help, encourage, and share your immense knowledge, guiding me through this process. You are the best mentor I could have asked for, thank you for giving me the opportunity to be your student. You have never failed me and I will be grateful to you for the rest of my life.

I would also like to thank to my co-supervisor, Dr. David Spence, for the feedbacks you provided in the last 3 years. Special thanks to Dr. Christopher Artlett, whose help was extremely valuable at the beginning of my PhD. Thank you to all my colleagues from the Terahertz Group and MQ Photonics for enriching my academic experience: Andrew, Tiago, Yameng, Tushar, Soumya, Ran, and all the others. Thank you to all academic and teaching staff from the Department of Physics and Astronomy, I've learnt a lot from all of you. In this regard, I would also like to thank Prof. Paulo Lana, Prof César de Castro Martins, Prof. Flávia Conde and Prof. Fernando D'Incao for all the academic support you gave me in this journey.

My story didn't begin in Australia, this country that I've learnt to love, but really far away from here in Brazil. I've always wanted to be a scientist and for many years this seemed like a distant dream, which became reality thanks to one person: my mother Lucia. She gave up on everything so I could have access to education, and her life of abnegation allowed me to get this far. Thank you to my grandparents, Hercilia and Murilo, who gave us shelter for some many years when we didn't have anywhere else to go. I have only the dearest memories from you.

Thank you to all my Brazilian friends, who put up with all this distance and made an effort to keep me in their lives, specially a friend who happens to be the sister I've never had. Nathalia, thank you for everything. I don't know what I would do without you. Special thanks to the friends who helped me moving to Australia: Dani, Mauricio and Auro. I owe you one. Thank you to Matthew, who was by my side during these 3 years of PhD.

This thesis was only possible because, despite of all economic and political problems in my country, we still believe that free education is the key to overcome social disparities. I was lucky enough to have access to high-level free public education for 13 years and I will be forever thankful to the Brazilian people for this opportunity. I hope to return to our society all the money invested in my education. I will **always** advocate in favour of a system that allows for people to change their own realities – as it allowed for me to change mine.

Thank you!



# Abstract

The measurement of water temperature provides essential information for the understanding of the water column dynamics, being important for research fields including oceanography, climate change, marine ecology, fisheries and coastal management. Traditional *in situ* measurements provide accurate depth-resolved information at limited spatial and temporal scales. As an alternative suitable for large scales studies, researchers may rely on remote sensing tools such as passive satellite sensors and active LIDAR (Light Detection and Ranging) methods. However, satellite-derived sea surface data are restricted to the first micrometres of the water column, not providing information regarding vertical structure and stratification. LIDAR methods employ active excitation and fast time-resolved detectors, allowing for depth-resolved measurements performed from airborne or ship-based platforms and, when coupled to spectroscopic measurements, have the potential to assess subsurface water temperature.

The aim of this research work is to develop LIDAR-compatible spectroscopic methods for monitoring water temperature based on the inelastic Raman scattering of photons in water. Raman scattering in water exhibits a temperature-dependent behaviour, which can be used to estimate temperature markers for remote sensing predictions. The analysis of Raman spectra from natural water samples, which were acquired by using a commercial Raman spectrometer (532 nm excitation) indicated that the presence of other optical signals in natural waters, such as fluorescence, may compromise the accuracy of Raman temperature sensing. In order to circumvent this issue, I proposed methods for spectral correction which resulted in temperature determination with improved accuracy.

I designed and assembled multichannel LIDAR-compatible Raman spectrometers integrated to excitation lasers having green and blue wavelengths. The design allowed for simultaneous collection of unpolarised and polarised Raman signals, enabling the calculation of four temperature markers carrying different types of temperature information. Each marker was analysed in terms of accuracy of temperature predictions, sensitivities and percentage errors associated with signal-to-noise ratios. A novel linear combination method was employed to use all four temperature markers and was effective in enabling enhanced temperature predictions.

The relative merits of using green and blue excitation were considered in the context of laboratory studies and proposed field implementation. The work presented in this thesis represents a major step forward in the quest for a LIDAR-based optical system to measure subsurface water temperature with an accuracy of  $\pm 0.5^{\circ}\text{C}$  and depth resolution of 0.5 m in near real-time.



# List of Acronyms

ANN	Artificial Neural Networks
AOL	Airborne Oceanographic LIDAR
AVHRR	Advanced Very High Resolution Radiometer
CDOM	Coloured Dissolved Organic Matter
Chl-a	Chlorophyll-a
CTD	Conductivity, Temperature, Depth
CW	Continuous-Wave
DOM	Dissolved Organic Matter
ENSO	El Niño South Oscillation
FWHM	Full Width of Half Maximum
IOP	Inherent Optical Properties
IPCC	Intergovernmental Panel for Climate Change
LIDAR	Light Detection and Ranging
Nd:YAG	Frequency-doubled Neodimium-doped Yttrium Aluminium Garnet
NOAA	National Oceanic and Atmospheric Administration
PLADS	Pulsed Light Airborne Depth Sounder
PMT	Photomultiplier
RS	Raman Spectrometer
SBS	Stimulated Brillouin scattering
SNR	Signal-to-Noise Ratio
SSST	Skin Sea Surface Temperature
SST	Sea Surface Temperature
VSF	Volume scattering Function
XBT	Expendable Bathythermograph



# Table of Contents

<b>Declaration.....</b>	<b>ii</b>
<b>Acknowledgements.....</b>	<b>iv</b>
<b>Abstract.....</b>	<b>vi</b>
<b>List of Acronyms .....</b>	<b>viii</b>
<b>Table of Contents .....</b>	<b>x</b>
<b>Chapter 1 .....</b>	<b>1</b>
<b>Introduction.....</b>	<b>1</b>
1.1.    Sensing of water temperature.....	3
1.1.1.    Satellite remote sensing.....	3
1.1.2.    Buoys and floats .....	5
1.1.3.    Expendable bathythermographs (XBTs).....	8
1.1.4.    Light Detection and Ranging (LIDAR) methods .....	9
1.2.    How light interacts with water at the molecular level.....	11
1.2.1. Molecular absorption of light in water .....	12
1.2.2. Rayleigh scattering .....	13
1.2.3. Brillouin scattering .....	14
1.2.4. Raman scattering .....	16
1.2.4.1. Two-colour method.....	24
1.2.4.2. Depolarisation ratio method.....	25
1.3.    Raman remote sensing of oceanic waters .....	26
1.3.1. Fluorescence .....	26
1.3.1.1. Chlorophyll-a and other photosynthetic pigments .....	27
1.3.1.2. Dissolved Organic Matter - DOM .....	28
1.3.2. Optically active particles in oceanic waters .....	29
1.4.    Raman spectroscopy and LIDAR-compatibility .....	30
1.4.1. Past research on LIDAR-compatible Raman spectroscopy of natural waters..	32



1.5. Thesis context and outline .....	36
<b>Chapter 2 .....</b>	<b>39</b>
<b>Experimental and Analysis Methods .....</b>	<b>39</b>
2.1. Water samples .....	41
2.2. Water cell and cuvette holder .....	43
2.3. Measuring accuracies on temperature predictions .....	44
2.4. Assessing water temperature information from Raman spectra acquired by a commercial dispersive spectrometer.....	45
2.4.1. Spectrometer Enwave EZRaman-I at 532 nm .....	45
2.4.2. Two-colour unpolarised temperature markers .....	47
2.4.3. Determining temperature from two-colour(unpol) markers.....	47
2.4.4. Multivariate analysis (Principal Component Analysis).....	49
2.5. Water temperature predictions performed by custom-built, multichannel, LIDAR- compatible Raman spectrometers (532 nm and 473 nm excitation lasers).....	50
2.5.1. Green multichannel RS (532 nm excitation laser) .....	50
2.5.2. Multichannel RS (blue) .....	56
2.5.3. Temperature markers calculations.....	61
2.5.4. Temperature markers sensitivities.....	63
2.5.5. SNR calculations .....	63
<b>Chapter 3 .....</b>	<b>65</b>
<b>Raman spectroscopy as a technique for natural water temperature determination...65</b>	
3.1. Manuscript 1: “The impact of fluorescence on Raman remote sensing of temperature in natural water samples” .....	68
3.2. Principal Component Analysis – understanding spectral signatures in natural waters .....	79
3.3. Baseline Correction methods .....	87
3.3.1. Method 1 – tilted baseline correction.....	88
3.3.2. Method 2 – correction by temperature markers .....	91
3.4. Discussion: field implementation .....	92
3.5. Summary and conclusion .....	95

**Chapter 4 .....97**

**LIDAR-compatible multichannel Raman spectrometer using green (532 nm) excitation light 97**

4.1. Manuscript 2: “A LIDAR-compatible, multichannel Raman spectrometer for remote sensing of water temperature” .....	100
4.2. Acquisition overview.....	113
4.2. A more comprehensive analysis of temperature markers and their usefulness.....	114
4.3. Individual contributions of markers to linear combination models .....	122
4.4. Markers sensitivities in natural water samples.....	125
4.5. Summary and conclusion .....	130

**Chapter 5 .....132**

**LIDAR-compatible multichannel Raman spectrometer using blue (473 nm) excitation light 132**

5.1. Manuscript 3: “Remote sensing of temperature in natural water samples using a multichannel, lidar-compatible Raman spectrometer and blue excitation (473 nm)” .....	135
5.2. Acquisition overview.....	155
5.3. A more comprehensive analysis of temperature markers and their usefulness.....	156
5.4. Markers sensitivities in natural water samples .....	165
5.5. Considerations for LIDAR implementation .....	171
5.5.1. Background and approach .....	171
5.5.2. Propagation (transmission) of excitation photons .....	174
5.5.4. Transmission of Raman photons .....	179
5.5.5. Comparing the Raman returns for blue and green excitation.....	182
5.6. Summary and conclusion .....	185

**Chapter 6 .....187**

**Conclusions and future outlook.....187**

6.1. Research outcomes.....	189
6.2. Future outlook .....	191

**Bibliography .....193**

<b>Appendix A</b> .....	<b>204</b>
A.1. Green multichannel Raman spectrometer markers .....	204
A.2. Blue multichannel Raman spectrometer markers .....	206
<b>Appendix B</b> .....	<b>208</b>
<b>Appendix C</b> .....	<b>214</b>
<b>Appendix D</b> .....	<b>222</b>



# CHAPTER 1

## INTRODUCTION

Oceanography is a multidisciplinary science which aims to understand the processes occurring in the ocean without compartmentalization *i.e.* the biological, physical, geological and chemical processes are all connected. There are several challenges inherent to collecting oceanographic data [1] as traditional *in situ* acquisition methods, despite providing highly accurate data: (i) are expensive, (ii) demand human operation and analysis, (iii) are limited to providing non-continuous information from sampling stations instead of covering large areas; iv) are not compatible with temporal and spatial scale of many processes in the oceanic

and coastal zones. As an alternative, researchers have been using remote sensing data when traditional acquisition methods are not feasible.

Remote sensing is the action of collecting data without direct contact with the object under investigation. In the context of oceanography, the traditional view of remote sensing involves the study of ocean, atmosphere and their interactions by analysing electromagnetic radiation emitted by these media [2]. Although the most used remote sensing tools in oceanography do analyse the electromagnetic spectra, the authors of [3] acknowledge the existence of other remote sensing systems based on seismic waves, gravitational forces and sonic waves. In this study we accept the broader view of the “remote sensing” term as simply retrieving data at a physical distance from the target by using sensors detecting electromagnetic, acoustic and electric signal [4].

Independently of the type of signal being analysed, the choice of remote sensing tool needs to consider the high spatial and temporal variability of the oceanic processes being studied; the accuracy and frequency at which the information of interest is needed also plays a decisive role on this decision. The development of new technologies during the last centuries changed the scale of interest of oceanographic studies and allowed a transition from a “century of under sampling” to a better, yet inadequate, sampling rate for addressing oceanic processes [5]. Until the 1970’s, the accepted theory of a steady ocean with no temporal variability (as proposed by [6] and [7]) was broadly accepted and studied by traditional sampling methods deployed from ships. In 1978, the release of the first satellite designed for remote sensing of the oceans (SeaSat), brought a new vision to the field and attention to time-dependent mesoscale processes (100 km, 10 days) carrying up to 99% of total kinetic energy of the oceans. Satellite data were available at no cost for the scientific community and proved to be a valuable source for the remote study of eddies, internal waves, oceanographic fronts and other dynamic processes causing variability on the oceans [8]. The 21<sup>st</sup> century marked another change on course for oceanography, now interested in macroscale oceanic and atmospheric processes that were previously considered local (*e.g.* El-Niño South Oscillation, Pacific Decadal Oscillation, thermohaline circulation). More recently, discussions regarding anthropogenic impacts on the planet’s rising temperatures led to the foundation of Intergovernmental Panel for Climate Change (IPCC) which brought awareness to the oceans as heat sinks, leading to thermal expansion of water and consequent sea level rise at coastal areas. There is an increasing demand for depth-resolved temperature

data for all spatial scales that only remote sensing tools can provide at a frequency suitable for coastal management and risk assessment of coastal vulnerability [9].

## **1.1. Sensing of water temperature**

Water temperature measurements are important for climate change studies, characterisation of water masses, understanding the dynamics between physical and biological signals resulting in high productivity rates, to estimate the speed of sound in water and, along with salinity, to calculate oceanic geostrophic flows. Knowing the water temperature is a major step towards understanding the environment and evaluating the patterns of processes occurring at any scale.

Measuring oceanic and coastal water temperature is a challenging task, which can be performed by *in situ* or remotely. Traditional *in situ* tools were the main techniques to acquire temperature data from the oceans until 1970 and include thermometers, bathythermographs, temperature probes, CTDs (Conductivity, Temperature, Depth) and oceanographic buoys [5]. The logistics behind *in situ* measurements is complex, including the use of vessels, ships, calibration, human operation and periodic maintenance. The precision, accuracy and portability of these equipment have improved throughout the last few decades, providing high quality depth-resolved temperature data for local sampling points, along with other information necessary to characterize the aquatic environment [10]. Regardless its usefulness for local studies ( $< 10$  km), *in situ* tools are impractical for systematic temperature measurements over larger spatial scales, such as mesoscale (10 to 100 km) and macroscale ( $> 100$  km) systems. For these larger spatial scales, continuous water temperature monitoring is performed mainly by satellite sensors and other remote sensing tools. In this section a selection of instruments used to measure water temperature is briefly reviewed.

### **1.1.1. Satellite remote sensing**

At the beginning of 2018, there were hundreds of environmental satellites orbiting the planet, equipped with passive sensors built to measure oceanic and atmospheric properties. Their main advantage over traditional methods is the ability to provide a synoptic view of oceanic and coastal processes [9], being the most valuable tool for the understanding of oceanographic variabilities at larger scales. The fact that the majority of this data is provided to the scientific community at no direct cost also helps to spread its use as the main remote sensing tool in environmental sciences.

Passive temperature sensors collect signals derived from the interaction between sunlight and the surface of the Earth. It takes around 8 minutes for light emitted by the sun to reach the top of the Earth's atmosphere, with the majority of this radiation being in the visible and ultraviolet spectral regions. Our planet absorbs the sunlight and re-emits this radiation towards longer wavelengths, which can be either absorbed by greenhouse gases or reach the top of the atmosphere without major disturbances. In the latter case, this long-wavelength radiation can be detected by satellite sensors and, after processing, provide valuable temperature information. Radiometers are sensors traditionally employed in water temperature measurements, operating within the range of infrared and microwave wavelengths.

Infrared radiometers collect signal emitted by the oceans at various spectral channels from middle infrared to longwave thermal infrared. The main sensors operating within this range is the Advanced Very High Resolution Radiometers (AVHRRs), continuously collecting data with high temporal and spatial variability (Nadir resolution of up to 1.1 km) since 1978. As infrared radiation is highly absorbed by water molecules, the signal collected by radiometers arises from the first mm (skin sea surface temperature, SSST) to tenths of meters (sea surface temperature, SST), depending on the depth of the mixing layer [8,9]. AVHRR retrieves SSST data, which are typically 0.2 to 0.3 K lower than the water mass underneath [8,11], requiring post-acquisition corrections by using *in situ* measurements. After leaving the water, atmospheric corrections are also necessary, as the infrared signal is highly affected by CO<sub>2</sub>, H<sub>2</sub>O and O<sub>3</sub> absorption and by sea surface rugosity [12]. The presence of clouds is particularly concerning at intertropical convergence zones as IR signals are strongly absorbed by H<sub>2</sub>O, impacting the periodicity at which temperature data can be retrieved from these areas. To circumvent this problem, researchers can use data collected at bandwidths that are less impacted by atmospheric absorption and scattering, such as microwaves. Microwave sensors (1 cm to 1 m collection range) exhibit the advantage of operating at spectral regions where signals undergo minimum attenuation by the atmosphere, allowing for SST data acquisition in the presence of clouds. Nevertheless, passive microwave measurements are limited by the low intensity of microwave signals emitted spontaneously by the oceans resulting in final products with coarse spatial resolution (from 25 km) [8].



Advances in satellite technology have, undoubtedly, changed the course of oceanic temperature measurements; however, data acquire remotely by sensors still rely on *in situ* measurements for correction, calibration and validation. This task can be challenging in coastal areas where signals from several optically active constituents interact and overlap each other, compromising the accuracies of temperature predictions by remotely acquired infrared radiation. In [13], the authors compared the accuracies of AVHRR and *in situ* temperature measurements at coastal and offshore sampling sites, finding values from  $\pm 0.4^{\circ}\text{C}$  to  $\pm 0.6^{\circ}\text{C}$  for offshore stations and reduced accuracies towards the coastal zone ( $\pm 1.0^{\circ}\text{C}$  to  $\pm 2.0^{\circ}\text{C}$ ). The authors also found a delay of up to three hours between AVHRR and *in situ* measurements, evidencing that the timescale of processes occurring at coastal zones may not be fully covered by satellite sensors. In summary, satellite-derived SST data are valuable for assessment of global phenomena, but don't allow for a tridimensional assessment of the water column structure and still depend on algorithms and *in situ* measurements for calibration and validation.

### 1.1.2. Buoys and floats

Oceanic buoys and floats are observational platforms that don't need a vessel for operation after being deployed into the environment, incorporating multiple meteorological and oceanographic sensors sampling at systematic frequencies.

Buoys (or moored buoys) are anchorage, large and expensive platforms commonly installed at harbour vicinities and coastal areas. The equipment incorporates several meteorological and oceanographic sensors, enabling for collection of depth-resolved parameters at systematic timescales. According to the National Data Buoy Centre, operated by the US National Oceanic and Atmospheric Administrations (NOAA), as in March/2018 there were 1372 oceanographic buoys operating on the Atlantic, Pacific and Indian oceans, located at latitudes from  $65^{\circ}\text{N}$  to  $46^{\circ}\text{S}$ . The broad spatial distribution of the buoys attempts to cover regions of interest to the merchant navy and the scientific community; yet there are still numerous gaps compromising this spatial coverage. Another concern is the maintenance of the buoys, which are susceptible to extreme environmental conditions and biofouling therefore requiring periodic maintenance (figures 1.1 and 1.2).



Figure 1.1. Maintenance activities of an oceanographic buoy operating at the Brazilian coast. Photo courtesy of Camilla Bonatto and SIMCOSTA team.



Figure 1.2. Bioincrustation accumulating inside an oceanographic buoy. Photo courtesy of Camilla Bonatto and SIMCOSTA team.

Unlike buoys, “float” is a common designation to small, simple devices which are not mooring at a fixed point of the oceans. Some models, such as ARGO floats, spend most part of the time at depths of neutral buoyance and emerge every 10 days, profiling the water column. While at the surface ARGO floats transmit temperature, salinity and pressure data along with latitude and longitude coordinates, which are received by satellites. The lack of spatial variability is compensated by the extensive net of ARGO floats deployed around the world, including 3768 devices as in August/2018. Despite their limitations, they represent extremely valuable tools for validating satellite data and providing vertical profiles of temperature [1,14]. It is through the analysis of data acquired from buoys around the Pacific Equatorial that scientists study the ENSO (El Niño South Oscillation) as a coupled process between atmosphere and oceans, bringing an understanding which has had massive impact in weather prediction [15].

### 1.1.3. Expendable bathythermographs (XBTs)

Bathythermographs are instruments deployed from ships, vessels or submarines capable of measuring vertical profiles of temperature, salinity and speed of sound in water. The first bathythermographs were mechanical devices developed to suit military needs of rapid vertical temperature profiling. Due to poor accuracy and also the need to reduce vessel speeds during operation, these were replaced by expendable bathythermographs (XBTs) [16].



Figure 1.3. Expendable bathythermographs (probes) and hand launcher. Image acquired from [17].

The first XBTs were developed by the end of the 60's and have the advantage of providing highly accurate temperature ( $0.15^{\circ}\text{C}$ , [14]). XBTs consist of a probe with a torpedo shape which estimates water temperature based on the differences in electric resistance between a reference thermistor and a thermistor in contact with the surrounding environment. Depth-resolved information collected by the XBT is transferred to a central computer by copper leads and, after transmission, the instrument is discarded.

A major part of studies investigating oceanic subsurface water and the thermal balance at the upper ocean rely on XBT data collected during oceanographic cruises. The method, however, exhibits its own limitations: systematic data acquisition is restricted to major ship routes; the data is collected at sampling stations, instead of covering larger areas; and the

operation of XBTs is not fully autonomous, requiring a person to be responsible for launching the probes into the water.

#### **1.1.4. Light Detection and Ranging (LIDAR) methods**

Light Detection and Ranging (LIDAR) refer to remote sensing methods where light signals typically in the visible or near-infrared spectral regions are retrieved from a target and interpreted to derive desired information. Unlike infrared or microwave radiation, visible light penetrates in the water column, enabling assessment of bulk characteristics, vertical profiles of various water properties and the systematic bathymetric mapping in coastal areas [18,19].

With the evolution of operational oceanography and the need of new tools for validating satellite products, the need for faster profiling techniques led to the design of airborne laser systems [20]. As monochromatic light transmits in the water column, its speed varies due to changes in density of the medium (dependent on temperature and salinity) and interacts with water molecules and other optically active dissolved and particulate constituents; hence, the development of LIDAR techniques was intrinsically dependent of ocean optics and the radiative transfer energy theory [21].

The early development of LIDAR systems was fostered by military agencies, with classified results not being fully disclosed to the scientific community at the time. Some of these agencies include NASA, the Australian Defence, Science and Technology Organisation (DSTO) and the U.S. Naval Air Development Centre (NADC). The main focus of these studies was to develop a new technique able to provide rapid bathymetry data with better spatial coverage than measurements from vessels. From these efforts, the first laser built exclusively for bathymetry studies was commercially released in 1972 and named Pulsed Light Airborne Depth Sounder (PLADS) [22].

The requirements for building a LIDAR compatible system depended on the excitation source and detectors. Pulsed green lasers (532 nm) became the choice for bathymetric studies, as green light has good penetration in coastal waters, which can have high concentrations of dissolved organic matter (DOM) [23] and can be generated by doubling the frequency of 1064 nm (infrared) lasers. The duration of the pulse is also important, as it correlates with the vertical resolution of the measurements. Accordingly, the use of short-pulsed lasers (periods  $< 2$  ns at the full width of half maximum (FWHM)) is desirable for vertical resolutions better than  $\pm 0.5$  m. The choice of detectors is also

primordial, as they need to acquire the backscattered signal with time-dependency from the excitation light in order to estimate the total time of travel, distance travelled and potential scattering layers in the water column. Photomultipliers are the common choice, often in conjunction with time-gated electronics to amplify signals that are many times smaller than the environmental radiance.

In the years that followed PLADS, the development of LIDAR technology was intrinsically associated with the need for validating satellite data and acquisition of bathymetry data. Despite being able to provide depth-resolved information, the interpretation of the backscattered signal was challenging, the signal-to-noise ratios (SNR) were not optimal and the excitation signal was also affected by Fresnel reflection at the air-sea interface. In 1978, NOAA organised a scientific seminar to promote a discussion within the academic community about the use of lasers and LIDAR methods in oceanography [24]. Several researchers analysed and assessed pathways and limitations to establish new instruments for monitoring oceans properties as temperature, chlorophyll-a fluorescence and speed of currents by using different spectroscopy techniques associated with LIDAR methods. This conference was a milestone for consolidating active LIDAR methods as technologies with potential to provide data for all areas in marine sciences.

Attempting to overcome some of the LIDAR implementation challenges, [25] proposed strategies such as collecting signals at night and the use of filters to minimize the impact of optical interactions in spectral regions of interest. Utilising the NASA Airborne Oceanographic LIDAR (AOL), operating integrated to a 532 nm pulsed laser (pulse duration of 7.7 ns at the FWHM), the authors were able to detect the main scattering layers of a subsurface water plume on platform waters. Since then, attempts have been made to retrieve subsurface water information from spectroscopic techniques associated with LIDAR methods, but no methodology has been fully established, reproduced and made commercially available for water temperature measurements.



## 1.2. How light interacts with water at the molecular level

Water is the most commonly found liquid substance in the world and, yet, its structure and molecular behaviour are not fully understood by the scientific community. As stated by D. H. Lawrence:

*“Water is H<sub>2</sub>O, hydrogen two parts, and oxygen one  
But there is also a third thing, that makes it water  
And no one knows what that is”*

One of the main challenges when working with optical methods in natural waters is circumventing the complex behaviour of light-matter interactions, which may happen for both excitation and scattered signals. Nevertheless, the understanding of these complex processes and their contribution for spectral signals emitted by the oceans may ultimately help scientists to derive information about water molecular structure from Inherent Optical Properties (IOPs) collected by LIDAR methods [26]. IOPs are optical properties intrinsic to the medium and invariant under changes in angular distribution of the surrounding light field or excitation source. Several IOPs can be retrieved from the oceans by remote sensing tools, such as absorption coefficient and Volume Scattering Function [27,28]. The characteristics of IOPs are influenced by the origin, composition and concentration of particles and dissolved substances in water.

Oceanic and coastal waters are complex mixtures of water molecules with different concentrations of various particulate and dissolved substance. Prior to investigating all possible light-matter interactions for natural waters, it is necessary understanding the basics of light behaviour in a theoretical pristine, pure-water environment; in this scenario, light-matter interactions are dictated by water molecular processes such as polarizability and clustering formation. In this section, I will sequentially explore the processes of absorption, the elastic Rayleigh scattering process, and the inelastic processes of Brillouin and Raman scattering.

### 1.2.1. Molecular absorption of light in water

Light absorption by water is a wavelength-dependent process. When a photon of frequency  $\nu_0$  interacts with a molecule with similar natural frequency of vibration, the molecule's electrons are excited to higher energy levels. The energy acquired from the photon is transmitted to other electrons and dissipated as thermal energy inside the molecule, with no light being re-emitted.

Visible light (390 to 700 nm) has low absorbance in pure water and the energy from photons of  $\lambda > 450$  nm is transferred to vibrational modes associated with OH bonding processes around the infrared region of electromagnetic spectra (3049 nm, 6079 nm, and 2865 nm) [29,30]. This behaviour is responsible for the strong absorption of IR radiation by water molecules, imposing a challenge for retrieving depth-resolved data from passive infrared signals acquired by satellite sensors as discussed in section 1.1.1.

Aiming to circumvent absorption by water molecules, many LIDAR technologies operate with both excitation/emission signals in the visible range. Ultimately, absorption of light around blue-green regions of the visible spectrum is minimum, increasing towards a maximum around red. The coefficients of light absorption in pure water  $a_w(\lambda)$  and saltwater  $a_{sw}(\lambda)$  indicate the wavelength-dependent light absorption behaviour per unit of travelled distance in the water column ( $\text{m}^{-1}$ ). Estimations for  $a_w(\lambda)$  from 380 nm to 700 nm from [31] are shown in figure 1.4.

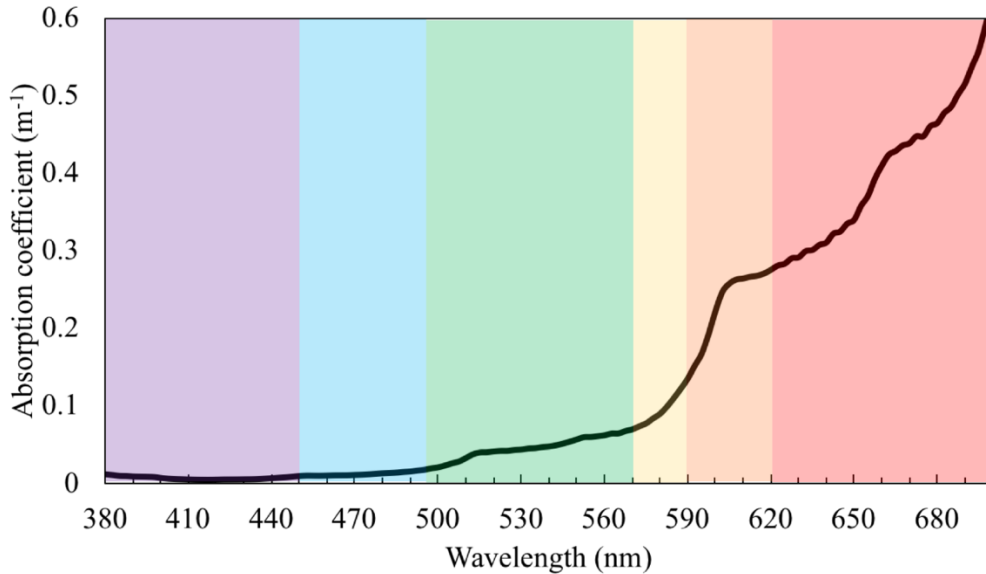


Figure 1.4. Absorption coefficients of light in pure water (from [31]).



In addition to absorption, light photons in water are also susceptible to scattering. In pure water, scattering can be interpreted as derived from fluctuations in the dielectric constant  $\epsilon$  of the medium due to random motion of molecules. Additionally, these scattering events can be understood as due to fluctuations in the refractive index of water  $n$ , as a result of local fluctuations in the density and concentration of the medium [32,33]. In the liquid state, pure water is a polar tetrahedral molecule with unique properties given by its capacity to form Hydrogen bonds with neighbouring molecules [34,35]. Light-water molecules interactions are then dictated by intra and intermolecular vibrational, translational and stretching modes linked to Hydrogen-bonded clusters and, ultimately, light is re-emitted (scattered) undergoing either elastic or inelastic processes.

### 1.2.2. Rayleigh scattering

Rayleigh scattering is an elastic scattering process where photons of given frequency  $\nu_0$  interact with a scatterer at ground energy state, exciting the scatterer to a higher virtual energy level. To return to ground state, the molecule emits a photon of same frequency  $\nu_0$ , resulting in an interaction with no net change in energy (figure 1.5). Elastic scattering will occur under conditions where the volume of the scatterer interacting with light is small compared to the wavelength of excitation, which is true for water molecules and clusters [28]. In water, Rayleigh scattering accounts for signals at least one order of magnitude higher than other scattering processes and, in the absence of other scatterers besides water molecules, information regarding Rayleigh scattering for pure water can be derived from total scattering coefficients  $b_w(\lambda)$  calculated for pure water by [36].

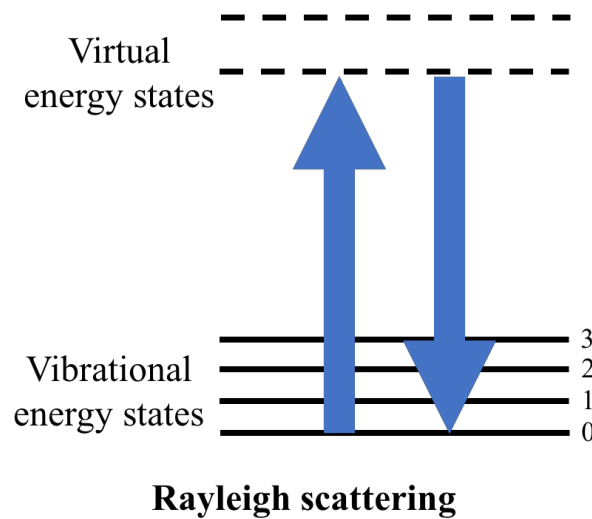


Figure 1.5. Energy transitions involved in a Rayleigh scattering event.

Several researchers studied the origin of Rayleigh scattering in water analysing the time of relaxation for each interaction (*i.e.* time for emission of a photon at frequency  $\nu_0$ ) and associating with relaxation times for known molecular processes [37,38]. For temperatures under 20°C and room temperatures, the authors found two Lorentzian fits for the Rayleigh signal:  $\tau_a$  on the same order of magnitude as molecular rotational processes (dielectric and nuclear magnetic) and  $\tau_b$ , not correlated with any known relaxation times for H<sub>2</sub>O molecules. Further investigations of  $\tau_b$  revealed an activation energy  $\Delta E = 3.0$  kcal/mole, the same proposed for Hydrogen bonding processes and the total relaxation time was also in agreement with the lifetime of Hydrogen-bonded systems. Ultimately, at molecular level, Rayleigh scattering can be interpreted as a conjunction of molecular rotational and Hydrogen-bonded processes.

Spectral distribution of Rayleigh lines is marked by the Doppler shift from moving molecules and the translational velocity distribution is related to the temperature of the system [39]. Even though it is broadly used to determine atmospheric temperature, few attempts have been made to use Rayleigh scattering as a parameter to measure liquid water temperatures accordingly to the Maxwell-Boltzmann relationship. In order to evaluate the potential of using Rayleigh scattering for water temperature predictions, the authors of [40] ran computer simulations and found that Rayleigh lines resolutions of 1 MHz at the FWHM could provide temperature accuracies of up to 0.35 K.

Rayleigh scattering accounts for much of the light scattered by the oceans; however, it is not the only scattering process occurring between light and water molecules. Inelastic light-matter interactions, such as Brillouin and Raman scattering, are characterised by a net change in energy between excitation and scattered photons. Despite exhibiting much lower intensities when compared with Rayleigh scattering ( $\sim 10,000$  times weaker), the study of inelastic scattering processes can provide valuable information regarding water temperature.

### 1.2.3. Brillouin scattering

Brillouin scattering is an inelastic interaction between photons from a light source and phonons arising from vibrations due to periodic density fluctuations in a liquid. As result of this interaction, light photons of a particular frequency are scattered with a shift in frequency proportional to the speed of sound in the medium [41,42]. The final spectrum comprises two smaller intensity Brillouin bands flanking each side of the Rayleigh peak, one blue-shifted

and the other red-shifted. The Brillouin shift of these lines for backscattered light ( $\Delta\nu_B$ ) is given by Bragg's Law (equation 1.1):

$$\Delta\nu_B = \pm 2 \frac{n(S,T,P,\lambda)V_s(S,T,P,\lambda)}{\lambda} \quad (1.1)$$

where  $n(S,T,P,\lambda)$  represents the refractive index of water,  $V_s$  is the sound velocity in the medium and  $\lambda$  is the wavelength of scattered light. Assuming standard conditions of temperature and pressure,  $\Delta\nu_b = 0.27 \text{ cm}^{-1}$  for each Brillouin peak in the water spectrum.

The temperature-dependent behaviour of both speed velocity and Brillouin scattering in water brought attention to Brillouin spectroscopy as an interesting tool to assess subsurface water information. Sharp and well-defined Brillouin lines on water spectrum were another advantage of working with Brillouin signals, exhibiting less potential overlapping with fluorescence signals present in natural waters [41]. Nevertheless, the necessity of knowing salinity values to estimate the speed of sound in water and derive temperature data makes real-time Brillouin methods challenging in saltwater.

The prerequisites for building a LIDAR-compatible Brillouin spectrometer to investigate subsurface water temperature information were summarised in [43] as it follows: (1) laser requirements: wavelength from 380 to 550 nm, short-pulsed, high energy; (2) detector requirements: high sensitivity and able to resolve Brillouin shifts, *e.g.* Fabry-Perot interferometers. According to this evaluation, the author proposed the first Brillouin LIDAR compatible spectrometer using an Yb:doped pulsed fibre amplifier operating at 532 nm, 17.7  $\mu\text{J}$  per pulse and <10 ns at FWHM. Adjustments were made in the fibre in order to minimize Stimulated Brillouin Scattering (SBS) and the system was operated at a stable level below the SBS threshold. A Fabry-Perot interferometer was used coupled to photomultipliers to allow for time-resolution and accurate detection of Brillouin lines. To avoid salinity effects, the authors measured Brillouin shifts of double-distilled water in laboratory and compared the results with the theoretical curve of frequency shifts for pure water. Average accuracies of  $\pm 0.57^\circ\text{C}$  were found for these measurements, limited mostly by the measurement of the position of Brillouin peaks for each acquisition. Further laboratory experiments with ultrapure water reported in [44] indicated that temperature errors of  $0.6^\circ\text{C}$  and vertical resolutions of up to 1.5 m could be achieved when using a Brillouin spectrometer integrated to a pulsed laser with duration of 7.7 ns at FWHM.

The use of Brillouin lines as temperature markers showed to be promising due to the temperature-dependent behaviour of their shifts and the method is indeed used, along with Rayleigh scattering, for measuring temperature of atmospheric gases [45,46]. Still, challenges regarding signal-to-noise-ratios and the need to know the water column salinity distribution for accurate calibration restricts the use of Brillouin scattering as a temperature marker, feasible only for freshwater environments or saltwater areas with virtually constant vertical salinity distribution.

#### 1.2.4. Raman scattering

Raman scattering is an inelastic process firstly observed in 1928 by Raman and Krishnan. It occurs when a photon of frequency  $\nu_0$  interacts with a molecule (vibrational frequency  $\nu_m$ ), exciting this molecule from the ground state of energy to a virtual excited state. When returning to lower energy levels, the molecule emits a photon with frequency different than  $\nu_0$  and the remainder incident energy is transferred to/from vibrational, rotational or lattice structure molecular modes. The emitted photon (scattered) photon, now named the Raman (or Stokes) photon, is shifted in frequency  $\nu_0 \pm \nu_m$  related to the incident photon: if the shift in frequency corresponds to  $\nu_0 - \nu_m$ , the photon is scattered towards lower frequencies (red-shifted) and named Stokes Raman; if the shift is frequency is given by  $\nu_0 + \nu_m$ , the photon is scattered towards higher frequencies (blue-shifted) and known as Anti-Stokes Raman [47] (figure 1.6). All results presented in this thesis refer to vibrational Raman scattering and Stokes Raman shifts.

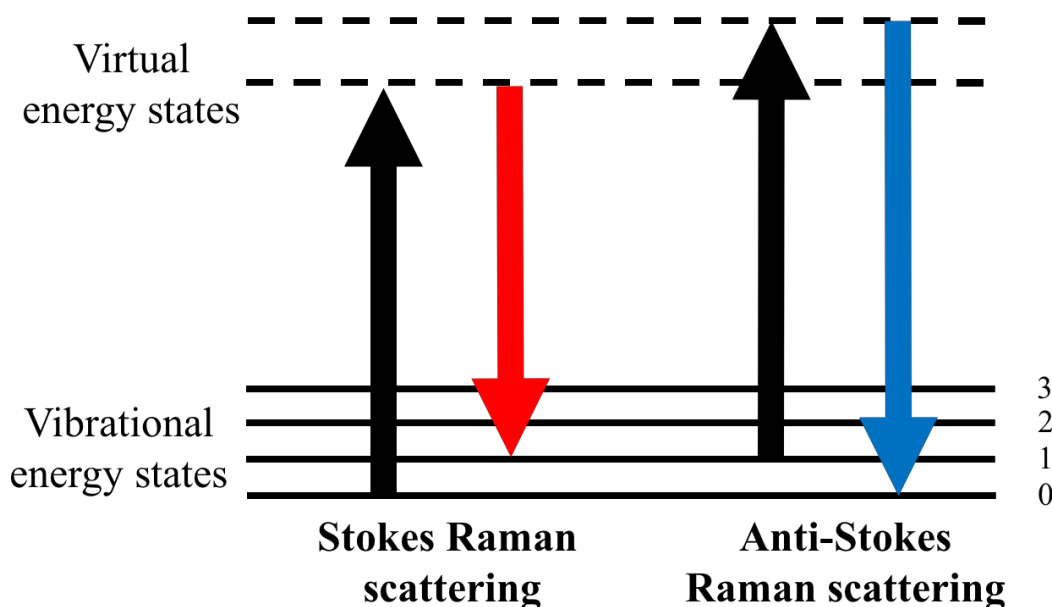


Figure 1.6. Energy transitions involved in Stokes and Anti-Stokes Raman scattering events.

In order to be Raman-active, a molecule must undergo a change in its polarizability constant during the vibrational process [47]. The shift in frequency between incident and scattered photon (or Raman shift) is traditionally presented in wavenumbers ( $\text{cm}^{-1}$ ) and is independent on the wavelength of excitation. Each Raman-active mode is substance-specific and this information is broadly used by pharmaceutical industries in order to determine chemical composition of unknown substances. Raman spectroscopy is a technique used to investigate specific Raman-active modes in a given molecule and their interactions with a light source of known excitation wavelength  $\lambda_0$ .

Water is a triatomic molecule and it is expected that all nuclei will perform their own harmonic oscillations (symmetric stretching, asymmetric stretching and symmetric bending modes), which are shown on figure 1.7. Nevertheless, water molecules are not found isolated in nature but assembled in clusters held together by Hydrogen bonds, resulting in as many 7 intramolecular and 9 intermolecular active Raman-active modes associated with bending, symmetric stretching and asymmetric stretching processes [47,48].

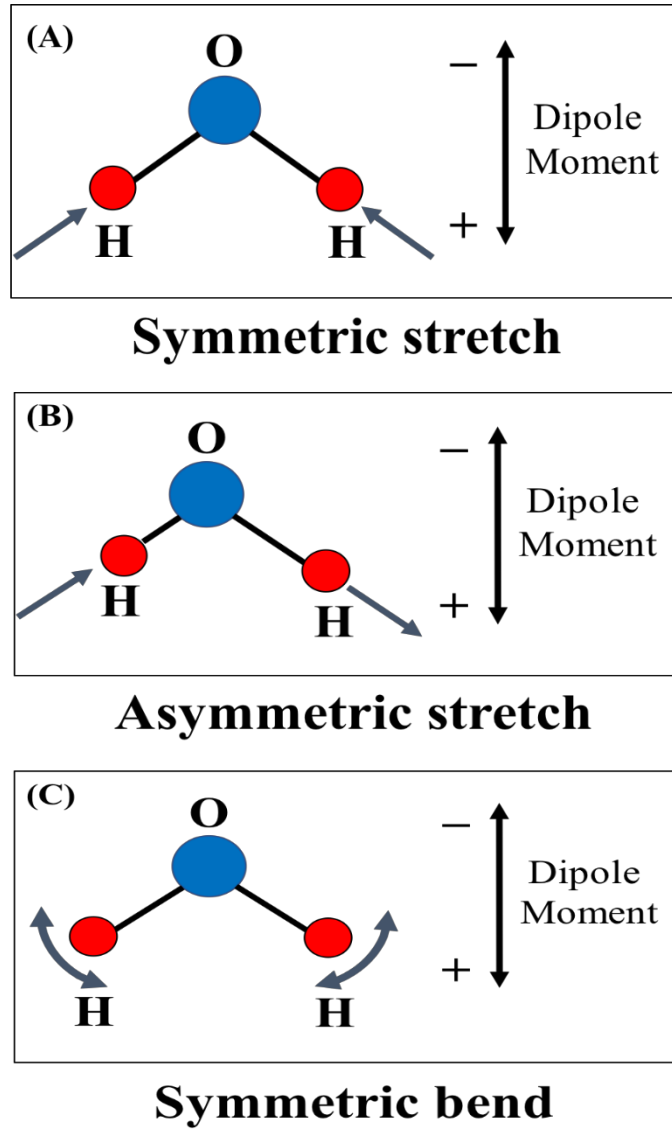


Figure 1.7. Raman-active vibrational modes of a free water molecule. (A) symmetric stretch; (B) asymmetric stretch; (C) symmetric bend.

The probability of a Raman photon being generated from the interaction between an excitation photon with a molecule at a given energy level is known as Raman cross-section ( $\sigma$ ) and expressed in terms of  $\text{cm}^2 \text{ molecule}^{-1} \text{ sr}^{-1}$ . The wavelength-dependence of the Raman cross-sections in water was studied in a  $90^\circ$  geometry by [49,50] for 407, 488 and 532 nm excitation. Cross-section values for other excitation wavelengths between 215 and 550 nm were extrapolated according to equation 1.2 (from [51]).

$$\frac{d\sigma}{d\Omega} = \frac{A\nu_s^4}{(\nu_i^2 - \nu_0^2)^2} \quad (1.2)$$

where  $A$  is a constant which value is derived from laboratory measurements,  $\nu_s$  corresponds to the frequency of scattered Raman photons,  $\nu_i$  is the frequency of intermediate resonance,

and  $\nu_0$  relates to the frequency of excitation photons. Ultimately, in terms of signal intensity, the number of scattered Raman photons of wavelength  $\lambda_s$  arising from a light-matter interaction exhibits a dependence of  $\lambda_s^{-4}$ , hence the use of shorter excitation light sources in the UV and visible (blue-green region) is a common practice in the field.

An extensive study describing Raman-active modes in pure liquid water, spectral features and responses to changes in temperature was reported by [48]. Raman-active modes investigated by [48] are shown in table 1.1., and full unpolarised Raman spectra acquired from near-ultrapure water at 25°C by [52] is shown in figure 1.8. For any given Raman-active mode, intensities and shapes of peaks are influenced by temperature and by the presence of salts dissolved in water, as they affect the chemistry of the OH bond processes and clustering activities [53–56]. The focus of this work is exploring the temperature-dependent behaviour of water Raman signals, not quantitatively accounting for salinity effects.

Table 1.1. Raman-active modes for liquid ultrapure water (from [48])

<b>Vibrational modes</b>	<b>Emission peaks/Gaussian centres</b>
Translational (2 modes)	65 cm <sup>-1</sup> and 165 cm <sup>-1</sup>
Librational (3 modes)	430 cm <sup>-1</sup> , 650 cm <sup>-1</sup> and 795 cm <sup>-1</sup>
Intramolecular Bending (overtones)	2 Gaussians: 1640 cm <sup>-1</sup> and 1581 cm <sup>-1</sup>
OH stretching band (overtones)	5 Gaussians, from 2700 cm <sup>-1</sup> to 3800 cm <sup>-1</sup>

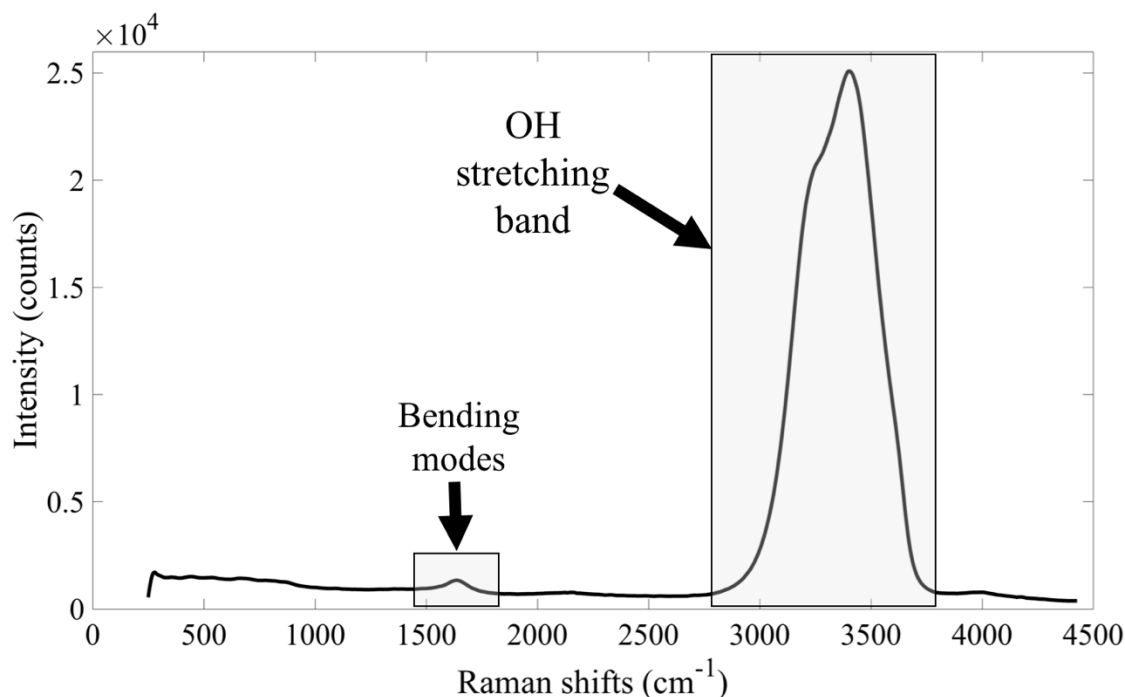


Figure 1.8. Unpolarised Raman spectra from a near-ultrapure water sample in the liquid state. Re-plotted from [52].

Low-frequency Raman modes  $\Delta\nu = 0 - 350 \text{ cm}^{-1}$  are dominated by translational processes, when two Oxygen atoms from different molecules are bonded to the same Hydrogen atom by covalent forces. Vibrations of one Oxygen atom against another originate a restricted translational movement, causing changes in the molecule polarizability and emitting Raman signal [57]. Segré [58] firstly identified the peak at  $170 \text{ cm}^{-1}$  and its anomalous behaviour of decreasing intensity with increased temperatures; in 1932, the authors of [59] described the peak at  $60 \text{ cm}^{-1}$ , weaker and not sensitive to changes in temperature [48].

Raman-active modes described for the frequencies of  $430 \text{ cm}^{-1}$ ,  $650 \text{ cm}^{-1}$  and  $795 \text{ cm}^{-1}$  are derived from librational forces, which are associated with Hydrogen-bonding processes inside the water molecule. Raman signal intensities for these modes reduce with increasing temperature, as a consequence of water clusters breaking due to the amount of kinetic energy in the system. Overtones of bending modes are found on the spectral region from  $1600 \text{ cm}^{-1}$  to  $170 \text{ cm}^{-1}$ , which appear to be linked to intramolecular Hydrogen bonding processes and depend on the number of nuclei participating on this activity [48].

The most prominent feature of the water Raman spectra, the OH stretching band, can be found over a broad spectral region from  $2700 \text{ cm}^{-1}$  to  $3800 \text{ cm}^{-1}$ . This region has been extensively studied over the last decades due to maximum Raman signal intensities and



temperature-dependent behaviour, which could potentially be used on water temperature predictions [53,60–63]. Here, “unpolarised” Raman spectra refers to the collection of all Raman photons scattered by a molecule, regardless of their polarisation state; “parallel-polarised” spectra relates to all Raman photons scattered at same polarisation state as the excitation source; and “perpendicularly-polarised” indicates the Raman photons scattered polarised orthogonal to the excitation light.

For pure water unpolarised Raman spectra, an isosbestic point (*i.e.*, a point of equal light scattering, insensitive to changes in temperature) was found at the OH stretching band around  $3425\text{ cm}^{-1}$  for temperatures between  $3^{\circ}\text{C}$  and  $72^{\circ}\text{C}$  [57]. These features are also found in polarised components of water Raman spectra [64], as shown in figure 1.9a-c (from [52]).

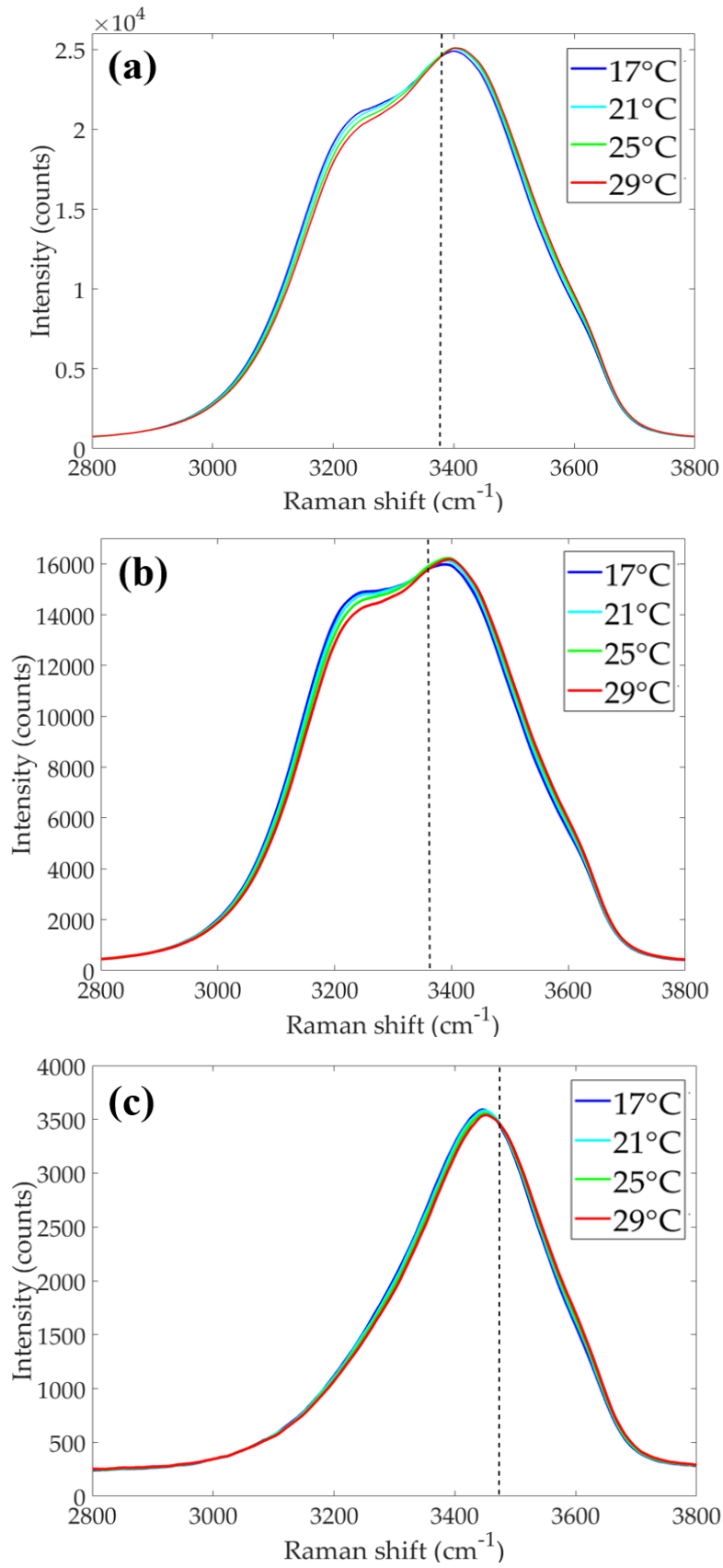


Figure 1.9. Temperature-dependent Raman spectra from ultrapure (reverse osmosis) water. (a) unpolarised spectra; (b) parallel-polarised spectra; (c) perpendicularly-polarised spectra. Isosbestic points are indicated by a dashed line. Spectra acquired by [52].

The origin of the isosbestic point is a matter of intense discussion in the scientific community. According to [65], the sole existence of an isosbestic point indicates the presence of more than one type of Hydrogen-bonding configuration in water. It was suggested that the tetrahedral structure of water allowed for two types of bonding configuration, with hydrogen-bonded (HB) and non-Hydrogen-bonded (NHB) molecules constantly forming and breaking influenced by the amount of heat in the system. The assumption that the isosbestic point would represent the point of equal concentration of these both forms in the system was accepted by the scientific community for many years; nevertheless, simulations made in 2005 [66] estimated the time taken for re-aggregation of NHB molecules into HB clusters to be 200 fs, indicating that NHB forms are transitory in the system. These results were endorsed by [67], who conducted laboratory experiments along with simulations and found that the relative proportion of HB and NHB molecules did not depend on temperature. An agreement regarding the molecular processes giving rise to the isosbestic point has not yet been achieved.

Despite of its uncertain origin, the isosbestic point is an important spectral feature and marks a change in behaviour of the temperature-dependent Raman signal. Regions below the isosbestic point (“low shift” regions), higher Raman signal intensities are found associated with lower temperatures; in regions after the isosbestic point (“high shift” regions), higher signal intensities are found for higher temperatures. This behaviour is identified for both unpolarised and orthogonally-polarised Raman spectra (figures 1.9a-c).

Since the first observations of the temperature-dependent Raman signal behaviour at the OH stretching band [65], several researchers concentrated efforts in measuring water temperature with high accuracy in laboratory, supporting the use of Raman spectroscopy as a potential remote sensing tool for environmental studies. Regardless of the promising results found in laboratory, Raman signal intensities in the environment are much weaker when compared with elastic scattering and other background signals, imposing a challenge for Raman detection. Pioneers such as the authors of [68,69] explored the feasibility of Raman signal temperature predictions by using temperature markers: ratios calculated from temperature-dependent Raman signals collected at different portions of the spectra. From the linear relationship between the markers and reference temperatures, it is possible to build temperature prediction models and estimate the accuracy at which these models can measure

water temperatures. Two main markers can be calculated: two-colour and depolarisation ratios, which give rise to corresponding named methods for predicting temperature.

#### 1.2.4.1. Two-colour method

First proposed by the authors of [70], two-colour temperature markers are ratios of unpolarised Raman signal intensities on either side of the isosbestic point. Traditionally, the water Raman spectrum for each temperature was divided in a series of Gaussians and a linearly correlated temperature marker was determined by calculating a ratio between areas of different curves. Although the number and positioning of Gaussians didn't carry any spectral information or significance, for many years this process of fitting Gaussians to acquired spectra was the dominant method for water temperature prediction when using Raman spectroscopy [69,71–78].

Recently, the authors of [56,63] proposed the use of two-colour markers from unpolarised Raman spectra by integrating signals in channels of  $200\text{ cm}^{-1}$ , commonly located on opposite sides of the isosbestic point (figure 1.10). The authors reported accuracies of up to  $\pm 0.1^\circ\text{C}$  for ultrapure water temperature predictions in laboratory by using two-colour markers calculated from unpolarised Raman spectra acquired by a dispersive Raman spectrometer (Enwave EZRaman-I, which incorporates a continuous-wave (CW), Nd:YAG, 532 nm excitation laser). This approach represents a transition towards the use of two-colour markers in LIDAR methods, as the authors proposed that Raman signals could be collected in spectral channels by using optical filters.

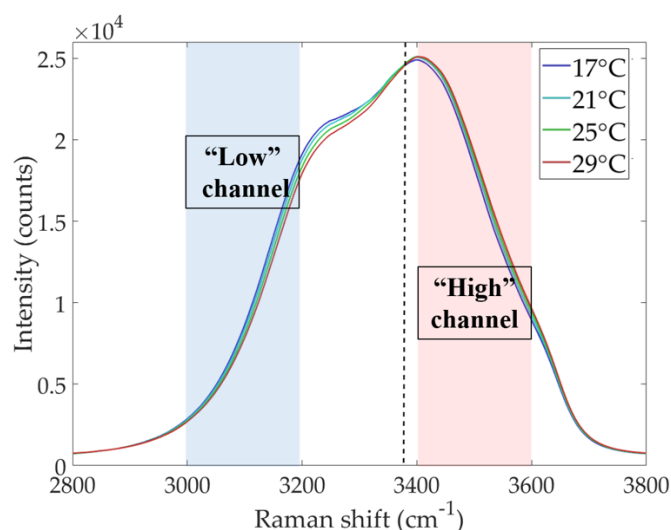


Figure 1.10. Suggested unpolarised Raman signal acquisition in channels ( $200\text{ cm}^{-1}$ ) for two-colour markers calculation.

Two-colour methods are promising tool for measuring water temperature in laboratory; field implementations in natural waters, however, may be challenging due to different absorption, scattering and transmission of light at different wavelengths.

#### 1.2.4.2. Depolarisation ratio method

Depolarisation ratio is a parameter traditionally calculated as a ratio between perpendicularly and parallel-polarised signals at a given wavelength (equation 1.3). In water, these ratios exhibit a linear temperature-dependent behaviour and can be used as temperature markers.

$$Depolarisation = \frac{I_{\perp}^{\lambda_{xxx}}}{I_{\parallel}^{\lambda_{xxx}}} \quad (1.3)$$

Attempts to use depolarisation markers for temperature predictions were made in [68,79], using a circularly-polarised dye laser (460 nm) to collect temperature-dependent Raman spectra from a saline aqueous solution (NaCl 40%). Theoretical accuracies of  $\pm 0.5^{\circ}\text{C}$  were proposed to be achieved by the depolarisation method. The authors concluded that analysing orthogonally polarised Raman signals collected from the same wavelength was effective in avoiding different light absorption and scattering effects reported for the two-colour method. Moreover, laser induced fluorescence is usually isotropic, *i.e.*, both parallel and perpendicular components have equal intensities along the axis of polarisation and, as consequence, depolarisation markers would be less impacted by fluorescence signals present in natural waters. Following these first investigations, the authors of [80] reported an accuracy of up to  $\pm 0.5^{\circ}\text{C}$  for water temperature predictions using depolarisation markers to process Raman spectra acquired by using a 470 nm pulsed dye laser as excitation source.

Ultimately, both two-colour and depolarisation techniques have shown potential to be explored in remote sensing of ultrapure and artificial seawater temperatures in laboratory, with maximum temperature predictions of  $\pm 0.1^{\circ}\text{C}$  being achieved by two-colour markers [52].

### 1.3. Raman remote sensing of oceanic waters

Theoretical and laboratory predictions for pure and standard saltwater are valuable results for showing the potential of Raman spectroscopy as a temperature remote sensing tool, however they do not account for potential signal interactions with optically active constituents commonly found in natural waters. Excitation (laser) and scattered (Raman) photons may interact with particles and dissolved substances in water, undergoing absorption, further scattering or being overlapped by fluorescence signals. In this section, I discuss which optical interactions in natural waters are more likely to impact the implementation of Raman spectroscopy as a water temperature sensing technique and which strategies can be adopted to minimize the negative effects of these interactions.

#### 1.3.1. Fluorescence

Fluorescence is frequently said to be the “enemy” of Raman spectroscopy, since the same laser source can excite both optical processes. Fluorescence can be described as it follows: photons of wavelength  $\lambda_0$  are absorbed by a molecule, exciting its electrons to higher energy levels; in order to return to the lowest energy level, these electrons may undergo a radiative process and emission of photons of wavelengths  $\lambda_F$ , longer than the incident light ( $\lambda_F > \lambda_0$ ) [28]. This red-shifted photon is always emitted at the same wavelength range and this characteristic makes the fluorescence signal a valuable tool on identification of organic and inorganic compounds.

Pure water doesn't fluoresce when interacting with light, but optical constituents in natural waters such as chlorophyll-a (Chl-a) and DOM will readily absorb and fluoresce at visible wavelengths and contribute significantly to the total backscattered signal [28]. Depending on the emission range, fluorescence signals may impose a logistic issue for using optical and LIDAR methods in the environment, overlapping with signals of interest for Raman spectroscopy techniques and compromising the accuracy of final temperature measurements.

### 1.3.1.1. Chlorophyll-a and other photosynthetic pigments

Chlorophyll-a (Chl-a) is the mandatory photosynthetic pigment present in all autotrophic organisms. It is responsible for the absorption of sunlight used for the photosynthetic process, hence being a key element for primary productivity, carbon fixation and organic matter production at the lowest levels of food webs. In the oceans, this pigment is present in major functional group known as phytoplankton.

By definition, phytoplankton is the group of all small organisms living in suspension in aquatic environments, depending on local dynamics to move in the water column, and providing the majority of Carbon available for the higher levels of aquatic food webs [81]. In order to incorporate inorganic Carbon and produce organic matter, phytoplankton organisms rely on the absorption of UV and visible light by photosynthetic pigments, such as Chl-a, with range of absorption known as Photosynthetic Active Radiation (PAR) [28]. As UV and visible light have a nearly-exponential decay in intensity along the water column, phytoplankton organisms need to be positioned, during the day, at depths where PAR is available for assimilation.

After absorption by Chl-a, sunlight can either be dissipated as heat -contributing for photochemistry- or as fluorescence. Chl-a fluorescence signals exhibit a clear peak at 685 nm, invariant in spectral position with excitation wavelength but with higher signal intensities found for UV/violet-blue excitation and decreasing towards longer wavelengths. This behaviour coincides with the maximum absorption peaks for Chl-a (300 to 400 nm) [28], linking the photosynthetic activity with intensity of fluorescence signals and becoming an important ecological parameter used to estimate total phytoplankton biomass and productivity. Chl-a fluorescence spectroscopic methods also have the advantage of being effective measurement techniques at low cell concentrations and suitable for working in the marine environment [82,83].

Besides Chl-a, many phytoplankton species synthesize accessory pigments with absorption maxima at different regions of the UV-visible spectrum (*e.g.* chlorophyll-b, phycobilins,  $\beta$ -carotene). This adaptive strategy allows for the cell to optimize the photosynthetic process in response to various light conditions and can be used by researchers to identify taxonomic groups through fluorescence spectrometry and imagery [84,85].

Overlapping between Raman signals at the Raman OH stretching band and fluorescence from Chl-a, has been addressed by many authors [56,86,87]. The issue is particularly concerning when green light (532 nm) is used as excitation source, as the OH stretching band will have maximum Raman signals from 640 to 670 nm, considerably close and being overlapped by the Chl-a fluorescence peak around 685 nm. This overlapping implicates in compromised accuracies for Raman water temperature predictions, especially when the “two-colour” technique is used due to collection of Raman signal at two wavelengths undergoing different attenuation processes in natural waters [68,69,86]. Excitation in the blue range, around 480 nm, has been suggested as an alternative to avoid overlapping between Raman and Chl-a fluorescence signals, since the OH stretching band for this excitation is located between 540-560 nm, further away from the fluorescence peak.

#### **1.3.1.2. Dissolved Organic Matter - DOM**

Dissolved Organic Matter (DOM) is a general name for the portion of optically active constituents that can't be mechanically separated from natural waters ( $< 2\mu\text{m}$ ), some of which may fluoresce. Different types of organic compounds interacting simultaneously with light generate multiple overlapping of absorbance and emission peaks, giving rise to a broad fluorescence band commonly characterized from 308 to 600 nm [28].

Coloured Dissolved Organic Matter (CDOM or *Gelbstoff*) is the portion of DOM responsible for intense light absorption on UV-blue regions of the spectrum and have direct impact on remote sensing data acquisition [88,89]. CDOM fluorescence signals were found to be compatible with the concentration of these compounds in the environment, exhibiting peaks of maximum intensity between 400 and 450 nm when excited by 308 nm light [90]. Protein-like substances are also constituents of total DOM and fluorescence signals with maxima from 300 to 350 nm have been reported in the literature [89–91]. A complete description of all DOM components is not yet available, evidencing the complexities of finding spectral signatures on LIDAR data. For Raman spectroscopy studies and satellite sensors collecting signals in visible range, the impacts of CDOM fluorescence and absorption of light need to be corrected by a final data analysis.

The occurrence and concentration of CDOM in aquatic environments depend on the influence of rivers, groundwater influx and local tidal and waves dynamics, imposing a challenge for optical characterization and classification of water masses. In [77], artificial



neural networks (ANN) were used to determine simultaneous temperature and salinity information from waters samples in the presence of DOM (concentrations up to 350 mg/L). A 488 nm, Argon-Ion laser was used to retrieve temperature-dependent Raman spectra; the signals were processed by a five-layer ANN and the “two-colour” technique was applied to the processed data. Accuracies of  $\pm 0.8^{\circ}\text{C}$  and 1.1 psu were found for temperature and salinity predictions, respectively. More recently, the authors of [92] also used ANN to predict temperature and salinity in natural waters from Raman signals retrieved from samples exhibiting high DOM concentrations, finding accuracies of up to  $\pm 0.1^{\circ}\text{C}$  and 0.2 psu, respectively. Although effective on neutralizing interactions between Raman signal and DOM fluorescence, none of these studies presented LIDAR-compatible solutions.

### **1.3.2. Optically active particles in oceanic waters**

By definition, “particles” represent the portion of natural water constituents which can be mechanically separated from the water ( $> 0.7\ \mu\text{m}$ ), usually by filtration or centrifugation processes. Particulate matter of diverse organic and inorganic origins is found in suspension in the oceans, with higher concentrations typically found at the coastal zone and decreasing towards the open sea. Both absorption and scattering characteristics of saltwater are impacted by the presence of particulate matter and need to be considered when working with remote sensing methods.

As previously discussed, light is absorbed by water molecules exhibiting a near-exponential decay with travelled vertical distance. Besides molecular absorption, light propagating in natural waters may also be absorbed by other constituents such as phytoplankton cells, CDOM and both organic and inorganic non-algal- particles, reducing the vertical transmission of both excitation and scattered signals.

Particles in suspension in water are also major contributors to the total scattered signal when their diameter is larger than the wavelength of excitation. In this scenario, differences between the refractive index of light when leaving water and interacting with the particle result in changes on direction of the light beam, contributing to changes in the transparency of water and light propagation. Sediments in suspension [93], bubbles [94], colloidal particles [95] and many phytoplankton species [96] may act as scatterers reducing the vertical transmission of visible light signals in water.

Enhanced light absorption and scattering by water constituents has a direct impact on the accuracy of measurements made by remote sensing tools, as the concentration and types of constituents are highly variable. From these unpredictable interactions arise the need for *in situ* validation of remote sensing measurements as a continuous process to correlate the spectral signals retrieved by sensors and optically active particles in water.

#### 1.4. Raman spectroscopy and LIDAR-compatibility

Raman spectroscopy methods have been evaluated as promising tools for monitoring subsurface water temperature by previous authors [69,71,97,98]. In order to be LIDAR-compatible, a Raman spectrometer is required to operate with a short-pulsed laser ( $< 2$  ns at FWHM) and operate with fast (short response time) detectors. This configuration would allow for depth determination calculated from the time taken for the Raman photon to reach the detectors at the surface. In this matter, the IOP represented by the total beam attenuation coefficients  $c(\lambda)$  indicates the distance travelled by light of given wavelength until all photons are either scattered or absorbed by water. For seawater with no other optical constituents,  $c_{sw}(\lambda)$  is given in  $m^{-1}$  by equation 1.4.

$$c_{sw}(\lambda) = a_{sw}(\lambda) + b_{sw}(\lambda) \quad (1.4)$$

where  $a_{sw}$  and  $b_{sw}$  are the wavelength-dependent absorption and scattering coefficients for light in seawater estimated by [99]. By using the coefficient  $c_{sw}$  it's possible to determine the maximum depth of penetration and depth of extinction for light in seawater, given by:

$$I(\lambda, z_n) = I(\lambda, z_0) e^{-c_{sw}(z_n - z_0)} \quad (1.5)$$

where  $I(\lambda, z_n)$  indicates the intensity of light of wavelength  $\lambda$  at a given depth  $z_n$ ;  $I(\lambda, z_0)$  is the initial intensity of light of wavelength  $\lambda$  at the surface  $z_0$ ; and  $c_{sw}$  is the wavelength-dependent coefficient of total light attenuation.

Measurements of downwelling plane irradiance ( $E_d(z, \lambda)$ ) are easy to obtain during field activities. From downwelling plane irradiance information, a quasi-inherent optical property (*i.e.* marginally affected by environmental conditions) can be calculated, known as downwelling diffuse attenuation coefficient ( $K_d(z, \lambda)$ ) [100].

As seen in section 1.3.2., the presence of salts and other optical constituents in seawater may also impact the light absorption and scattering coefficients and, ultimately,  $K_d$ . In order to account for the majority of particulate and dissolved optically active constituents in natural waters Jerlov proposed a classification scheme, known as “Jerlov water types” [101]. The scheme is based on the transmittance of light of different wavelengths in oceanic and coastal waters of different compositions, allowing for the estimation of light propagation at different environmental conditions. Recently, [100] conducted a detailed study in laboratory attributing chlorophyll-a and CDOM concentrations to different Jerlov water types and calibrating  $K_d$  values proposed by Jerlov in 1968 (figure 1.11).

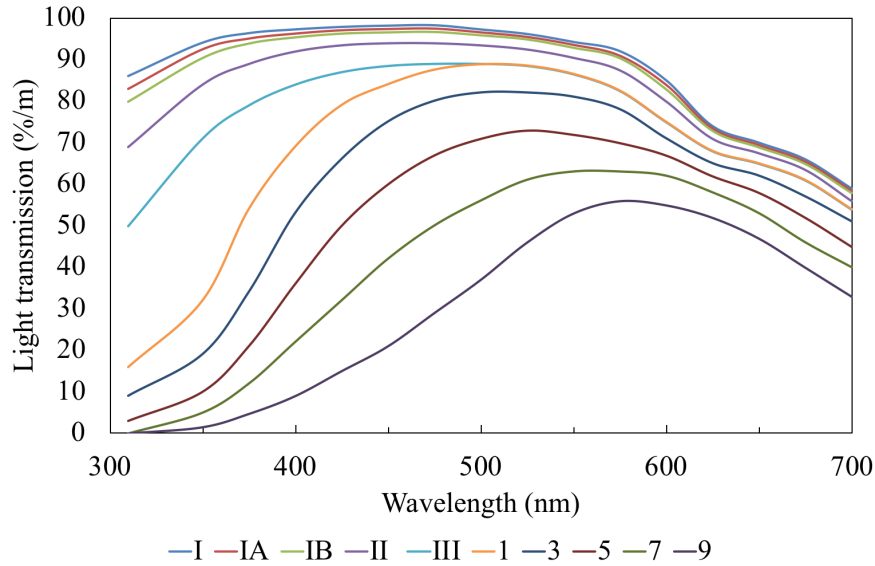


Figure 1.11. Jerlov water classification. Vertical transmissions along 1 m of water column are shown for oceanic water types (I-III) and coastal water types (1-9). Data obtained from [102].

For LIDAR implementations, the study of both downwelling and upwelling diffuse attenuation is important, as the final goal is retrieving backscattered photons at the surface. Downwelling photons interact with water molecules, particles and dissolved organics, undergoing elastic and inelastic scattering and change in their directions of propagation. In the case of solar irradiance (where there is a large angular distribution), the change from downwelling (downwards) to upwelling (upwards) direction occurs with pronounced horizontal angular distributions; hence, it has been shown that the upwelling attenuation coefficients  $K_u(z, \lambda)$  are  $\sim 2.5$  times the values attributed to  $K_d(z, \lambda)$  [103]. In a LIDAR scenario, where the irradiance is confined to a low-divergence beam at near normal incidence to the surface, the upwards and downwards coefficients can be assumed to be equal.

### 1.4.1. Past research on LIDAR-compatible Raman spectroscopy of natural waters

The idea of assembling a LIDAR-compatible Raman spectrometer for depth-resolved remote sensing of natural waters temperatures has been around since 1970's. A summary of the main findings in this field is presented in this section.

Laboratory studies showed potential to achieve accuracies of up to  $\pm 0.5^{\circ}\text{C}$  when determining temperatures from a saline solution [68], picturing Raman spectroscopy as a promising technique for studying the oceans and opening the field for further investigations. In 1977, [69] attempted the first field measurements of subsurface water temperature using Raman spectroscopy. Unpolarised Raman spectra from an estuary were retrieved by using a 337.1 nm pulsed laser (10 ns) as excitation source yielding accuracies of  $\pm 2.0^{\circ}\text{C}$  for subsurface water temperature determination. Interactions between both incident and backscattered photons with IOPs were considered a major source of noise in the spectra, compromising the final temperature accuracies achieved by the method. As IOPs are wavelength-dependent, the authors theorized that using the depolarisation method could reduce the impact of absorption and fluorescence from IOPS overlapping with Raman photons since Raman signals at same wavelengths are used to calculate temperature markers. In 1979, the authors of [71] conducted further field measurements using same experimental design and analysis as in [69], retrieving unpolarised Raman signals from depths up to 30 m. Accuracies of  $\pm 1.2^{\circ}\text{C}$  were achieved for temperature determination of signals up to 3 m depth and even better accuracies were achieved for laboratory experiments with saline solutions. The compromised accuracies were, again, attributed to light interactions with optically active constituents in natural waters and researcher focused on proposing a Raman spectrometer able to fulfil the needs for depolarisation analysis. In 1983, the authors of [97] performed experiments in an artificial water tank using a 470 nm Dye laser as excitation source and calculating depolarisation markers from orthogonally polarised components of Raman spectra. Temperature gradients of  $\pm 0.5^{\circ}\text{C}$  were detected and the authors proposed an airborne-based system able to perform these measurements.

Liu *et al.* [73] designed and evaluated the performance of a Raman-compatible LIDAR system on measuring water temperature in laboratory and field trials, achieving accuracies of  $\pm 0.4$  and  $\pm 0.5^{\circ}\text{C}$ , respectively. The setup included a 532 nm pulsed (15 ns) Nd:YAG laser collecting full unpolarised Raman spectra, collected by a telescope (120 mm

of aperture) and detected by a photomultiplier (PMT). Measured Raman spectra were deconvolved into two Gaussians and used to calculate two-colour markers. Field trials were successful on measurements on depths up to 3 m ( $\pm 1.5$  m).

By the end of 1990's it was a consensus among researchers that fluorescence and attenuation from optically active constituents in natural waters affected the final accuracies for two-colour temperature predictions. Depolarisation ratios, otherwise, could potentially be less impacted by other signals and IOPs in natural waters but its implementation was challenging due to (1) low intensities of perpendicularly polarised Raman signals and (2) the need for simultaneous collection of both orthogonally polarised spectral components [52,63].

The need for enhancing results obtained from two-colour markers led researchers to evaluate which background correction techniques could increase temperature prediction accuracies. The authors of [86] simulated the origins of laser-induced fluorescence in natural waters from excitation sources ranging from 510 to 570 nm. The authors found two main sources of background signal, independent on the wavelength of excitation: 440 and 580 nm, associated with *Gelbstoff* and at 685 nm linked to Chl-a fluorescence. Background correction was performed by subtracting averaged fluorescence signals from Raman spectra, reducing their impact on final two-colour temperature markers.

In 1999, the authors of [104] investigated how the choice of excitation wavelength could improve two-colour analysis and reduce overlapping between fluorescence and Raman peaks in natural waters. Using a pulsed tunable laser (480 nm to 530 nm) the author collected unpolarised Raman spectra from Chesapeake Bay using various wavelengths of excitation and evaluated which laser-induced fluorescences overlapped with Raman peaks. The authors found the same fluorescence peaks as reported by [86] and observed that overlapping between Raman and Chl-a fluorescence could be avoided when using excitations from 495 to 510 nm; DOM fluorescence, however, could not be avoided by using any excitation. The author also evaluated wavelength dependence of laser-induced background signals scattered by natural waters [87], suggesting the use of laser sources within the range of 495 and 520 nm for coastal water studies.

Almost all experimental designs and analysis required full collection of water Raman spectra and subsequent Gaussian decomposition for two-colour processing. In 2015, the authors of [63] proposed a new approach for this analysis and calculated temperature

markers by integrating unpolarised Raman signal in channels of  $200\text{ cm}^{-1}$  width and finding the ratios of intensities between channels on opposite sides of the isosbestic point. Temperature-dependent water Raman spectra were acquired with a green laser as excitation source (532 nm, CW,  $2\text{ cm}^{-1}$  of spectral resolution) and accuracies of  $\pm 0.1^\circ\text{C}$  were found for ultrapure water samples. This was an important step towards the feasibility and implementation of a LIDAR-compatible Raman spectrometer, as the need of full spectral collection and complex analysis was extinguished; moreover, general optical filters could be used to fulfil the task of collecting signal at spectral channels with high sensitivity to temperature changes, making possible the design of a robust system to be used in field activities.

A summary of selected results achieved in the field of Raman spectroscopy applied to water temperature prediction is shown in table 1.2.

Table 1.2. Summary of selected past research aimed at water temperature sensing.

Publication	Water type	Laser source	Temperature marker	Laboratory temperature accuracy (°C)	Marker sensitivity (% change/°C)	Field experiments and accuracy (°C)	LIDAR compatibility
Chang and Young, 1972 [61]	NaCl (40% solution)	Dye laser, 460 nm, circularly polarised	Depolarisation (circular)	±0.5 (theoretical)	1.7 (theoretical)	-	No
Leonard <i>et al.</i> , 1977 [69]	Natural (coastal)	Nitrogen laser, 337.1 nm, pulsed	Two-colour	-	-	Yes ±2.0	Yes
Leonard <i>et al.</i> , 1979 [71]	Natural (oceanic)	Nitrogen laser, 337.1 nm, pulsed	Two-colour	-	1	Yes ±1.0	Yes
Leonard <i>et al.</i> , 1983 [97]	Natural	Dye laser, 470 nm, pulsed	Depolarisation	±0.5	1	-	Yes
Breschi <i>et al.</i> , 1992 [72]	Purified	Argon-ion, 515.5 nm, CW	Two-colour	±0.5	1	No	No
Liu <i>et al.</i> , 1992 [73]	Purified (lab), oceanic (field)	Nd:YAG, 532 nm, pulsed	Two-colour	±0.4	-	Yes ±0.5	Yes
Oh <i>et al.</i> , 2015 [105]	Purified	Nd:YAG, 532 nm, CW	Two-colour	±0.2	0.5	No	No
Artlett <i>et al.</i> , 2015 [63]	Purified	Nd:YAG, 532 nm, CW	Two-colour	±0.1	1.48	No	No
Artlett <i>et al.</i> , 2015 [63]	Tap water	Nd:YAG, 532 nm, pulsed	Two-colour	±0.5	0.4	No	Yes
Artlett <i>et al.</i> , 2017 [56]	Natural (filtered)	Nd:YAG, 532 nm, CW	Two-colour	±0.2	-	-	No

## 1.5. Thesis context and outline

There is an increasing demand for new technologies able to rapidly profile the water column from airborne and ship-based platforms. To achieve this purpose, Raman spectroscopy has been investigated by several research groups as a potential technique to be coupled to LIDAR methods for the remote sensing of water temperature. Laboratory investigations aiming to operationalise Raman spectroscopy as a technique for measuring water temperature have been conducted since the 1970's [61,69,71], however, they were limited by the technology available at the time. The majority of these studies consisted of laboratory measurements of potential accuracies that could be achieved by Raman temperature markers, and the equipment used did not fulfil LIDAR-compatibility requirements. In recent years, a reduced number of studies have re-assessed the potential of the technique for water temperature measurement by using commercial Raman spectrometers, achieving accuracies as high as  $\pm 0.1^{\circ}\text{C}$  for ultrapure water predictions [63]. This was the starting point for the work in this thesis, where I intend to benefit from the technological development in lasers, detectors and data acquisition methods to build LIDAR-compatible Raman spectrometers.

Advances in laser technologies led to an increased number of lasers compatible with LIDAR methods. Pulsed light sources operating at wavelengths suitable for underwater LIDAR investigations, such as green and blue, are broadly available nowadays. LIDAR bathymetric measurements are commonly obtained employing frequency-doubled Neodymium lasers (Nd:YAG), with wavelengths varying in the green range (527-532 nm).

Compact, sensitive, fast-response detectors such as photomultipliers are desirable for fulfilling LIDAR-compatibility requirements. Technological improvements in photomultipliers detectors technologies have also occurred since the incipient studies of [69,79,97]. Nowadays, commercial photomultipliers are reduced in size, exhibit lower rise times and demand lower power input (tens of milliWatts) in comparison with the equipment used in the early investigations. Oscilloscope and other data acquisition technologies now allow for simultaneous signal collection in multiple channels, enabling assessment of different spectral channels carrying distinctive information in near-real time. This is particularly important for calculation of Raman temperature markers and investigation of other signals of interest, such as fluorescence from optical constituents in natural waters.



Lastly, computers and data processing methods have experienced enormous advancements in the last decades, allowing for straightforward application of multivariate analysis such as Principal Component Analysis, multiple linear regression models, etc. The possibility of easily manipulating temperature-dependent water Raman signals enabled exploration of different methods for calculating temperature markers in this thesis.

The development of LIDAR technologies for remote sensing of the oceans has also been in evidence in the last few decades. Bathymetry measurements performed by airborne laser systems is now a major source of data for coastal management, with excitation lasers traditionally operating in the green range (532 nm). The signal backscattered from water is acquired by several spectral channels in the visible and infrared ranges in order to determine the position of the water surface and the different light scattering. The lasers and detectors employed in LIDAR systems for bathymetry have similar requirements to those used for Raman remote sensing of water temperature. Both measurements, Raman and bathymetry, could possibly be performed simultaneously by adding new collection channels for acquiring Raman signals at wavelengths of high temperature sensitivity. The work presented in [52,56,63] include extensive reasoning regarding the spectral widths and wavelengths of such channels, serving as a starting point for the LIDAR implementation of Raman remote sensing of water temperature work presented in this thesis.

This thesis explores the potential of Raman spectroscopy for measuring temperatures from natural water samples in laboratory with target accuracies of  $\pm 0.5^{\circ}\text{C}$ , allowing for LIDAR-compatibility and minimum vertical resolution of 0.5 m (primary goal). It includes experimental investigations conducted by using a commercial dispersive Raman spectrometer and two custom-designed multichannel Raman spectrometers, each integrated to pulsed lasers of different wavelengths (green and blue light), aiming to determine which is the best excitation wavelength for Raman sensing of water temperature (secondary goal).

Chapter 2 outlines the equipment and analyses methods used throughout this research, including description of spectrometers designs and temperature markers calculations.

Chapter 3 explores methods for understanding and minimizing the impact of fluorescence signals in Raman remote sensing of natural waters temperature by using a commercial dispersive Raman spectrometer (532 nm excitation). It comprises one article,

referred as manuscript 1, which is intended to be submitted to *Optics Express*, as well as a detailed analysis regarding the potential origins of spectral baseline in natural waters.

Chapter 4 introduces a custom-built multichannel LIDAR-compatible Raman spectrometer, operating with excitation wavelength of 532 nm (green light) and demonstrates its use for temperature measurements on ultrapure and natural water samples in laboratory. The main experimental findings are shown in an article which is intended to be submitted to the journal *Sensors*, referred as manuscript 2. Further analyses regarding accuracies of temperature predictions, sensitivities and percentage errors associated with the temperature markers are also presented in the Chapter.

Chapter 5 contains the design and operation of a custom-built multichannel LIDAR-compatible Raman spectrometer integrated to a 473 nm excitation laser (blue light). The main findings of water temperature prediction experiments conducted in laboratory are shown in an article which is intended to be submitted to *Frontiers in Marine Science* journal, referred as manuscript 3. Additional material in this Chapter includes incipient LIDAR simulations exploring Raman returns from depths calculated for both blue and green light excitation, which is critical to the field implementation of Raman remote sensing of oceanic and coastal waters temperatures.

Chapter 6 summarises the main conclusions of this work and explores further work which is intended to be done towards field implementation of the custom-built multichannel LIDAR-compatible Raman spectrometers presented in this thesis.

Finally, appendices are presented including (A) simulations of temperature predictions in the field; (B) technical specifications of optical filters used in this research; (C) conference publications of work related to this research; (D) a white paper submitted to the U.S. Office of Naval Research Global.

# **CHAPTER 2**

## **EXPERIMENTAL AND ANALYSIS METHODS**

In this Chapter I will present a detailed summary of all experiments and data analysis conducted throughout this research project, providing information regarding acquisition and post-processing methods. The topics addressed here include the presentation of three

spectrometers employed in these investigations, the nature of water samples under analysis, and temperature markers calculations including accuracies and Signal-to-Noise ratios.

Regarding the spectrometers (RS), three devices will frequently be referred to during this thesis:

- i) A commercial dispersive RS utilising green laser excitation (532 nm), hereafter referred as the “Enwave Raman spectrometer”;
- ii) A custom-built (by the author and colleagues) multichannel, LIDAR-compatible RS utilising green laser excitation (532 nm) hereafter referred as the “green multichannel RS”;
- iii) A custom-built (by the authors and colleagues) multichannel, LIDAR-compatible RS utilising blue laser excitation (473 nm) hereafter referred as the “blue multichannel RS”.

## 2.1. Water samples

Natural and ultrapure water samples were investigated by this research work. For samples collected in 2013, Raman spectra acquisition was performed in the laboratory by former PhD student Christopher Artlett [52] with the commercial Enwave spectrometer and were re-analysed during my PhD (Chapter 3). Experiments involving Raman signal acquisition of samples from years 2015 to 2017 were performed as part of my PhD laboratory activities (Chapters 4 and 5). Raman spectroscopic measurements were performed within few hours of collection for all water samples presented in this study. Table 2.1 correlates the origin of all water samples analysed in this study with respective years of collection, spectrometers used for Raman acquisitions and the Chapters where each water type was analysed.

Table 2.1. Water samples sources and techniques for Raman signal acquisitions.

<b>Location/Source</b>	<b>Years</b>	<b>Water type</b>	<b>Raman acquisition</b>	<b>Chapter</b>
<b>Milli-Q water</b>	2015, 2016, 2017	Ultrapure	Enwave RS; Green Multichannel RS; Blue Multichannel RS;	4,5
<b>Manly Dam</b>	2013	Fresh	Enwave RS	3
<b>Rose Bay</b>	2013	Saline (filtered)	Enwave RS	3
<b>Manly Beach</b>	2013	Saline	Enwave RS	3
<b>Clontarf</b>	2013, 2015, 2016, 2017	Saline	Enwave RS; Green Multichannel RS Blue Multichannel RS	3,4,5
<b>Sugarloaf Bay</b>	2013	Saline	Enwave (532 nm)	3
<b>Rhodes</b>	2013	Saline	Enwave (532 nm)	3

Milli-Q water (also referred in this work as “ultrapure” water) samples were obtained from a filtration unit located at Macquarie University Wetchemistry Lab (Millipore Direct-Q 3). These samples were filtered and deionised, exhibiting high level of purity and typical resistivity of  $18.2 \text{ M}\Omega$  at  $25^\circ\text{C}$ . Raman signal acquisitions from Milli-Q water samples were performed with both multichannel LIDAR-compatible spectrometers (green and blue) in order to determine accuracies, sensitivities and errors associated with temperature predictions in the absence of dissolved and particulate substances. Milli-Q water temperature markers were also used as “standard” for self-calibrated studies in Chapters 4 and 5.

Natural water samples were collected directly from the environment or from research storage facilities. Rose Bay water samples were obtained from the Macquarie University Seawater Storage Facility and were collected in conditions of at least 10 days without pluvial precipitation in the area. These samples were filtered (sand filter) and UV treated prior Raman spectra acquisitions, hence they exhibit reduced fluorescence signals when compared with other natural water samples. Due to this reduced background signal, Rose Bay samples were used as “standard” for saltwater temperature markers presented in Chapter 3. A map showing the locations for each sampling site is shown in figure 2.1.

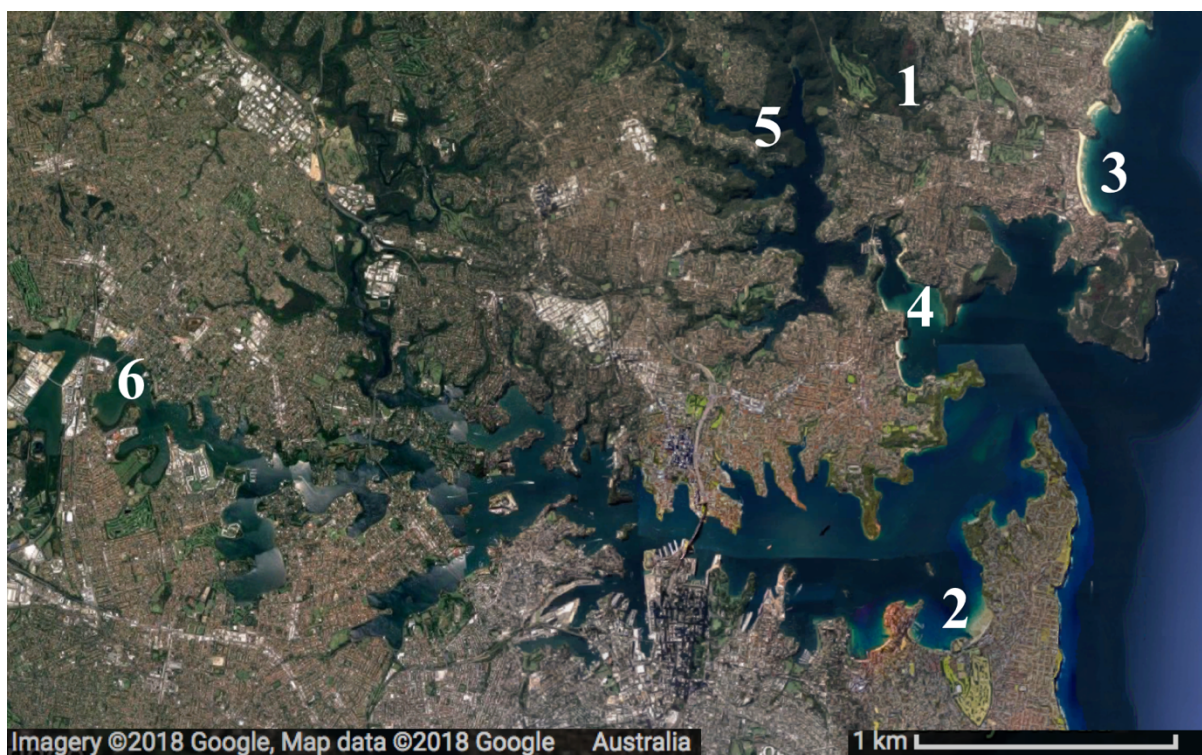


Figure 2.1. Natural water sample collection locations. (1) Manly Dam, (2) Rose Bay, (3) Manly Beach, (4) Clontarf, (5) Sugarloaf Bay, (6) Rhodes.

Clontarf water samples were also investigated by both multichannel LIDAR-compatible Raman spectrometers (green and blue). Clontarf Reserve is located at Sandy Bay, approximately 1 km from the Sydney Harbour entrance and the samples collected at this location are referred as “natural water samples” in Chapters 4 and 5.

## 2.2. Water cell and cuvette holder

Water samples were conditioned inside quartz cuvettes with path length of 10 mm and approximate volume of 3.5 mL. These cuvettes exhibit low fluorescence in the spectral regions of interest in this research and allow for transmission of both excitation and Raman photons.

In order to acquire temperature-associated Raman signals, water samples were placed inside a temperature-controlled cuvette holder Quantum Northwest QPod2e (figure 2.2). This sample compartment is specific for optical spectroscopy investigations, with ports allowing for excitation and detection of backscattered signals. The system is integrated to a Peltier heat exchanger, enabling thermoelectric cooling for temperatures in the range from  $-15^{\circ}\text{C}$  to  $+105^{\circ}\text{C}$ . The temperature controller sensitivity, *i.e.*, its capacity of keeping the cuvette at constant temperatures is estimated to be better than  $\pm 0.01^{\circ}\text{C}$ ; and temperature accuracy, *i.e.*, the accuracy with which the internal temperature probe measures the absolute temperature of the water inside the sample holder, is within  $\pm 0.15^{\circ}\text{C}$ .

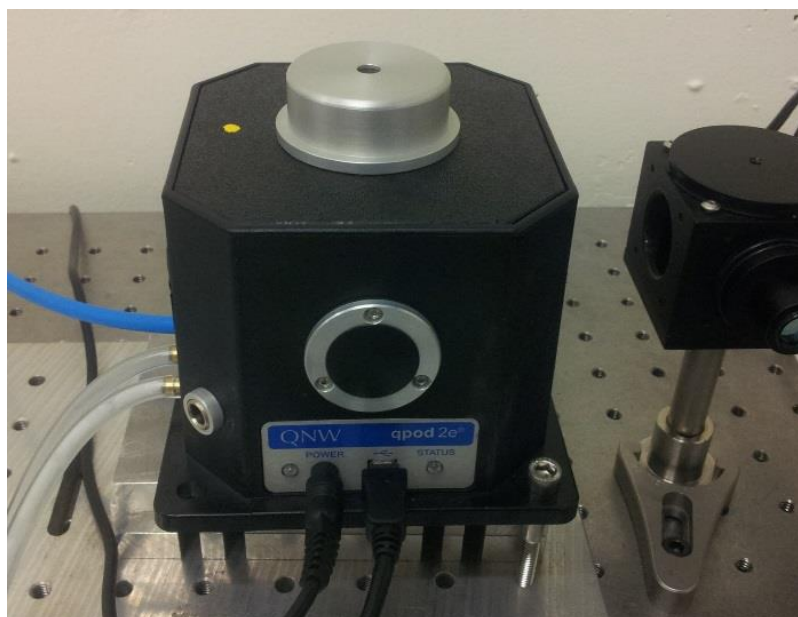


Figure 2.2. Temperature-controlled cuvette holder Qpod2e.

### 2.3. Measuring accuracies on temperature predictions

Water temperature predictions were estimated from Raman signals for all samples under analysis in this study. In order to determine the accuracy of these predictions in comparison with the reference temperature values (measured by the temperature-controlled cuvette holder), Root Mean Squared Errors were calculated for every prediction. Here we will refer to these values as Root Mean Squared Temperature Errors (RMSTEs) (equation 2.1).

$$RMSTE = \sqrt{\sum_{i=1}^N \frac{(T_{\text{Ref}} - T_{\text{pred}})^2}{N}} \quad (2.1)$$

where  $T_{\text{Ref}}$  is the set of reference temperatures and  $T_{\text{Pred}}$  is the set of temperatures predicted from Raman signals. The ultimate goal of this research project is measuring water temperature with accuracy better or equal to  $\pm 0.5^\circ\text{C}$ , hence, RMSTE values  $\leq$  to  $\pm 0.5^\circ\text{C}$  are desirable for our water temperature predictions.

Three spectrometers were used to acquired Raman signals in this study: the commercial Enwave EZRaman-I series integrated to a 532 nm continuous-wave (CW) laser; and two customised multichannel Raman spectrometers coupled to 532 nm and 473 nm pulsed laser sources, respectively. In the next section, I will describe the technical specifications of each RS and describe the analysis performed with the Raman signals acquired for each spectrometer.



## 2.4. Assessing water temperature information from Raman spectra acquired by a commercial dispersive spectrometer

This section is dedicated to providing a detailed description of the measurements performed with the commercial Raman spectrometer Enwave-EZRaman-I. Raman spectra acquisitions and preliminary analysis were performed by Christopher Artlett as part of the laboratory activities of his PhD [52]. Here I re-analysed the spectra acquired by C. Artlett accordingly to the methodology described below.

### 2.4.1. Spectrometer Enwave EZRaman-I at 532 nm

Full unpolarised and polarised Raman spectra from various water samples were collected by a dispersive Enwave Raman spectrometer with low floor noise (Enwave EZRaman-I, 532 nm excitation), shown in figure 2.3. The spectrometer specifications are listed in table 2.2.



Figure 2.3. Enwave EZRaman-I spectrometer (photo from [52]).

Table 2.2. Technical specifications for the Enwave EZRaman-I Raman spectrometer.

<b>Excitation laser</b>	532 nm CW Nd:YAG
<b>Laser power</b>	30 mW
<b>Spectral range</b>	240 – 4400 $\text{cm}^{-1}$
<b>Spectral resolution</b>	$\sim 8 \text{ cm}^{-1}$
<b>Detector type</b>	TEC CCD ( $-50^\circ\text{C}$ )
<b>Rayleigh scattering rejection</b>	OD > 8 at 532 nm

Raman spectra acquisitions were performed on each sample within hours of collection from their sources, and the Raman signals were detected using a  $180^\circ$  backscattering configuration. Wavelength calibrations were conducted using a acetonitrile ( $\text{CH}_3\text{CN}$ ) reference sample. Integration time for each acquisition was typically of 30 seconds, and each final spectrum corresponds to an average of 3 acquisitions. Water samples were transferred to a cuvette and conditioned inside the Q-Pod2e cuvette holder, which allowed for controlled changes in the water samples temperatures. Raman spectra were typically acquired for the temperatures of  $13^\circ\text{C}$ ,  $17^\circ\text{C}$ ,  $21^\circ\text{C}$ ,  $25^\circ\text{C}$ ,  $29^\circ\text{C}$  and  $33^\circ\text{C}$ , with a waiting time of several minutes after reaching the target temperature. This was necessary to ensure that the thermal equilibrium had been reached in the water sample. The results achieved from these measurements are exhibited in Chapter 3 and a scheme for unpolarised Raman signal collection is shown in figure 2.4.

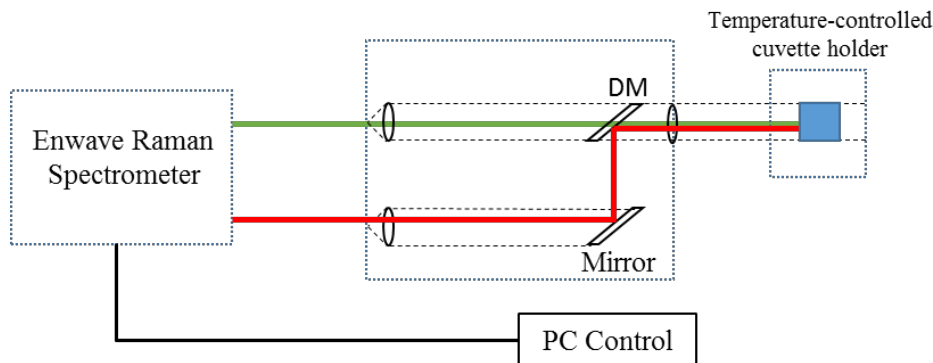


Figure 2.4. Experimental setup for Raman signal collection with Enwave spectrometer.

Orthogonally polarised Raman spectra were obtained by inserting parallel-polarised filters (Thorlabs LPVISB050) in the pathway of Raman photons before detection. The RS configuration didn't allow for simultaneous collection of polarised Raman spectra components and, as consequence, temperature markers could not be estimated with sufficient accuracy as discussed in [52]. However, full polarised Raman spectra will be used as reference for Band Pass filter positioning in Chapters 4 and 5.

The Savitsky-Golay smoothing filter was applied to these spectra in order to minimize the noise without corrupting spectral features. A second-order polynomial fit was applied to the centre of a 25-point moving window ( $\sim 50 \text{ cm}^{-1}$ ) and the centre of this window is changed to conform to the desired polynomial fit.

#### 2.4.2. Two-colour unpolarised temperature markers

Two-colour markers from unpolarised Raman spectra acquired by the Enwave RS were calculated by integrating spectral channels ( $200 \text{ cm}^{-1}$  width) positioned on opposite sides of the isosbestic point, as proposed by the authors of [63] and described in Chapter 1. Optimal spectral positions for these channels were determined for natural water samples by the authors of [56], which correspond to central positions at  $3200 \text{ cm}^{-1}$  for the “low shift” and  $3600 \text{ cm}^{-1}$  for the “high shift” channel. Signal integration within these ranges was performed by applying the trapezoidal numerical integration method in Matlab (R2015b, The MathWorks). The trapezoidal method provides an estimation of the area under a curve of unknown function, dividing the interval of interest into a series of trapezoids of known areas. In my analyses, the interval of interest is the spectral range corresponding to the high and low channels and the width of each trapezoid corresponded to the interval of  $2 \text{ cm}^{-1}$ .

Two-colour unpolarised temperature markers ( $\text{two-colour}(\text{unpol})$ ) were calculated by taking a ratio between the integrated signals for the high and low shift channels, as shown in equation 2.2.

$$\text{two-colour}(\text{unpol}) = \frac{I_{\text{unpol}}^{\text{high}}}{I_{\text{unpol}}^{\text{low}}} \quad (2.2)$$

where  $I_{\text{unpol}}^{\text{xxx}}$  indicates the intensity of integrated Raman signals at a certain channel (high or low). It is important to note that in manuscript 1 and in Chapter 3 these markers are referred simply as “two-colour”.

#### 2.4.3. Determining temperature from two-colour(unpol) markers

Sets of temperature-associated Raman signals were acquired for each water sample, with reference temperatures  $T_{\text{Ref}}$ . Linear regression models were established from the relationships found between the two-colour(unpol) markers and their respective  $T_{\text{Ref}}$ , and the coefficients from these models (*gradient*, *intercept*) were obtained for each water sample.

When re-arranged, these coefficients allow for calculating a new set of temperatures, here denominated predicted temperatures  $T_{\text{Pred}}$  (equation 2.3).

$$T_{\text{Pred}} = (\text{two-colour}(\text{unpol}) \times \text{gradient}) + \text{intercept} \quad (2.3)$$

The accuracies obtained for each linear model when predicting temperature were estimated by their RMSTEs, as discussed in section 2.3. Typical plots for the two-colour markers vs temperature and  $T_{\text{Pred}}$  vs  $T_{\text{Ref}}$  are shown in figures 2.5a and 2.5b, respectively.

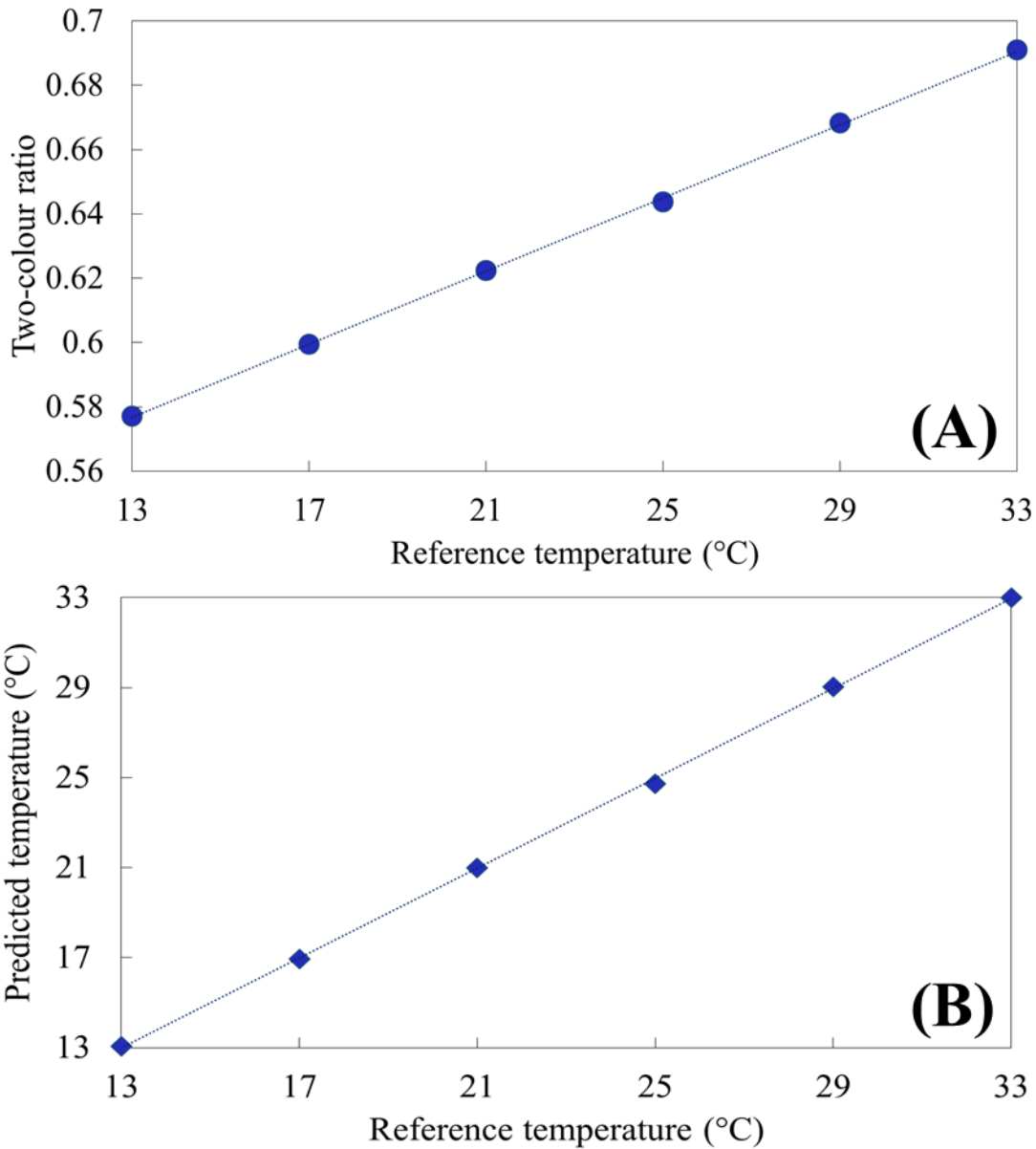


Figure 2.5. Typical plots for the two-colour markers. (a) Two-colour ratio vs reference temperature, and (b) Predicted temperature vs reference temperature.

#### 2.4.4. Multivariate analysis (Principal Component Analysis)

Principal Component Analysis (PCA) is the simplest multivariate statistical method for analysis of complex information, such as spectral acquisitions. It reduces the number of dimensions associated with the “raw” dataset, inter-correlated and noisy, and generates a new coordinate system based on variables associated with maximum *variance* within the dataset [106]. These new variables associated with maximum variance are orthogonal do each other and known as *components*. The first principal component (PC-1) is responsible for maximum variation in the sample; part of the variance not-explained by PC-1 (residuals) is associated to PC-2, and so on. The first component always accounts for the largest variation possible, and the subsequent components are associated with the residuals not explained by previous PCs.

Here, covariance matrixes were used to generate PCs in the software “The Unscrambler®X”. Firstly, the “raw” dataset was mean-centred, forcing the origin of the PCs to be located at the central position, ensuring the PC is in the direction of maximum variance [107]; then, the covariance matrix for this mean-centred dataset was calculated. Two types of information are extracted from the covariance matrix: *eigenvectors* (loadings) and *eigenvalues* (scores), and this relationship is expressed in terms of (equation 2.4):

$$D = SL^S + E \quad (2.4)$$

where D represents the matrix with the mean-centred data, S is the scores matrix (*eigenvalues*) and L is the loading matrix (*eigenvectors*), and E represents the residual variance which was not explained by the model.

According to the authors of [108,109], the goals of the PCA are (1) extracting the most *meaningful* information from the data, *i.e.*, the variables associated with the maximum variance; (2) summarizing the variability in the dataset whilst keeping meaningful information; (3) revealing the structure and distribution of this dataset; (4) analysing the new dataset structure. In Chapter 3, Principal Component Analysis is performed in datasets containing Raman spectra acquired from natural water samples from different locations, aiming to identify the main spectral differences between the samples due to fluorescence from optically active constituents.

## **2.5. Water temperature predictions performed by custom-built, multichannel, LIDAR-compatible Raman spectrometers (532 nm and 473 nm excitation lasers)**

Regardless of its usefulness for full Raman spectra acquisition from small water volumes in laboratory, the Enwave RS is not suitable for LIDAR measurements or field activities. In order to fulfil these requirements, we designed and built two custom-built RS with excitation wavelengths of 532 nm (green) and 473 nm (blue).

In this section I will present the methodology to acquire temperature information from signals acquired by two custom-built Raman spectrometers, integrated to pulsed excitation sources operating a 532 nm (green) and 473 nm (blue) wavelengths. These RS were built based on the findings published in [56,63] aiming to fulfil the requirements for LIDAR-compatibility.

I start by presenting each spectrometer design separately, as they were built by using different optical parts and elements. I then proceed to describe the Raman signals analyses proposed for temperature prediction by these RS regardless of the excitation wavelength, which include calculating temperature markers and estimating their sensitivities, signal-to-noise ratios and % errors associated with each temperature marker.

### **2.5.1. Green multichannel RS (532 nm excitation laser)**

I designed and assembled a multichannel, LIDAR-compatible Raman spectrometer integrated to a 532 nm (green) pulsed laser. This setup is also referred as “green multichannel Raman spectrometer” throughout this report. A simplified scheme of this instrument is shown in figure 2.6. This multichannel RS comprises of a pulsed laser source emitting light at 532 nm, a series of Long Pass (LP) and Band Pass (BP) filters and polarisation optics for selecting portions of the Raman spectra which are sensitive to changes in temperature and Photomultipliers (PMTs) for detecting Raman signals.

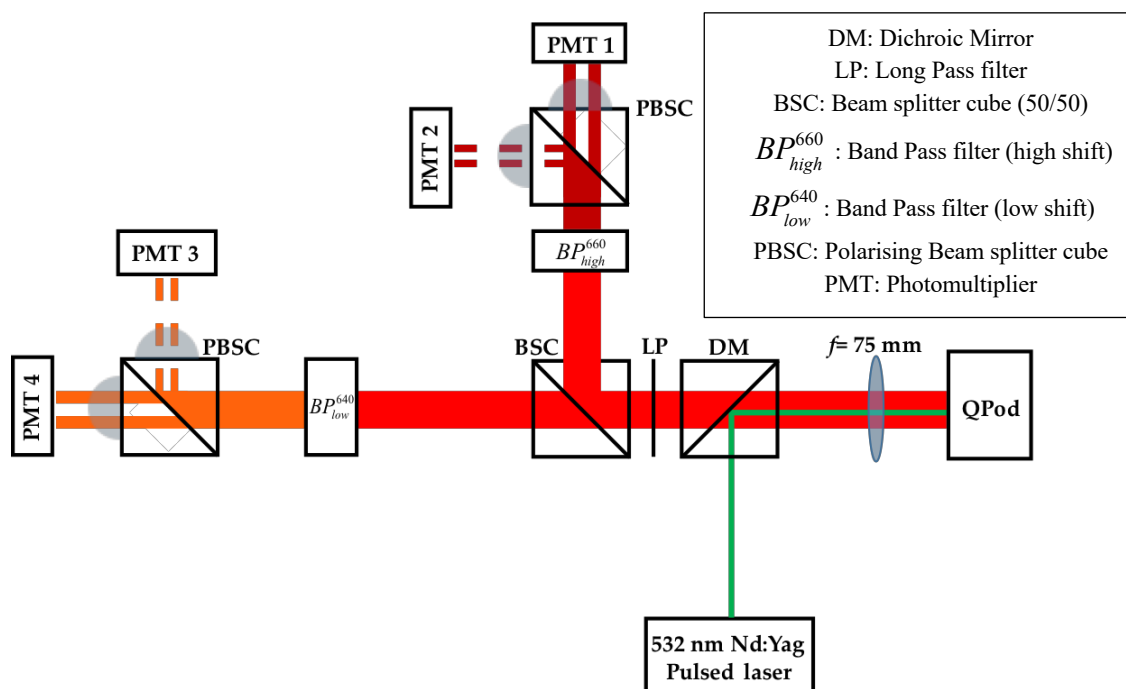


Figure 2.6. Experimental design for a LIDAR compatible green multichannel Raman spectrometer (532 nm excitation).

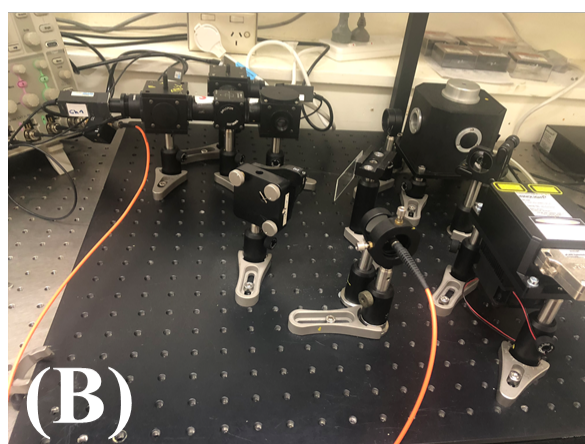
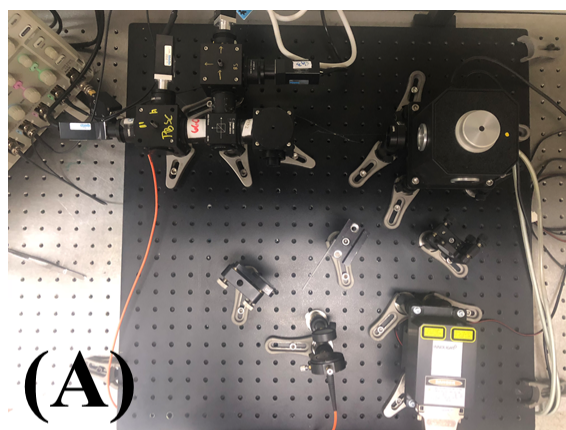


Figure 2.7. Multichannel RS green (532 nm excitation laser). (A) Top view, (B) side view.

### **Excitation source (532 nm)**

A linearly-polarised, pulsed, doubled-frequency Nd:YAG laser emitting light at 532 nm was used as excitation source in this multichannel RS. A summary of the laser technical specifications is shown in table 2.3. This laser is classified as a light source of class 3B, requiring appropriate protection such as laser safety goggles. A pulse profile for this laser is shown in figure 2.8, and the pulse duration measured was approximately 0.9 ns at the Full Width of Half Maximum (FWHM).

Table 2.3. Technical specifications for the pulsed laser source used in the green multichannel LIDAR-compatible RS (532 nm excitation).

<b>Model no.</b>	Innolight $\mu$ -Flare –532
<b>Emission wavelength</b>	532 nm
<b>Polarisation state</b>	Linearly (horizontal) polarised
<b>Average power</b>	115 mW
<b>Pulse duration</b>	0.9 ns (at the FWHM)
<b>Pulse repetition rate</b>	4.5 kHz
<b>Pulse energy</b>	25.5 $\mu$ J

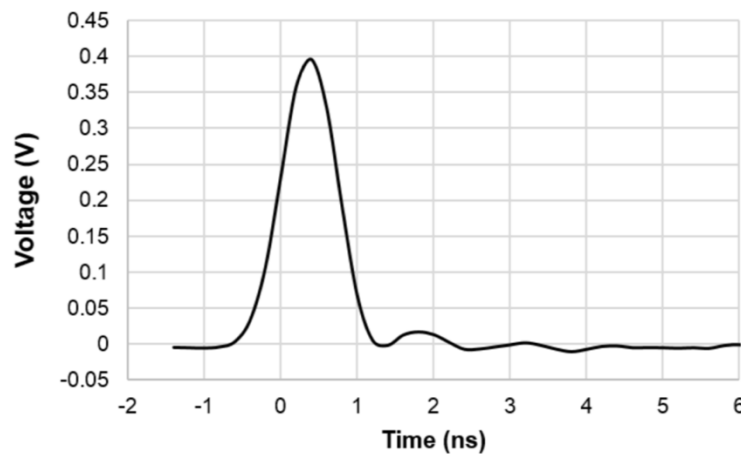


Figure 2.8. Pulse profile acquired from the Innolight  $\mu$ -Flare –532 laser (from [52]).



### Optical components (532 nm excitation wavelength)

A series of optical filters, lenses, beam splitter cubes and mirrors were used to assemble this RS, which are shown in table 2.4 and in figure 2.9.

Table 2.4. Optical parts (filters and lenses) used in the green multichannel LIDAR-compatible RS (532 nm excitation)

Optical part	Part number	Function in the RS
Dichroic Mirror (DM)	Semrock FF538-FDi01	Reflecting green (excitation) photons ( $R > 93\%$ between 350–532 nm); transmitting red-shifted (Raman) photons ( $T \sim 93\%$ between 547.7–950 nm)
Long Pass filter (LP)	Semrock BLP01-532R	Rejecting Rayleigh photons ( $T \sim 93\%$ between 546.9–900 nm) $OD_{\text{abs}} > 6$ between 425.6 – 532 nm
Non-polarising Beam Splitter Cube (BSC)	Thorlabs BS007	Dividing the backscattered Raman signal into two non-polarised beams of near-equal intensity (50/50)
Polarising Beam Splitter Cube (PBSC)	Thorlabs PBS251	Dividing the backscattered Raman photons into two polarised components (parallel and perpendicular)
Band Pass filters (BP)	Semrock LD01-640/8-25	Selecting Raman signals of spectral range between 627.1 nm to 652.9 nm (FWHM)
	Semrock FF01-660/13-25	Selecting Raman signals of spectral range between 639.8 nm and 680.2 nm (FWHM)
Focal lenses ( $f=75\text{mm}$ )	LA1608-A	Focussing the excitation beam into the temperature-controlled cuvette holder
Focal lenses (PMTS) ( $f=25\text{ mm}$ )	Thorlabs LA1951-A-ML	Focussing the backscattered Raman photons onto detector

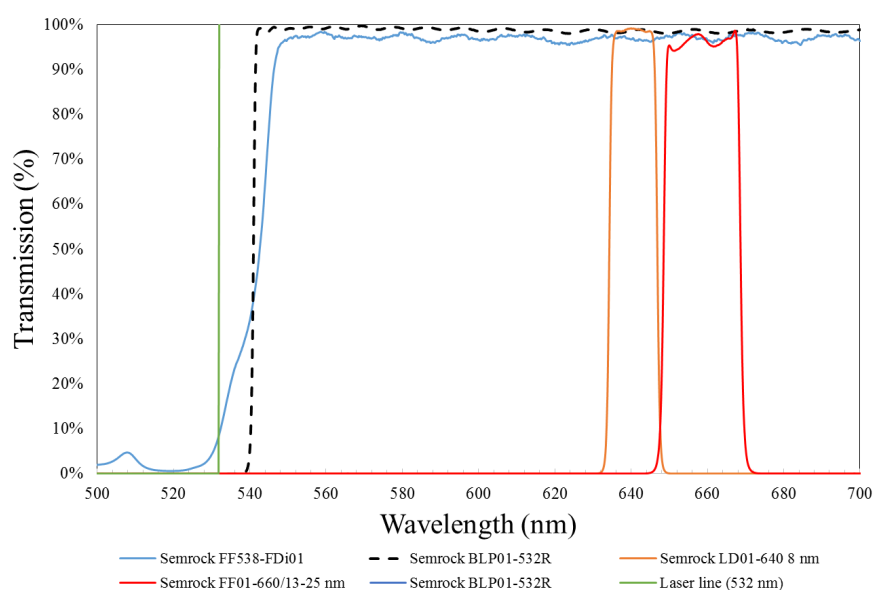


Figure 2.9. Wavelength-dependent light transmission for several optical components used to assemble the green multichannel RS at 532 nm excitation laser.

### **Detectors**

Photomultiplier tubes (PMTs) with fast response to optical signals, exhibiting rise time  $\sim 0.57$  ns (Hamamatsu model H10721-20), were selected as detectors for our multichannel RS. These characteristics are required for LIDAR measurements, which are the ultimate goal of this research project. The PMT modules were compact (5.0x2.0x2.0 cm) and required an input voltage of 5.5. V for operation (maximum current draw around 2.7 mA) (figure 2.10). The spectral range of operation for the photocathode (multi-alkali) varied from 230 nm to 920 nm, (maximum sensitivities at 630 nm), compatible with the Raman signal bandwidths selected by this RS.



Figure 2.10. Photomultiplier Hamamatsu H10721 (from[110]).

**Data acquisition overview (532 nm excitation wavelength)**

Raman signals were registered by a multichannel digital oscilloscope (Tektronix DPO4104B), exhibiting a bandwidth of 1 GHz, a sample rate of 5 GS/s and record length of 20 MS. The multichannel configuration allowed for simultaneous collection in 4 different spectral channels. Each measurement registered by the oscilloscope consisted of an average of 512 pulses, for improved SNRs during acquisitions. A summary of characteristics for each channel of Raman signal collection regarding polarisation state of signals and Band Pass filters used is shown in table 2.5.

Table 2.5. Nomenclature adopted for each channel (green multichannel RS).

Channel number	Polarisation state	Band Pass filter	Nomenclature
1	Parallel	$BP_{high}^{660}$	$I_{  }^{high}$
2	Perpendicular	$BP_{high}^{660}$	$I_{\perp}^{high}$
3	Perpendicular	$BP_{low}^{640}$	$I_{\perp}^{low}$
4	Parallel	$BP_{low}^{640}$	$I_{  }^{low}$

### 2.5.2. Multichannel RS (blue)

I designed and assembled a multichannel, LIDAR-compatible Raman spectrometer integrated to a 473 nm (blue) pulsed laser source. This setup is also referred to as “blue multichannel Raman spectrometer” throughout this report. A simplified scheme of this instrument is shown in figure 2.11. This multichannel RS is comprised of a pulsed laser source emitting light at 473 nm, a series of Long Pass (LP) and Band Pass (BP) filters for selecting portions of the Raman spectra which are sensitive to changes in temperature and Photomultipliers (PMTs) for detecting Raman signals.

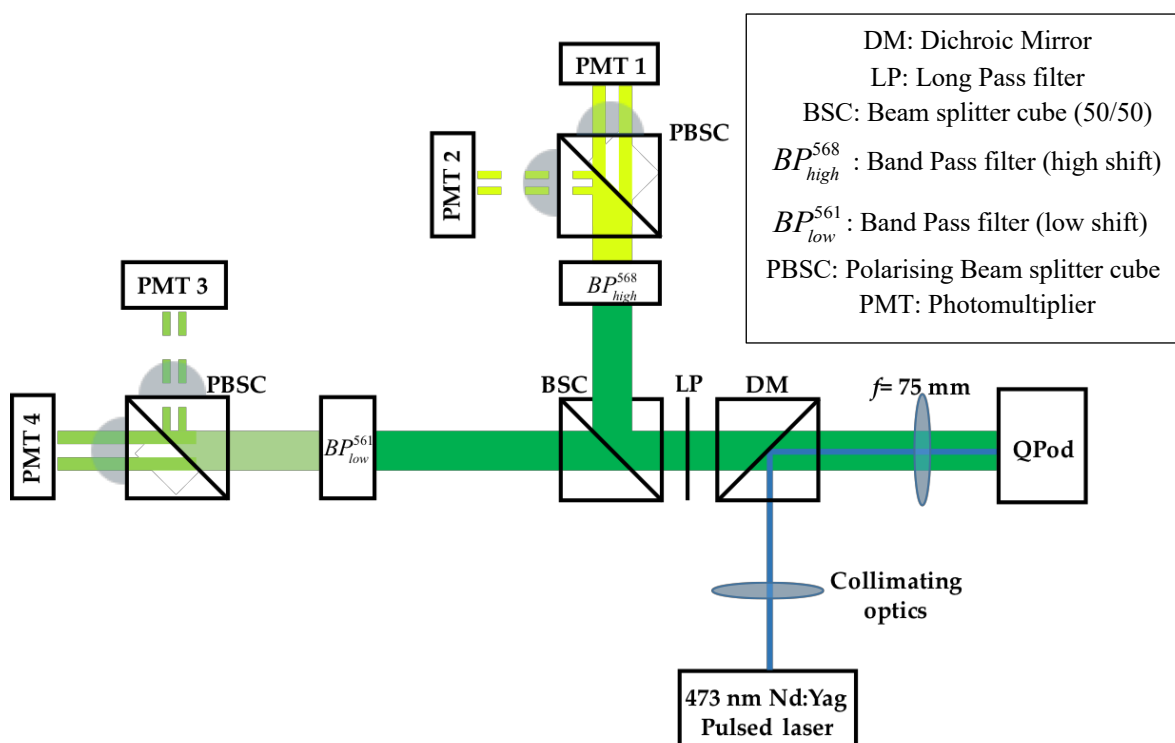


Figure 2.11. Experimental design for a LIDAR compatible multichannel Raman spectrometer (473 nm excitation).

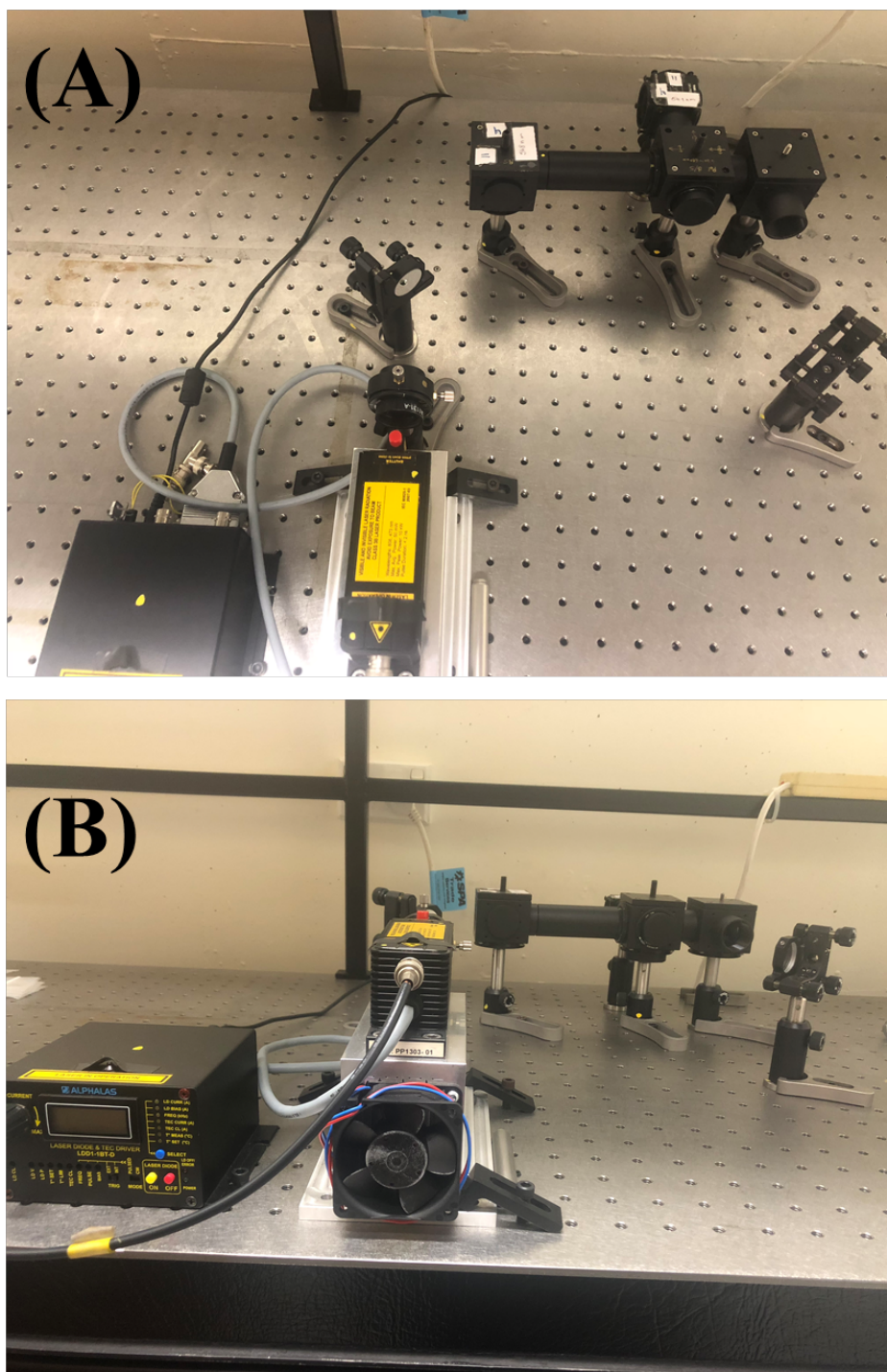


Figure 2.12. Multichannel RS blue (473 nm excitation laser). (A) Top view, (B) side view.

### **Excitation source (473 nm)**

The excitation source chosen to be integrated to this multichannel RS was the Alphalas PULSELAS-P-473-6-SP, emitting pulsed blue light at 473 nm (doubled-frequency of the fundamental emission wavelength 946 nm). This laser exhibits a pulse duration around 1.5 ns at the FWHM, within the threshold for LIDAR measurements with vertical resolutions of  $\pm 0.5$  m. Technical specifications for this laser are shown in table 2.6 and the pulse profile is shown in figure 2.13.

Table 2.6. Technical specifications for the pulsed laser source used in the blue multichannel LIDAR-compatible RS (473 nm excitation)

<b>Model no.</b>	Alphalas PULSELAS-P-473-6-SP
<b>Emission wavelength</b>	473 nm
<b>Polarisation state</b>	Linearly (horizontal) polarised
<b>Average power</b>	25 mW
<b>Pulse duration</b>	1.5 ns (at the FWHM)
<b>Pulse repetition rate</b>	5 kHz
<b>Pulse energy</b>	5 $\mu$ J

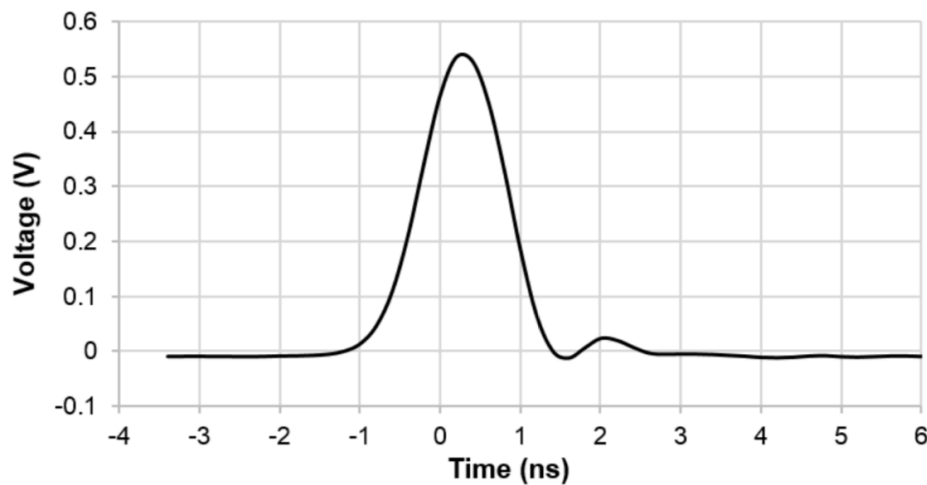


Figure 2.13. Pulse profile acquired from the Alphalas PULSELAS-P-473-6-SP (473 nm) laser (from [52]).

The laser beam exhibited a significant divergence ( $\sim 30$  mrad), characterise by a poor collimation in the horizontal axis which was compensated by using focal lenses.

### **Optical components (473 nm excitation wavelength)**

A series of optical filters, lenses, beam splitter cubes and mirrors were used to assemble this RS, which are shown in table 2.7 and in figure 2.14.

Table 2.7. Optical parts (filters and lenses) using in the blue multichannel LIDAR-compatible RS (473 nm excitation)

Optical part	Part number	Function in the RS
Dichroic Mirror (DM)	Semrock Di02-R488	Reflecting blue (excitation) photons (R ~ 94% between 471 – 491 nm; transmitting red-shifted (Raman) photons (T~ 93% between 499.8 – 900 nm)
Long Pass filter (LP)	Semrock BLP01-473R	Rejecting Rayleigh photons (T~ 93% between 486.2 – 900 nm) $OD_{abs} > 6$ between 378.4 – 473 nm
Non-polarising Beam Splitter Cube (BSC)	Thorlabs BS007	Dividing the backscattered Raman signal in two non-polarised beams of near-equal intensity (50/50)
Polarising Beam Splitter Cube (PBSC)	Thorlabs PBS251	Dividing the backscattered Raman photons in two polarised components (parallel and perpendicular)
Band Pass filters (BP)	Semrock FF01-561/4	Selecting Raman signals of spectral range between 557.0 – 565.0 nm (T~ 93%)
	Semrock LL01-568	Selecting Raman signals of spectral range between 566.0 nm and 570.4 nm
Focal lenses ( $f=75\text{ mm}$ )	LA1608-A	Focussing the excitation beam into the temperature-controlled cuvette holder
Focal lenses (PMTs) ( $f=25\text{ mm}$ )	Thorlabs LA1951-A-	Focussing the backscattered Raman photons onto detector

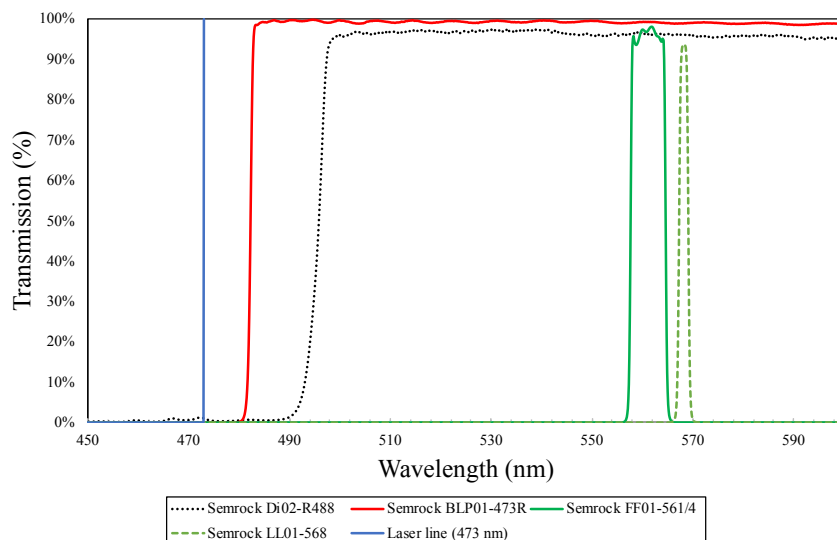


Figure 2.14. Wavelength-dependent light transmission for several optical components used to assemble the blue multichannel RS at 473 nm excitation laser.

### **Detectors**

The detectors chosen to be used in this system were PMT modules (Hamamatsu), which were discussed in detail in section 2.5.1.

### **Data acquisition overview (473 nm excitation wavelength)**

Raman signals scattered by water samples were registered by the multichannel digital oscilloscope Tektronix DPO4104B (bandwidth 1 GHz, 5 GS/s), presented in section 2.5.1. Signals were collected in 4 spectral channels, each corresponding to unique wavelengths and polarisation states, and a summarised in table 2.8.

Table 2.8. Nomenclature adopted for each channel (blue multichannel RS).

Channel number	Polarisation state	Band Pass filter	Nomenclature
1	Parallel	$BP_{high}^{568}$	$I_{  }^{high}$
2	Perpendicular	$BP_{high}^{568}$	$I_{\perp}^{high}$
3	Perpendicular	$BP_{low}^{561}$	$I_{\perp}^{low}$
4	Parallel	$BP_{low}^{561}$	$I_{  }^{low}$



### 2.5.3. Temperature markers calculations

The customised spectrometer design allowed for collection of polarised Raman signals in 4 channels, enabling the calculation of temperature markers from channels at the same polarisation state (two-colour) and of different polarisation states (depolarisation ratio). Each signal pulse was integrated around the FWHM, over a range of  $\sim 2$  ns by the trapezoidal method, in Matlab (R2015b, The MathWorks), as shown in figure 2.15a-b.

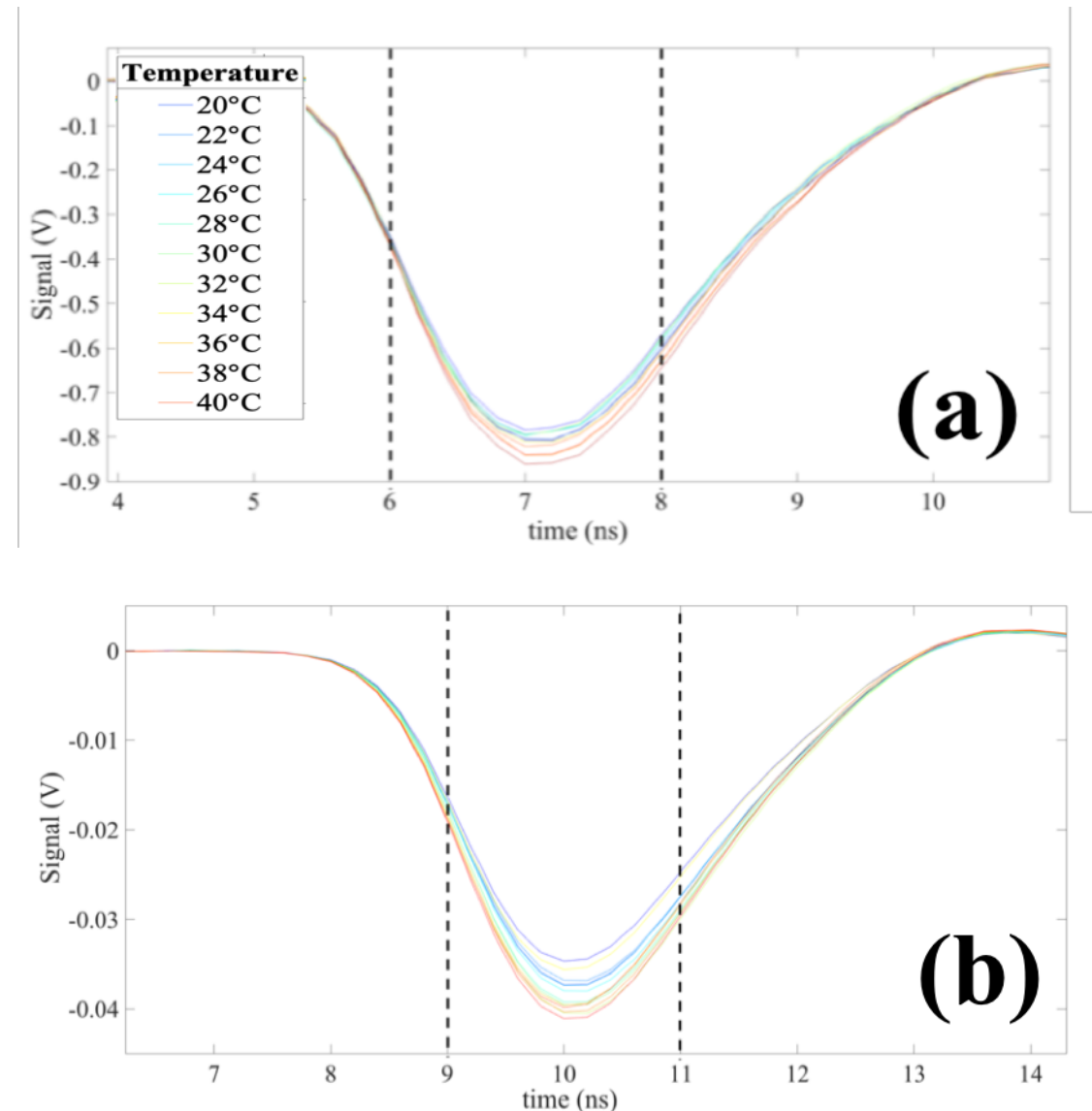


Figure 2.15. Area for trapezoidal integration of signals acquired by (a) 532 nm (green) multichannel RS and (b) 473 nm (blue) multichannel RS.

### **Two-colour markers**

Two-colour markers (ratios) were calculated for signals acquired by the multichannel RS (excitation laser 532 nm) according to equations 2.5 and 2.6.

$$two-colour(\parallel) = \frac{I_{\parallel}^{high}}{I_{\parallel}^{low}} \quad (2.5)$$

$$two-colour(\perp) = \frac{I_{\perp}^{high}}{I_{\perp}^{low}} \quad (2.6)$$

where  $I_{pol}^{xxx}$  indicates the intensity of integrated Raman signals at a given channel (high or low). Two-colour( $\parallel$ ) markers were calculated from channels 1 and 4, whilst two-colour( $\perp$ ) channels were calculated from channels 2 and 3.

### **Depolarisation markers**

The calculation of traditional depolarisation ratios was briefly explored in **section 1.2.4.2** as an alternative temperature marker which may be less affected by different attenuation effects and fluorescence in natural waters [80]. However, depolarisation ratios calculated for Raman signals at the OH stretching band exhibit temperature-insensitive regions at 3230 and 3630  $\text{cm}^{-1}$  [111]. The market availability for BP filters with particular spectral characteristics is limited, imposing a further challenge for evaluating the traditional depolarisation ratio; hence, we propose here a different approach for the method, where signals of different polarisation states at different wavelengths were used to calculate the depolarised temperature markers (equations 2.7 and 2.8).

$$Depolarisation(A) = \frac{I_{\perp}^{high}}{I_{\parallel}^{low}} \quad (2.7)$$

$$Depolarisation(B) = \frac{I_{\perp}^{low}}{I_{\parallel}^{high}} \quad (2.8)$$

### 2.5.4. Temperature markers sensitivities

Temperature markers sensitivities were estimated for an ultrapure (Milli-Q) water sample in order to determine the percentage change in the temperature markers per °C (%/°C). The authors of [63] suggest the use of mean-scaled temperature markers for sensitivity calculations, accounting for natural fluctuations in denominator values during markers calculations. Higher (lower) signal intensities in the denominators result in smaller (bigger) variations in the markers, not necessarily linked to changes in temperature.

Mean-scaled markers were calculated by scaling each marker by a mean of all markers within a set of temperature measurements (equation 2.9). A linear relationship between mean-scaled markers and reference temperatures was found, and sensitivity values were extracted from the slope estimated for these linear models. The use of mean-scaled markers also allows for comparison between different types of markers calculated for a given water sample.

$$\text{Mean-scaled markers} = \frac{d(\text{marker})}{dT} \frac{1}{\text{mean}(\text{marker})} \quad (2.9)$$

### 2.5.5. SNR calculations

There are several noise sources associated with LIDAR measurements, which include the natural fluctuations of the signal (quantum noise), the natural fluctuation of background noise (background radiation noise), the thermal noise associated with the current in absence of optical signals (dark current noise), and the laser-scattered noise generated by the excitation light used in RS measurements [112]. Signal-to-noise ratios are able to provide information regarding the usefulness of the Raman signals collected by the PMTs for temperature predictions. High signal-to-noise ratios are desirable for LIDAR measurements, considering the environmental irradiation during daylight and the fact that Raman scattering is significantly smaller than other elastic and inelastic scattering in water. The use of optical filters, such as LP and the BP filters employed in this RS, is effective in reducing the wavelength range of photons detected and the Rayleigh scattering associated with the excitation laser. Other noise sources, however, are inherent to the equipment being used for signal acquisition and to the environmental irradiance conditions during signal acquisition, and these account for the major fraction of noise in our measurements.

Noise acquisition was performed for each channel by registering the intensities identified by the oscilloscope in the absence of excitation light averaging over 512 pulses.

Traditionally, SNRs are calculated considering the intensities at the peaks of signal and noise, as stated by equation 2.10.

$$SNR = \frac{\text{Signal}_{(\text{peak})}}{\left( \frac{V_{(\text{p-p})}^{\text{noise}}}{\sqrt{2}} \right)} \quad (2.10)$$

where  $\text{Signal}_{(\text{peak})}$  indicates the average peak (maximum) signal for a given acquisition; and  $V_{(\text{p-p})}^{\text{noise}}$  refers to the peak-to-peak voltage of noise at maximum signal peaks. This approach, however, is not fully compatible with the trapezoidal signal integration performed for the temperature marker calculations as discussed in section 2.5.3. Taking this fact into consideration, SNRs for this study were calculated according to equation 2.11.:

$$SNR = \frac{\int \text{Signal}_{(\text{FWHM})}}{\left( \frac{\int \text{Noise}_{(\text{FWHM})}}{\sqrt{2}} \right)} \quad (2.11)$$

where  $\text{Signal}_{(\text{FWHM})}$  relates to the integrated signal around the FWHM ( $\sim 2$  ns), and  $\text{Noise}_{(\text{FWHM})}$  refers to the integrated noise in the same interval around the FWHM.

SNRs were calculated for each channel of collection for every acquisition performed by the multichannel RS. As a measurement of effectiveness in collecting temperature-dependent Raman signals, SNRs are also useful for estimating the percentage errors in the temperature markers associated with the noise during acquisitions. For any given temperature marker, estimated from a ratio between channel *A* and *B*, the percentage error in the marker due to noise can be estimated by equation 2.12.

$$\% \text{error in marker} = \left[ \frac{\text{SNR}_A^{-1}}{\text{Signal}_A} + \frac{\text{SNR}_B^{-1}}{\text{Signal}_B} \right] \times 100 \quad (2.12)$$

# **CHAPTER 3**

## **RAMAN SPECTROSCOPY AS A TECHNIQUE FOR NATURAL WATER TEMPERATURE DETERMINATION**

Previous studies have proposed methods for measuring the temperature-dependent behaviour of water Raman spectrum, dawning as a promising technique for remote sensing of the oceans as previously discussed in Chapter 1. Recently, the authors of [63] calculated temperature markers from unpolarised Raman spectra collected from ultrapure water samples in the laboratory by using a commercial spectrometer (532 nm excitation), achieving accuracies of up to  $\pm 0.1^\circ\text{C}$  by using the two-colour method. These results showed potential for using Raman spectroscopy coupled to LIDAR-compatible methods, allowing for depth-resolved temperature measurements on natural water bodies. Still, such LIDAR-compatible equipment is not commercially available and, prior the efforts of proposing a new instrument, it is necessary to explore possible interactions between water Raman signal and other optically active constituents in natural waters (e.g. photosynthetic pigments and coloured dissolved organic matter) which could potentially degrade the utility of this approach to determining temperature.

In 2013, the Remote Sensing Raman Laboratory (Macquarie University) started an interdisciplinary project aiming to understand the impact of fluorescence from different phytoplankton groups on water Raman spectra. Natural water samples were collected around Sydney Harbour and Raman spectra were acquired by using a commercial spectrometer coupled to a 532 nm excitation laser (green). The results suggested the presence of background signal on all natural water samples, giving rise to a baseline firstly attributed to chlorophyll-a and *Gelbstoff* fluorescence overlapping with the Raman peak, impacting the accuracy on temperature predictions by two-colour markers. These suggestions were made by simple comparison between spectra and analysis were conducted in order to explore the spectral heterogeneity of these datasets. The spectra and preliminary analysis were presented by C. Artlett in his PhD. thesis [52].

In 2015, Caro Derkenne (undergraduate student, Macquarie University) and Penelope Ajani (Research Assistant, Macquarie University) conducted experiments to explore which phytoplankton species would give rise to fluorescence with potential to overlap with Raman signals. Ajani grew and cultivated phytoplankton cells from various species and Derkenne collected fluorescence and Raman spectra from these cultures at various concentration. It was observed that the presence of phytoplankton cells in water could corrupt temperature measurements by Raman spectroscopy, corroborating the thesis work of C. Artlett [52].

The above works by Artlett, Ajani and Derkenne defined a starting point for the activities described in this Chapter. Aiming to determine the origins of all signal variability among natural water samples, in 2017 I performed a Principal Component Analysis on the water Raman spectra previously collected from samples around Sydney Harbour in 2013. These findings indicated the presence of photosynthetic pigments fluorescence as one of the sources of variability on Raman spectral analysis and exhibited connections with Derkenne and Ajani research from 2015. Based on these new discoveries I re-analysed the data presented in [52], evaluated a traditional baseline correction technique and proposed a completely new correction method based on standard temperature markers. Lastly, I proposed solutions for implementing Raman spectroscopy methods as temperature remote sensing tools in natural waters based on the major sources of background signal found in this study.

In the next section I present a manuscript that will be submitted to *Optics Express* entitled “Fluorescence impact on Raman remote sensing of temperature in natural waters”. In subsequent sections I provide greater detail in regard to exploring spectral variabilities of various natural water samples and baseline correction techniques, discussing practical implementations of these methods in the field. Finally, I present two multichannel LIDAR-compatible Raman spectrometers suitable for each baseline correction method and discuss the steps that would be involved in operationalization of these techniques.

### **3.1. Manuscript 1: “The impact of fluorescence on Raman remote sensing of temperature in natural water samples”**

#### **Statement of contribution**

My contribution to this work was outlined in section 3.1. Further to that I am the lead author, having written much of the paper, prepared the figures and so on. Figure 2 is the work of C. Artlett, the data in Figure 4 was collected by C. Derkenne, and the phytoplankton concentrations reported in Figure 4 were determined by P. Ajani.



# The impact of fluorescence on Raman remote sensing of temperature in natural water samples

ANDRÉA DE LIMA RIBEIRO,<sup>1,\*</sup> CHRISTOPHER ARTLETT,<sup>1,2</sup> PENELOPE A. AJANI,<sup>3</sup> CARO DERKENNE,<sup>1</sup> AND HELEN PASK<sup>1</sup>

<sup>1</sup>*MQ Photonics Research Centre, Department of Physics and Astronomy, Macquarie University, Sydney, NSW 2109, Australia*

<sup>2</sup>*Defence, Science and technology Group, Maritime Division, Eveleigh, NSW 2015, Australia*

<sup>3</sup>*University Technology Sydney, Ultimo, NSW 2007, Australia*

*\*andrea.delimaribeiro@mq.edu.au*

**Abstract:** A comprehensive investigation into the impact of spectral baseline on temperature prediction in natural marine water samples by Raman spectroscopy is presented. The origin of baseline signals is investigated using principal component analysis and phytoplankton cultures in laboratory experiments. Results indicate that fluorescence from photosynthetic pigments and dissolved organic matter may overlap with the Raman peak for 532 nm excitation and compromise the accuracy of temperature predictions. Two methods of spectral baseline correction in natural waters are evaluated: a traditional tilted baseline correction and a new correction by temperature marker values, with accuracies as high as  $\pm 0.2^\circ\text{C}$  being achieved in both cases.

© 2018 Optical Society of America under the terms of the [OSA Open Access Publishing Agreement](#)

## 1. Introduction

The use of Raman spectroscopy to predict water temperature was first proposed in [1,2] and the potential for extending this to determine depth-resolved temperature profiles using LIDAR methods was investigated in [3,4]. The applications for such knowledge are extensive, and include making predictions about underwater communication, validating hydrologic and climate change models, and obtaining habitat information. In principle, the methods could be compatible with airborne, surface, land-based or even underwater platforms. Since the comprehensive studies of several decades ago, there have been a modest number of studies that have advanced the field [5-7], accompanied by large advances in the sensitivity of photomultipliers, spectrometers and numerical statistical methods.

In 2015, we reported our first work in this field, harnessing these advances to obtain high quality Raman spectra, using statistical methods to identify the spectral parameters most sensitive to temperature change, and systematically predicting the accuracy with which temperature could be predicted from the ratio of Raman signal intensities at two particular frequencies within the broad Raman band associated with OH stretching [8]. The method is commonly known as the “two-colour method”. It was found that water temperature could be predicted with an accuracy better than  $\pm 0.2^\circ\text{C}$  in the case of pure (reverse-osmosis) water, and informed the design of a simple two-channel apparatus that used pulsed excitation, high fidelity filters and photomultipliers in proof of principle experiments to predict the temperature of tap water in a 1 m long cell to within  $\pm 0.5^\circ\text{C}$ . That was a first step towards optical instrumentation for vertically profiling water temperature in natural environments.

A key challenge to implementing the two-colour method for temperature determination in real environments is the presence of additional materials such as dissolved organic matter (DOM), phytoplankton and particulates. These constituents exist in different concentrations across locations, varying within the water column and over time according to tides, seasons and climatic factors. Furthermore, they have the potential to fluoresce at wavelengths that overlap the Raman band, absorb Raman photons, and scatter both excitation and Raman photons. DOM fluorescence has a short lifetime [9], exhibiting two characteristic components: from 300 to 350 nm (associated with protein decomposition) and from 400 to 580 nm associated with humic substances of organic origin, also known as *Gelbstoff* [10]. Phytoplankton fluorescence signals are typically around 685 nm due to the presence of chlorophyll-a (Chl-a), a mandatory photosynthetic pigment found in all phytoplankton species, and its intensity is proportional to phytoplankton concentration [11]. Depending on the species, physiological state of the cell and environmental conditions the concentration of accessory pigments (e.g. chlorophyll-b,c,d, carotenoids, phycobilins) may increase in the cell, giving rise to fluorescence at additional wavelengths.

Simulations in [12] explored the spectral overlap between the Raman signal and laser-induced fluorescence in natural marine waters, within an excitation range of 510-570 nm. The authors identified a distortion on the Raman signal due to Chl-a fluorescence, compromising the water temperature prediction methods based on Raman spectroscopy and proposed a fluorescence subtraction approach. Following on, the authors of [13] used a tunable laser (480 to 530 nm) to investigate laser-induced fluorescence in natural waters from Chesapeake

Bay. Three main spectral features were identified in addition to the Raman signal which occurred at a fixed separation (centred around  $3400\text{ cm}^{-1}$ ) from the excitation wavelength: the Chl-a fluorescence band at 685 nm, a weaker phytoplankton band at 730 nm, and low-level fluorescence from DOM at shorter wavelengths. With regard to temperature prediction, it was found that shorter excitation wavelengths (480 nm) generated Raman signals that were more likely to overlap with DOM fluorescence, while the Raman signals generated by longer wavelength excitation (530 nm) were more likely to overlap with Chl-a fluorescence signals and that these overlaps could compromise temperature prediction. The same author subsequently broadened his study to investigate the temperature dependence of the Raman and fluorescence signals [14]. It was observed that, within the excitation range from 490 to 520 nm, the Raman signal counts were higher for shorter-wavelength laser sources (blue) and reduced towards longer excitation (green). By comparison, any dependence of Chl-a and DOM fluorescence on excitation wavelength was found to be insignificant. For excitation within this range, there was minimal overlap of Raman and the Chl-a fluorescence signals at 685 nm, and that baseline subtraction could be used prior to applying the two-colour method. When a longer excitation wavelength of 535 nm was used, significant overlap between Raman and Chl-a fluorescence bands was observed and this was problematic for temperature prediction.

Here we note an essential difference between our approach, and that in most other works where the Raman spectra are decomposed into a series of Gaussians, the heights and/or widths of which are then analysed to determine water temperature. In this work, as in [8] we simply integrate the Raman signal that falls within pairs of selected spectral channels of typically  $200\text{ cm}^{-1}$  width. While the studies in [12-14] found the optimal wavelength for remote sensing of temperature to be between 488 nm and 520 nm, there are few commercial laser sources available in this band. On the other hand, 532 nm lasers are widely available and are typically used for laser bathymetry, and accordingly it is important to quantify the extent to which DOM and phytoplankton fluorescence might impact on the accuracy of temperature prediction in natural water samples by using 532 nm excitation, and to explore strategies for making corrections using our two-channel approach.

In the present study, we collected unpolarised Raman spectra for natural water samples from five locations around Sydney Harbour, which typically show the Raman band at  $3400\text{--}3600\text{ cm}^{-1}$  superimposed on a background signal, which we show is largely due to fluorescence. We have carried out a controlled experiment in which we grew 3 common species of phytoplankton and measured the concentrations that gave rise to a baseline large enough to perturb the Raman signal. These concentrations were within the normal range of concentrations along the coast of eastern Australia. We propose two methods for correcting for fluorescence and present the accuracy with which temperature can be predicted with and without baseline correction, considering the implications of our findings for developing future methods that are less susceptible to the presence of fluorescing matter.

## 2. Experimental Details

### 2.1 Raman spectral measurements and analysis

Natural water samples were collected from various locations around Sydney. These include Manly Beach, which is outside the Harbour, Clontarf and Sugarloaf Bay, which are located in Middle Harbour approximately 4 km and 7 km respectively from the Harbour entrance, and Rhodes which is located in the main harbour approximately 20 km from the Harbour entrance. Water samples from Rose Bay were of particular importance to this study. These samples were collected from deep waters in an open part of the harbour, approximately 2 km from its entrance and investigated after being filtered and UV treated. Water samples from Manly Dam, a freshwater body of approximately 2000 ML located in an urban bush reserve were investigated, along with pure (Milli-Q) laboratory water.

Raman spectroscopy was performed on each sample within a few hours of being collected, and all the data was collected, using methods that have been described in detail in [8]. Briefly the spectrometer used was an Enwave EZRaman-I, a dispersive Raman spectrometer having a spectral resolution of  $8\text{ cm}^{-1}$  and using 30 mW continuous-wave (CW) laser at 532 nm for excitation (fig. 1). The unpolarised Raman signal was detected using a  $180^\circ$  backscattering geometry, and wavelength calibration of the spectrometer was carried out using an acetonitrile ( $\text{CH}_3\text{CN}$ ) reference sample. Spectral data were smoothed with the Savitsky-Golay algorithm to reduce noise (2<sup>nd</sup> order, 25-point window). The spectrometer integration time was typically 30 seconds and each spectrum shown is an average of 3 acquisitions to improve consistency. Each sample was conditioned inside a quartz cuvette (pathlength of 10 mm) and stepped through a range of temperatures from 12 to  $33^\circ\text{C}$ , with a waiting time of several minutes allowed after reaching each set point to enable the water sample to reach thermal equilibrium. The reference temperature was measured using a temperature probe within the QNW QPod2e, which has a specified accuracy of  $\pm 0.2^\circ\text{C}$ .

The unpolarised Raman spectra were analysed using the “two-colour” technique, in which a ratio of the amplitudes at the two main peaks on either side of the isosbestic point of OH stretching band (point of equal scattering and absorption) is found to be proportional to water temperature. In this work, as in [8] we integrate the Raman signal that falls within pairs of selected spectral channels on either side of the isosbestic point. The

spectral resolution ( $8 \text{ cm}^{-1}$ ) was substantially lower than the channel widths over which Raman signals are integrated ( $200 \text{ cm}^{-1}$ ). The analysis method involves carrying out a linear least squares regression, using MatlabR2017b, of the two-colour ratio against the reference temperature to yield a temperature-predictive model. Each combination of wavenumber pairs produced sets of Root Mean Squared Temperature Errors (RMSTE), which were used as parameters for estimating the accuracies of temperature predictions.

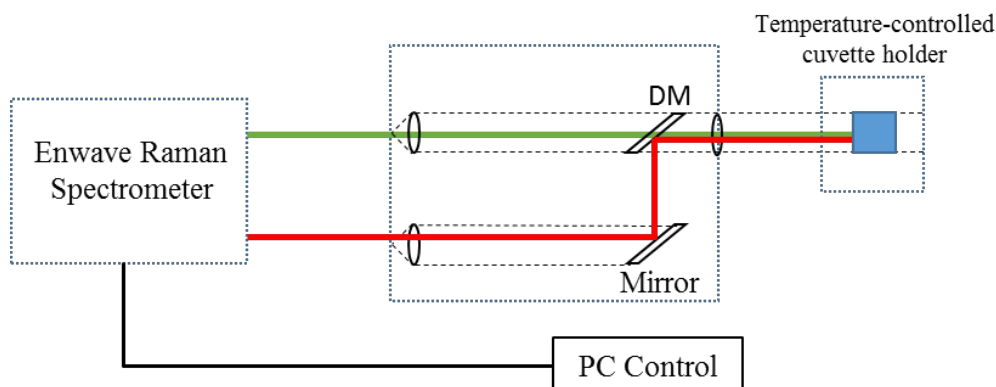


Fig.1. Experimental setup for collection of Raman spectra

## 2.2 Phytoplankton growth and spectral analysis

Non-axenic clonal cultures of *Synechococcus* Red, *Synechococcus* Green, *Nannochloropsis* sp., *Ditylum brightwelli*, *Dunallella tertiolecta*, *Ostreopsis siamensis* and *Rhodomonas salina* were obtained from collections held at Macquarie University and University of Technology Sydney and maintained in 2 x 200 mL culture flasks (replicates) containing F/2 media [15]. Cultures were grown under 24 hr LED lighting at  $20^\circ\text{C}$  and monitored using light microscopy. One mL of cultivated culture from each strain was transferred into fresh media every two weeks to maintain healthy and exponentially growing cultures over the duration of the study.

To investigate the extent to which phytoplankton fluorescence overlaps the water Raman spectra, three species were chosen: *Synechococcus* Red, *Synechococcus* Green, *Nannochloropsis* sp.. These three cover the major naturally fluorescing pigments found in most phytoplankton species [16], and are also relatively small in relation to the excitation volume in the Raman spectrometer. Raman spectra were first recorded for an f/2 growth medium sample, and then a pipette was used to add drops of each phytoplankton culture. Raman spectra were recorded after each drop, and an average of 10 spectra was taken for each sample. Two samples for each species were fixed using Lugol solution, and the concentration of phytoplankton in each sample was then measured by counting under a microscope.

## 3. Background signals, their implication for determining temperature, and their origin

Fig.2 shows two examples of temperature-dependent unpolarised Raman spectral data, corresponding to the OH stretching band, acquired for water samples from coastal locations: Rose Bay, Clontarf, and Rhodes. The Raman signal is given in terms of signal counts registered by the spectrometer (i.e. the CCD counts corrected for grating and detector spectral response) and have not been normalised. In the case of the Rose Bay water sample shown in Fig.2(a), which had been filtered and UV treated, the temperature-dependence is well-defined in terms of an isosbestic at  $\sim 3422 \text{ cm}^{-1}$ . However, the same cannot be said for the other examples, which lack a clear isosbestic point and exhibit higher baseline levels. It was observed that the baseline could be reduced by passing the water sample through filter paper and that it could be increased by stirring the water sample, both of which suggest that the baselines arise at least partially from suspended material. The samples analysed here were neither filtered nor stirred.

Maps depicting the accuracy with which water temperature can be predicted were generated from the measured Raman spectra and are shown in Fig. 2. Fairly wide spectral channels ( $200 \text{ cm}^{-1}$ ) were used in the analysis, motivated by our end goal being to implement the methods we develop in the field, rather than the laboratory. As found in [8] the optimal channel width is a compromise between temperature sensitivity and signal strength. In practice, its selection will depend on factors such as the laser source, receiver and detector characteristics. The RMSTE maps in Fig. 2 show that it is straightforward to predict the water temperature of the Rose Bay water (filtered and UV treated) with a relatively high accuracy of  $\pm 0.3^\circ\text{C}$ , and there is a reasonable amount of flexibility when selecting the optimal spectral channels. In the case of the water sample from Rhodes, for which a considerable baseline is present, the accuracy was somewhat lower at around  $\pm 1.0^\circ\text{C}$  and moreover there is a narrow window for selecting the optimal spectral channels.

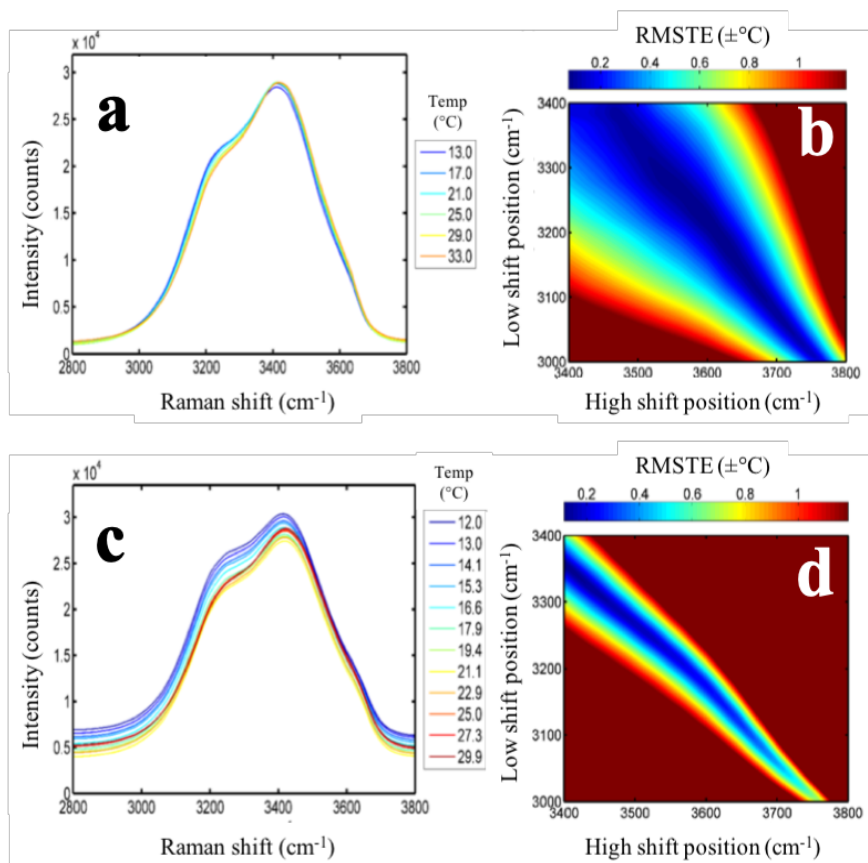


Fig. 2. (a) and (c) show unpolarised Raman spectra for Rose Bay and Rhodes samples, as a function of temperature; (b) and (d) show associated maps of RMSTE computed for all pairs of wavenumber channel centres (200  $\text{cm}^{-1}$  channel width).

The presence of background signals in Raman spectroscopy is very well-known and is frequently due to fluorescence from various constituents of the sample which interact with the excitation laser. In the case of natural waters, several studies [13,14] have shown that fluorescence arises from organic molecules excited at 532 nm, specifically DOM and Chl-a. To explore whether such fluorescence was responsible for the baselines observed in our measured Raman spectra, we sought to understand which portions of the spectra gave rise to higher variances between waters collected at different locations, by means of a spectral Principal Component Analysis (PCA) using the Single Value Decomposition algorithm, a non-iterative algorithm with optimum performance for spectral data. PCA is a technique able to summarize large multi-dimensional datasets, such as spectral data, into fewer dimensions of variability called Principal Components (PC). PCs are orthogonal to each other and represent axes of maximum variability between samples *i.e.*, PC-1 always accounts for the maximum variability, PC2 accounts for most of the variability not explained by PC-1 and so on. Interpretation of PCA results require prior knowledge regarding potential spectral signatures in the sample, as a PC might represent residual variations with no spectral significance [17, 18].

In our study, two data sets were selected to perform the PCA: a calibration set comprised an average of Raman intensities at different temperatures for each location (13°C, 17°C, 25°C, 29°C and 33°C) and a validation set of Raman intensities measured for 21°C. Both datasets were normalised by the peak aiming to reduce the temperature-dependent effect around the OH stretching band and isosbestic points. The Unscrambler®X, version 10.5, a software from CAMO, was used for the PCA.

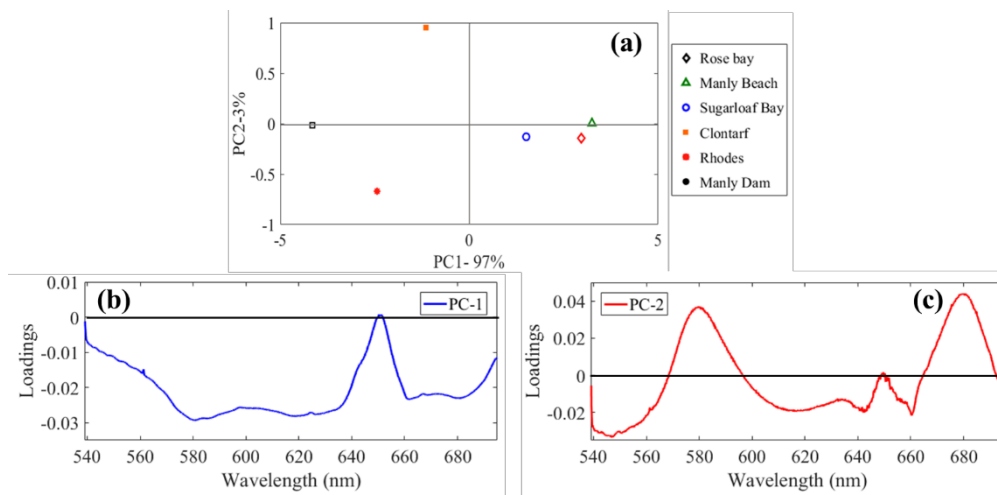


Fig. 3. PCA overview. (a) Scores plot. (b) PC-1 loadings plot. (c) PC-2 loadings plot.

PCA of Raman spectra generated a model explaining 99.5% (98.6%) of spectral variation among locations for the calibration (validation) data by using two principal components: PC-1 and PC-2. Rhodes and Clontarf (solid symbols) variances were associated with both PC1 (x axis) and PC2 (y axis); Rose Bay, Sugarloaf Bay, Manly Beach and Manly Dam (hollow symbols) had their variances explained by PC1 alone (Fig. 3(a)).

Loadings are estimations of how much each variable (in this study, the intensity of the Raman signal at a given wavelength) contributes to variability on each PC. In order to understand the origin of spectral variabilities from PCA findings, the loadings plots (Fig. 3(b,c)) need to be interpreted along with the scores plot (Fig. 3(a)). For a given PC, positive (negative) values on the scores plot exhibit higher (lower) than average values for wavelengths with positive (negative) loadings. Negative scores have lower (higher) than average values for wavelengths with positive (negative) loadings.

PC-1 explained 97% of the total variance in the general model and its loadings plot is shown in Fig. 3(b). There were two domains of variability, with negative loadings values for wavelengths from 560 nm to 635 nm, corresponding to the spectral region of DOM fluorescence; and from 665 nm to 700 nm, including the Chl-a fluorescence peak at 680 nm. Negative loadings at these spectral regions indicate higher than average values for samples with negative scores for PC-1 (Fig. 3(a)), represented by Rhodes, Clontarf and Manly Dam. Ultimately, these samples exhibited higher than average variance at spectral regions with known spectral signatures associated with fluorescence of common optically active constituents in natural waters. Rose Bay, Sugarloaf Bay and Manly Beach had positive PC-1 scores.

PC-2 accounted for 3% of total modelled variance among locations and its loadings plot show well-defined negative peaks at around 580 nm, area of *Gelbstoff* fluorescence and 680 nm (Chl-a) (Fig. 3(c)). Negative loading peaks were associated with high variabilities for negative scores, here attributed to Rhodes (Fig. 3(a)), indicating higher than average values for fluorescence on this sample. Conversely, the analysis indicated lower than average values for fluorescence at these well-defined peaks in the Clontarf sample. Rose Bay, Sugarloaf Bay, Manly Beach and Manly Dam samples exhibited PC-2 scores close to zero, indicating PC-2 doesn't explain significant spectral variances on these samples.

In summary, the PCA analysis reveals systematic but complex differences between the water samples investigated. It is interesting to note that including a freshwater sample (Manly Dam) didn't compromise the model performance. It may be indicative that, when temperature variation is excluded, background fluorescence seems to be more important than salinity effects on spectral variance among these natural water samples.

Having established that fluorescence largely accounts for the background effects we observe, we sought to explore the extent to which fluorescence from different species of phytoplankton might interfere with measurements of the Raman spectra for natural waters, and to quantify the concentration of phytoplankton that might substantially modify the Raman signal. To do this we selected species of phytoplankton that have a range of characteristic pigments that are broadly representative of the major phytoplankton groups such as zeaxanthin, phycocyanin, phycoerythrin, carotene and violaxanthin. These were *Synechococcus* Red, *Synechococcus* Green, *Nannochloropsis* sp., *Ditylum Brightwelli*, *Dunallia tertiolecta*, *Ostreopsis siamensis* and *Rhodomonas salina*. Dilute samples of each were placed in a Varian Eclipse fluorescence spectrometer and emission and excitation spectra recorded. Each species, with the exception of *Synechococcus* Red, when excited at 532 nm exhibited fluorescence with a broad (typically 10-30 nm full width at half maximum) peaks in the range 660-685 nm. When excited at the shorter wavelength of 473 nm, *Synechococcus* Red and *Rhodomonas salina*

exhibited additional peaks at 560 and 590 nm respectively. The fluorescence from phytoplankton has been widely studied and our observations are consistent with the literature [16].

Having observed the overlap between phytoplankton fluorescence and the Raman signal, we set about investigating what phytoplankton concentrations would cause significant distortion to the Raman signal. In order to do this, Raman spectra were recorded while small amounts of phytoplankton were added to the f/2 growth medium. The intensity of the Raman signal exhibited considerable variation after the phytoplankton was added, and we hypothesise that this variation was due to phytoplankton drifting across the excitation volume.

Selected fluorescence spectra obtained using 532 nm excitation are shown in Fig. 4. Fig. 4(a) shows the Raman spectrum obtained for the f/2 growth medium, and it can be seen that the Raman band is clean, with relatively low background. Substantial changes were observed as phytoplankton was added, with the Raman band then being superimposed upon a fluorescence pedestal. For *Nannochloropsis* and *Synechococcus* Green, the fluorescence was peaked around 680 nm, while for *Synechococcus* Red, substantial fluorescence occurred around 575 nm. The corresponding spectra are shown in Fig. 4, along with the corresponding phytoplankton cell counts that were determined using the counting procedure outlined earlier. The concentrations are comparable to those found in nature, and thus it is clear that the presence of phytoplankton in natural water samples can potentially compromise the efficiency with which temperature can be determined via Raman spectroscopy.

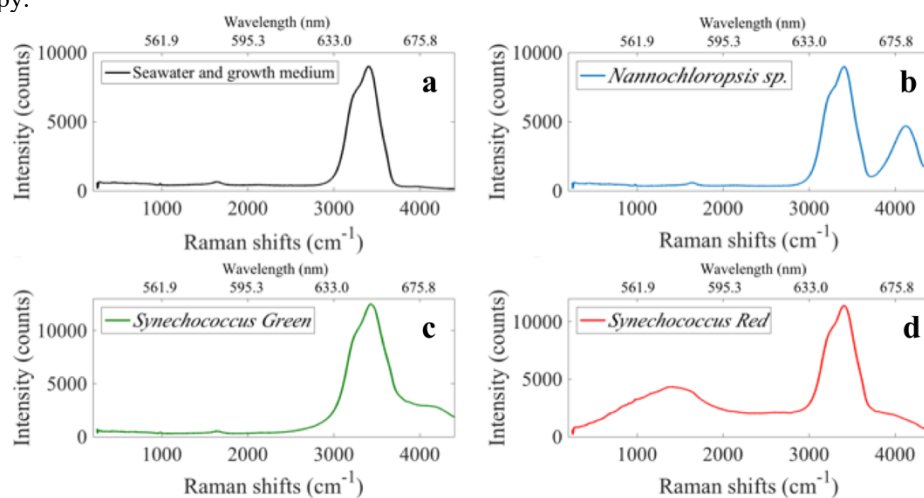


Fig. 4. Raman spectra obtained for autoclaved seawater with f/2 growth medium with (a) no added phytoplankton, (b) *Nannochloropsis* at  $9.14 \times 10^3$  cells per mL, (c) *Synechococcus* Green at  $7.78 \times 10^4$  cells per mL, and (d) *Synechococcus* Red at  $1.23 \times 10^5$  cells per mL.

#### 4. Improving RMSTE by post-acquisition baseline correction

On the basis of the foregoing measurements and analysis, we attribute the background signals observed for water samples to fluorescence, predominantly from DOM and phytoplankton. It has been further established that naturally occurring phytoplankton concentrations are sufficient to significantly perturb the Raman spectra collected using excitation at 532 nm. In [14] it was suggested that the optimal excitation wavelength for Raman excitation was below 520 nm, however 532 nm lasers are more readily available and already used for other oceanographic measurements. Next, we will explore baseline correction techniques which make it feasible predicting water temperature with high accuracy using the two-colour method in natural waters.

It is apparent from the temperature maps of Fig. 2 that fluorescence background signals reduce the accuracy with which temperature can be determined, and the optimal centre wavelength for the two channels is substantially constrained. Here we analyse the accuracy with which temperature can be predicted from the raw Raman spectra, and present two effective methods of correction post acquisition. The channels selected for two-colour prediction analysis are centred at  $3200 \text{ cm}^{-1}$  and  $3600 \text{ cm}^{-1}$ , a compromise based on the RMSTE maps for all the water samples investigated here. These channels are depicted in Fig. 5 and will be referred to as “low shift” and “high shift” channels hereafter.



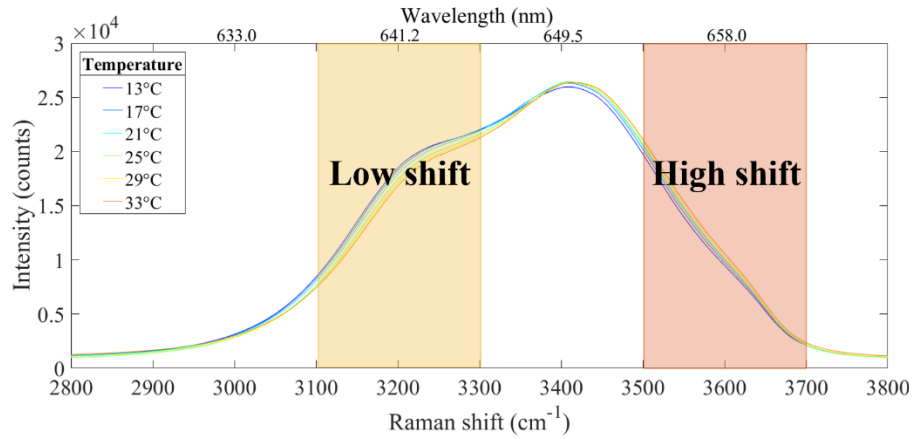


Fig. 5. Integration channels (200 cm<sup>-1</sup> bandwidth) superimposed on unpolarised Raman spectra for Rose Bay sample.

RMSTEs for uncorrected Raman signal of various water samples were determined simply by integrating the signals within the low shift and high shift bands, taking their ratios and making a linear regression against reference temperature. Accuracies varied from  $\pm 0.3^\circ\text{C}$  to  $\pm 2.6^\circ\text{C}$ , with lowest RMSTE values found for Rose Bay and higher values for freshwater samples from Manly Dam and the inner harbour location of Rhodes. The association between larger baselines and lower RMSTEs reinforces the notion that fluorescence compromises the accuracy of temperature prediction. It can be seen by inspecting the data in Fig. 7(a) that there are considerable differences in the slopes and the actual values of the two-colour markers for water samples from different locations.

Next, we present two methods by which this accuracy was found to be improved: tilted baseline correction and an entirely new method: correction by temperature marker values.

#### 4.1. Method 1: Tilted baseline correction

Tilted baseline is a background correction technique established on the premise that the measured Raman signal should be close to zero on either side of the OH stretching band. For this study, points at 2800 cm<sup>-1</sup> and 3750 cm<sup>-1</sup> for each spectrum were used to define a “tilted baseline” that was subtracted from each spectrum to yield new, “baseline-corrected” spectra which were then analysed according to the usual two-colour method.

Fig. 7(b) shows the predicted RMSTEs for the various water samples after applying the tilted baseline method. When compared to uncorrected RMSTE data all locations showed lower RMSTEs as a result of the tilted baseline correction. The technique has proven to be a simple data processing technique for reducing the impact of fluorescence on Raman spectroscopy water temperature prediction and inspection of Fig. 7(b) shows that while the tilted baseline correction has been effective in making the slopes more uniform, there is still considerable variation in the values of the two-colour markers. It was this observation, that fluorescence affects both slopes and marker values, that led us to propose a second correction method. It should be noted, however, that there is no physical reason to assume the baseline is in fact linear.

#### 4.1. Method 2: Correction by temperature marker values

Previously, it was observed that Rose Bay samples are the least impacted by fluorescence signals and have very low baseline. These samples had been subject to filtration and UV treatment leading to low concentrations of phytoplankton, and due to the location being close to the harbour mouth, DOM concentration is also expected to be low. Hence, we assume the temperature markers calculated by two-colour analysis for this location represent the “standard” Raman signal for seawater, with no fluorescence contribution.

We now present an entirely new approach to baseline correction based on the differences in temperature markers between natural water samples and the Rose Bay standard. Our premise (for the purpose of this correction method) is that the natural water sample comprises water that is similar to that at Rose Bay, plus additional constituents that fluoresce. Therefore, the two-colour markers for the natural water sample deviate from the two-colour markers for Rose Bay ratio by an amount due to that fluorescence (Eq. (1)).

$$R_{N_{T_1}} = R_{RB_{T_1}} + \Delta R_{Fl} \quad (1)$$

where  $R_{RB_{T_1}}$  indicates the two-colour marker for the Rose Bay standard at temperature  $T_1$ ,  $R_{N_{T_1}}$  is the ratio for a natural water sample and  $\Delta R_{Fl}$  represents the influence of fluorescence on the marker for natural water samples.

As established earlier, the distribution of fluorescence signals across the Raman spectrum of natural waters is not homogenous. Accordingly, we introduce two fluorescence variables into the model:  $X$  (corresponding to fluorescence in the low shift band) and  $Y$  (corresponding to fluorescence in the high shift band), as indicated in Fig. 6 and in Eq. (2).

$$R_{N_{T1}} = \frac{B_{N_{T1}}}{R_{N_{T1}}} = \frac{B_{RB_{T1}} + Y}{A_{RB_{T1}} + X} \quad (2)$$

with  $B_{N_{T1}}$  representing the integrated signal for the high shift channel (200  $\text{cm}^{-1}$  width and centred at 3600  $\text{cm}^{-1}$ ) and  $A_{N_{T1}}$  representing the integrated signal for the low shift channel (200  $\text{cm}^{-1}$  width and centred at 3200  $\text{cm}^{-1}$ ).

Two parameters were extracted from the measured spectra to solve Eq. (2) for  $X$  and  $Y$  values (Eq. (3) and Eq. (4)):

$$\Delta R_{Fl} = R_{N_{T1}} - R_{RB_{T1}} \quad (3)$$

and

$$C_{T1} = \frac{R_{N_{T1}}}{R_{RB_{T1}}} \quad (4)$$

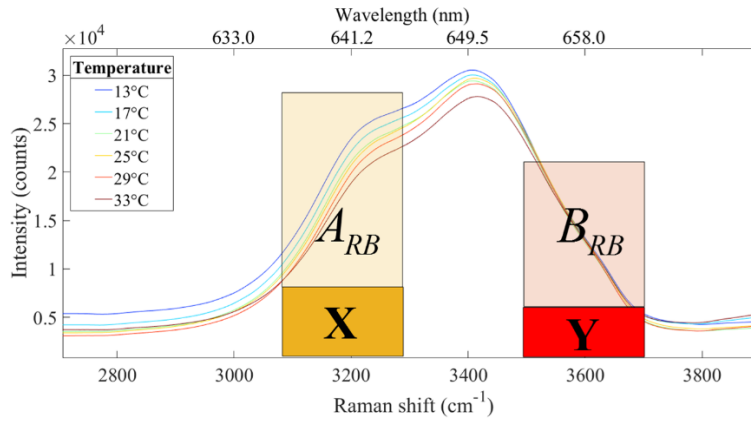


Fig. 6. Depiction of the premise underlying correction method 2. The Raman spectra for Clontarf within a channel comprises Raman photons plus fluorescence photons.

For each water sample considered here, the  $Y$  values were considerably smaller than the  $X$  values.  $Y$  values were found to be independent of temperature, allowing for the use of an average value when calculating the new temperature marker. Unexpectedly, and for reasons which are not clear,  $X$  values showed a systematic variability with temperature, and therefore temperature-dependent  $X$  values were used when calculating the new temperature marker (*i.e.*  $X_{T1}, X_{T2} \dots X_{Tn}$ ). By this process, corrected datasets were calculated, and are shown in Fig. 7(c). Predicted values for RMSTEs after correction by ratios, alongside the RMSTE for uncorrected data, are shown in Fig. 7(d). Method 2 was effective in that the corrected data for different location exhibited similar slopes and similar values, with improved temperature predictions in all water samples. RMSTEs after correction by method 2 ranged from  $\pm 0.2^\circ\text{C}$  to  $\pm 0.3^\circ\text{C}$ , therefore the method appears to be very effective and can in principle be applied to any water sample. In the case of our freshwater sample (Manly Dam). Reverse-osmosis water was used as the “standard”.

The RMSTEs for uncorrected data and the data after correction by either method 1 or method 2 are presented in Fig. 7(d) for the water samples from different locations. Both methods had the effect of improving the quality ( $R^2$  value) and the linear fit (Fig. 7(a-c)), and both methods were effective in substantially increasing the accuracy with which temperature can be predicted. Method 2 was more effective



than method 1 for Clontarf. and Manly Beach samples.

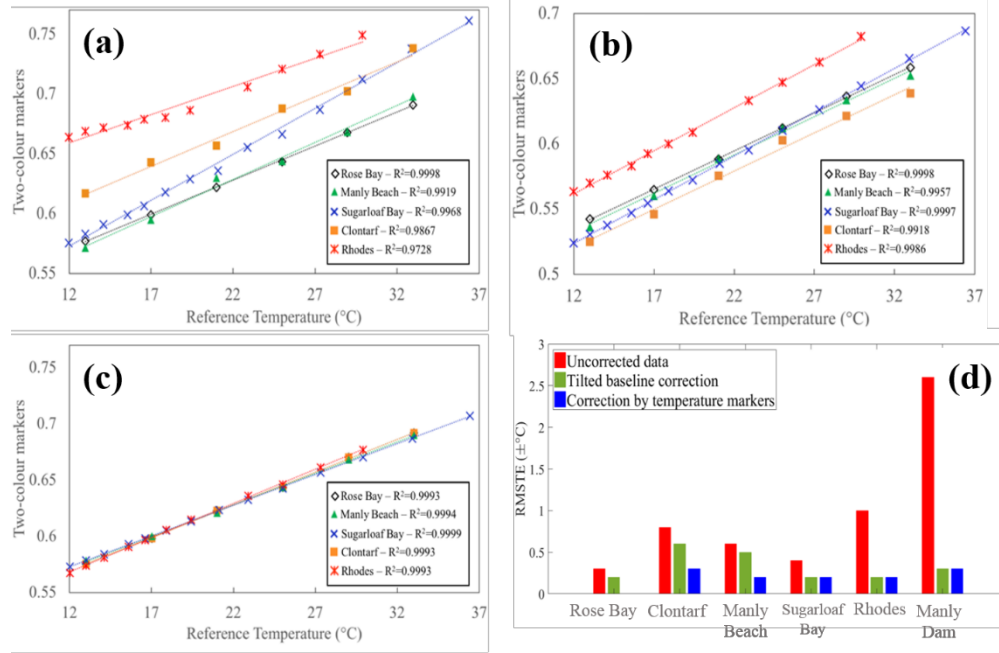


Fig. 7. Two-colour markers are plotted as a function of reference temperature for (a) uncorrected data; (b) data corrected by method 1; (c) data corrected by method 2; (d) presents the RSMTEs for samples from different locations with and without correction.

## 5. Discussion

The marine environment is known for its complex and dynamic nature, especially in coastal areas, resulting in high variability of water properties such as active optical components, salinity and vertical thermal stratification. The challenge of remotely sensing temperature in these environments using Raman spectroscopy began in the 70's [19,20] and continued, with recent studies by [8] and [21] reporting temperature accuracies better than  $\pm 0.2^\circ\text{C}$ . In subsequent studies using synthetic seawater, [22] achieved accuracies of  $\pm 0.2^\circ\text{C}$  on standard seawater temperature determination by using a commercial Raman spectrometer coupled to a 532 nm laser and applying the two-colour method, demonstrating that Raman Spectroscopy had also the potential to provide highly accurate temperature data on the presence of dissolved salts. For these methods to be truly useful, they need to be applicable to a range of water samples in which fluorescing material may be present, and this paper is intended to advance that cause.

We have taken a qualitative approach to establishing that the baseline found in our Raman spectra for natural water samples arise mainly from DOM and Chl-a fluorescence. Furthermore, we have measured the phytoplankton concentrations that give rise to substantial fluorescence which overlaps with the Raman spectral band.

We have demonstrated two methods for baseline correction which are effective in increasing the accuracy with which temperature can be determined in natural waters. In terms of ease of field implementation, both methods present distinctive challenges. The tilted baseline correction method would require an additional two channels for collecting the very weak signals arising from fluorescence on either side of the Raman band, thereby reducing the signal-to-noise ratio for each of the main channels. A second drawback of this method is that there is no physical reason to expect the fluorescence spectrum to be linear around the Raman feature, and this is the fundamental assumption of the method.

Method 2 does not require special filters or impact directly on signal-to-noise ratio but it does require a database of temperature-dependent ratios as standards for comparison. In principle, ratios for all Jerlov water types could be obtained and used for calibration; alternatively, a local water sample can be collected and analysed to determine the correction factors required for analysis. The work presented here provides proof of concept and future work will test the viability of this promising method.

## 6. Conclusion

The findings in this paper help us to move one step forward our final goal: a LIDAR- compatible custom-built multichannel Raman spectrometer able to measure depth-resolved temperature data *in situ* as firstly proposed in [8].

We have shown that Raman spectra collected from natural water samples around Sydney Harbour exhibit background signal levels that adversely affect the accuracy with which temperature can be determined. We

have shown the background signals arise from fluorescence, allegedly from DOM and Chl-a, and quantified the phytoplankton concentrations that cause distortion of the OH stretching band. We have proposed two methods of baseline corrections that are effective in improving temperature accuracy and considered how they could be implemented in the field. There is scope for a systematic fluorescence and Raman spectroscopic study that considers a wider range of samples which are characterised in terms of DOM concentration, chlorophyll-a concentration and salinity.

## Acknowledgments

Miss. Andréa de Lima Ribeiro and Dr. Christopher Artlett gratefully acknowledge receipt of Macquarie University iMQRES/MQRES PhD scholarships. Prof. Helen Pask gratefully acknowledges receipt of an Australian Research Council Future Fellowship (project number FT120100294).

## 7. References

1. G. E. Walrafen, "Raman Spectral Studies of the Effects of Temperature on Water Structure," *J. Chem. Phys.* **47**(1), 114 (1967).
2. G. E. Walrafen, M. R. Fisher, M. S. Hokmabadi, and W.-H. Yang, "Temperature dependence of the low- and high-frequency Raman scattering from liquid water," *J. Chem. Phys.* **85**(12), 6970–6982 (1986).
3. C. H. Chang and L. A. Young, *Seawater Temperature Measurement from Raman Spectra* (1972).
4. D. A. Leonard, B. Caputo, and F. E. Hoge, "Remote sensing of subsurface water temperature by Raman scattering," *Appl. Opt.* **18**(11), 1732–45 (1979).
5. B. Breschi, G. Cecchi, L. Pantani, V. Raimondi, D. Tirelli, and G. Valmori, "Measurement of Water Column Temperature by Raman Scattering," *EARsel Adv. Remote Sens.* **1**(2), 131–134 (1992).
6. Z. Liu, J. Zhang, and W. Chen, "Remote sensing of subsurface water temperature using Raman LIDAR," *SPIE* **1633**(Laser Radar VII), 321–329 (1992).
7. F. A. Bunkin, K. V. Klinkov, N. V. Lednev, L. D. Lushnikov, V. A. Marchenko, G. E. Morozov, M. S. Pershin, N. R. Yulmetov, A. F. Bunkin, V. K. Klinkov, V. N. Lednev, D. L. Lushnikov, A. V. Marchenko, E. G. Morozov, S. M. Pershin, and R. N. Yulmetov, "Remote sensing of seawater and drifting ice in Svalbard fjords by compact Raman lidar," *Appl. Opt.* **51**(22), 5477–5485 (2012).
8. C. P. Artlett and H. M. Pask, "Optical remote sensing of water temperature using Raman spectroscopy," *Opt. Express* **23**(25), 31844 (2015).
9. R. M. Measures, W. R. Houston, and D. G. Stephenson, "Laser Induced Fluorescent Decay Spectra - A New Form of Environmental Signature," **13**, 136494–136498 (1974).
10. K. Kalle, "The problem of the gelbstoff in the sea," *Ocean. Mar. Biol. Ann. Rev.* **4**, (1966).
11. C. D. Mobley, *Light and Water: Radiative Transfer in Natural Waters* (1994).
12. J. E. James, C. S. Lin, and W. P. Hooper, "Simulation of laser-induced light emissions from water and extraction of Raman signal," *J. Atmos. Ocean. Technol.* **16**(2–3), 394–401 (1999).
13. C. Lin, "Tunable laser induced scattering from coastal water," *IEEE Trans. Geosci. Remote Sens.* **37**(5), 2461–2468 (1999).
14. C. S. Lin, "Characteristics of laser-induced inelastic-scattering signals from coastal waters," *Remote Sens. Environ.* **77**(1), 104–111 (2001).
15. R. R. L. Guillard, "Culture of phytoplankton for feeding marine invertebrates," in *Culture of Marine Invertebrate Animals*, W. L. Smith and M. H. Chanley, eds. (Plenum Press, 1975), pp. 22–60.
16. S. Roy, C. Llewellyn, E. S. Egeland, and G. Johnsen, eds., *Phytoplankton Pigments* (Cambridge University Press, 2011).
17. H. E. Nystad, "Comparison of Principal Component Analysis and Spectral Angle Mapping for Identification of Materials in Terahertz Transmission Measurements," (2015).
18. H. Abdi and L. J. Williams, "Principal component analysis," *Wiley Interdiscip. Rev. Comput. Stat.* **2**(4), 433–459 (2010).
19. C. H. Chang and L. A. Young, *Seawater Temperature Measurement from Raman Spectra* (1972).
20. D. A. Leonard, B. Caputo, and R. L. Johnson, "Experimental remote sensing of subsurface temperature in natural ocean water," *Geophys. Res. Lett.* **4**(7), 279–281 (1977).
21. M. Oh, H. Kang, N. E. Yu, B. H. Kim, J. Kim, J. Lee, and G. W. Hyung, "Ultimate sensing resolution of water temperature by remote Raman spectroscopy," *Appl. Opt.* **54**(10), 2639–2646 (2015).
22. C. P. Artlett and H. M. Pask, "New approach to remote sensing of temperature and salinity in natural water samples," *Opt. Express* **25**(3), 2840 (2017).

### 3.2. Principal Component Analysis – understanding spectral signatures in natural waters

Coastal zones are highly dynamic areas influenced by waves, tides and rivers discharge which impact directly on the concentration of optically active components in water. Sediments in suspension, phytoplankton and CDOM are examples of optically active components which concentrations are variable in space and time, fluorescing when excited by light and producing spectral signatures detectable on backscattered signals retrieved from natural water samples. In manuscript 1 [113], we explored the spectral variance among samples from locations around Sydney Harbour. The PCA analysis indicated that the major sources of variabilities among locations were in agreement with spectral signatures for DOM and Chl-a fluorescence signals, *i.e.*, Raman spectra from those locations were different from each other due to the presence of various seawater optically active components. This valuable information allowed us to propose methods of correction to minimize overlapping between Raman and fluorescence signals which would result in more accurate. However, the analysis did not provide information regarding temperature effects on spectral signatures and local variations within each sampling site. Local PCAs could provide supplementary information for a fully understanding of origin and diversity of background signals found for coastal samples collected throughout this study. This section is dedicated to exploring local Raman spectral variabilities and identifying possible variance patterns associated with water temperature, which were missed by the general model presented in manuscript 1[113].

In order to assess the spectral variation within each sampling site, PCA analysis as outlined in manuscript 1 were performed for all uncorrected, temperature-dependent spectra acquired from saltwater samples (Rose Bay, Clontarf, Manly Beach, Sugarloaf Bay and Rhodes) without any normalisation. Due to the small number of spectra acquired for each location a full cross-validation technique was performed where each sample was used on both calibration and validation processes individually, as described in Chapter 2. PCA analysis for Rose Bay, Clontarf, Manly Beach, Sugarloaf Bay and Rhodes are shown on figures 3.1. to 3.5., respectively.

### **Rose Bay analysis**

Samples of Rose Bay water had been UV treated and filtered prior to spectroscopic analysis; hence, spectral variabilities arising from particulate matter and fluorescence from photosynthetic pigments were not expected to be major sources of variance on this sample.

PC-1 represented 81% of variances among Rose Bay spectra and its scores and loadings plot are shown in figures 3.1a and 3.1b, respectively. Two main peaks of variability were found by PC-1 loadings (figure 3.1b): a positive peak centred around 640 nm (low shift of OH stretching band); and a negative peak centred around 650 nm (high shift of OH stretching band) (figure 3.1b).

PC-2 loadings plot (figure. 3.1b) showed minor contributions for spectral variability, also on the OH stretching band region and possibly linked to temperature-dependent processes (figure 3.1b). It's possible to observe a minor negative shoulder on both PC loadings from 540 to 620 nm, regions of known DOM fluorescence; at this instance it's not possible to determine whether they are accounting for background fluorescences or residual variances from the model.

Both PC-1 and PC-2 presented higher variances at wavelengths associated with the OH stretching band, from 630 to 660 nm for 532 nm excitation, a region at which the Raman signal exhibits strong temperature-dependence. Together, PC-1 and PC-2 answered to 99% (95%) of the variance found on calibration (validation) datasets. Lastly, the absence of major signal sources other than water generating variation among spectra for Rose Bay allowed for calculation of refined and sensitive two-colour temperature markers, resulting in optimal accuracies on temperature predictions by Raman signals ( $\pm 0.3^{\circ}\text{C}$ ).

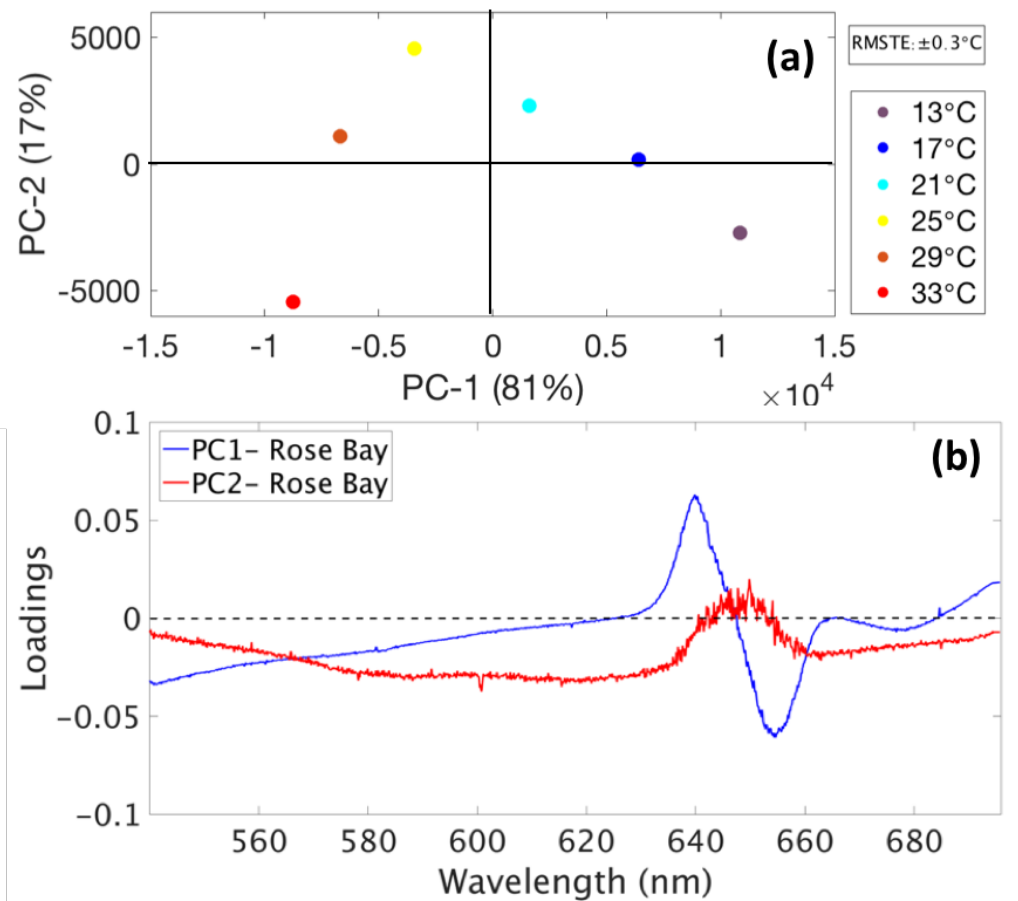


Figure 3.1. Principal Component Analysis for Rose Bay water, uncorrected data. a) scores; b) loadings plot.

### Clontarf analysis

PCA analysis of Raman spectra from Clontarf presented two PCs, totalling 98% of total variance between acquisitions for calibration data (95% for validation data) (figure 3.2.). PC-1 loadings (85% of variance) showed areas of variability on regions from 580 to 630 nm, overlapping with the area of maximum temperature-dependent behaviour of Raman signal around the OH stretching band (630 to 660 nm) (figure 3.2b). This spectral region is in conformity with reports of fluorescence by DOM and photosynthetic pigments.

PC-2 loadings (13% of calibration variance) complements the expected temperature-dependent signal variability around the OH stretching band; however, it also indicates a region with high variances around 680 nm for spectra with positive scores (33°C spectrum) (figure. 3.2a).

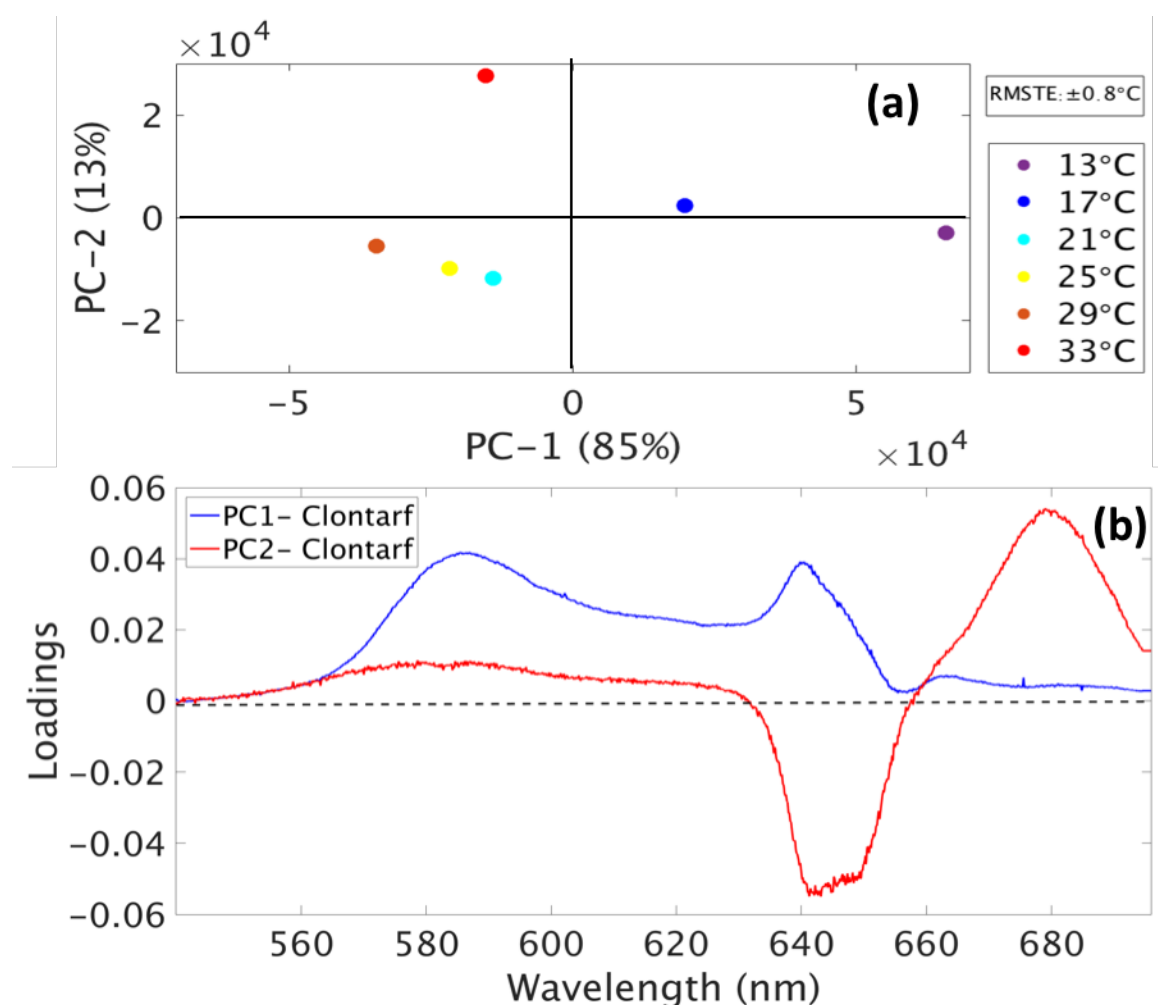


Figure 3.2. Principal Component Analysis overview for Clontarf water, uncorrected data.  
a) scores plot; b) loadings plot.

### Manly Beach analysis

Manly Beach (figure 3.3.) presented PCs loadings around the OH stretching band similar to the standard seawater sample (figure 3.1.), with a pronounced area of high variability found on PC-1 and PC-2 (74% and 15% of total variance for calibration data, respectively). A peak of high variance around 680 nm was identified by both PCs for all spectra except 33°C, compatible with Chl-a fluorescence and potentially overlapping with the Raman peak.

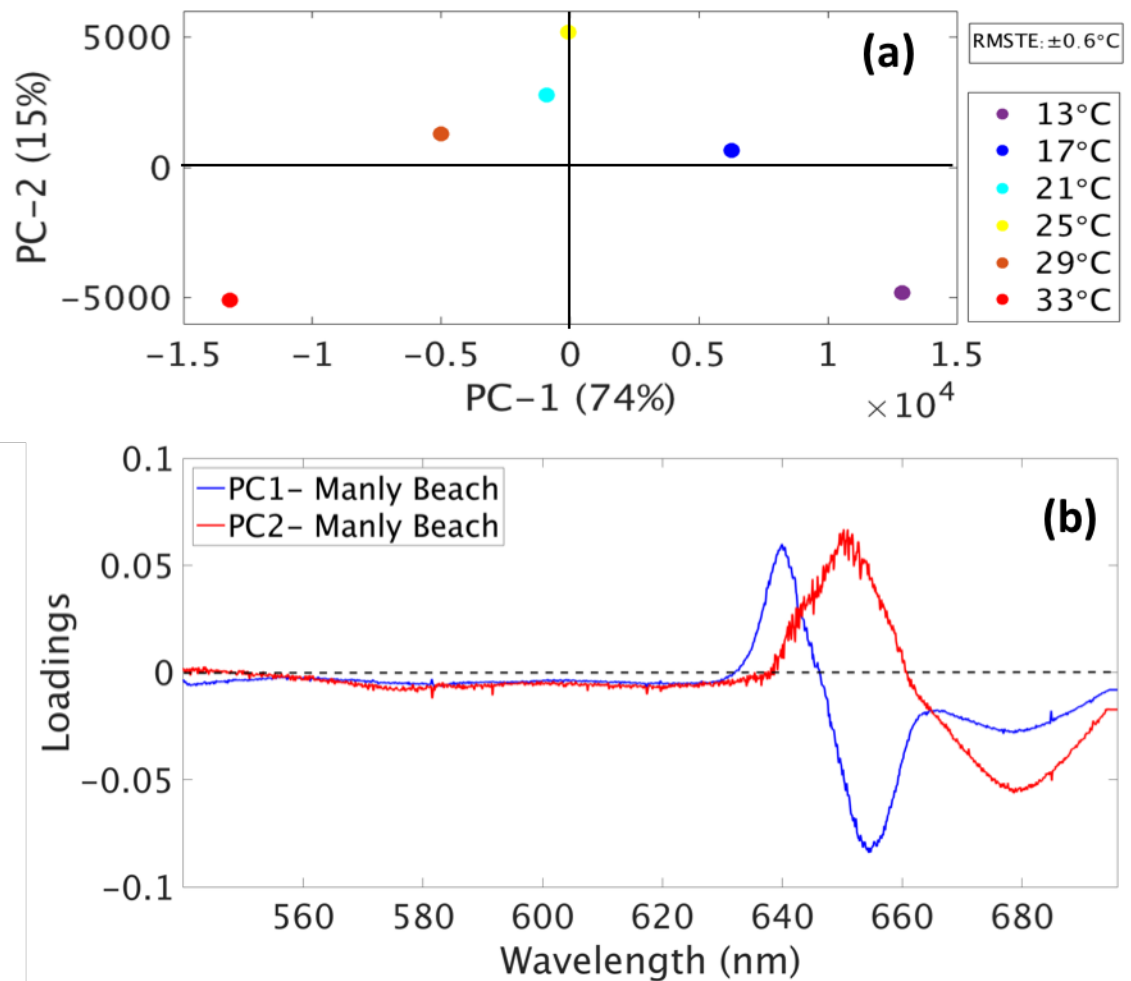


Figure 3.3. Principal Component Analysis overview for Manly Beach water, uncorrected data. a) scores plot; b) loadings plot.

### Sugarloaf Bay analysis

Variabilities on Sugarloaf Bay spectra were summarised by PC-1 and PC-2 loadings (94% and 5% of total variation found for calibration data, respectively) and where found to be in agreement with the expected behaviour of Raman signal around the OH stretching band (figure 3.4b). Additionally, PC-1 exhibited higher than average variances for regions around 680 nm, which might be linked to chlorophyll-a all fluorescence processes.

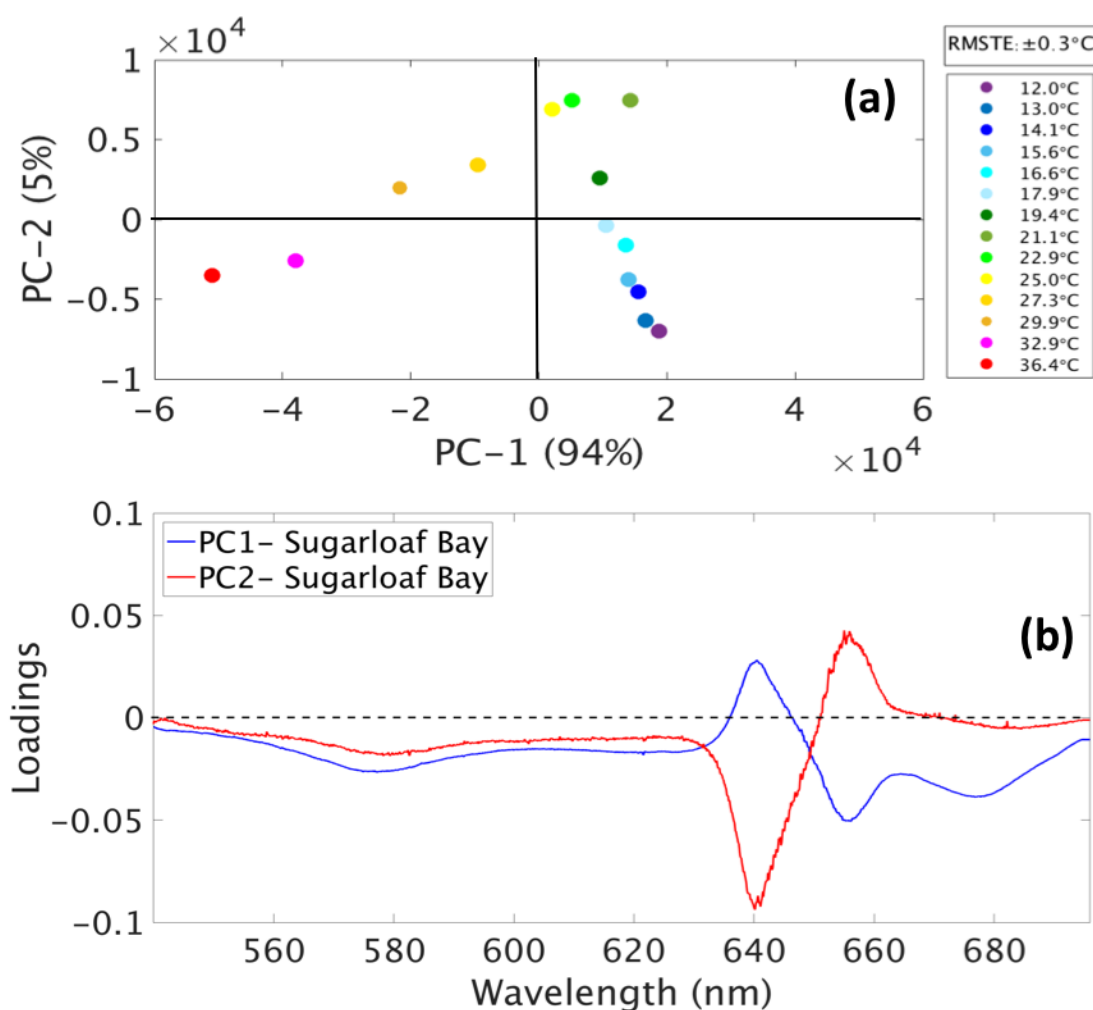


Figure 3.4. Principal Component Analysis overview for Sugarloaf Bay water, uncorrected data.  
a) scores plot; b) loadings plot.



### Rhodes analysis

Principal Component Analysis for Rhodes water showed the most erratic pattern for PC-1 loadings, accounting for 97% of variances among temperatures for calibration data (figure 3.5b). It exhibited a pedestal of variance underlying the whole spectra, with and a small peak around the OH stretching band. PC-2 (2% of variance for calibration data) displayed minor signs of temperature-dependent variances around the OH stretching band.

Rhodes was an atypical sample, and the origin of background signals could not be fully explained by DOM or Chl-a fluorescences. These variances might be associated with the presence of a ferry station near the collection site, with visible oil stains at the water surface.

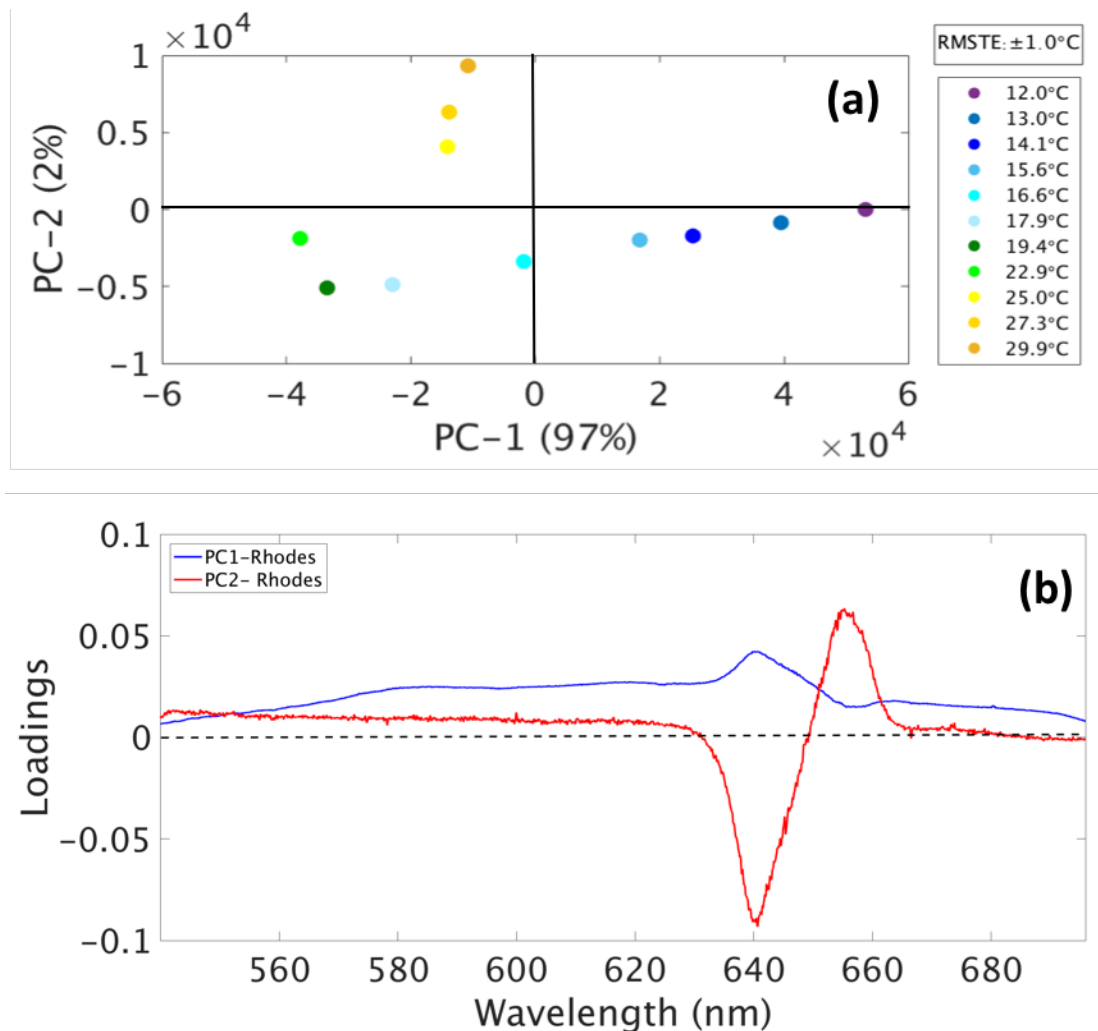


Figure 3.5. Principal Component Analysis overview for Rhodes water, uncorrected data. a) scores plot; b) loadings plot.

## **Discussion**

Although no temperature-dependent behaviour is documented for DOM or Chl-a fluorescence intensities, natural water samples are non-homogenous solutions and concentrations of optically active elements are constantly changing, particularly with phytoplankton cells undergoing sedimentation, changes in physiologic functions and bleaching when interacting with the laser beam. These phenomena are further enhanced by conditioning water inside a cuvette, resulting in a small cubic volume being sampled at each time, added to laser energy fluctuation inherent to spectroscopic studies. Ultimately, different Chl-a fluorescence intensities may be found for spectra collected from the same sample simply due to fluctuations on the number of phytoplankton cells interacting with the laser beam at the time of each acquisition.

As previously discussed, in the absence of optically active components interacting with the excitation light, PCAs for coastal saltwater samples should present spectral variance signatures similar those found for Rose Bay, which was filtered and UV treated (figure 3.1.); nevertheless, this condition is virtually impossible to be achieved and interpretation is necessary to assess which optical components are interacting with Raman

Local PCA analyses made clear that spectral variation regimes were different for each natural water sample, with spectral variances associated with wavelengths known for being result of fluorescence processes and diverging from the expected pattern found for Rose Bay “standard” waters. This qualitative approach can provide useful information regarding characteristics of a site, serving as an initial spectral assessment.

The PCA method is effective in revealing zones of signal variance other than Raman around the OH stretching band may cause direct impact on temperature predictions by two-colour markers, as shown in manuscript 1[113] and also in [86,87,104]. Sugarloaf Bay and Manly Beach exhibited PCs loadings closer to the Rose Bay “standard” and the best RMSTEs for uncorrected data ( $\pm 0.6$  and  $\pm 0.4^{\circ}\text{C}$ , respectively). Conversely, Clontarf and Rhodes exhibited many spectral regions in their PCs with high variances associated with fluorescence signals giving rise poor RMSTE values. This indicates that PCAs are valuable tools for exploring the origin of background signals in natural water Raman spectroscopy and their findings may help us to propose strategies in order to enhance temperature predictions by two-colour markers.

### 3.3. Baseline Correction methods

Temperature-dependent two-colour markers were calculated for uncorrected Raman spectra of coastal water samples according to methodology described in manuscript 1 and are shown collectively in figure 3.6 as a function of reference temperature, along with their respective  $R^2$  values.

Marker values for a given temperature varied widely between samples, diverging from the expected “standard” marker values calculated for Rose Bay water. Smaller, yet significant variations in the slopes and y-axis intercepts of linear functions were also found between locations. Ultimately these are the parameters used for predicting temperature, resulting in different RMSTEs between locations.

Considering the PCA findings indicating sources of spectral variabilities associated with background fluorescence, we infer that differences on two-colour markers among natural water samples arise from overlapping between Raman and other background signals, *i.e.*, in the absence of other signal sources, temperature markers would account solely for Raman signal and should converge towards the same standard values. Post-acquisition correction techniques have the potential to artificially improve the accuracy with which temperature can be predicted.

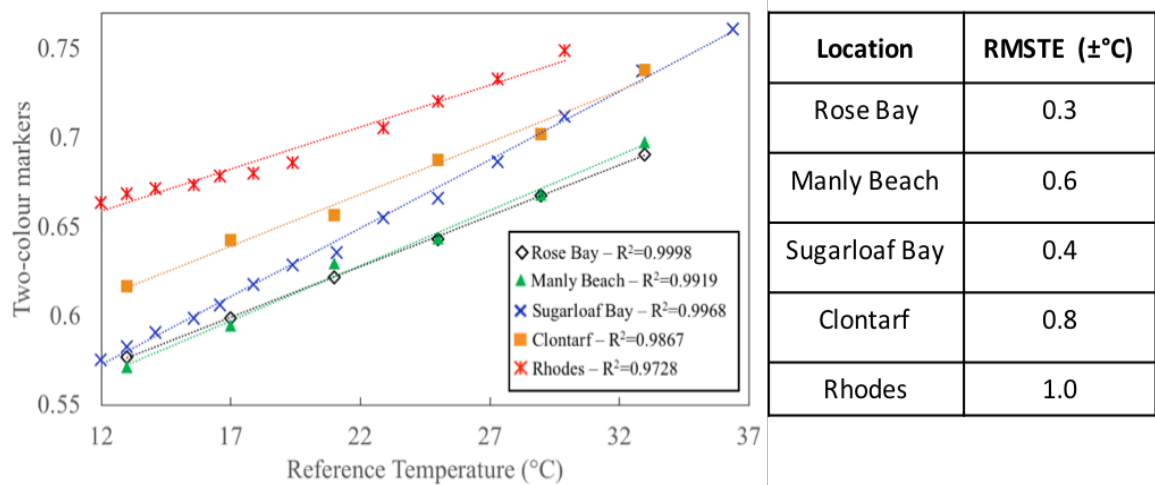


Figure 3.6. Temperature-dependent uncorrected two-colour markers for various natural water samples and respective  $R^2$  and RMSTEs for each location.

Two methods of background signal correction were evaluated by this work: method 1, the traditional tilted baseline correction broadly used in spectroscopic studies; and a new correction method, proposed based on comparisons between Raman temperature markers for standard saltwater and natural water samples. Methodologies and impacts of these correction methods on accuracy of temperature predictions were discussed in [113]; this

section is dedicated to providing a greater level of detail on how each correction method changes the temperature markers.

### 3.3.1. Method 1 – tilted baseline correction

The temperature-dependent two-colour markers for natural water samples after tilted baseline correction (method 1) are shown as a function of temperature in figure 3.7. Intercept and slope parameters of linear trendlines after correction were closer to Rose Bay standard values when compared with uncorrected data (figure 3.7). However, still a significant spread can be identified in the values of two-colour markers at any given temperature.

Manly Beach and Sugarloaf Bay two-colour markers found optimum agreement with Rose Bay standard values; Rhodes and Clontarf, otherwise, still diverged significantly from standard values.

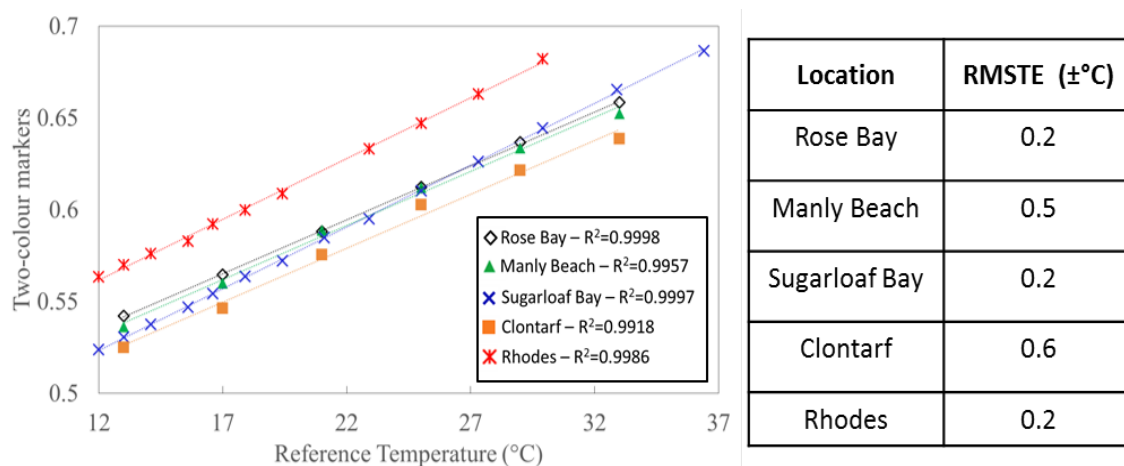


Fig 3.7. Temperature-dependent two-colour markers for various natural water samples after spectral correction by method 1.  $R^2$  and respective RMSTEs for each location are shown.

In order to understand why correction method 1 performed better for some locations than others, local PCA analysis were performed on corrected spectra accordingly to methodology described in section 3.2. A comparison between PC-1 loadings plots for uncorrected and corrected data (method 1) is shown on figures 3.8a-d, indicating low and high shift channels of signal integration used for two-colour analysis. Vertical dashed lines indicate the points of minimum Raman signal from which baseline was estimated (respectively 2800 and 3750  $\text{cm}^{-1}$ ).

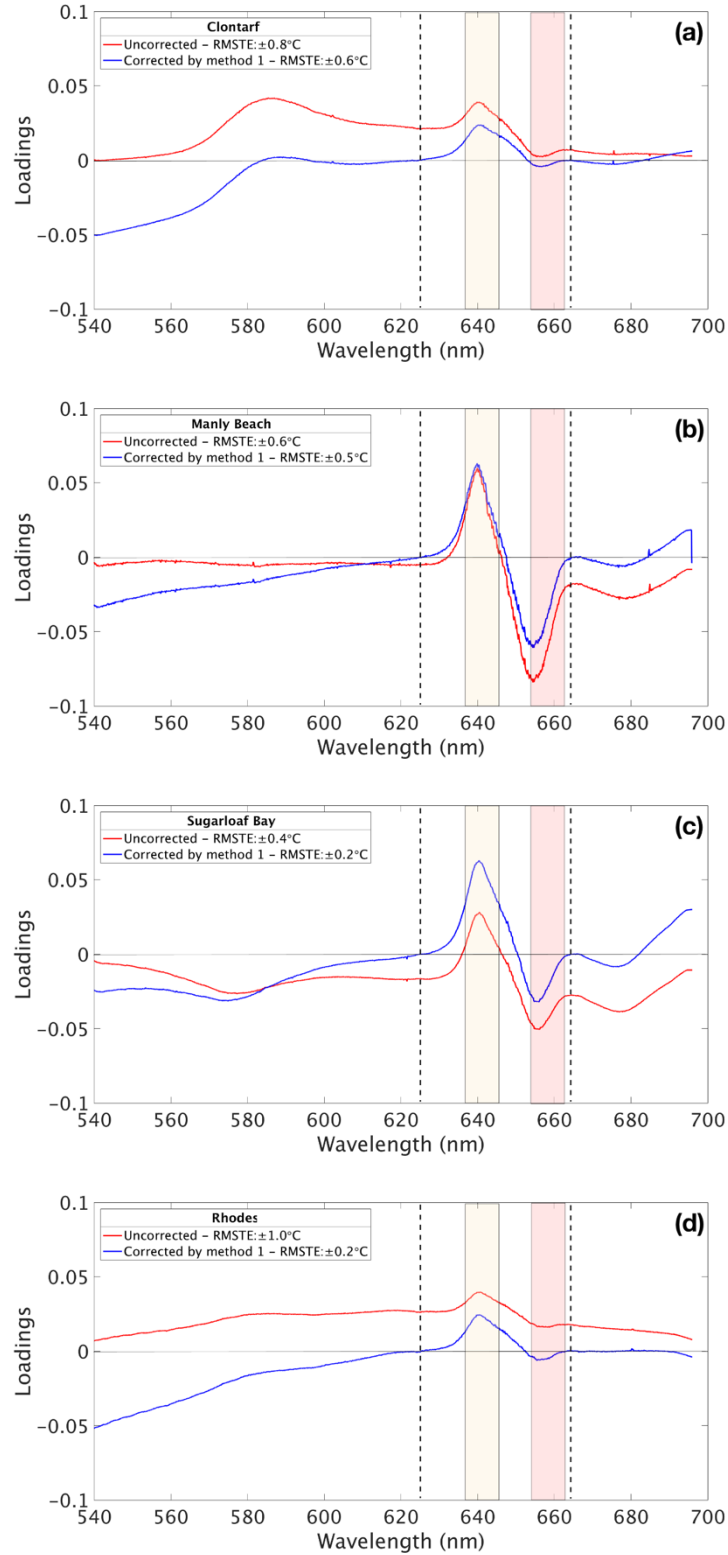


Figure 3.8. Saltwater sample analysis: PC-1 loadings plot before baseline correction (uncorrected data) and after correction by method 1 for a) Clontarf; b) Manly Beach; c) Sugarloaf Bay; d) Rhodes.

All samples showed less variability for spectral regions on either side of the OH-stretching band after correction, with minimum variances achieved on wavelengths used for baseline calculation, as expected. Nevertheless, the technique promoted different effects on

signal variances among the samples, as expected due to the artificial nature of the method. Clearly, the background fluorescence giving rise to spectral variation is not linear in nature.

In each natural water sample the method was effective, to a reasonable extent, in revealing the variance around the water Raman peak, and accordingly the two-colour markers are less perturbed by fluorescence. The correction technique, however, was not able to fully isolate Raman signals from other sources of spectral variation, resulting in different performances depending on original spectral characteristics of each water sample.

### 3.3.2. Method 2 – correction by temperature markers

Correction method 2 was proposed after it was recognised that there was a physical significance associated with the value of the two-colour markers. The two-colour method itself is independent on the marker values, relying only on the *rate of change* of the value with temperature. In total absence of fluorescence signals, two-colour markers calculated for natural and “standard” seawater should have the same values. In natural samples, two-colour markers are influenced by fluorescences and diverge from standard values, as shown in figure 3.6. For the purpose of evaluating method 2, the standard marker values were taken to be those of Rose Bay markers after correction by method 1.

All locations exhibited adjustments on slope and intercept of linear models after correction by method 2, with new temperature markers converging towards standard values and indicating an effective correction on baseline signals (figure 3.9).

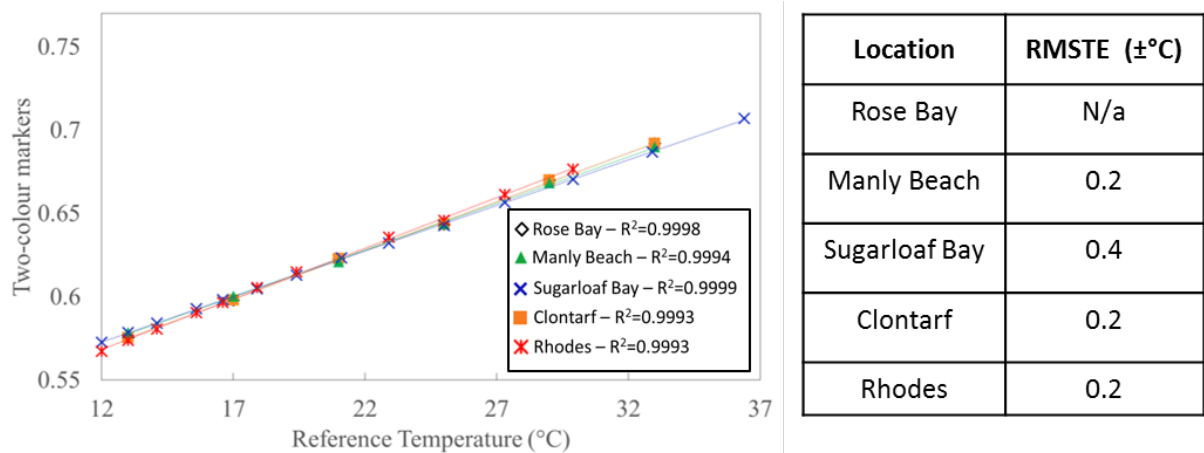


Fig 3.9. Temperature-dependent two-colour markers for various natural water samples after spectral correction by method 1.

### 3.4. Discussion: field implementation

The ultimate goal for our research project is to develop a Raman spectrometer able to determine depth-resolved water temperature *in situ* with accuracy better than  $\pm 0.5^\circ\text{C}$  without prior knowledge about optically active constituents in the environment. As seen in section 3.3, background signals have high variability even for samples collected at neighbouring locations, with best approximation of seawater “standards” found for Rose bay. We qualitatively explored spectral variances arising from background signals and proposed two correction methods for enhanced accuracy on temperature predictions performed by Raman markers. In this section we propose strategies for field implementation and LIDAR-compatibility of both Raman temperature markers and correction techniques.

Commercial Raman spectrometers as the one used in this investigative study (Enwave EZRaman-I) study are not LIDAR-compatible; however, Raman spectra collected by our commercial spectrometer can be used to simulate the performance of a simple LIDAR-compatible multichannel Raman spectrometer. Based on this information, here we propose the design and methodology of two Raman spectrometers with potential to provide depth-resolved data, allowing for estimations of two-colour temperature markers and correction factors for methods 1 and 2.

A setup compatible with LIDAR measurements and correction method 1 is shown on figure 3.10. A 532 nm, short-pulsed laser, is coupled into water by a dichroic mirror (DM) pointing downwards; backscattered photons pass through a long pass filter (LP) and the remaining signal is divided into two unpolarised streams by a Beam Splitter Cube (BSC). One of the streams is used for retrieving Raman signal on either side of the isosbestic point by channels “high” and “low”; the other stream is divided into two channels at spectral regions around the OH stretching band with minimum Raman signal intensities to be used as parameters for correction method 1.



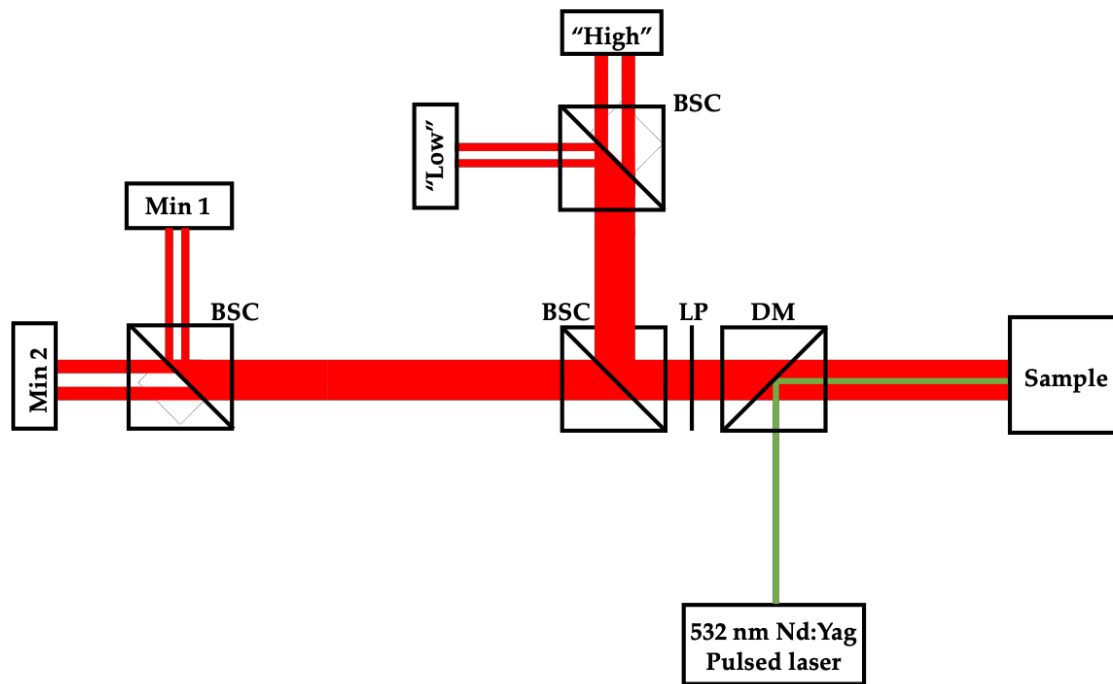


Figure 3.10. LIDAR-compatible experimental setup for correction method 1.

Unlike method 1, correction method 2 doesn't require accessory channels for baseline calculations, allowing for coupling of other filters collecting fluorescence signals in natural waters. Figure 3.11. shows a LIDAR-compatible Raman spectrometer integrated to a 532 nm pulsed laser. The design allows for collecting Raman signal for temperature markers calculations, chlorophyll-a and DOM fluorescence simultaneously. Backscattered signal is firstly divided into two components by a BSC: one of these components collects Raman signal at high and low shifts channels and the other collects signals at any two wavelengths of importance for background signals. These channels would provide estimations of X and Y parameters and could be used on correction method 2; accordingly, there is scope for future studies to extract information about fluorescence components, such as phytoplankton and DOM concentrations.

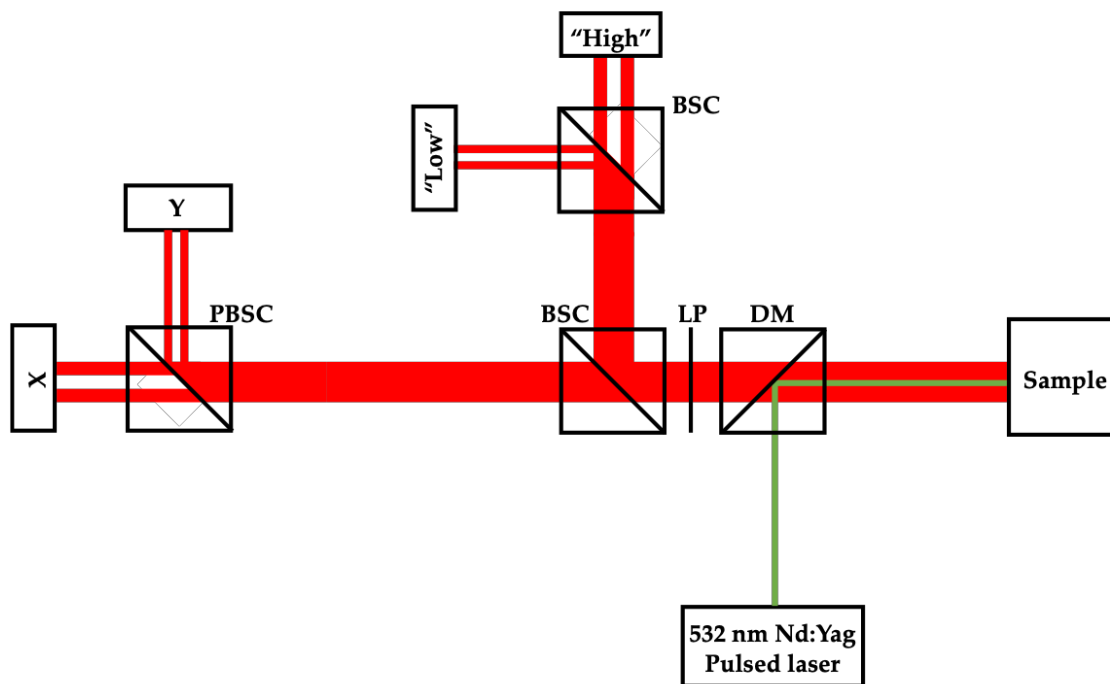


Figure 3.11. LIDAR-compatible experimental setup for correction method 2.

Having two accessory channels might be a problem when working in waters with limiting signal-to-noise-ratio and the use of only two-channels of collection for temperature markers is advised. In this case, reference temperatures could be obtained at the surface by buoys, thermometers, CTDs or satellite sensors and compared with “standard” markers of same temperature. This calibration process would then allow for calculating  $\Delta R$  and  $C$  parameters, which provide insights into which optical constituents might be present in water.

### 3.5. Summary and conclusion

I explored the origins of baseline signals in Raman spectra acquired from natural waters, which could be associated with fluorescence from optical constituents found in the environment. Principal Component analysis showed that baseline signals were consistent with fluorescence from chlorophyll-a and dissolved organic matter. The presence of this baseline compromised temperature predictions by two-colour markers in natural water samples, and two methods of background correction were explored: tilted baseline correction (method 1) and correction by temperature marker values (method 2).

Method 1 has proven to be a straightforward tool for local spectral correction, allowing for increased accuracies on natural waters temperature measurements in laboratory (general improvement of 41% when compared to uncorrected data). I presented the concept of a custom-built Raman spectrometer compatible with method of correction 1 and depth-resolved measurements, which requires two accessory channels for collecting signals at the wavelengths of minimum Raman signal for baseline calculations. Potential drawbacks include low signal-to-noise ratios in the accessory channels.

The innovative correction method 2 resulted in higher accuracies on temperature predictions for all locations, ranging from  $\pm 0.3$  to  $\pm 0.2^\circ\text{C}$  (general improvement of 65% compared to uncorrected data). This correction method does not depend on signal collection in accessory channels, but it requires either a local measurement of temperature for reference or the collection of a sample for laboratory analysis. In addition to enhancing temperature measurements, method 2 made feasible correcting signals collected in spectral channels, which led to the design of the multichannel Raman spectrometers presented in next Chapters.



## **CHAPTER 4**

# **LIDAR-COMPATIBLE MULTICHANNEL RAMAN SPECTROMETER USING GREEN (532 NM) EXCITATION LIGHT**

Remote sensing tools have been used to study the oceans since the late 1970's, with the development of technologies such as satellite sensors and LIDAR methods. LIDAR technologies are useful tools for depth-resolved measurements, being broadly used in bathymetric studies, and with the majority of systems coupled to green pulsed lasers operating from airborne platforms. Attempts have been made to extract other types of information from backscattered signals retrieved by LIDAR systems such as temperature; however, interpreting the signals retrieved by the sensors and proposing effective temperature markers have been a challenge for establishing a methodology in the field.

In 2015 [52], our research group evaluated the potential of using Raman temperature markers for temperature predictions in ultrapure waters. Two types of markers were analysed: two-colour (from unpolarised Raman spectra), and depolarisation ratios (from polarised spectra). The dispersive spectrometer used for this work was an Enwave EZRaman-I, which incorporated a CW Nd:YAG laser operating at 532 nm. Raman scattered photons were registered by CCD detectors. Accuracies as high as  $\pm 0.1^{\circ}\text{C}$  were achieved using two-colour markers in the case of ultrapure water (Reverse-Osmosis); however, the potential of depolarisation markers could not be fully explored, as the spectrometer didn't allow for simultaneous collection of polarised components. Following investigations using ultrapure water, natural water samples were collected at various sites around Sydney Harbour and analysed by the same Raman spectrometer (RS), as detailed in Chapter 3. The overlapping of fluorescence baseline signals with the water Raman peak for 532 nm excitation was a serious issue, impacting directly the two-colour temperature markers values and their accuracies on temperature prediction. Baseline correction techniques were effective in reducing the overlapping between fluorescence signals from constituents in natural waters, resulting in enhanced accuracies for two-colour temperature predictions for natural water samples.

The experimental evidence that two-colour markers could be effectively used for temperature measurements in natural waters led us to the next step of implementation: designing and constructing a customised LIDAR-compatible multichannel RS. According to the authors of [86,87,104], the best excitation source for Raman photons measurements in natural waters should be in the blue range; however, there are many LIDAR systems already being used in oceanographic studies operating at 532 nm. This makes the use of a green laser-based RS a logical starting point for our investigations.

In this Chapter, I will present the multichannel LIDAR-compatible Raman spectrometer operating at 532 nm (green excitation) assembled by me as part of my PhD. laboratory activities. Drawing upon the work in [63], I designed and assembled this RS, and used it to investigate the prediction of water temperature in both ultrapure and natural water samples, in the laboratory. The innovative design allowed for concurrent collection of both parallel and perpendicularly-polarised Raman photons, and as consequence two-colour and depolarisation markers could be calculated. For each marker I investigated the accuracy with which temperature could be predicted, the sensitivity to changes in water temperature, and the errors associated with signal-to-noise ratios. After this evaluation, I conducted an innovative linear combination analysis, using all temperature markers acquired simultaneously for enhanced temperature predictions. The methodology, results and analyses are presented in manuscript 2, which will be submitted to the journal *Sensors*.

Also relevant to this green Raman Spectrometer is the work presented in Appendix A, where the “correction by temperature markers” method (proposed in manuscript 1 [113] and Chapter 3) was used for simulating temperature predictions in the field.

#### **4.1. Manuscript 2: “A LIDAR-compatible, multichannel Raman spectrometer for remote sensing of water temperature”**

##### **Statement of contribution**

I designed and assembled the multichannel, LIDAR-compatible Raman spectrometer for the experiments reported in manuscript 2. I conducted all experiments and analyses shown in the report and am also responsible for writing much of the paper, prepared the figures, and formatting the document for publication. The Raman spectra shown in figure 1(a-c) and figure 3 were acquired by C. Artlett



## A LIDAR-compatible, multichannel Raman spectrometer for remote sensing of water temperature

ANDRÉA DE LIMA RIBEIRO<sup>1</sup>, CHRISTOPHER ARTLETT<sup>1,2</sup>, HELEN PASK<sup>1,\*</sup>

<sup>1</sup>*MQ Photonics Research Centre, Department of Physics and Astronomy, Macquarie University, Sydney, NSW 2109, Australia*

<sup>2</sup>*Defence Science & Technology Group, Maritime Division, Eveleigh, NSW, 2015 Australia*

*\*andrea.delimaribeiro@mq.edu.au*

### ABSTRACT

The design and operation of a custom-built LIDAR-compatible, four-channel Raman spectrometer integrated to a 532 nm pulsed laser is presented. The multichannel design allowed for simultaneous collection of Raman photons at spectral regions identified as highly sensitive to changes in water temperature. Four independent temperature markers were calculated from the Raman signals: two-colour(II), two-colour(I), depolarisation(A) and depolarisation(B). A total of 16 datasets were analysed for 1 ultrapure (Milli-Q) and 3 samples of natural water. Temperature accuracies of  $\pm 0.4^{\circ}\text{C}$  –  $\pm 0.8^{\circ}\text{C}$  were achieved using the two-colour(II) marker. When multiple linear regression models were constructed (linear combination) utilising all simultaneously acquired temperature markers, resulting in improved accuracies of  $\pm 0.3^{\circ}\text{C}$  -  $\pm 0.7^{\circ}\text{C}$  were achieved.

### 1. Introduction

Water temperature is a primary hydrographic parameter in aquatic environments, directly influencing the water column structure and allowing for the investigation of physical and biological processes such as ocean currents, heat exchange, pycnocline depths, geostrophic flow, detection of upwelling systems and primary productivity. Researchers rely on both traditional *in situ* sampling methods and remote sensing techniques to gain water temperature information.

Traditional methods, such as thermometers and temperature probes deployed from ships and vessels, allow for acquisition of depth-resolved highly accurate data; operational logistics, however, are complex, with information collected at a limited number of sampling stations and not compatible with meso and macroscale processes at oceanic and coastal zones [1]. Efforts to overcome these issues resulted in development of new technologies to remotely monitor the oceans, for instance satellite sensors and LIDAR (Light Detection and Ranging) methods.

Remote sensing methods retrieve data from an object without direct interaction by using sensors to detect electromagnetic, acoustic or electrical signals [2]. Infrared satellite sensors, such as the Advanced Very High Resolution Radiometers (AVHRRs), retrieve signals spontaneously emitted by the oceans and are currently the main contributors for water temperature monitoring programs, providing a synoptic view of the oceans at larger scales than *in situ* measurements [3]. However, infrared radiation undergoes pronounced absorption in water and only signals emitted by the first micrometres of water column are retrieved by the sensors, rendering ineffective collection of subsurface information. Besides depth limitations, data acquisition is restricted to areas without cloud coverage and requires validation with *in situ* data for increased accuracies. Recent AVHRR accuracy estimations indicates errors of up to  $\pm 2.0^{\circ}\text{C}$  in temperature predictions at the coast and  $\pm 1.0^{\circ}\text{C}$  for oceanic zones [4].

Limitations of both *in situ* and satellite methods expose a technological gap to be filled by a remote sensing technique able to provide depth-resolved temperature data at scales not covered by either of the abovementioned, such as LIDAR methods. LIDAR methods in oceanography include active and passive remote sensing techniques where signals in the visible or near-infrared range emitted by a target are retrieved by a sensor and interpreted to derive depth-resolved information. Active LIDAR equipment requires monochromatic short-pulsed light as an excitation source, which is transmitted down the water column interacting with molecules and other optically active constituents. By considering the arrival time of returning excitation photons and/or photons at

different frequencies it is possible to assess depth-resolved environmental information such as bathymetry, fluorescence from optical constituents and, ultimately, water temperature. In this regard, optical methods retrieving backscattered light such as Raman spectroscopy have the potential to be coupled to LIDAR technologies and provide real-time reliable data of subsurface water temperature for regional and global studies [5– 8].

Raman spectroscopy (RS) is a technique based on the inelastic scattering of an incident photon by a molecule, resulting in photons being scattered with a shift in frequency relative to the excitation source [9]. In the liquid state, water molecules exhibit Raman active modes associated with translational, librational, bending and stretching forces [10,11]. These Raman active modes present temperature-dependent behaviour, the origin of which is somewhat contentious. The OH stretching band is the most prominent feature in the water Raman spectrum, extending from 2900 to 3900  $\text{cm}^{-1}$  and exhibiting an isosbestic point at which signal intensities are insensitive to changes in temperature [10,12].

Polarised RS reveals different shapes and intensities for Raman signals according to their state of polarisation relative to that of the excitation laser. The unpolarised and polarised Raman spectra presented in Fig. 1 were measured using a dispersive commercial Raman spectrometer (Enwave EZRaman-I, integrated to a 532 nm CW laser), with polarising filters inserted as required. “Unpolarised” refers to all Raman photons, regardless of their state of polarisation (Fig 1a); “parallel-polarised” refers to photons scattered having the same state of polarisation as the excitation sources (Fig 1b); and “perpendicularly-polarised” implies Raman photons being scattered with polarisation state orthogonal to that of the excitation light (Fig 1c). Parallel-polarised components exhibit higher signal intensities than perpendicularly polarised signals, in conformity with the tetrahedral geometry of water molecules [13] (Figs 1b,c).

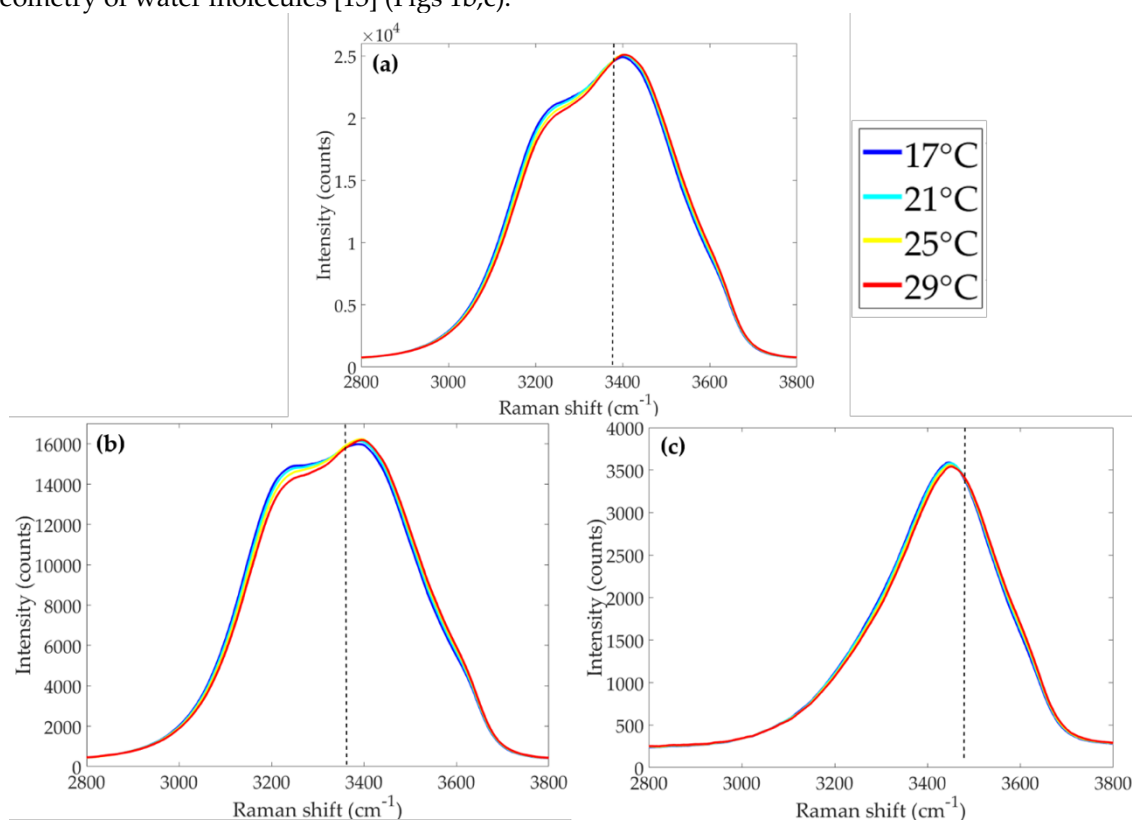


Figure 1. Temperature-dependent Raman spectra from ultrapure (reverse osmosis) water. (a) unpolarised spectra; (b) parallel-polarised spectra; (c) perpendicularly-polarised spectra.

Isosbestic points are indicated by a dashed line.

Regardless of the polarisation state, the isosbestic point marks an inversion of Raman signal behaviour: for shifts below (above) the isosbestic point, higher intensities are associated with lower (higher) temperatures. Following the first studies correlating the temperature-dependent behaviour of water Raman signal around the OH-stretching band, temperature markers were proposed for unpolarised and polarised water Raman spectra, known respectively as two-colour and depolarisation ratios.

Two-colour temperature markers, also referred as “two-colour ratios”, have been most widely used in Raman temperature prediction studies [6–8,14]. In most studies, full, unpolarised water Raman spectra are decomposed in two or more Gaussian curves and a ratio is taken of the areas under these Gaussians or some other feature such as their spectral widths. More recently, a different approach for the two-colour method was reported in [8,15] which did not require spectral decomposition. Raman signals were integrated within channels on both sides of the isosbestic point and temperature markers were calculated based on the ratio of integrated signal intensities for each channel. By using two-colour markers calculated from channel integrations, accuracies as high as  $\pm 0.1^\circ\text{C}$  were achieved for ultrapure water (Reverse-Osmosis) and  $\pm 0.2^\circ\text{C}$  for natural water samples [8,16] measured in laboratory.

Depolarised temperature markers have been calculated as ratios between the perpendicularly-polarised and parallel-polarised Raman signal intensities within a band of wavelengths. In water, these ratios exhibit a linear temperature-dependent behaviour and can be used for temperature predictions. In [17], polarised Raman components were acquired from a saline solution (NaCl 40%) and used for estimating depolarisation markers, achieving accuracies of  $\pm 0.5^\circ\text{C}$  for temperature predictions. Later, the same temperature prediction accuracies of  $\pm 0.5^\circ\text{C}$  were achieved when collecting Raman spectra from water excited by a 470 nm laser [18]. Many Raman spectrometers, including the one used to acquire Fig. 1, do not allow for simultaneous acquisition of orthogonally-polarised spectral components. Accordingly, the use of depolarisation markers has not been investigated in recent years.

Raman spectroscopy has proven to be an effective technique for determining water temperature in the laboratory with high accuracies of up to  $\pm 0.1^\circ\text{C}$  and  $\pm 0.5^\circ\text{C}$  using two-colour or depolarisation markers, respectively [8,18]. The reports in [16,19,20] propose the possibility of measuring subsurface water temperature using RS in combination with LIDAR methods, collecting time-resolved Raman signals in channels selected by optical filters, and this is the ultimate goal of our research program.

In this work, we report a custom-built multichannel Raman spectrometer incorporating a short- pulsed excitation source, optical filters and fast detectors. Our arrangement is LIDAR-compatible, but here we study small volumes of ultrapure (Milli-Q) and natural waters which were collected from Sydney Harbour. Our multichannel spectrometer enabled simultaneous collection of parallel and perpendicularly-polarised Raman signals, enabling the investigation of both two-colour and depolarisation temperature markers. Root Mean Squared Temperature Error (RMSTE) values were estimated for temperature predictions performed by both types of markers and the sensitivity of each marker (% change per  $^\circ\text{C}$ ) was also evaluated. Lastly, we propose a new, innovative, linear combination method which uses both two-colour and depolarisation markers for enhanced temperature predictions.

## 2. Methods and analysis

### 2.1. Spectrometer design

The excitation source for the multichannel Raman spectrometer was a 532 nm Nd:YAG, passively Q-switched, pulsed laser (Innolight  $\mu\text{Flare}$ ) having 25  $\mu\text{J}$  per pulse, 0.9 ns pulse duration full width at half maximum (FWHM), and pulse repetition rate of 4.5 kHz. The water samples used in the study were ultrapure (Milli-Q) and three natural water samples collected from Sydney Harbour at different times. These were analysed within a few hours of collection.

Our experimental setup is shown in Fig. 2. A water sample was placed inside a temperature-controlled cuvette holder (QPod2e, accurate to  $\pm 0.15^\circ\text{C}$ ) and its temperature was varied from  $18^\circ\text{C}$  to  $40^\circ\text{C}$  (stepping every  $2^\circ\text{C}$ ). The oscilloscope was triggered by inserting a glass window in the laser path, before it was coupled into the spectrometer, deflecting  $\sim 4\%$  of the incident beam towards a photodiode connected to the oscilloscope. Excitation photons ( $532\text{ nm}$ ) were reflected by a Dichroic Mirror (DM, reflectivity  $R \sim 94\%$  at  $532\text{ nm}$ , transmission  $T \sim 98\%$  between  $620$  and  $670\text{ nm}$ ) and focused into the water sample by a converging lens ( $f = 70.0\text{ mm}$ ). Red-shifted Raman photons scattered by the sample passed through a Long Pass filter (LP,  $R \sim 99.9\%$  at  $532\text{ nm}$  and  $T \sim 98\%$  at  $620$ - $670\text{ nm}$ ) in order to reject most Rayleigh-scattered photons. The Stokes photons were split into two directions, by a non-polarising beam splitting cube (BSC), one beam then passing through  $BP_{low}^{640}$  (Semrock LD01-640/8-25, central wavelength:  $640\text{ nm}$ , band-pass:  $12.9\text{ nm}$  at FWHM), and the other through  $BP_{high}^{660}$  (Semrock FF01-660/13-25 nm, central wavelength:  $660\text{ nm}$ , and band-pass:  $20.2\text{ nm}$  at FWHM). The choice of these filters was constrained by commercial availability and total spectral widths at FWHM were  $315\text{ cm}^{-1}$  and  $463\text{ cm}^{-1}$  for low and high shift channels, respectively. Their spectral pass bands are shown superimposed on the polarised Raman spectra in Fig. 3. These filters had high rejection ( $\text{OD} > 5$ ) outside their pass bands.

Each beam was then divided into two polarised components by a polarisation beam splitting cube (PBSC), prior to detection by a fast Photomultiplier (Hamamatsu H10721-20, rise time  $\sim 1\text{ ns}$ ) coupled to a converging lens ( $f = 25\text{ mm}$ ) to focus the backscattered Raman photons into the detectors aperture. The PMT gain values were set around  $700\text{ V}$  for all channels, well below the maximum gain allowed by our PMTs ( $900\text{ V}$ ). Raman signal intensities were simultaneously registered by a multichannel oscilloscope (Tektronix DPO4104B), each being an average of  $512$  pulses. Signal-to-noise (SNR) ratios were calculated for each channel according to equation 1.

$$SNR = \frac{\int \text{Signal}_{(\text{FWHM})}}{\int \text{Noise}_{(\text{FWHM})}} \quad (1)$$

where  $\int \text{Signal}_{(\text{FWHM})}$  represents the integrated Raman signal pulse over the full width of half maximum (FWHM); and  $\int \text{Noise}_{(\text{FWHM})}$  refers to the integration of the noise signals over the FWHM.

For each water sample, three independent acquisitions were performed for each temperature, hence three sets of two-colour and depolarisation markers could be calculated for each temperature. Aiming to increase robustness, the markers calculated from the independent datasets were averaged, giving origin to a new (fourth) dataset for each temperature marker hereafter referred as the “average markers dataset”.

Table 1 shows a list with information regarding all spectral channels collected by this setup and correspondent nomenclatures adopted in this study.

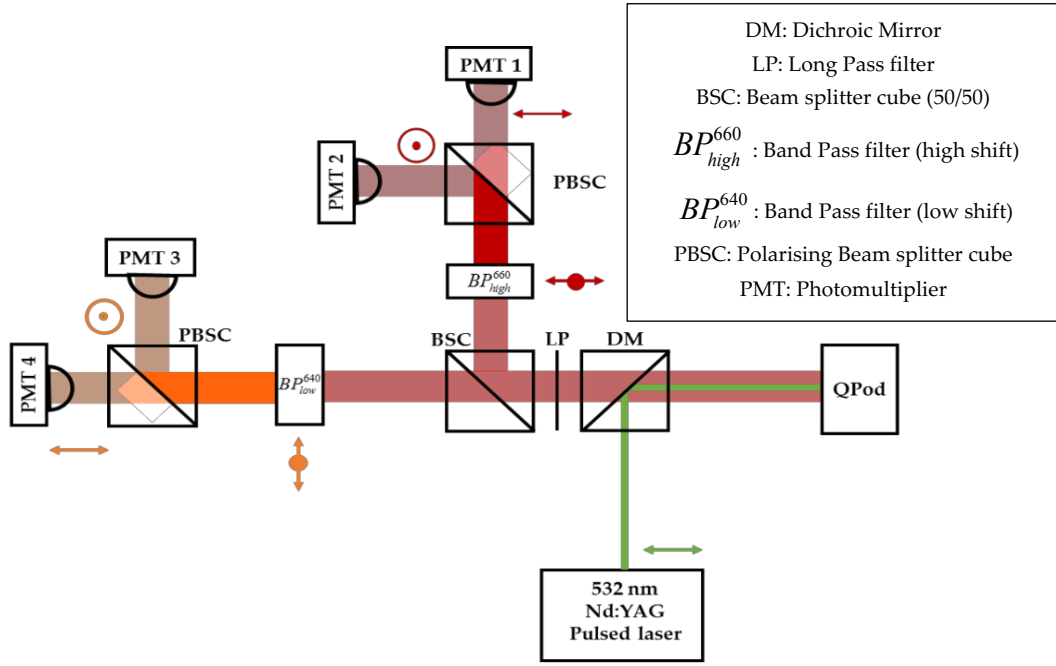


Figure 2. Experiment setup.

Table 1. Nomenclature adopted for each spectral channel.

Channel number	Polarisation state	Band Pass filter	Nomenclature	Typical SNR values
1	Parallel	$BP_{high}^{660}$	$I_{  }^{high}$	$1.9 \times 10^4$
2	Perpendicular	$BP_{high}^{660}$	$I_{\perp}^{high}$	$1.6 \times 10^4$
3	Perpendicular	$BP_{low}^{640}$	$I_{\perp}^{low}$	$2.3 \times 10^4$
4	Parallel	$BP_{low}^{640}$	$I_{  }^{low}$	$7.7 \times 10^4$

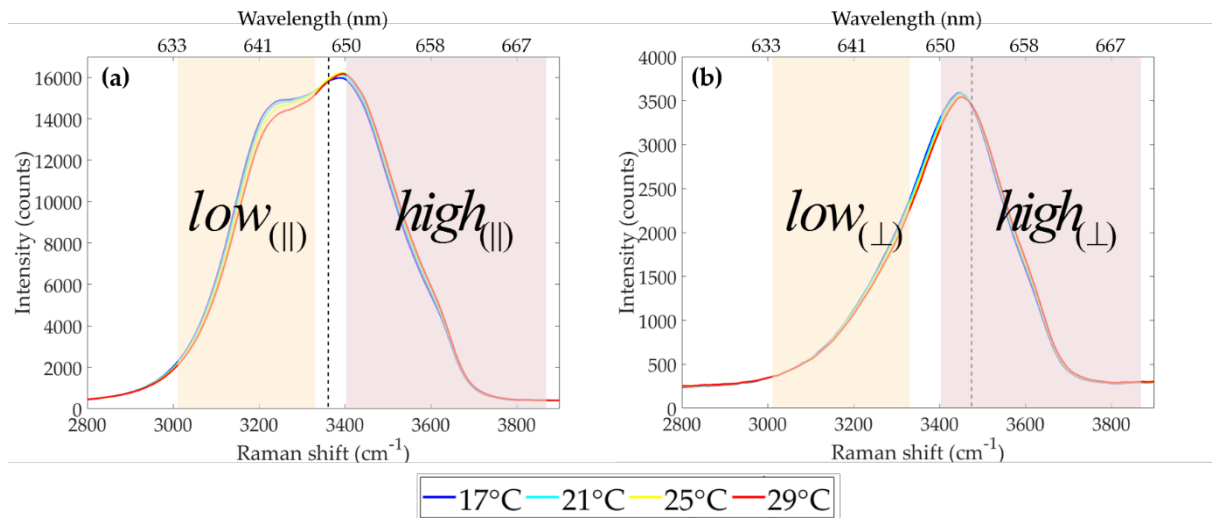


Figure 3. Band pass filter transmissions superimposed on (a) parallel and (b) perpendicularly-polarised Raman spectra. Low and high channels are indicated by shaded areas.

## 2.2. Temperature markers

Each pulse registered by the oscilloscope was integrated over a range of 2.0 ns (10 data points), as indicated in Fig. 4, using the Trapezoidal rule. Integrated signals for each channel were used to calculate four temperature markers as expressed by equations 2-5.

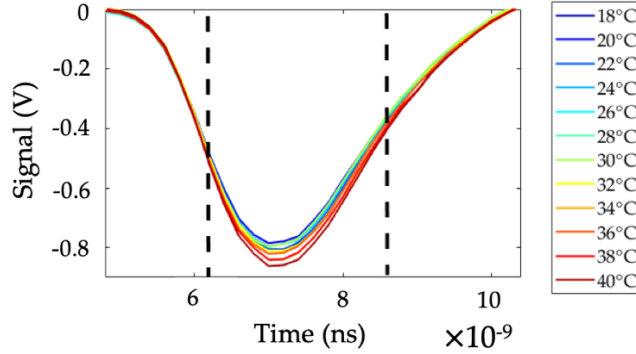


Figure 4. A typical set of signals (channel 1), recorded for different temperatures and showing the area over which the signals were integrated.

$$Two-colour(\parallel) = \frac{I_{\parallel}^{high}}{I_{\parallel}^{low}} \quad (2)$$

$$Two-colour(\perp) = \frac{I_{\perp}^{high}}{I_{\perp}^{low}} \quad (3)$$

$$Depolarisation(A) = \frac{I_{\perp}^{high}}{I_{\parallel}^{low}} \quad (4)$$

$$Depolarisation(B) = \frac{I_{\perp}^{low}}{I_{\parallel}^{high}} \quad (5)$$

## 2.3. Predicting Temperatures

Linear regression models were constructed from the relationships between temperature markers and reference temperature, and their coefficients (*gradient*, *intercept*) were obtained for each marker analysis. These coefficients were rearranged in order to calculate a new set of temperatures dependent on the markers, hereafter called “predicted temperatures” (equation 6).

$$T_{predicted} = (\text{gradient} \times \text{marker}) + \text{intercept} \quad (6)$$

where  $T_{predicted}$  represents the predicted temperature estimated by a two-colour or depolarisation ratio (marker). Plotting these predicted temperatures against the measured reference temperatures enabled RMSTE values to be calculated; these RMSTE values provided our measure of temperature prediction accuracy.

## 2.4. Marker sensitivities to temperature

Marker sensitivities were also estimated for an ultrapure water sample, representing the percentage change in the marker values per °C. For natural water samples variations in the markers values may be associated with the presence of fluorescence from other optically active components in water, as reported in [19], hence not representing the markers sensitivity to temperature only.

As described in [8], the use of mean-scaled temperature markers is appropriate for sensitivity calculations, accounting for natural fluctuations in denominator values. Higher (lower) signal intensities in denominators result in smaller (bigger) variations in the markers, not necessarily linked to the effects of temperature. Mean-scaled markers account for this variation by scaling each marker by a mean of all markers within a set of temperature measurements (equation 7). Sensitivity information was extracted from the slope calculated for the linear model correlating mean-scaled markers and their respective temperatures. The use of mean-scaled markers also enables comparison between different types of markers calculated for a given water sample, determining which markers are associated with higher sensitivities.

$$\text{Mean-scaled marker sensitivity} = \frac{d(\text{marker})}{dT} \frac{1}{\text{mean}(\text{marker})} \quad (7)$$

### 2.1. Linear combination method (LC)

Multiple linear regression (or linear combination) is a multivariate analysis method used for modelling linear relationships between two or more independent variables (in this study, temperature markers) and a set of dependent measurements (reference temperatures). Our spectrometer design enabled simultaneous collection of signal at all channels, allowing for combining temperature markers into one model to enhance the accuracy of temperature predictions (equation 8).

$$T_{\text{predicted}} = \beta_0 + \beta_1 \times \text{two-colour}(\parallel) + \beta_2 \times \text{two-colour}(\perp) + \beta_3 \times \text{depol}(A) + \beta_4 \times \text{depol}(B) + \varepsilon \quad (8)$$

where  $\beta_0$  is an independent term,  $\beta_1$ - $\beta_4$  are calibration terms generated by the model and correlated with each marker and  $\varepsilon$  are the residual errors.

### 3.3. Results and discussion

#### 3.3. Milli-Q (ultrapure) water analysis

Temperature markers calculated from Raman signals scattered by a Milli-Q (ultrapure) water samples were analysed in order to determine sensitivities, % errors in the markers associated with SNRs and the accuracy with which temperature could predicted (RMSTEs). Due to the absence of other signals overlapping with the Raman peak, these values should indicate the maximum performances that could be achieved by our RS in laboratory experiments. A summary with the main results found for ultrapure water analysis is shown in table 2.

The response of each marker to changes in temperature was investigated by comparing their mean-scaled temperature markers (Fig. 5), and the sensitivities were extracted from the slope of the linear relationships between mean-scaled markers and their respective temperatures (table 2).

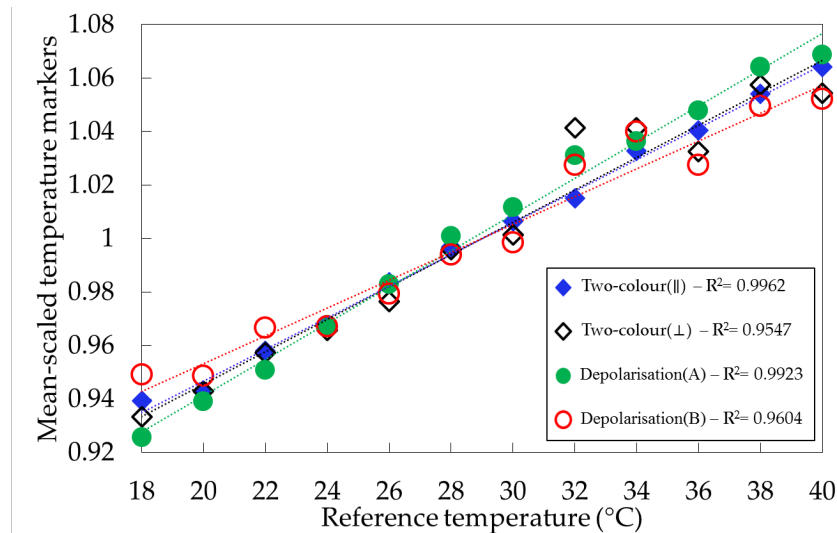


Figure 5. Mean-scaled temperature markers for Milli-Q water.

Similar sensitivities were found for all temperature markers calculated from the ultrapure water sample, varying from 0.52%/°C (depolarisation(B)) to 0.68%/°C (depolarisation(A)).  $R^2$  values were found to be poor for two-colour( $\perp$ ) and depolarisation(B) when compared with other temperature markers and it can be seen in table 2 that these were also the markers that had higher % errors. The sensitivities are somewhat lower than the values around 1%/°C for two-colour markers

calculated from full unpolarised Raman spectra reported by the authors of [5,6,14]. We attribute this to our use of spectral channels and the inevitable trade-off between sensitivity and signal intensity. These trade-offs were explored in [8], where the authors simulated the impact of channel widths on two-colour markers sensitivities calculated from unpolarised Raman signals. Analysis of an ultrapure water sample (Reverse-Osmosis) showed a systematic decrease in the marker sensitivities when increasing the spectral channels widths for Raman signal acquisition. In that simulation, sensitivities of  $0.52\%/^{\circ}\text{C}$  were reported for channels of  $300\text{ cm}^{-1}$  width, and an optimal channel width of  $200\text{ cm}^{-1}$  was suggested to provide a reasonable trade-off between temperature sensitivities and SNRs.

Table 2. RMSTEs, sensitivities and the absolute percentage errors in each marker for a Milli-Q water sample. Data in brackets is based on the analysis of 4 datasets; data without brackets is based on the “average markers” dataset. Refer to section 2.1. for details.

Temperature marker	Milli-Q water sample		
	RMSTE ( $\pm^{\circ}\text{C}$ )	Sensitivity ( $\%/^{\circ}\text{C}$ )	Absolute % error in marker (%)
Two-colour( $\parallel$ )	0.4 [0.4 – 0.7]	0.59	0.00093
Two-colour( $\perp$ )	1.5 [1.5 – 1.7]	0.61	0.0035
Depolarisation(A)	0.8 [0.8 – 1.0]	0.68	0.0021
Depolarisation(B)	1.8 [1.4 – 2.1]	0.52	0.0023

Accuracies found for Milli-Q water analysis varied from  $\pm 0.4^{\circ}\text{C}$  to  $\pm 2.1^{\circ}\text{C}$ , as shown in table 2. RMSTEs were more aligned with the % errors calculated for each marker, derived from channels SNRs, than with the markers sensitivities. The best RMSTEs of  $\pm 0.4^{\circ}\text{C}$  were found for two-colour( $\parallel$ ) analysis, and are comparable to the values of  $\pm 0.4^{\circ}\text{C}$  reported in other LIDAR-compatible RS reports [8,21]. Ultimately, improved temperature accuracies could be achieved by (1) limiting the channels widths of our RS to  $200\text{ cm}^{-1}$  (thus improving sensitivities); (2) refining optics to maximize the number of Raman photons collected in each channel; (3) using higher power excitation lasers. Using two channels suitable for two-colour( $\parallel$ ) calculations instead of four would also improve SNRs and yield higher accuracies.

### 3.4. Natural waters analyses

RMSTEs, sensitivities and % errors calculated for all temperature markers retrieved from natural water samples are shown in table 3. The data is compiled from 12 datasets, as detailed in section 2.1. We first start by considering the markers sensitivities in natural waters. All markers exhibited sensitivities lower than the ones found for Milli-Q waters, which can be explained by the presence of other optically active constituents in natural waters. Issues regarding fluorescence from chlorophyll-a and Dissolved Organic Matter overlapping with the Raman peak when excitation is at  $532\text{ nm}$  and temperature predictions have already been addressed in [19,22]. Unwanted fluorescence signals contribute to the overall signal counts leading to higher SNR (and therefore lower % errors in the temperature markers), which can be seen in nearly all natural water samples under analysis (table 3) when compared with the Milli-Q water results (table 2). Thus the % errors determined for natural waters need to be interpreted cautiously, and the values in table 2 may be more meaningful.



Table 3. RMSTEs, sensitivities and the absolute percentage errors in each marker for natural water sample analysed by two-colour markers. Data in brackets is based on the analysis of 4 datasets; data without brackets is based on the “average markers” dataset. Refer to section 2.1. for details.

		Temperature markers			
		Two-colour(∥)	Two-colour(⊥)	Depolarisation (A)	Depolarisation(B)
Natural 1	RMSTE (±°C) [Range]	0.4 [0.4 – 0.6]	2.6 [2.3 – 2.6]	1.6 [1.6 – 1.7]	2.1 [2.1 – 2.5]
	Sensitivity (°/°C)	0.50	0.30	0.48	0.30
	Marker % error (%)	0.00098	0.0026	0.0019	0.0017
Natural 2	RMSTE (±°C) [Range]	0.7 [0.5 – 0.7]	1.3 [1.0 – 1.3]	1.4 [0.8 – 3.4]	1.1 [1.1 – 2.2]
	Sensitivity (°/°C)	0.57	0.57	0.59	0.56
	Marker % error (%)	0.00089	0.00276	0.00179	0.00187
Natural 3	RMSTE (±°C) [Range]	0.8 [0.8 – 0.9]	0.9 [0.9 – 1.7]	6.5 [5.6 – 8.1]	2.6 [2.5 – 2.7]
	Sensitivity (°/°C)	0.53	0.49	0.25	0.78
	Marker % error (%)	0.00084	0.0024	0.0017	0.0016

Higher accuracies (*i.e.* lower RMSTEs) were found when using two-colour(∥) markers for all natural water samples, with RMSTEs ranging from  $\pm 0.4^{\circ}\text{C}$  to  $\pm 0.9^{\circ}\text{C}$ . This is consistent with the findings for Milli-Q water. The RMSTE values are also similar, and we note that the sensitivities found for natural water samples are within 15% of the Milli-Q water values. The accuracies obtained using the two-colour(⊥) marker were more variable, with RMSTEs ranging from  $\pm 0.9^{\circ}\text{C}$  to  $\pm 2.6^{\circ}\text{C}$ . There was more variation in the marker sensitivity between samples, with the values differing from the Milli-Q results by as much as 50%. The higher RMSTEs were associated with lower sensitivity, which suggests this marker is less immune to the presence of fluorescing constituents.

This was the first time, to our knowledge, that two-colour markers were calculated from polarised Raman signals selected by optical filters. The accuracies achieved using the two-colour(∥) markers ( $\pm 0.4^{\circ}\text{C}$  –  $\pm 0.9^{\circ}\text{C}$ ) are broadly consistent with the accuracies reported in [19], where RMSTEs within the range of  $\pm 0.3^{\circ}\text{C}$  –  $\pm 1.0^{\circ}\text{C}$  were predicted for natural water samples based on the full unpolarised Raman spectra collected by a commercial RS, integrating Raman signals in channels of  $200\text{ cm}^{-1}$  width. Strategies were presented in [19] which corrected for fluorescence, and reduced the RMSTEs to  $\pm 0.2^{\circ}\text{C}$  –  $\pm 0.5^{\circ}\text{C}$ . We anticipate the “correction by temperature marker values” method presented in [19] could be implemented in the multichannel RS described here. We hope to achieve better accuracies with our LIDAR-compatible, multichannel RS with the use of custom-built Band Pass filters with smaller bandwidths.

Next, we consider the use of depolarisation temperature markers. The RMSTEs varied widely from  $\pm 0.8^{\circ}\text{C}$  to  $\pm 8.1^{\circ}\text{C}$  (table 3), and it was not possible to infer which of the depolarisation markers had the better performance. For each marker, the smaller RMSTEs were associated with higher sensitivity. There is a limited literature with which to compare our RMSTEs based on

depolarisation markers. As explained in [18], depolarisation markers are traditionally calculated from signals at different state of polarisations but within the same spectral band (unlike the present study), exhibiting the advantage of not being impacted by fluorescence signals and differential attenuation when propagating in water. The authors of [18] determined water temperature from polarised Raman spectra acquired by using a 470 nm dye laser as excitation, achieving accuracies of up to  $\pm 0.5^\circ\text{C}$ . Based on our observations, the depolarisation markers predict temperatures less accurately than the two-colour ratios. It is possible, however, that in the future field studies the benefits outlined by Leonard [18] might become significant and a better selection of filters excluding the temperature-insensitive points for the depolarized Raman band identified by the authors of [23].

### 3.5. Enhancing the accuracy of temperature predictions using linear combination methods

While the two-colour(II) markers clearly enabled the most accurate prediction of temperature for all the water samples investigated here, it is equally clear that the other markers also exhibit temperature dependence, albeit to a lesser degree. Accordingly, we now apply the linear combination method described in section 2.1 to our four water samples. RMSTE values of temperature predictions for natural and Milli-Q water samples after LC are shown in table 4.

Table 4. RMSTE improvement after linear combination (LC) methods.

Sample	Best RMSTE for single marker [Range for all markers] ( $\pm^\circ\text{C}$ )	Best RMSTE after LC [Range] ( $\pm^\circ\text{C}$ )	Improvement due to LC (%)
Milli-Q water sample	0.4 [0.4 – 2.1]	0.3 [0.3 – 0.5]	25
Natural sample 1	0.4 [0.4 – 2.6]	0.3 [0.3 – 0.5]	25
Natural sample 2	0.5 [0.5 – 3.4]	0.4 [0.3 – 0.5]	20
Natural sample 3	0.8 [0.8 – 8.1]	0.5 [0.5 – 0.7]	38

RMSTEs after the LC method exhibited average improvements of 30% relative to the best RMSTE obtained using a single marker, with final accuracies after LC equal or better than  $\pm 0.5^\circ\text{C}$  for all samples. The effectiveness of the LC method is largely due to the nature of the multiple linear regression, where lower weightings ( $\beta$  values) are associated with markers that are less useful. Allied with simultaneous signal collection by our spectrometer, LC was effective in extracting temperature-related information from all markers and maximizing the accuracies of temperature predictions for all water samples.

## 4. Conclusions

In this paper we presented a custom-built multichannel Raman spectrometer, operating with a 532 nm pulsed laser and commercial optical filters collecting polarised signals on spectral regions of interest for temperature predictions in natural waters. The design is LIDAR-compatible, employing (1) a pulsed laser source of  $\leq 2$  ns full-width at half maximum, desirable to achieve a depth resolution better than 0.5 m; (2) collection of Raman signals from optical channels through the use of Band Pass filters; (3) fast, sensitive detection by photomultipliers.

This was the first time that polarised Raman signals collected from different spectral channels were simultaneously selected by optical filters and used effectively for temperature prediction, achieving accuracies as high as  $\pm 0.4^\circ\text{C}$  with minimal processing. The innovative 4-channel design of our equipment enabled 4 temperature-dependent markers to be utilised. It also

allowed for the use of linear combination methods, which significantly enhanced the accuracy of temperature predictions. Temperature accuracies were closely associated with the sensitivities of each marker, and the percentage error within each marker, derived from signal-to-noise ratios at the channels of Raman signal collection.

The fact that our setup is compatible with LIDAR technologies and allows for LC methods to be used represents a major advance for using Raman spectroscopy as a potential technique able to determine natural waters temperature with accuracies higher than current remote sensing tools. We intend to refine our spectroscopic acquisition and processing methods by using custom-made optical filters with optimum spectral widths ( $200\text{ cm}^{-1}$ ) located at areas with maximum change in Raman signal intensities with temperature and anticipate this will lead to further increase in accuracy in temperature predictions.

### 5. References

1. Dickey, T. D. A vision of oceanographic instrumentation and technologies in the early twenty-first century. In *Oceans 2020*; Field, J. G., Hempl, G., Summerhayes, C. P., Eds.; Island Press: Washington DC, 2002; pp. 209–254.
2. Solan, M.; Germano, J. D.; Rhoads, D. C.; Smith, C.; Michaud, E.; Parry, D.; Wenzhöfer, F.; Kennedy, B.; Henriques, C.; Battle, E.; Carey, D.; Iocco, L.; Valente, R.; Watson, J.; Rosenberg, R. Towards a greater understanding of pattern, scale and process in marine benthic systems: A picture is worth a thousand worms. *J. Exp. Mar. Bio. Ecol.* **2003**, 285–286, 313–338, doi:10.1016/S0022-0981(02)00535-X.
3. Rajesh, R.; Dwarkish, G. S. Satellite Oceanography– A review. *Aquat. Procedia* **2015**, 4, 165–172, doi:10.1016/j.aqpro.2015.02.023.
4. Brewin, R. J. W.; de Mora, L.; Billson, O.; Jackson, T.; Russell, P.; Brewin, T. G.; Shutler, J. D.; Miller, P. I.; Taylor, B. H.; Smyth, T. J.; Fishwick, J. R. Evaluating operational AVHRR sea surface temperature data at the coastline using surfers. *Estuar. Coast. Shelf Sci.* **2017**, 196, 276–289, doi:10.1016/j.ecss.2017.07.011.
5. Leonard, D. A.; Caputo, B.; Johnson, R. L. Experimental remote sensing of subsurface temperature in natural ocean water. *Geophys. Res. Lett.* **1977**, 4, 279–281.
6. Leonard, D. A.; Caputo, B.; Hoge, F. E. Remote sensing of subsurface water temperature by Raman scattering. *Appl. Opt.* **1979**, 18, 1732–45, doi:10.1117/12.958276.
7. Liu, Z.; Zhang, J.; Chen, W. Remote sending of subsurface water temperature using Raman Lidar. *SPIE* **1992**, 1633, 321–329.
8. Artlett, C. P.; Pask, H. M. Optical remote sensing of water temperature using Raman spectroscopy. *Opt. Express* **2015**, 23, 31844, doi:10.1364/OE.23.031844.
9. Ferraro, J.; Nakamoto, K. *Introductory Raman Spectroscopy*; Elsevier, 2003; ISBN 9780122541056.
10. Walrafen, G. E.; Fisher, M. R.; Hokmabadi, M. S.; Yang, W.-H. Temperature dependence of the low- and high-frequency Raman scattering from liquid water. *J. Chem. Phys.* **1986**, 85, 6970–6982, doi:10.1063/1.451384.
11. Carey, D. M.; Korenowski, G. M. Measurement of the Raman spectrum of liquid water. *J. Chem. Phys.* **1998**, 108, 2669, doi:10.1063/1.475659.
12. Walrafen, G. E.; Hokmabadi, M. S.; Yang, W.-H. Raman isosbestic points from liquid water. *J. Chem. Phys.* **1986**, 85, 6964, doi:10.1063/1.451383.
13. Tominaga, Y.; Fujiwara, A.; Amo, Y. Dynamical structure of water by Raman spectroscopy. *Fluid Phase Equilib.* **1998**, 144, 323–330, doi:10.1016/S0378-3812(97)00276-8.
14. Breschi, B.; Cecchi, G.; Pantani, L.; Raimondi, V.; Tirelli, D.; Valmori, G. Measurement of Water Column Temperature by Raman Scattering. *EARsel Adv. Remote Sens.* **1992**, 1, 131–134.
15. Oh, M.; Kang, H.; Yu, N. E.; Kim, B. H.; Kim, J.; Lee, J.; Hyung, G. W. Ultimate sensing resolution of water temperature by remote Raman spectroscopy. *Appl. Opt.* **2015**, 54, 2639–2646, doi:10.1364/AO.54.002639.
16. Artlett, C. P.; Pask, H. M. New approach to remote sensing of temperature and salinity in

natural water samples. *Opt. Express* **2017**, 25, 2840, doi:10.1364/OE.25.002840.

17. Chang, C. H.; Young, L. A. Remote measurement of ocean temperature from depolarization in Raman scattering. In *The use of lasers for hydrographic studies*; 1975; pp. 105–112.

18. Leonard, D. A.; Caputo, B. Raman Remote Sensing Of The Ocean Mixed-Layer Depth. *Opt. Eng.* **1983**, 22, doi:10.1117/12.7973107.

19. de Lima Ribeiro, A.; Arlett, C.; Ajani, P.; Derkenne, C.; Pask, H. Manuscript 1. “The impact of fluorescence on Raman remote sensing of temperature in natural water samples”. *To be Submitt. to Opt. Express*.

20. Artlett, C. P.; Pask, H. Remote sensing of water temperature and salinity using Raman spectroscopy. **2015**, 114, 62269, doi:10.1364/OE.23.031844.

21. Oh, M.; Kang, H.; Yu, N. E.; Kim, B. H.; Kim, J.; Lee, J.; Hyung, G. W. Ultimate sensing resolution of water temperature by remote Raman spectroscopy. *Appl. Opt.* **2015**, 54, 2639–2646, doi:10.1364/AO.54.002639.

22. James, J. E.; Lin, C. S.; Hooper, W. P. Simulation of laser-induced light emissions from water and extraction of Raman signal. *J. Atmos. Ocean. Technol.* **1999**, 16, 394–401.

23. Cunningham, K.; Lyons, P. A. Depolarization ratio studies on liquid water. *J. Chem. Phys.* **1973**, 59, 2132–2139, doi:10.1063/1.1680299.

## 4.2. Acquisition overview

Temperature-dependent Raman signals from ultrapure water samples were acquired in spectral channels by our multichannel RS (532 nm excitation) and a complete set of four photomultiplier signals, recorded by the oscilloscope channels are shown in are shown in figure 4.1.

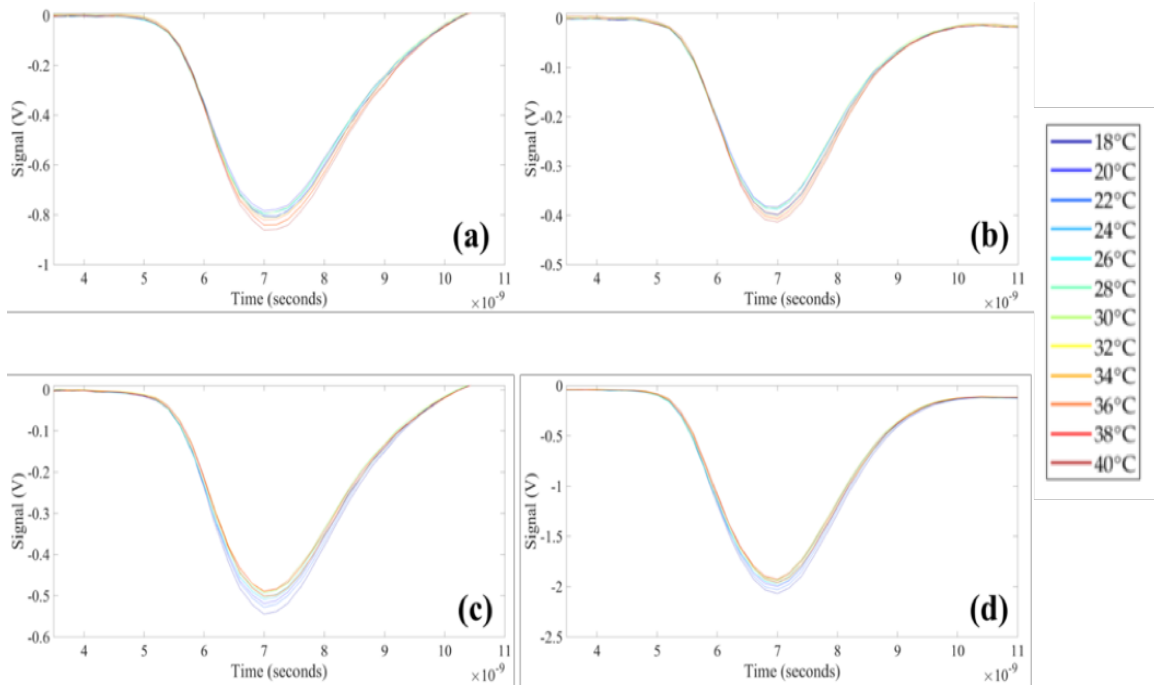


Figure 4.1. Typical Raman signals acquired for a Milli-Q water sample. “High shift” channels: (a) parallel-polarised and (b) perpendicularly-polarised; and “low shift” channels: (c) parallel-polarised and (d) perpendicularly-polarised.

It is not possible to compare the *intensities* of the Raman signals between each channel, as filters of different bandwidths were used to select portions of the Raman spectra; however, it is possible to compare the *temperature-dependency* of the Raman signals. Regardless of the water type, higher temperatures were associated with higher signals for channels collecting at the high Raman shift (figures 4.1a-b); conversely, higher temperatures were associated with lower signal intensities in channels collecting at the low Raman shift (figures 4.1c-d). This behaviour is in agreement with what was found by the authors of [63] when analysing temperature changes in the Raman spectra, indicating that the channel signal collection by our RS was effective in capturing the temperature-dependent behaviour of Raman signals scattered by water.

## 4.2. A more comprehensive analysis of temperature markers and their usefulness

In manuscript 2 [114], I presented accuracies (RMSTEs) for averaged temperature markers summarizing the main findings of my research; however, for each water sample three independent datasets of Raman signals were acquired: dataset 1, dataset 2 and dataset 3, which results were not included in the publication. In this section I will present the RMSTEs for all data sets collected from natural and Milli-Q water samples in order to discuss the reliability, repeatability and robustness of temperature predictions performed using my custom-built multichannel Raman spectrometer. RMSTEs were also calculated using “average markers”, these being an average of the marker values calculated for datasets 1,2 and 3. The results presented in the foregoing manuscript are those obtained for the “average markers dataset”.

The RMSTE was the parameter chosen to express the accuracy of temperature predictions, as detailed in Chapter 2. Achieving a low RMSTE is desirable for our ultimate goal of predicting water temperatures with accuracy better or equal to  $\pm 0.5^{\circ}\text{C}$ ; nevertheless, it is also necessary to evaluate the extent to which the temperature predictions can be replicated. This evaluation was made by calculating standard deviations for RMSTEs of markers sets 1,2,3, and the “average markers”. Low standard deviation values indicate that the different data sets provided similar accuracies when measuring temperatures from a given sample; otherwise, high standard deviation values indicate a higher range of accuracies on temperature predictions by the marker. In this section, I will evaluate which marker is the most suitable for our studies in terms of RMSTEs and means of repeatability of predictions; hence, low RMSTEs (high accuracies) and low RMSTEs standard deviation values are desirable.

RMSTEs and their respective standard deviations for markers calculated from water samples analysed in manuscript 2 [114] are shown in tables 4.1-4.4 and in figures 4.2-4.5. Accuracies better (smaller) or equal to  $\pm 0.5^{\circ}\text{C}$  are indicated in green; accuracies between  $\pm 0.6^{\circ}\text{C}$  and  $\pm 1.0^{\circ}\text{C}$  are shown in blue; from  $\pm 1.1^{\circ}\text{C}$  to  $2.0^{\circ}\text{C}$  are presented in yellow; and RMSTEs from  $\pm 2.0^{\circ}\text{C}$  are indicated in red. This data is presented both graphically and in tables on the following pages, each page relating to a different water sample. Figure 4.6. shows a summary of RMSTEs found for each of the water samples under analysis, calculated from the “average markers” dataset.

## Milli-Q water sample

Table 4.1. RMSTEs for two-colour and depolarisation markers calculated for a Milli-Q water sample (multichannel RS, 532 nm excitation).

Temperature Markers	RMSTE using Dataset 1 ( $\pm^{\circ}\text{C}$ )	RMSTE using Dataset 2 ( $\pm^{\circ}\text{C}$ )	RMSTE using Dataset 3 ( $\pm^{\circ}\text{C}$ )	RMSTE using “average markers” ( $\pm^{\circ}\text{C}$ )	RMSTE standard deviation
Two-colour( $\parallel$ )	0.4	0.6	0.7	0.4	$\pm 0.10$
Two-colour( $\perp$ )	1.5	1.7	1.5	1.5	$\pm 0.08$ ( $< 0.1$ )
Depolarisation(A)	0.8	1.0	0.8	0.8	$\pm 0.08$ ( $< 0.1$ )
Depolarisation(B)	1.9	2.1	1.4	1.8	$\pm 0.30$

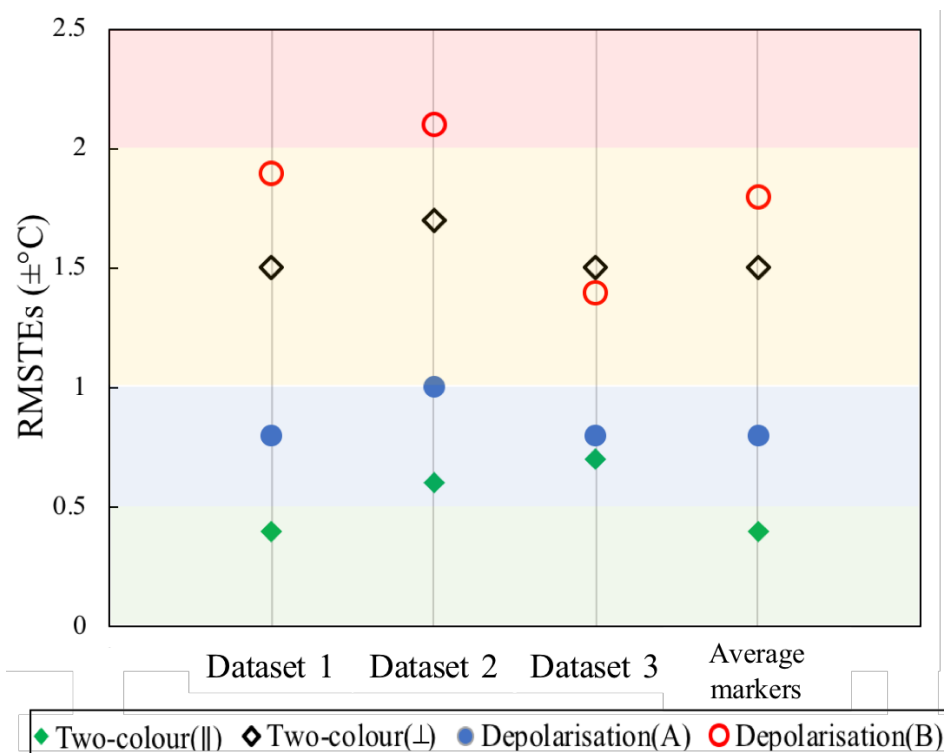


Figure 4.2. Graphical representation of the data in Table 4.1.

## Key observations - Milli-Q water sample

- Best RMSTE for two-colour( $\parallel$ ),  $\pm 0.4^{\circ}\text{C}$ .
- RMSTEs  $\leq \pm 1.0^{\circ}\text{C}$  for both two-colour( $\parallel$ ) and depolarisation(A).
- All RMSTEs  $\leq \pm 2.1^{\circ}\text{C}$ .
- All standard deviations  $\leq 0.1$ , except depolarisation(B)
- Depolarisation(B) exhibited the lowest accuracies and the worst consistencies when predicting temperature.

### Natural water sample 1

Table 4.2. RMSTEs for two-colour and depolarisation markers calculated for natural water sample 1 (multichannel RS, 532 nm excitation).

Temperature markers	RMSTE using Dataset 1 ( $\pm^{\circ}\text{C}$ )	RMSTE using Dataset 2 ( $\pm^{\circ}\text{C}$ )	RMSTE using Dataset 3 ( $\pm^{\circ}\text{C}$ )	RMSTE using “average markers” ( $\pm^{\circ}\text{C}$ )	RMSTE Standard deviation
Two-colour( $\parallel$ )	0.5	0.6	0.6	0.4	$\pm 0.08$ ( $< 0.1$ )
Two-colour( $\perp$ )	2.6	2.3	2.5	2.6	$\pm 0.1$
Depolarisation(A)	1.6	1.6	1.7	1.6	$\pm 0.04$ ( $< 0.1$ )
Depolarisation(B)	2.5	2.2	2.1	2.1	$\pm 0.20$

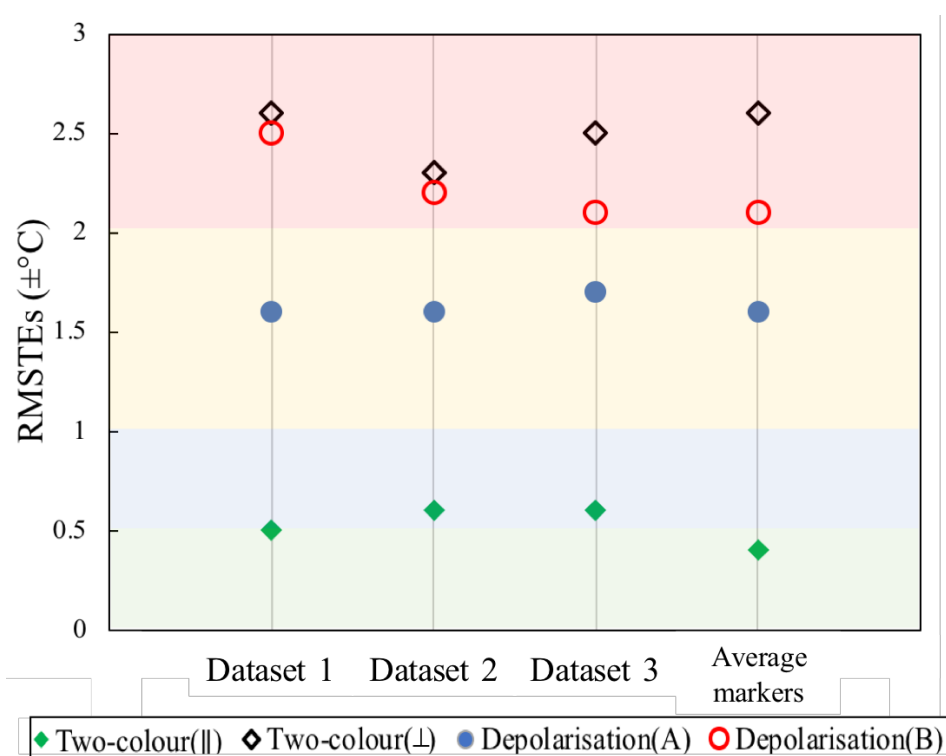


Figure 4.3. Graphical representation of the data in Table 4.2.

### Key observations - Natural water sample 1

- Best RMSTE for two-colour( $\parallel$ ),  $\pm 0.4^{\circ}\text{C}$ .
- Two-colour( $\parallel$ ) was the only marker which predictions were  $\leq \pm 1.0^{\circ}\text{C}$ .
- All RMSTEs  $\leq \pm 2.6^{\circ}\text{C}$ .
- Good consistency between 3 datasets, with standard deviations for all markers  $\leq 0.20$ .
- Depolarisation(B) exhibited the lowest accuracies and the worst consistencies when predicting temperature.



## Natural water sample 2

Table 4.3. RMSTEs for two-colour and depolarisation markers calculated for natural water sample 2 (multichannel RS, 532 nm excitation).

Temperature markers	RMSTE using Dataset 1 ( $\pm^{\circ}\text{C}$ )	RMSTE using Dataset 2 ( $\pm^{\circ}\text{C}$ )	RMSTE using Dataset 3 ( $\pm^{\circ}\text{C}$ )	RMSTE using “average markers” ( $\pm^{\circ}\text{C}$ )	RMSTE Standard deviation
Two-colour( $\parallel$ )	0.5	0.6	0.7	0.7	$\pm 0.07$ ( $<0.1$ )
Two-colour( $\perp$ )	1.0	1.0	1.2	1.3	$\pm 0.15$
Depolarisation(A)	3.4	2.2	0.8	1.4	$\pm 1.0$
Depolarisation(B)	1.7	2.2	1.4	1.1	$\pm 0.40$

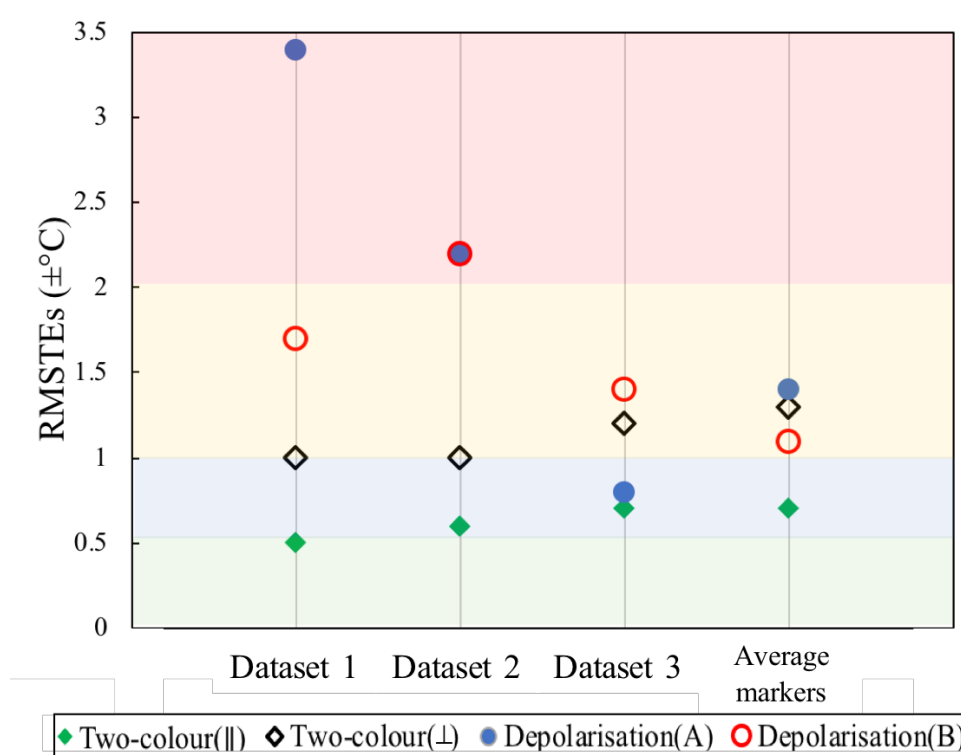


Figure 4.4. Graphical representation of the data in Table 4.3.

## Key observations - Natural water sample 2

- Best RMSTE for two-colour( $\parallel$ ),  $\pm 0.8^{\circ}\text{C}$ .
- Only two-colour( $\parallel$ ) analysis results in  $\text{RMSTEs} \leq \pm 1.0^{\circ}\text{C}$ .
- 15 out of 16 predictions gave  $\text{RMSTE} \leq \pm 2.2^{\circ}\text{C}$  (94%).
- Good consistency between 3 datasets for two-colour( $\parallel$ ), markers with standard deviation  $\leq 0.15$ .
- Worst consistencies for depolarisation(A) and depolarisation(B).
- Depolarisation(A) prediction for dataset 1 seems uncharacteristically high, suggesting some experimental error.

### Natural water sample 3

Table 4.4. RMSTEs for two-colour and depolarisation markers calculated for natural water sample 3 (multichannel RS, 532 nm excitation).

Temperature markers	RMSTE using Data set 1 ( $\pm^{\circ}\text{C}$ )	RMSTE using Data set 2 ( $\pm^{\circ}\text{C}$ )	RMSTE using Data set 3 ( $\pm^{\circ}\text{C}$ )	RMSTE using “average markers” ( $\pm^{\circ}\text{C}$ )	RMSTE Standard deviation
Two-colour( $\parallel$ )	0.9	0.8	0.8	0.8	$\pm 0.09 (< 0.1)$
Two-colour( $\perp$ )	1.5	1.7	1.5	0.9	$\pm 0.15$
Depolarisation(A)	8.1	5.6	7.8	6.5	$\pm 1.2$
Depolarisation(B)	2.5	2.5	2.7	2.6	$\pm 0.40$

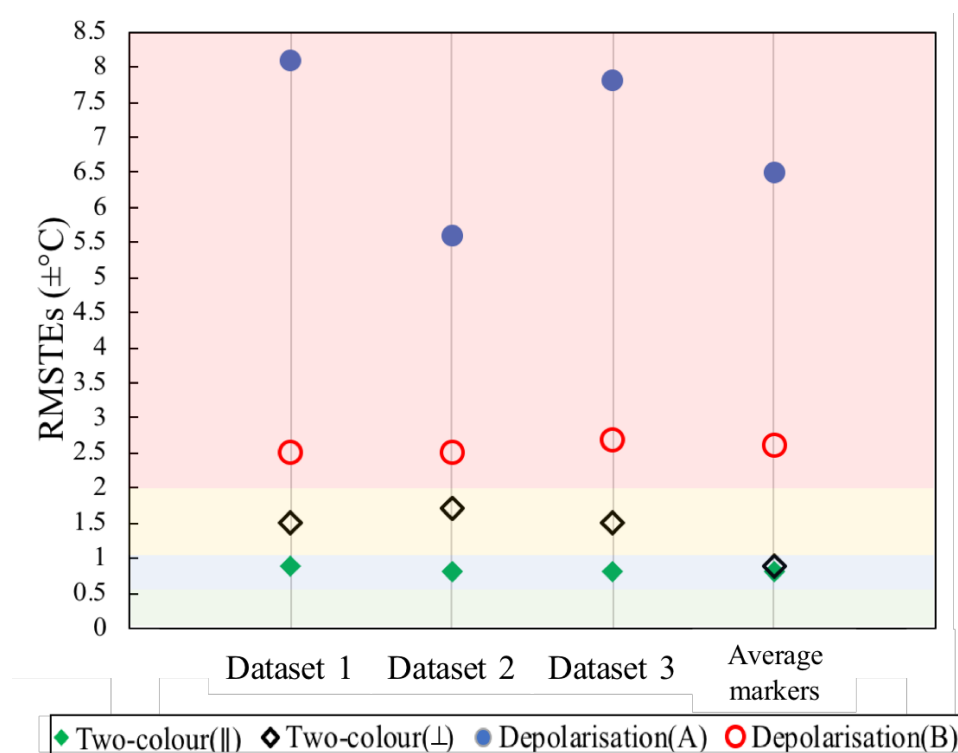


Figure 4.5. Graphical representation of the data in Table 4.4.

### Key observations - Natural water sample 3

- Best RMSTE for two-colour( $\parallel$ ),  $\pm 0.8^{\circ}\text{C}$ .
- Only two-colour( $\parallel$ ) analysis results in  $\text{RMSTEs} \leq \pm 1.0^{\circ}\text{C}$ .
- 12 out of 16 predictions gave  $\text{RMSTE} \leq \pm 2.7^{\circ}\text{C}$  (75%).
- Good consistency between 3 datasets for two-colour( $\parallel$ ) (standard deviations  $\leq 0.15$ ) and two-colour( $\perp$ ) (standard deviation of 0.15).
- Worst consistencies for depolarisation(A).
- Extremely high RMSTEs for depolarisation(A) over all datasets, suggesting some source of experimental error. Hereafter, this marker will be treated as an outlier in our analyses.

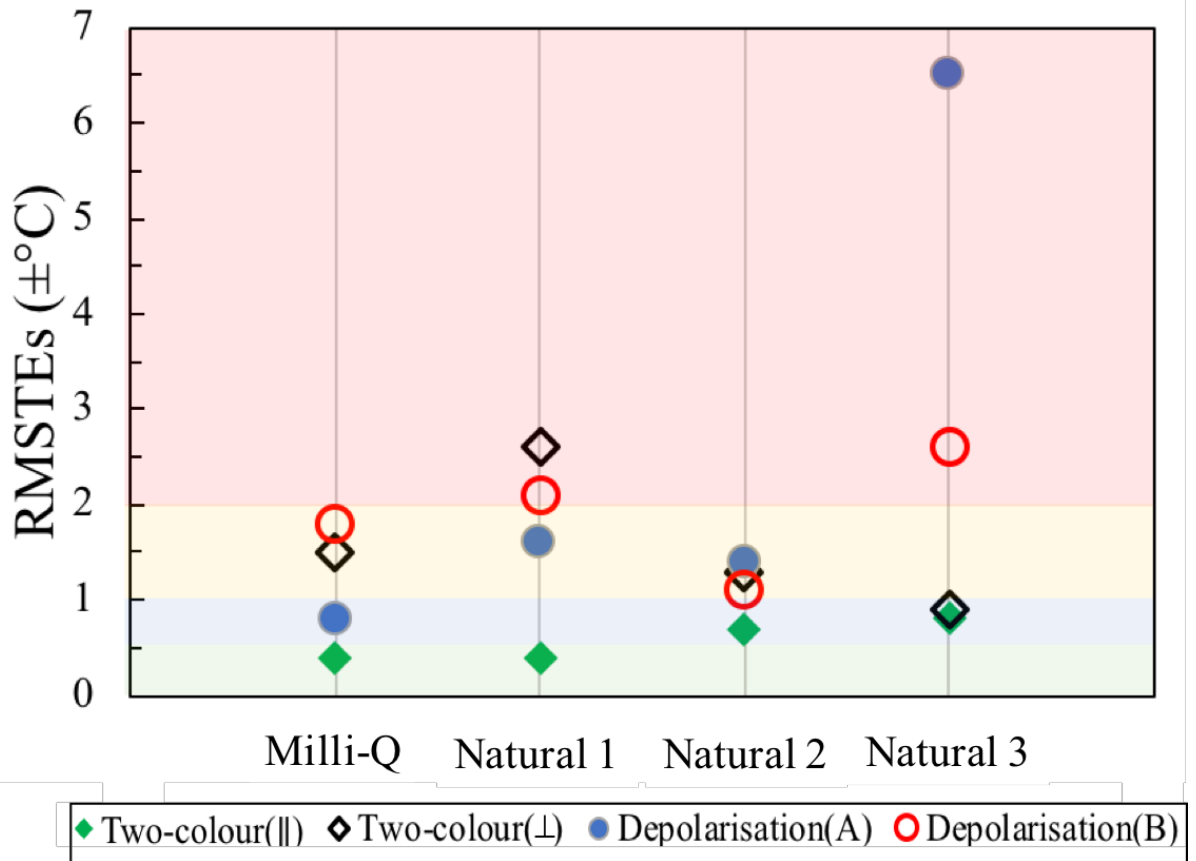


Figure 4.6. RMSTEs calculated from the “average markers dataset” for each of the water samples analysed.

## Discussion

The previous tables and figures correspond to 4 water samples, with 16 temperature predictions for each, making a total of 64 temperature predictions. We start this discussion with some comparative observations of these predictions, which are listed below:

- For each sample, two-colour(∥) delivered the best accuracy.
- For Milli-Q water, RMSTEs  $\leq \pm 1^\circ\text{C}$  were found for all predictions performed by two-colour(∥) and depolarisation(A) markers; however, for natural waters only two-colour(∥) consistently delivered RMSTEs  $\leq \pm 1^\circ\text{C}$ .
- For Milli-Q water, all markers delivered RMSTE  $\leq \pm 2.1^\circ\text{C}$ , whilst for natural waters only 19 out of 36 predictions ( $\sim 53\%$ ) had RMSTEs  $\leq \pm 2.1^\circ\text{C}$ .
- Temperature prediction by two-colour(⊥) markers analyses did not result in accuracies better than  $\pm 0.9^\circ\text{C}$  for any of the water sample analysed in this study.
- Depolarisation(B) markers exhibited poor performances when predicting temperatures for both Milli-Q and natural water samples, with average of RMSTEs for all measurements of  $\pm 2.1^\circ\text{C}$ .

- The high RMSTEs obtained for natural sample 3 using depolarisation(A) are suggestive of some source of experimental error.
- Regarding repeatability of measurements, it would be necessary to acquire a higher number of datasets for each sample in order to achieve meaningful statistics results, hence the discussion here is limited to these datasets and could not be extrapolated to future measurements.
- The best consistency between datasets was found using the two-colour(II) markers, whilst predictions by depolarisation(B) exhibited the lowest consistency.

Generally, two-colour(II) markers exhibited better accuracies on temperature predictions for all water samples, with RMSTEs as high as  $\pm 0.4^{\circ}\text{C}$  for Milli-Q (table 4.1 and figure 4.2) and natural water sample 1 (table 4.2 and figure 4.3). These accuracies are in agreement with reports by the authors of [63], where unpolarised two-colour markers were used for predicting tap water temperatures, achieving values as high as  $\pm 0.5^{\circ}\text{C}$  by using a custom-built two-channel Raman spectrometer. The similarities between the system evaluated in [63] and the one used in the present study include the use of a 532 nm pulsed laser, commercial band pass filters to optically select Raman spectral channels highly sensitive to changes in temperature, and PMTs for detecting time-resolved Raman photons. However, the authors of [63] assembled a RS collecting unpolarised Raman signals in two spectral channels and used different Band Pass filters than the ones used in this report. In [105], full unpolarised water Raman spectra was decomposed *numerically* into two Gaussians and two-colour markers were calculated by taking ratios between the area of these curves. Accuracies of  $\pm 0.4^{\circ}\text{C}$  were found for ultrapure water temperature determination in laboratory in a “remote sensing” configuration, with the water cell position 7 m apart from the spectrometer, as described by the authors. The fact that the accuracies reported by [63,105] were found in this study for both ultrapure and natural water samples predicted by two-colour(II) places this marker as a major contributor for Raman remote sensing of water temperature.

Two-colour(II) markers exhibited consistently low standard deviations ( $< \pm 0.1^{\circ}\text{C}$ ). This indicates that similar accuracies were found when predicting temperature with two-colour(II) markers calculated from 3 independent Raman signal acquisitions from a given sample. When comparing the RMSTEs found for average of markers dataset among water samples (figure 4.6), it also becomes clear that two-colour(II) exhibited the best performance

when predicting water temperature. It is possible to claim that two-colour( $\parallel$ ) markers were the markers which exhibited best results when predicting temperature in the laboratory measurements with our multichannel RS (532 nm excitation).

Next, we focus our discussion on the depolarisation analysis. Traditionally, depolarisation markers are not affected by fluorescence signals by collecting parallel and perpendicularly-polarised Raman signals at same wavelengths; however, the depolarisation spectra for water exhibits temperature-insensitive regions at 3230 and 3630  $\text{cm}^{-1}$ , which were included in the bandwidth selection of our optical filters; hence, our approach here does not benefit from these characteristics. By collecting signals in channels centred at different wavelengths, depolarisation measurements are susceptible to fluorescence overlapping with the Raman peak, which can compromise temperature predictions. Depolarisation(A) markers for Milli-Q waters exhibited accuracies as low as  $\pm 0.8^\circ\text{C}$  when predicting water temperature (table 4.3 and figure 4.4). Regardless the reasonable performance in ultrapure water, depolarisation(A) predictions in natural waters oscillated from  $\pm 0.8^\circ\text{C}$  (natural sample 1, table 4.2) to  $\pm 8.1^\circ\text{C}$  (natural sample 3, table 4.4 and figure 4.5). High standard deviations ( $> \pm 1.0^\circ\text{C}$ ) were found for predictions made by different markers sets collected from natural samples 2 and 3, indicating a challenge to replicate temperature measurements with same accuracy in these samples.

Despite of not exhibiting maxima accuracies when predicting water temperature, depolarisation(B) and two-colour( $\perp$ ) markers carry a different type of Raman temperature-dependent information than two-colour( $\parallel$ ) and depolarisation(A), which can be useful in field measurements and for linear combination methods. We hope that by using narrower, custom-designed band pass filters in the future we will improve the performance of depolarisation(B) and two-colour( $\perp$ ) and allow for calculation of traditional depolarisation markers.

Overall, figure 4.6 summarises the main findings for the “average markers” datasets, providing an overview of all predictions analysed in this study. Considering the outlier behaviour of depolarisation(A) predicting temperatures for natural sample 3, the effectiveness of each marker can be ranked as follows:

- i) Two-colour( $\parallel$ );
- ii) Depolarisation(A)
- iii) Two-colour( $\perp$ )
- iv) Depolarisation(B)

### 4.3. Individual contributions of markers to linear combination models

Linear combination (LC) methods presented in manuscript 2 [114] were found to be effective in increasing the accuracies of water temperature predictions performed using multiple Raman markers (two-colour( $\parallel$ ), two-colour( $\perp$ ), depolarisation(A) and depolarisation(B)). Although four different Raman-based parameters were used, the majority of information extracted by LC models tended to be strongly linked to two-colour( $\parallel$ ) and depolarisation(A). This is consistent with the findings of the previous sections, as these were the markers that had the best performance when predicting temperatures. In this section, I will evaluate the contributions from two-colour( $\perp$ ) and depolarisation(B) for LC models.

LC analyses were firstly performed by using all four temperature markers for every water sample, as discussed in manuscript 2 [114] and shown in equation 4.1.

$$T_{predicted} = \beta_0 + \beta_1 \times two-colour(\parallel) + \beta_2 \times two-colour(\perp) + \beta_3 \times depol(A) + \beta_4 \times depol(B) + \varepsilon \quad (4.1)$$

In this section, LC models will be calculated by using as input information two-colour( $\parallel$ ) and depolarisation(A) markers, as indicated by equation 4.2.

$$T_{predicted} = \beta_0 + \beta_1 \times two-colour(\parallel) + \beta_2 \times depol(A) + \varepsilon \quad (4.2)$$

where  $\beta_0$  is an independent term,  $\beta_1$ - $\beta_2$  are calibration terms correlated with each marker and  $\varepsilon$  represents the residual errors.

RMSTEs for LC models with four markers (two-colour( $\parallel$ ), two-colour( $\perp$ ), depolarisation(A) and depolarisation(B)) and two markers (two-colour( $\parallel$ ) and depolarisation(A)) for all water samples analysed in this study are shown in tables 4.5-4.8. The percentage improvements shown in the tables have been determined with respect to the two-colour( $\parallel$ ) RMSTE: improvements in accuracy compared with the two-colour( $\parallel$ ) are shaded, and the best accuracies are highlighted in green boxes.

Tables 4.5. RMSTEs of Milli-Q water temperature predictions for linear combination models based on four and two Raman temperature markers.

Milli-Q water sample	Two-colour(II) RMSTE ( $\pm^{\circ}\text{C}$ )	LC with 2 terms (RMSTE $\pm^{\circ}\text{C}$ )	2 term LC improvement (%)	LC with 4 terms (RMSTE $\pm^{\circ}\text{C}$ )	4 term LC improvement (%)
Dataset 1	0.4	0.4	0	0.3	25
Dataset 2	0.6	0.5	17	0.4	33
Dataset 3	0.7	0.6	14	0.5	29
“Average markers”	0.4	0.4	0	0.3	25

Tables 4.6. RMSTEs of Natural water sample 1 temperature predictions for linear combination models based on four and two Raman temperature markers.

Natural sample 1	Two-colour(II) RMSTE ( $\pm^{\circ}\text{C}$ )	LC with 2 terms (RMSTE $\pm^{\circ}\text{C}$ )	2 term LC improvement (%)	LC with 4 terms (RMSTE $\pm^{\circ}\text{C}$ )	4 term LC improvement (%)
Dataset 1	0.5	0.3	40	0.3	40
Dataset 2	0.6	0.5	17	0.4	33
Dataset 3	0.6	0.4	33	0.4	33
“Average markers”	0.4	0.4	0	0.3	25

Tables 4.7. RMSTEs of Natural water sample 2 temperature predictions for linear combination models based on four and two Raman temperature markers.

Natural sample 2	Two-colour(II) RMSTE ( $\pm^{\circ}\text{C}$ )	LC with 2 terms (RMSTE $\pm^{\circ}\text{C}$ )	2 term LC improvement (%)	LC with 4 terms (RMSTE $\pm^{\circ}\text{C}$ )	4 term LC improvement (%)
Dataset 1	0.5	0.3	40	0.3	40
Data set 2	0.6	0.5	17	0.4	33
Data set 3	0.7	0.6	0	0.5	17
“Average markers”	0.7	0.4	43	0.4	43

Tables 4.8. RMSTEs of Natural water sample 3 temperature predictions for linear combination models based on four and two Raman temperature markers.

Natural sample 3	Two-colour(II) RMSTE ( $\pm^{\circ}\text{C}$ )	LC with 2 terms (RMSTE $\pm^{\circ}\text{C}$ )	2 term LC improvement (%)	LC with 4 terms (RMSTE $\pm^{\circ}\text{C}$ )	4 term LC improvement (%)
Dataset 1	0.9	0.8	11	0.7	25
Dataset 2	0.8	0.7	13	0.6	25
Dataset 3	0.8	0.5	38	0.5	38
“Average markers”	0.8	0.6	25	0.5	38

## **Discussion**

Approximately 69% of the data sets presented above resulted in better accuracies for LC models using 4 temperature markers; 31% exhibited same accuracies for 4 terms LC and 2 terms LC models; and there were no cases where RMSTEs for 2 terms LC were better than the 4 terms LC. This indicated that there is some temperature information added to the LC models by two-colour( $\perp$ ) and depolarisation(B), increasing RMSTEs up to  $\pm 0.1^\circ\text{C}$ . Accordingly, LC methods have proven to increase accuracies on temperature predictions for all water samples considered here, reaching accuracies as high as  $\pm 0.3^\circ\text{C}$ . Considering that the reference temperature measurements had an uncertainty of  $\pm 0.2^\circ\text{C}$ , linear combination methods were able to extract near-maximum temperature information from the water Raman signals acquired by our custom-built spectrometer.

Additionally, in order to calculate two-colour( $\parallel$ ) (channel 1, channel 4) and depolarisation(A) (channel 1, channel 3) markers, it is necessary to divide the Raman signal into 4 polarised channels which will be collected by our spectrometer. Ultimately, the information necessary for calculating two-colour( $\perp$ ) (channel 2, channel 3) and depolarisation(B) (channel 2, channel 4) will be collected by our spectrometer regardless its usefulness for predicting temperature isolated, but allow for LC models with 4 markers resulting in enhanced RMSTEs for almost all samples. In summary, our four-channel spectrometer was designed and built to enable the effectiveness of the four temperature markers to be compared, and the concept for LC to be explored. Clearly more channels (required for better LC) will result in lower SNR, and this is a trade-off that could be explored in the future.



#### 4.4. Markers sensitivities in natural water samples

In manuscript 2 [114] we showed the sensitivity values found for markers calculated for the Milli-Q water sample. The sensitivities represented the percentage change in the markers values per °C (%/°C), and reached values between 0.50 and 0.59%/°C. Since the variations in Raman markers values for ultrapure water are considered to be solely due to water temperature fluctuations, these were assumed to be the maximum sensitivities that could be achieved by our RS. Natural waters, otherwise, are non-homogeneous solutions and suspensions, and the markers sensitivities could be impacted by overlapping of other signals with the Raman peak, resulting in changes in the marker per °C which are nor related to changes in water temperature.

In order to compare the markers sensitivities for different water samples, mean-scaled markers were analysed in function of temperature, as described in Chapter 2, and are shown in figures 4.7-4.10. The “average markers dataset” was chosen to be used in this analysis for all water samples. In ideal conditions, mean-scaled markers should vary linearly with temperature, and the slope found for this relationship is indicative of the marker sensitivity for a given sample.

Two-colour(II) markers led to the best accuracies when predicting temperatures for all water samples analysed in this study, as discussed in section 4.3. In terms of sensitivities, values around 0.55%/°C were found for all samples and no abrupt changes on linear trends could be identified (figure 4.7).

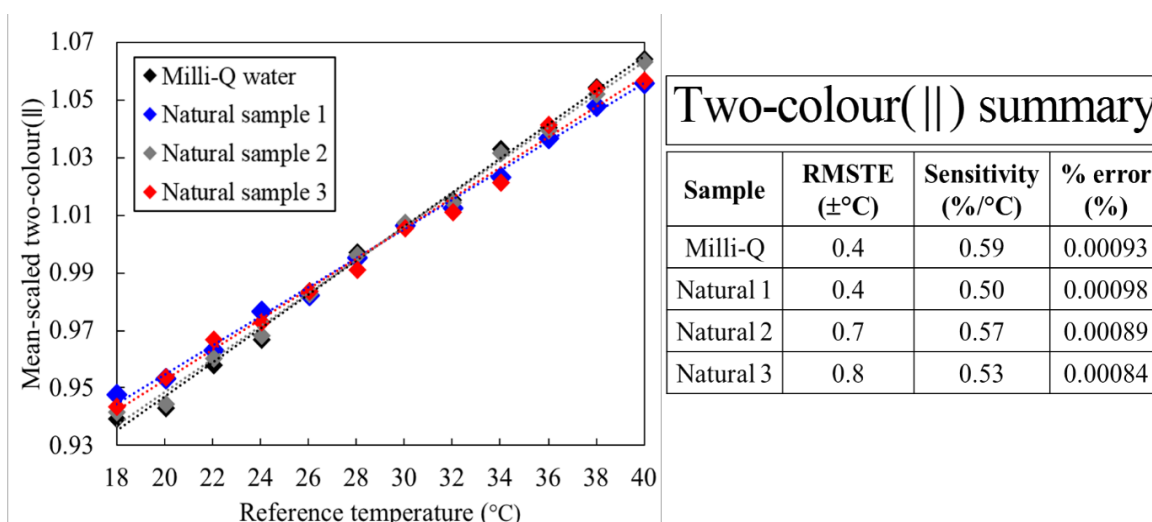


Figure 4.7. Mean-scaled temperature sensitivity data for the two-colour(II) marker. All water samples.

Unlike two-colour( $\parallel$ ), the other three markers sensitivities exhibited clear differences when comparing their performances in different water samples. For two-colour( $\perp$ ) (figure 4.8), maximum sensitivities were identified for the Milli-Q water sample ( $0.61\%/^{\circ}\text{C}$ ); however, best RMSTEs ( $\pm 0.9^{\circ}\text{C}$ ) for this marker were associated with Natural sample 3 (sensitivities of  $0.49\%/^{\circ}\text{C}$ ). Higher RMSTEs for Natural sample 3 could not be linked to maximum sensitivities or to any other factor evaluated in this study. Nevertheless, low sensitivities impacted directly RMSTEs for two-colour( $\perp$ ) in Natural water sample 2 (RMSTE  $\pm 2.6$ ; sensitivity  $0.27\%/^{\circ}\text{C}$ ).

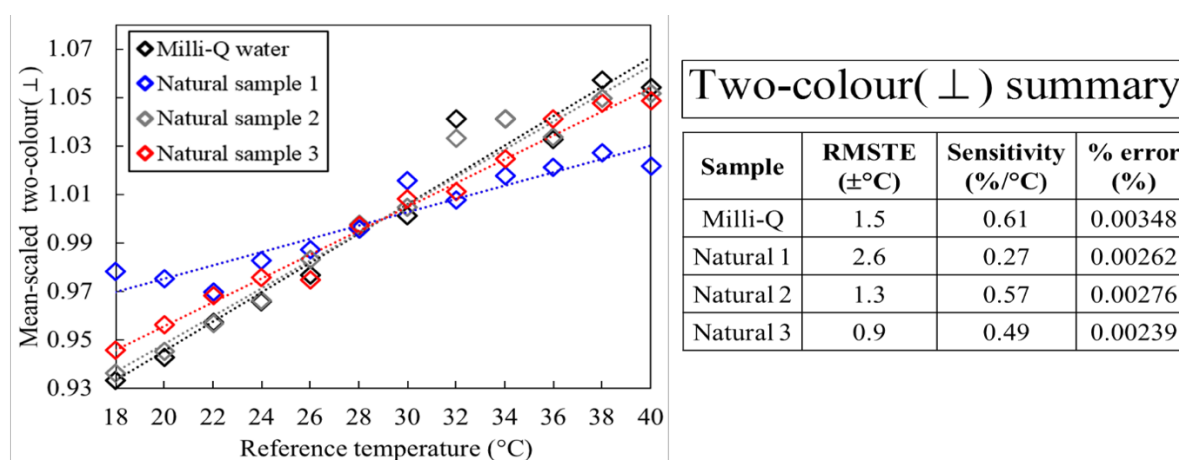


Figure 4.8. Mean-scaled temperature sensitivity data for the two-colour( $\perp$ ) marker. All water samples.

Sensitivities for depolarisation(A) exhibited maximum of  $0.75\%/^{\circ}\text{C}$  (Milli-Q water) and minimum of  $0.25\%/^{\circ}\text{C}$  (natural sample 3). In addition to exhibiting the lowest depolarisation(A) sensitivities, the RMSTEs found for natural sample 3 was of  $\pm 6.5^{\circ}\text{C}$ , the lowest performance for the marker among all water samples (figure 4.9).

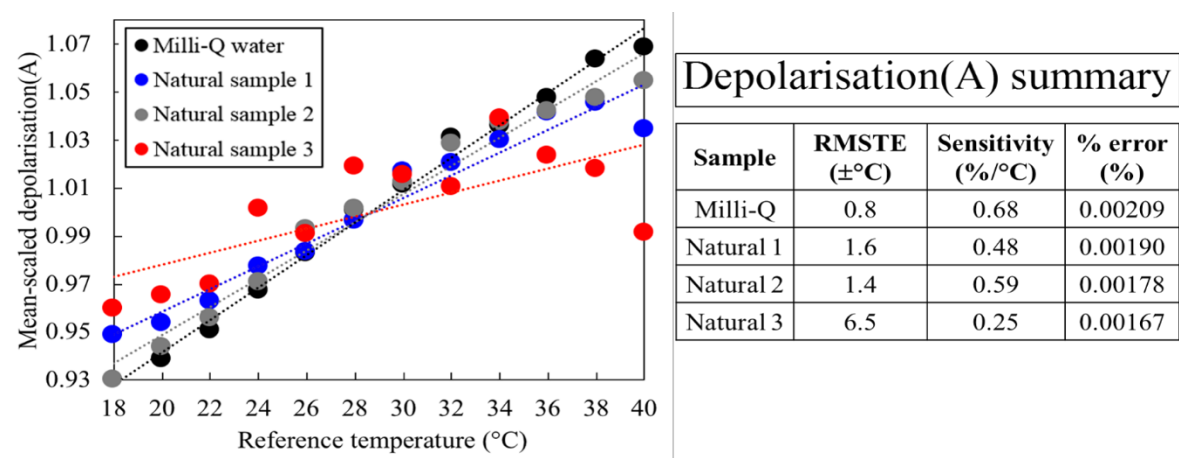


Figure 4.9. Mean-scaled temperature sensitivity data for the depolarisation(A) marker. All water samples.

Depolarisation(B) markers sensitivities (figure 4.10) exhibited smaller values in comparison with other temperature markers analysed in this study. For natural water sample 3, a high sensitivity of 0.78%/°C was found associated with a RMSTE of  $\pm 2.6^{\circ}\text{C}$ , indicating that the variation in the marker values was not only due to changes in temperature.

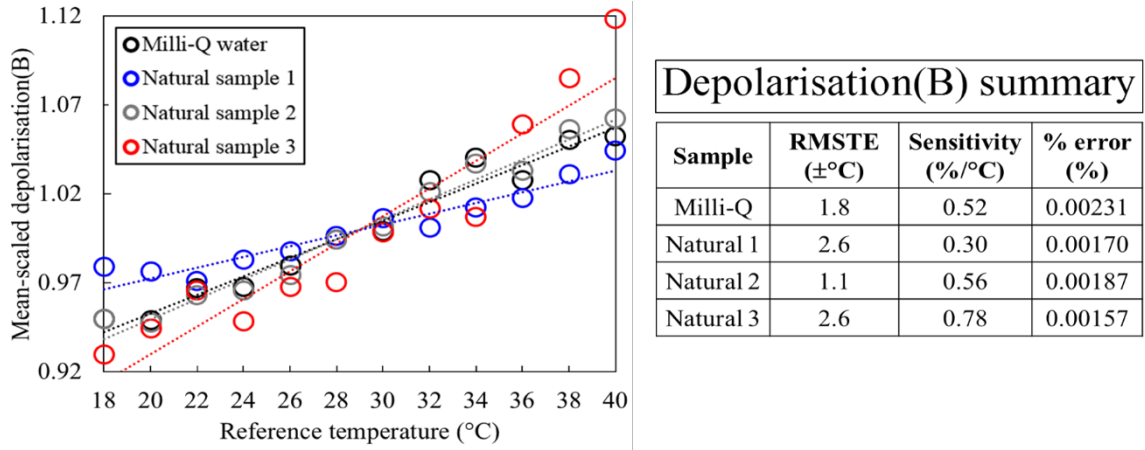


Figure 4.10. Mean-scaled temperature sensitivity data for the depolarisation(B) marker. All water samples

Temperature sensitivity is not the only factor impacting the RMSTEs of temperature predictions made using the markers, and the % errors in the marker, derived from SNRs from spectral channels collecting Raman signals, are also expected to have a bearing on RMSTE values. It is reasonable to propose that high marker sensitivity and low % errors in marker values would lead to higher RMSTEs. In order to explore this proposition, the ratio of the (% error in the markers/sensitivities) was plotted against the RMSTEs and shown in figures 4.11a (including outliers) and 4.11b (excluding outlier markers).

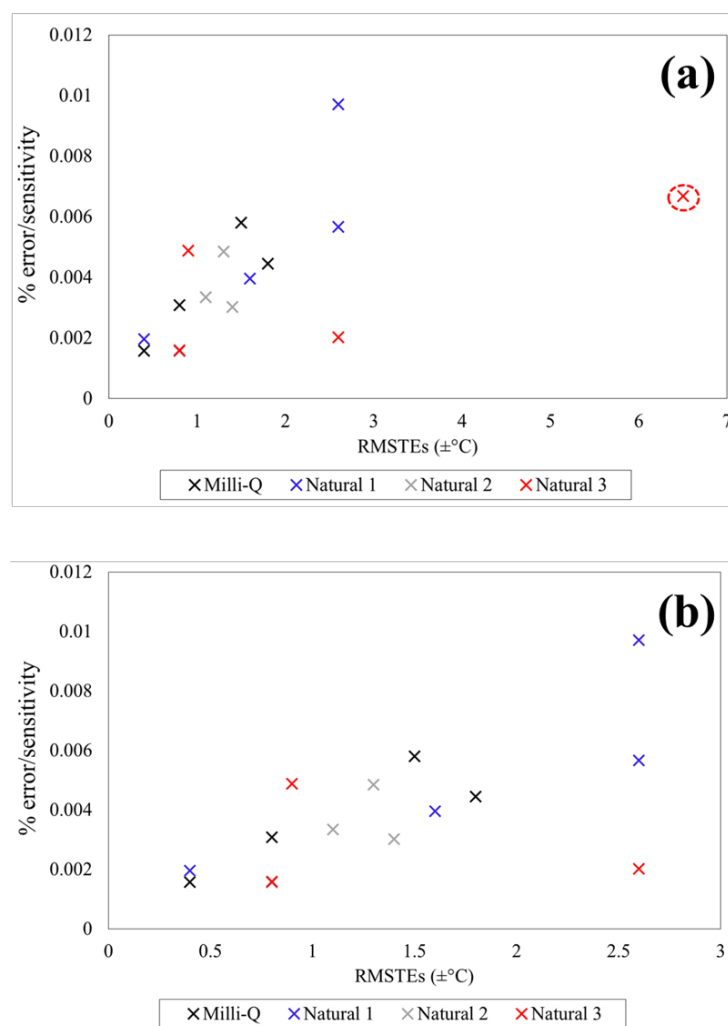


Figure 4.11. Ratios of % error to sensitivity vs. RMSTEs for all markers calculated for ultrapure and natural water samples. (a) including outlier circled in red; (b) excluding outlier.

Both graphs exhibit a clustering which is consistent with the abovementioned proposition and is evidenced in the absence of outliers (figure 4.11b). Any changes in the RS design that result in decreasing % errors for markers or improving their sensitivities can be expected to lead to better RMSTE.

## **Discussion**

In this section, I reported two-colour and depolarisation markers sensitivities calculated from Raman signals acquired by a RS integrated to a 532 nm pulsed laser. Band pass filters centred at 640 and 660 nm with spectral widths of  $315\text{ cm}^{-1}$  and  $463\text{ cm}^{-1}$  collected polarised Raman photons scattered from Milli-Q and natural water samples, achieving general average sensitivities around  $0.55\%/^{\circ}\text{C}$ . These values are smaller than the ones reported in [61,71], where sensitivities close to  $1\%/^{\circ}\text{C}$  were achieved when calculating temperature markers by spectral decomposition of the full Raman spectra. Another factor contributing to these lower sensitivities is the spectral width attributed to the channel of collections, here related to the Band Pass filters bandwidths. The relationship between channel widths and two-colour (unpol) sensitivities was explored in [63], where sensitivities were found to decrease from 1% to 0.52% when spectral channel width was reduced from  $2\text{ cm}^{-1}$  to  $300\text{ cm}^{-1}$ . The authors of [63] also conducted experiments with a two-channel custom built RS by selecting spectral channels of  $393\text{ cm}^{-1}$  and  $464\text{ cm}^{-1}$  widths, achieving sensitivities of  $0.6\%/^{\circ}\text{C}$  when analysing tap water.

Regardless of exhibiting lower temperature sensitivities when compared with other studies, accuracies better than  $\pm 0.5^{\circ}\text{C}$  were achieved by two-colour(II) markers in this study. This indicated that final RMSTEs were the result of a trade-off between the markers sensitivities and the % errors calculated for the markers, derived from SNRs. For each channel, this trade-off is adversely impacted by the presence of fluorescing constituents in natural waters, which tend to reduce sensitivities, as discussed in **Chapter 3**. These effects can be somewhat subtle; in particular, fluorescence gives rise to larger received signals and, consequently, higher SNRs and lower % errors in comparison with values calculated for Milli- Q water. This behaviour was observed for 11 out of 12 markers in this section. However, fluorescence does not contain useful information relating to temperature and accordingly the sensitivities are typically reduced. This was observed for 2 out of 3 water samples in this section. A strategy to minimize this impact from signals other than Raman would include positioning the spectral channels at wavelengths away from these regions of overlapping of Raman and fluorescence signals.

Dividing the precious Raman photons into 4 channels enables the calculation of multiple markers and LC methods; however, it comes at a cost of higher % errors for the

temperature markers. Future work could compare the performances of a 2-channel and a 4-channel RS.

## 4.5. Summary and conclusion

I designed and assembled a LIDAR-compatible multichannel Raman spectrometer integrated to a 532 nm laser. The design enabled simultaneous collection of parallel and perpendicularly-polarised Raman signals in two channels located on different sites of the isosbestic point. This configuration allowed for calculation of four temperature markers: two-colour( $\parallel$ ) and two-colour( $\perp$ ), from Raman signals of same state of polarisation, and depolarisation(A) and depolarisation(B), for channels collecting signals at different states of polarisation. I analysed temperature markers acquired from Milli-Q and natural water samples regarding their accuracies predicting temperature (RMSTEs) and sensitivities (% change in marker values/ $^{\circ}\text{C}$ ). Two-colour( $\parallel$ ) markers exhibited best RMSTEs and sensitivities. Depolarisation(A) exhibited reasonable potential to be used as temperature marker and had the benefit of extracting temperature information relating to polarisation, *i.e.*, independent for two-colour methods. This was the first time Raman polarised signals were successfully used to retrieve water temperatures with accuracy better than  $\pm 0.5^{\circ}\text{C}$ . In the future, the use of narrower band pass filters and more powerful laser sources might result in higher accuracies for temperature predictions performed by all marker types.

This was the first-time that linear combination methods were used for enhancing temperature predictions by Raman markers. This improvement was possible thanks to the innovative multichannel spectrometer design simultaneously collecting Raman signals at different states of polarisation and wavelengths. In the future, we hope to evaluate whether including additional channels (and consequently allowing for the calculation of a higher number of temperature markers) is beneficial for the linear combination analysis without compromising the signal-to-noise ratio.

Markers sensitivities and % errors (derived from signal-to-noise ratios) were calculated for all markers, and best values for both analysis were found for two-colour( $\parallel$ ) markers (average of  $\pm 0.55\%/^{\circ}\text{C}$  and  $0.0091\%$ , respectively). The % errors calculated for natural water samples were consistently lower than for Milli-Q water for all markers investigated in this study. This is indicative that, in general, higher signal counts were found for natural waters; however, these signals did not necessarily contain temperature

information and hence sensitivity values were lower. Referring to the results in Chapter 3, it is possible to argue that the higher signal counts found for natural waters could be due to overlapping between the Raman and chlorophyll-a fluorescence peaks. In the future, we intend to include accessory channels to acquire signal at 680 nm to quantify the intensity of chlorophyll-a fluorescence and apply the “correction by temperature markers” method aiming for improving RMSTEs.

The overlapping between the Raman peak for green (532 nm) excitation and chlorophyll-a fluorescence peak at 680 nm is inevitable, and always compromises temperature predictions by Raman markers. One alternative to avoid this overlapping is the use of shorter wavelengths for excitation, such as blue lasers.

# CHAPTER 5

## LIDAR-COMPATIBLE MULTICHANNEL RAMAN SPECTROMETER USING BLUE (473 NM) EXCITATION LIGHT

The adverse impact of fluorescence from natural waters constituents in Raman remote sensing temperature measurements has been evaluated by several authors and explored for green (532 nm) excitation in Chapter 3 and manuscript 1 [113]. For studies conducted using green laser excitation the chlorophyll-a fluorescence peak at 680 nm overlaps with the high end of the water OH stretching band, having direct impact in the Raman temperature markers



calculations. Regardless of this overlapping, the use of green laser is common-place in oceanographic LIDAR operations and so the logical starting point for evaluating the technique was exploring green excitation.

In Chapter 4, I presented the design, operation and temperature predictions obtained by a custom-built LIDAR-compatible multichannel RS integrated to a 532 nm pulsed laser, achieving accuracies as high as  $\pm 0.4^{\circ}\text{C}$  for a single marker predicting temperatures from a natural water sample in laboratory. As seen in Chapter 3, it is possible to increase the accuracy of water temperature predictions by applying baseline correction techniques and achieve accuracies as high as  $\pm 0.2^{\circ}\text{C}$  for natural waters temperature predictions in laboratory using 532 nm light for Raman excitation.

Besides post-acquisition baseline correction techniques, some authors propose the use of shorter wavelengths as the excitation source in Raman remote sensing studies, such as blue light around 480 nm [86,87]. This approach would be effective on avoiding overlapping between chlorophyll-a and water Raman signals, as the water Raman peak for blue excitation lies around 565 nm. In this Chapter, I will present the design, operation and key laboratory experimental findings obtained by a custom-built multichannel LIDAR-compatible Raman spectrometer (RS) integrated to a 473 nm pulsed laser source, assembled by me as part of my PhD project. The design is similar to the RS presented in Chapter 4, allowing for simultaneous collection of parallel and perpendicularly-polarised Raman photons at narrow spectral channels and the same two-colour and depolarisation markers could be calculated and used for predicting water temperature. I conducted laboratory experiments and acquired temperature-associated Raman signals from both Milli-Q and natural (coastal) water samples, and for each marker I estimated accuracies for temperature predictions (RMSTE), sensitivities and percentage errors associated with signal-to-noise ratios. Finally, the four temperature markers were combined by multiple linear regression methods to deliver enhanced accuracies. The methodology, results and analyses behind these experiments conducted with blue light excitation and comparisons with the green multichannel RS introduced in Chapter 4 are presented in manuscript 3, which will be submitted to the journal *Frontiers in Marine Sciences*, in a special issue entitled “*Emerging Technologies with High Impact for Ocean Sciences, Ecosystem Management, and Environmental Conservation*”.

As a complementary investigation, I simulated the performance of blue and green light in LIDAR Raman signal acquisitions in different Jerlov water types, determining which excitation source is more suitable for Raman remote sensing of water temperature according to environmental conditions. Also relevant to the blue Raman spectrometer is the analysis presented in Appendix A, where the “correction by temperature markers” method proposed in manuscript 1 [113] and Chapter 3 was used for simulating temperature predictions in the field.

### **5.1. Manuscript 3: “Remote sensing of temperature in natural water samples using a multichannel, lidar-compatible Raman spectrometer and blue excitation (473 nm)”**

#### **Statement of contribution**

I designed and assembled the multichannel, LIDAR-compatible Raman spectrometer integrated to a 473 nm (blue) laser and conducted the experiments which led to the results presented in manuscript 3. This manuscript is intended to be submitted to the journal “*Frontiers in Marine Sciences*” and published in the special issue “*Emerging Technologies with High Impact for Ocean Sciences, Ecosystem Management, and Environmental Conservation*”. I was responsible for performing all analyses reported in the manuscript, and also responsible for writing much of the paper and prepared the figures for publication. The Raman spectra shown in figure 1(b) and figure 3 were acquired by C. Artlett.

# REMOTE SENSING OF TEMPERATURE IN NATURAL WATER SAMPLES USING A MULTICHANNEL, LIDAR-COMPATIBLE RAMAN SPECTROMETER AND BLUE EXCITATION (473 NM)

ANDRÉA DE LIMA RIBEIRO<sup>1\*</sup> AND HELEN PASK<sup>1</sup>

<sup>1</sup>*MQ Photonics Research Centre, Department of Physics and Astronomy, Macquarie University, Australia*

*[\\*andrea.delimaribeiro@mq.edu.au](mailto:andrea.delimaribeiro@mq.edu.au)*

## ABSTRACT

The design and operation of a custom-built LIDAR-compatible, four-channel Raman spectrometer integrated to a 473 nm pulsed laser is presented. The multichannel design allowed for simultaneous collection of Raman photons at spectral regions identified as highly sensitive to changes in water temperature. Four independent temperature markers were calculated for ultrapure (Milli-Q) and natural water samples (two-colour(II), two-colour( $\perp$ ), depolarisation(A) and depolarisation(B)). Temperature accuracies of up to  $\pm 0.5^\circ\text{C}$  were achieved for both water types when predicted by two-colour(II) markers. Multiple linear regression models were constructed considering all simultaneously acquired temperature markers, resulting in improved accuracies of up to  $\pm 0.2^\circ\text{C}$ . The potential benefits of blue laser excitation in relation to avoiding overlap between the Raman signal and fluorescence by chlorophyll-a are discussed, along with the higher Raman returns anticipated compared to the more-conventional green laser excitation.

## 1. INTRODUCTION

Temperatures on our planet have increased at concerning rates following the industrial developments from the 19<sup>th</sup> and 20<sup>th</sup> centuries due to changes in Earth's radiative balance [1], an equilibrium relationship between how much of the heat received by our planet can be either re-emitted back to space or absorbed by the planet's heat sinks, such as the oceans. The oceans act as massive thermal reservoirs due to the high specific heat capacity of water, demanding large amounts of heat in order to change its temperature. Increased greenhouse gases emissions from industrial and agricultural activities have reduced the amount of radiation re-emitted by the Earth, generating a radiation unbalance which needs to be compensated by increased heat absorption by the heat sinks. Recent discussions regarding climate changes brought public awareness to the consequences of this thermal unbalance, leading to increased temperatures, thermal expansion of water and sea level rise at coastal areas directly impacting human activities. In a world undergoing accelerated climate changes, measuring water temperatures is essential for risk assessment and continuously monitoring oceanic and coastal zones.

Water temperature information can be assessed by traditional and remote sensing methods. Traditional *in situ* methods such as thermometers, CTDs and buoys have been broadly used in oceanographic investigations, collecting highly accurate depth-resolved temperature data; however, they are restricted to providing non-continuous information from sampling stations, present high costs associated with data acquisition and processing and are not compatible with time and space scales of many processes occurring at oceanic and coastal zones [2]. As an alternative when traditional methods are not compatible with the scales being studied, researchers rely on remote sensing tools to collect information from the environment.

Remote sensing techniques retrieve information from a target without direct interaction with the object under investigation. In oceanography, it involves the study of the oceans, the atmosphere and their interactions by analysing electromagnetic radiation emitted by these media. Satellite sensors and LIDAR methods (Light Detection and Ranging) are the most conventional remote sensing techniques for studying the oceans [3,4].

Satellite sensors, such as AVHRRs (Advanced Very High Resolution Radiometers) collect infrared signal passively emitted by the first micrometers of water column, exhibiting accuracies for temperature measurements up to  $\pm 0.1^\circ\text{C}$  and typical spatial resolution of 4 km. However, the accuracy and periodicity of AVHRR measurements are compromised by the presence of clouds and require several atmospheric corrections, as the infrared signal is absorbed by water vapour, Carbon dioxide and methane present in the atmosphere [5,6]. Recently, [7] compared sea surface temperature acquired by AVHRR sensors with *in situ* reference measurements performed by buoys and surfers along the UK coast, finding discrepancies from  $\pm 0.4$  to  $\pm 0.6^\circ\text{C}$  for measurements on offshore sites and from  $\pm 1.0$  to  $\pm 2.0^\circ\text{C}$  for coastal stations. This indicates that, additionally to not providing depth-resolved information, infrared satellite temperature predictions may vary substantially from real values at coastal zones.

The evolution of operational oceanography and the increasing need for new tools to validate satellite data and fast vertical profiling of aquatic environments. led to the development of a new class of remote sensing techniques, known as LIDAR. Active LIDAR systems comprise (1) a pulsed light source in the visible or near-infrared range; and (2) fast detectors allowing for time-resolved signal collection. As the excitation light is transmitted in water, it interacts with water molecules and other active optical constituents, with a fraction of the incident photons being scattered back to the surface (backscattered signal). Laser Airborne Depth Sonar (LADS) is perhaps the most mainstream use of LIDAR in oceanography today. The interpretation of the backscattered, time-resolved, signal enables assessment of water bulk characteristics and systematic bathymetric mapping in coastal areas [8,9].

In 1979 a scientific seminar was organised to discuss the use of LIDAR methods for monitoring the oceans, and consideration was given to the use of several spectroscopic techniques for measuring water temperature, such as Raman spectroscopy [10]. Raman spectroscopy is a technique based on the inelastic scattering of an incident photon, usually from a laser source, such that scattered photons exhibit lower (Stokes) or higher (anti-Stokes) frequencies, corresponding to the natural frequencies of vibrational modes in the scattering media. Liquid water is a substance governed by hydrogen-bonding processes, exhibiting a tetrahedral structure with several intra and intermolecular Raman-active modes [11]. The water Raman spectrum exhibits temperature-dependent behaviour, firstly identified by the authors of [12], which can be clearly seen at the spectral region known as OH stretching band. For pure water, the OH stretching band is located between  $2900\text{ cm}^{-1}$  and  $3900\text{ cm}^{-1}$  and includes a temperature-insensitive point known as the isosbestic point. The polarisation properties of Raman-scattered photons are also temperature-dependent [13].

As a consequence of the temperature-dependent behaviour found for unpolarised and polarised components of the water Raman spectra, there exist Raman temperature markers: ratios calculated from signals at distinct spectral positions whose values vary linearly with water temperature (hereafter referred to as “markers”). These markers can be calculated from Raman signals having the same polarisation state and are known as “two-colour ratios, or from the number of photons having perpendicular/parallel polarisation, referred to as “depolarisation” ratios. These ratios form the basis for numerous studies [14–17] undertaken from the 1970s until the present time, aimed at using Raman spectroscopy to remotely determine water temperature. When used in combination with LIDAR methods, there exists great potential to obtain depth-resolved measurements of subsurface water temperature. Such a capability would address currently un-met needs of modern oceanography and is, in principle, compatible with airborne, surface or underwater platforms. The over-arching goals of our research project, of which this paper is a part, is to develop a straightforward

instrumentation that could be used to determine subsurface water temperature with accuracy  $\leq \pm 0.5^\circ\text{C}$ , depth resolution  $\leq 0.5$  m in near-real time.

In [17] accuracies of  $\pm 0.1^\circ\text{C}$  were reported for water temperature measurements performed in the laboratory using a commercial dispersive Raman spectrometer (Enwave-EZRaman I), incorporating a 532 nm, CW, excitation laser. That work utilised unpolarised Raman spectra, two-colour markers, and Reverse-Osmosis laboratory water. When trying to conduct the same analysis for temperature predictions in natural waters, we found substantially lower accuracies (higher RMSTEs), which we attribute to the overlapping of the Raman peak for 532 nm excitation and fluorescence signals. The commercial dispersive Raman spectrometer (RS) used in [17] did not fulfil LIDAR-compatibility requirements and, in order to transition from commercial equipment towards LIDAR-compatible technologies, we designed and assembled a LIDAR-compatible multichannel RS integrated to a 532 nm pulsed excitation laser [19]. The equipment allowed for simultaneous Raman signal collection in four spectral channels, and two-colour and depolarisation markers were estimated for ultrapure (Milli-Q) and natural water sample, achieving best accuracies of  $\pm 0.3^\circ\text{C}$  in both cases. The simultaneous Raman signal collection enabled the Linear Combination (LC) methods to be used; these enabled temperatures to be predicted based on all four temperature markers.

The complexities of working with Raman spectroscopy in natural waters include laser-induced fluorescence arising from optically-active constituents and overlapping of these signals with the water Raman peak [20–22]. These issues are particularly concerning when using 532 nm (green) excitation as the water Raman peak overlaps with fluorescence from Chlorophyll-a (Chl-a), compromising the accuracy of temperature predictions. The authors of [20–22] recommended using shorter wavelengths for excitation, such as blue light around 480 nm in order to avoid overlapping with the broad Chl-a fluorescence band, which is centred around 680 nm. For comparative purposes, the water Raman peak (OH stretching band) lies between 550 nm and 575 nm when excited by blue light at 473 nm, and between 635 nm and 660 nm when excited by green light at 532 nm. Figure 1 shows our measured Raman spectra for milli-Q water at various temperatures, when using (a) blue and (b) green laser excitation. Note the differences in shape are due to different spectral resolutions for the two measurements (the spectra in Fig 1a are not fully resolved). Nevertheless, the temperature dependent behaviour is clear in both cases.

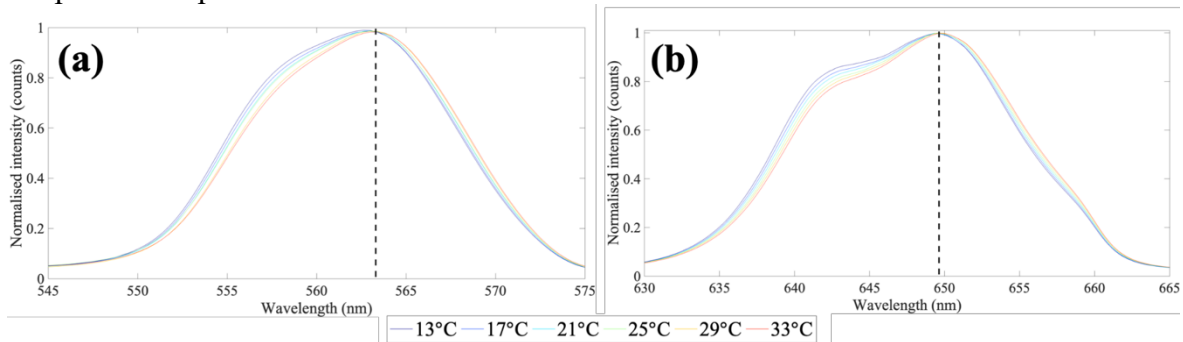


Figure 1. Temperature-dependent Raman unpolarised spectra from a Milli-Q water sample using (a) blue excitation at 473 nm (QE65000 Raman spectrometer, average sampling interval of  $14\text{ cm}^{-1}$  for the OH stretching band region); (b) green excitation at 532 nm (Enwave EZ-Raman spectrometer,  $2\text{ cm}^{-1}$  sampling interval).

Blue excitation light has not been widely used for Raman remote sensing of water temperature, and most oceanographic LIDAR methods for bathymetric measurements employ green excitation at 532 nm. Nevertheless, the use of blue lasers would be beneficial for LIDAR implementations in natural waters for the following reasons: (1) avoiding direct overlapping between the Raman peak and fluorescence from Chl-a at 680 nm [21,22];

(2) Blue light has high transmission in most coastal and oceanic waters, achieving higher depths than green light [23]; (3) the Raman cross-section of liquid water is inversely proportional to the wavelength of Stokes-shifted photons [24]; (4) wavelengths for Raman shifted photons generated by blue excitation are in the green range, undergoing lower transmission losses for returned Raman photons around 560 nm (for blue excitation) than 650 nm (for green excitation). Despite being effective in avoiding overlap with the Chl-a fluorescence peak, Raman signals scattered from blue excitation are more susceptible to overlap with DOM fluorescence. Accordingly, it is necessary to evaluate which excitation wavelength will be less likely to overlap with fluorescence from natural water constituents and provide better accuracy for Raman temperature predictions.

In this work we present a multichannel, LIDAR-compatible Raman spectrometer (RS) integrated to a 473 nm (blue) pulsed laser which is used to determine the temperature of small volumes (cuvettes) of ultrapure and natural samples. We have evaluated the effectiveness of the two-colour and depolarisation temperature markers, each of which is calculated from spectral channels acquired simultaneously by the RS, in terms of sensitivity to temperature change, % error in the markers and the accuracy with which temperature can be predicted. Finally, we explore the relative merits of using blue vs green laser excitation, with a view to understanding which source might ultimately be best for use in field measurements. This is firstly in terms of comparing the measured accuracies with those reported in [19] using green excitation. Second, we use simple LIDAR equations to estimate the relative Raman returns for the cases of blue and green excitation.

## 2. METHODS AND ANALYSIS

### 2.1. SPECTROMETER DESIGN

The experimental setup for our multichannel LIDAR-compatible Raman spectrometer using a 473 nm laser is shown in figure 2 (hereafter this will be referred as “blue multichannel RS”). Milli-Q (ultrapure) and natural water samples collected at a location inside Sydney Harbour were placed inside a temperature-controlled cuvette holder (QNW QPod2e, accuracy of  $\pm 0.2^\circ\text{C}$ ) and their temperature was varied from  $18^\circ\text{C}$  to  $40^\circ\text{C}$ , stepping every  $2^\circ\text{C}$ . For natural water samples, Raman signals were acquired within a few hours of collection. Blue light produced by a linearly-polarised 473 nm pulsed laser (Nd:YAG, 5  $\mu\text{J}$  per pulse, 1.5 ns at FWHM, 5 kHz repetition rate) was collimated by lenses and coupled into the samples via a Dichroic Mirror (DM, Semrock Di02-R488,  $R \sim 94\%$  from 471 to 491 nm,  $T \sim 93\%$  between 499.8 and 900 nm). Raman-scattered photons passed through a Long Pass filter (LP, Semrock BLP01-473R,  $T \sim 93\%$  between 486 and 900 nm) in order to eliminate Rayleigh scattering, and were split into 2 beams by means of a 50/50 Beam Splitter Cube (BSC). Each beam then passed through a Band Pass filter:  $BP_{low}^{561}$  acquiring photons at the low shift end (Semrock FF01-561/4, central wavelength at 561 nm and band pass of 8 nm at the FWHM) and  $BP_{high}^{568}$  acquiring Raman photons at the high shift end (Semrock LL01-568, central wavelength of 568 nm and band pass of 4 nm at the FWHM). The choice of BP filters was constrained by commercial availability, and the pass band for each of these filters is indicated in figure 3. In units of wavenumbers, the spectral widths at the FWHM were  $254\text{ cm}^{-1}$  for the low shift channel and  $136\text{ cm}^{-1}$  for the high shift channel.

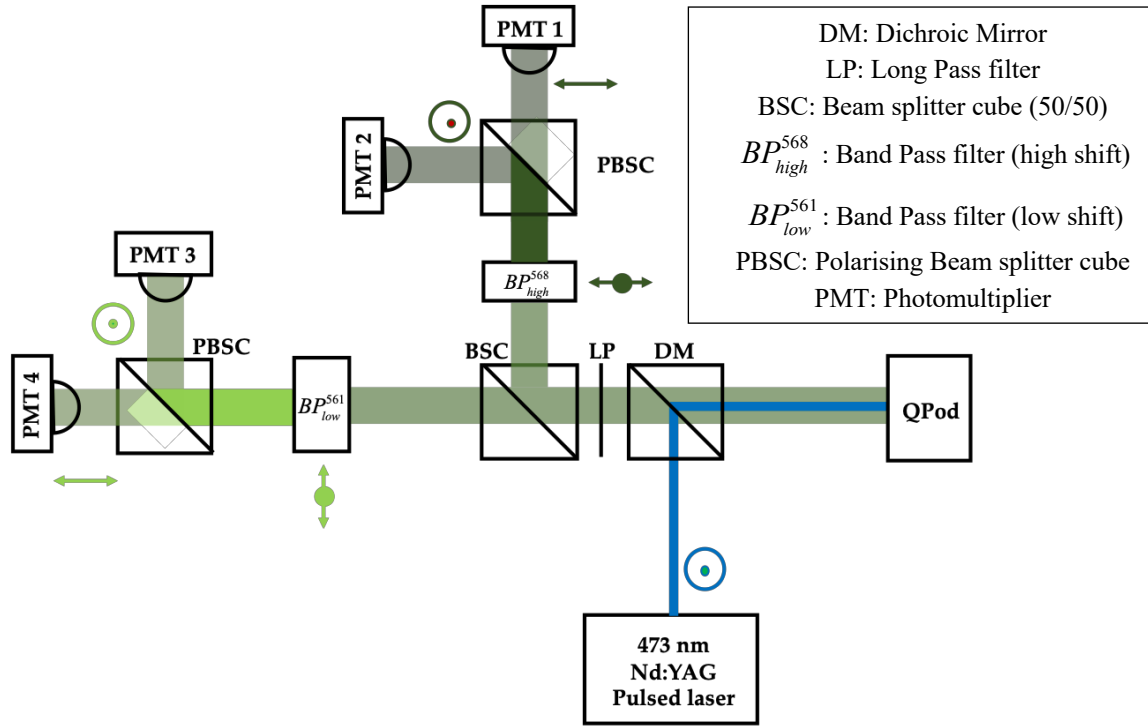


Figure 2. Experimental design of the 4-channel Raman spectrometer.

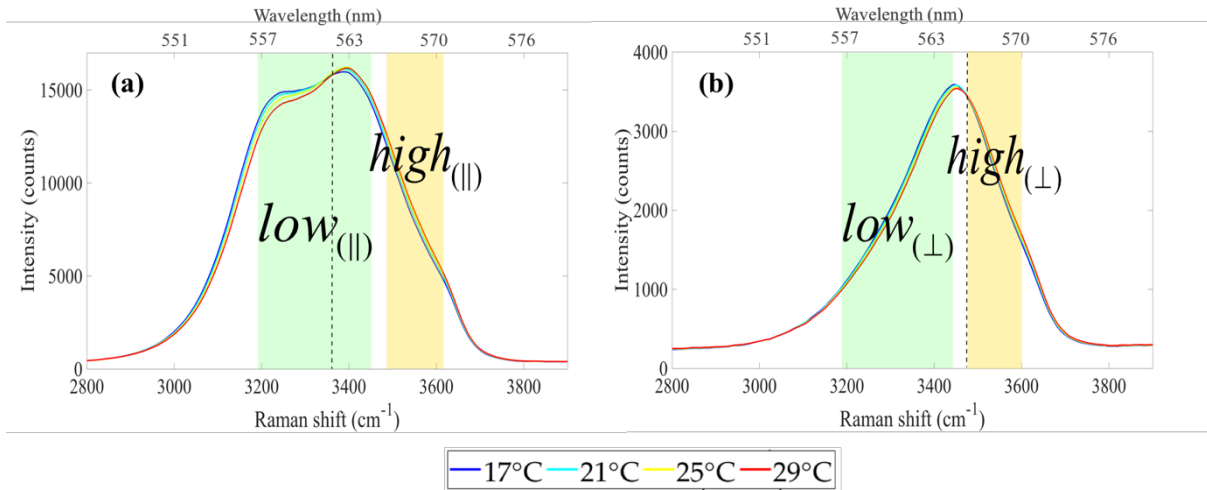


Figure 3. Band pass filter transmissions superimposed on (a) parallel and (b) perpendicularly-polarised temperature-dependent water Raman spectra.

After passing through the BP filters, each beam was divided into two polarised components by a Polarising Beam Splitter Cube (PBSC), which were finally focused by lenses ( $f=25$  mm) onto fast-response photomultipliers (PMT, Hamamatsu H10721-20). The PMT gains were set around 700 V, well below the setting for maximum gain (900 V). Signals from each channel were registered by a four-channel oscilloscope (Tektronix DPO4104B), with averaging over 512 pulses.

In order to estimate signal-to-noise ratios (SNR), acquisitions were performed with and without excitation light, with averaging over 512 pulses. SNRs were calculated for each spectral channel according to equation 1:



$$SNR = \frac{\int \text{Signal}_{(FWHM)}}{\int \text{Noise}_{(FWHM)}} \quad (1)$$

where  $\int \text{Signal}_{(FWHM)}$  represents the integrated Raman signal pulse around the full width of half maximum (FWHM); and  $\int \text{Noise}_{(FWHM)}$  refers to the integrated noise signals over the same time period.

Table 1 shows a list of information regarding each spectral channel of collection, including polarisation state, band pass filter used, typical SNRs and the nomenclature which will adopted in this paper.

Table 1. Nomenclature adopted for each spectral channel and typical SNRs.

Channel number	Polarisation state	Band Pass filter	Nomenclature	Typical SNR
1	Parallel	$BP_{high}^{568}$	$I_{  }^{high}$	6,221
2	Perpendicular	$BP_{high}^{568}$	$I_{\perp}^{high}$	1,749
3	Perpendicular	$BP_{low}^{561}$	$I_{\perp}^{low}$	3,255
4	Parallel	$BP_{low}^{561}$	$I_{  }^{low}$	4,533

## 2.2. TEMPERATURE MARKERS CALCULATIONS

Each average of 512 pulses acquired by the oscilloscope was integrated in Matlab (Mathworks, R2017b) using the trapezoid method over an approximate range of 2.0 ns around the FWHM, corresponding to 10 data points (figure 4). Raman signals corresponding to those spectral channels were used to calculate four types of temperature markers, according to equations 2-5.

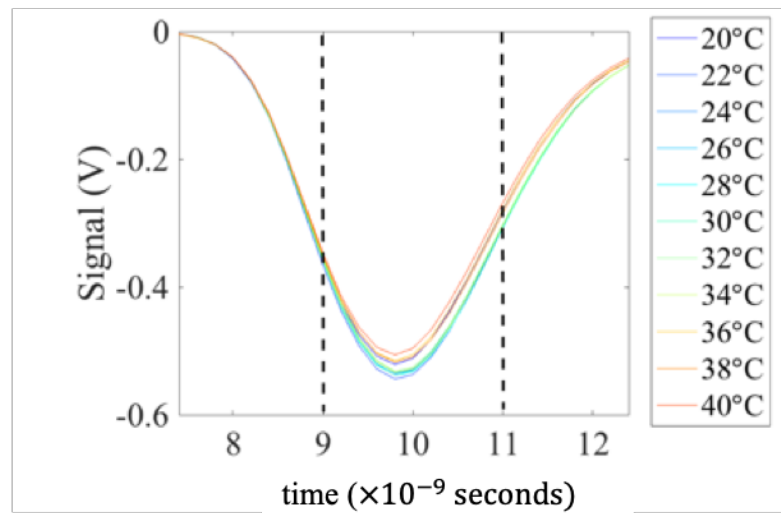


Figure 4. A typical set of signals (channel 4), recorded for different temperatures and showing the area over which the signals were integrated.

$$Two-colour(\parallel) = \frac{I_{\parallel}^{high}}{I_{\parallel}^{low}} \quad (2)$$

$$Two-colour(\perp) = \frac{I_{\perp}^{high}}{I_{\perp}^{low}} \quad (3)$$

$$Depolarisation(A) = \frac{I_{\perp}^{high}}{I_{\parallel}^{low}} \quad (4)$$

$$Depolarisation(B) = \frac{I_{\perp}^{low}}{I_{\parallel}^{high}} \quad (5)$$

where  $I_{pol}^{xxx}$  indicates the intensity of Raman signal at a certain channel (high/low) on a given polarisation state.

For each water sample, three independent acquisitions were performed for each temperature, hence three sets of two-colour and depolarisation markers could be calculated for each temperature. Aiming to increase robustness, the markers calculated from the independent acquisitions were averaged, giving origin to a new (fourth) dataset for each temperature marker hereafter referred as the “average markers dataset”. In order to determine the uncertainties in the temperature markers, percentage errors (%) were estimated by adding the percentage uncertainties associated with SNRs calculated for each channel used in the marker calculation.

### 2.3. MARKER SENSITIVITIES AND PREDICTING TEMPERATURE

In keeping with previous studies [17–19,25], the relationships between temperature markers and reference temperatures are found to be linear, allowing for the use of linear regression models with coefficients *gradient* and *intercept*. These coefficients were then rearranged in order to calculate a new set of temperatures dependent on the markers, hereafter called “predicted temperatures” (equation 6).

$$T_{predicted} = (\text{gradient} \times \text{marker}) + \text{intercept} \quad (6)$$

where  $T_{predicted}$  represents the predicted temperature estimated by a temperature marker. RMSTE values ( $\pm^{\circ}\text{C}$ ) were calculated for the predicted temperature in comparison with the reference temperature values and used as a measure of the accuracy of temperature determination by the various markers.

Sensitivities, *i.e.* the % change in a marker per  $^{\circ}\text{C}$ , were estimated for markers calculated for an ultrapure water sample. As outlined in [17] the use of mean-scaled temperature markers is most useful for sensitivity calculations. Those are determined by scaling each marker by the mean value of all markers within a set of temperature measurements (equation 7). The linear model generated from the relationship between mean-scaled markers and reference temperatures provided the information necessary to estimate sensitivities for each water sample under analysis.

$$\text{Mean-scaled markers sensitivity} = \frac{d(\text{marker})}{dT} \frac{1}{\text{mean}(\text{marker})} \quad (7)$$

## 2.4. LINEAR COMBINATION METHODS: ENHANCING TEMPERATURE PREDICTIONS

Our spectrometer design enabled signals to be collected from all spectral channels simultaneously, hence the four temperature markers described in equations 2-5 have the same origin and contain different types of temperature-dependent Raman information. This multivariate analysis, which we will call the linear combination (LC) method combines all four markers into one model to enhance temperature predictions according to equation 8.

$$T_{predicted} = \beta_0 + \beta_1 \times two-colour(\parallel) + \beta_2 \times two-colour(\perp) + \beta_3 \times depol(A) + \beta_4 \times depol(B) + \varepsilon \quad (8)$$

where  $\beta_0$  is an independent term,  $\beta_1$ - $\beta_4$  are calibration terms generated by the model and correlated with each marker and  $\varepsilon$  are the residual errors. LC models for the set of “average markers” were constructed for each sample analysed in this paper.

## 3. RESULTS AND DISCUSSION

### 3.1. MILLI-Q WATER ANALYSIS

In this section, we explore the temperature markers calculated from Raman signals retrieved by our blue multichannel RS for an ultrapure (Milli-Q) water sample. Specifically, we consider the accuracy of temperature predictions, markers sensitivities and % errors in the temperature markers. We consider that the Raman signals acquired from the ultrapure water sample are solely due to the interactions between the excitation light and water molecules, and will give rise to optimum performance of our RS. A summary with the main results found for ultrapure water analysis is shown in table 2.

The mean-scaled value of each temperature marker is shown as a function of temperature in Fig. 5. Their sensitivities extracted from the slope of each curve are summarised in Table 2.

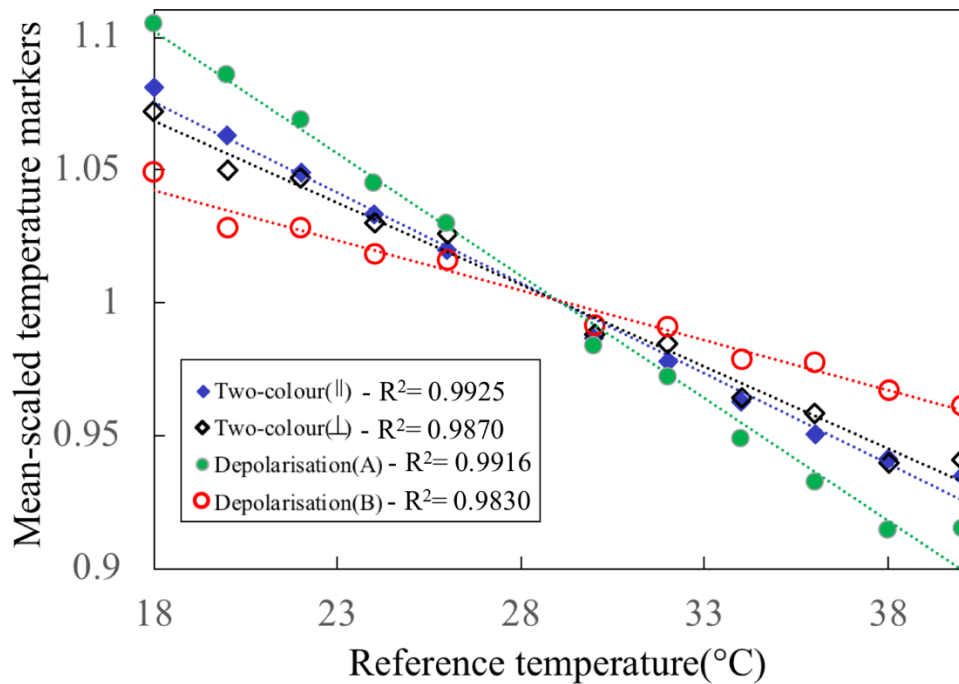


Figure 5. Mean-scaled temperature markers for Milli-Q water.

Table 2. RMSTEs ( $\pm^\circ\text{C}$ ), SNRs, sensitivities (% change/ $^\circ\text{C}$ ) and absolute percentage errors in markers (%) for a Milli-Q water sample. Data in brackets is based on the analysis of 4 datasets; data without brackets is based on the “average markers” dataset. Refer to section 2.2 for details.

Temperature marker	Milli-Q water sample		
	RMSTE ( $\pm^\circ\text{C}$ )	Sensitivity (%/ $^\circ\text{C}$ )	Marker % error (%)
<b>Two-colour(<math>\parallel</math>)</b> [Range]	0.5 [0.5 – 0.7]	0.68	0.04
<b>Two-colour(<math>\perp</math>)</b> [Range]	0.7 [0.7 – 1.6]	0.62	0.12
<b>Depolarisation(A)</b> [Range]	0.5 [0.5 – 0.6]	0.92	0.09
<b>Depolarisation(B)</b> [Range]	3.2 [2.5 – 3.2]	0.38	0.07
<b>Linear combination</b>	0.3 [0.3 – 0.6]	-	-

Maximum sensitivities of  $0.92\%/^\circ\text{C}$  were found for depolarisation(A) markers, significantly higher than the second best sensitivities found for two-colour( $\parallel$ ) ( $0.68\%/^\circ\text{C}$ ). Additionally, these were the markers which exhibited lowest absolute % errors ( $0.04\%$  for two-colour( $\parallel$ ) and  $0.09\%$  for depolarisation(A)) and the best RMSTEs of  $\pm 0.5^\circ\text{C}$  were found for both markers. Sensitivity values were generally smaller than the  $1\%/^\circ\text{C}$  reported by the authors of [14,16], however, it is necessary to consider the impact of the spectral channels widths on the final sensitivities. The authors of [17] evaluated the trade-offs between spectral channels and sensitivities by performing simulations with unpolarised Raman signals acquired from ultrapure (Reverse-Osmosis) water samples. The mean-scaled markers sensitivities calculated from two spectral channels of  $250\text{ cm}^{-1}$  width exhibited values around  $0.68\%/^\circ\text{C}$ ; and sensitivities for channels widths around  $150\text{ cm}^{-1}$  were estimated to be around  $1.03\%/^\circ\text{C}$ . Considering that the spectral channels used in our work had widths of  $234\text{ cm}^{-1}$  and  $137\text{ cm}^{-1}$  at the FWHM, the sensitivities found for both depolarisation(A) and two-colour( $\parallel$ ) markers were reasonably in agreement with the values proposed in [17].

Two-colour( $\perp$ ) and depolarisation(B) had inferior performance for all parameters analysed, exhibiting lower sensitivities, higher absolute % errors and higher RMSTEs. This was particularly true for depolarisation(B) markers, with RMSTEs of  $\pm 3.2^\circ\text{C}$ , sensitivities of  $0.38\%/^\circ\text{C}$  and %errors of  $0.07\%$ , indicating that the markers showed low efficiency when extracting temperature-dependent information from water Raman signals. LC methods resulted in an average improvement of  $40\%$  in RMSTEs for the Milli-Q water sample, showing it to be a valuable technique for enhancing accuracy of temperature prediction..

There is a lack of LIDAR-compatible studies in the Raman remote sensing of water temperature using blue lasers, restricting the discussion of the results from this article to comparisons with the reports of [16]. In the occasion, the authors reported the use of a LIDAR-compatible custom-built RS integrated to a  $470\text{ nm}$  laser ( $15\text{ mJ}$  per pulse,  $2\text{ kHz}$  repetition rate) measuring water temperature in laboratory from depolarisation markers and finding accuracies of  $\pm 0.5^\circ\text{C}$ . These were the same accuracies found for our multichannel blue RS when measuring Milli-Q water temperature from depolarisation(A) information.

In [19], we reported a multichannel LIDAR-compatible RS integrated to a  $532\text{ nm}$  excitation laser (green) which configuration was similar to our multichannel LIDAR compatible RS integrated to a  $473\text{ nm}$  laser (blue) presented in this work. The similarities between both systems include: (1) same number of collection channels; (2) simultaneous collection of both orthogonally-polarised components of the water Raman signal; (3) same

methods of calculation for temperature markers. In [19], RMSTEs as low as  $\pm 0.4^{\circ}\text{C}$  were achieved for temperature predictions from two-colour(II) markers, similar to the findings in this report ( $\pm 0.5^{\circ}\text{C}$ ). Regarding sensitivities, maximum values for maximum sensitivity for the green multichannel RS were  $0.68\%/^{\circ}\text{C}$ , whilst sensitivities for the blue multichannel RS reached values as high as  $0.92\%/^{\circ}\text{C}$ . However, comparisons between RMSTEs and sensitivities achieved in this report and the findings in [19] are limited by the following factors: (1) the laser power used for excitation in [19] was five times larger than the laser power used for excitation in this study; (2) channels widths for the green multichannel RS were twice as large as the channel widths used in the blue multichannel RS; and (3) there were differences in the central wavelength relative to the Raman spectra for the blue and green RS. Both RS, blue and green, allowed for temperature predictions equal or better than  $\pm 0.5^{\circ}\text{C}$ .

### 3.2. NATURAL WATER ANALYSES

Natural water samples from Sydney Harbour were collected on various dates and analysed with our blue multichannel RS. We start by acknowledging that comparisons between the results obtained for the samples are somewhat limited, considering the presence of different (unquantified) concentration of optically active components in water for each natural sample. Our intention here was to use a range of authentic natural samples in our analyses rather than “fine-tune” our methods to one particular sample.

Accuracy of temperature predictions (RMSTEs), sensitivities and % errors in the temperature markers were calculated for each natural water sample and results for the fourth dataset (“average markers”) are summarised in table 3. The range of RMSTEs found for all datasets (1, 2, 3 and “average markers”) is also indicated in the table.

Table 3. RMSTEs ( $\pm^\circ\text{C}$ ), sensitivities (% change/ $^\circ\text{C}$ ) and absolute percentage errors in markers (%) for natural water sample analysed by two-colour and depolarisation markers. Data in brackets is based on the analysis of 4 datasets; data without brackets is based on the “average markers” dataset. Refer to section 2.2 for details.

		Temperature markers				
		Two-colour( $\parallel$ )	Two-colour( $\perp$ )	Depol (A)	Depol(B)	LC
Natural 1	RMSTE ( $\pm^\circ\text{C}$ ) [Range]	0.70 [0.70 – 0.80]	1.50 [1.50 – 1.60]	1.30 [1.20 – 1.70]	7.20 [4.70 – 7.20]	0.4 [0.4 – 0.7]
	Sensitivity (%/ $^\circ\text{C}$ )	0.71	0.42	0.71	0.42	-
	Marker % error (%)	0.05	0.12	0.42	0.07	-
Natural 2	RMSTE ( $\pm^\circ\text{C}$ ) [Range]	0.70 [0.70 – 1.0]	1.20 [1.20 – 2.0]	1.30 [1.10 – 1.70]	2.30 [2.30 – 5.60]	0.5 [0.5 – 0.7]
	Sensitivity (%/ $^\circ\text{C}$ )	0.62	0.50	0.74	0.38	-
	Marker % error (%)	0.04	0.74	0.09	0.06	-
Natural 3	RMSTE ( $\pm^\circ\text{C}$ ) [Range]	0.70 [0.50 – 1.10]	0.90 [0.90 – 1.50]	0.80 [0.80 – 1.00]	4.90 [3.70 – 5.60]	0.3 [0.3 – 0.8]
	Sensitivity (%/ $^\circ\text{C}$ )	0.71	0.51	0.85	0.38	-
	Marker % error (%)	0.03	0.09	0.09	0.06	-
Natural 4	RMSTE ( $\pm^\circ\text{C}$ ) [Range]	0.50 [0.50 – 0.8]	0.80 [0.80 – 1.30]	0.70 [0.70 – 1.20]	2.20 [1.20 – 3.70]	0.2 [0.2 – 0.7]
	Sensitivity (%/ $^\circ\text{C}$ )	0.60	0.54	0.70	0.44	-
	Marker % error (%)	0.05	0.15	0.11	0.09	-

We start by analysing the temperature sensitivity for each marker in natural waters. For two-colour( $\parallel$ ), two-colour( $\perp$ ) and depolarisation(A) markers, sensitivities from all natural samples were smaller or marginally greater than the ones found for ultrapure water (0.68%/°C, 0.62%/°C and 0.92%/°C, respectively). This is in agreement with the findings reported in [19], where lower sensitivities were reported in natural waters due to the fluorescence of optically active constituents. Here, the main purpose of using excitation at 473 nm was avoiding Chl-a fluorescence at 680 nm, as the water Raman peak for blue excitation lies around 560 nm. However, constituents other than Chl-a exhibit fluorescence peaks around 560 nm, including DOM and other photosynthetic pigments [18,20–22], and it is virtually impossible to avoid overlapping between the water Raman peak and all possible signal sources in natural waters. In [19], the presence of Chl-a fluorescence signals overlapping with the water Raman signals excited by green light (532 nm) led to higher signal counts and consequent higher SNRs, and lower % errors in the markers calculated for all-natural water sample. The same pattern was not so clearly identified in all natural water samples analysed in the present study using blue excitation, indicating that signal counts

were generally less impacted by the presence of fluorescence when using blue excitation. Comparisons between both studies, however, are limited due to the use of different natural water samples which will have particular optical characteristics. To allow for full comparison and reasoning regarding fluorescence impact in total signals, further investigations could be conducted in the future where the same natural sample is analysed by both green (532 nm) and blue (473 nm) Raman spectrometers.

RMSTE values varied from  $\pm 0.5^{\circ}\text{C}$  (two-colour(II), natural sample 4)) to  $\pm 7.1^{\circ}\text{C}$  (depolarisation(B), natural water sample 1). The two-colour(II) marker consistently delivered the best RMSTEs ( $\pm 0.5^{\circ}\text{C}$  to  $\pm 0.7^{\circ}\text{C}$ ) for all samples. Next was the depolarisation(A) marker, which delivered RMSTEs ranging from  $\pm 0.7^{\circ}\text{C}$  to  $\pm 1.3^{\circ}\text{C}$ . These were also the markers with highest temperature sensitivities found in this investigation. Depolarisation(B) exhibited consistent poor accuracies when predicting water temperature (RMSTEs higher than  $\pm 2.2^{\circ}\text{C}$ ) and was also the marker with lowest sensitivities in all water samples. This indicates that the temperature marker is not effectively extracting temperature information from Raman signals, and its use should be re-evaluated in future investigations.

The LC analyses resulted in average improvements in temperature accuracies of 47% when compared to the best RMSTE obtained using a single marker. Final accuracies after the LC method were equal or better than  $\pm 0.5^{\circ}\text{C}$  for all natural water samples under investigation, indicating the method was effective extracting meaningful temperature-dependent information from multiple markers.

#### 4. CONSIDERING THE RELATIVE MERITS OF SPECTROMETERS USING BLUE AND GREEN EXCITATION

The design of our multichannel LIDAR-compatible RS using blue excitation is conceptually similar to the RS reported in [19], which used a green excitation laser. In practice, the two excitation lasers differed, most notably in pulse energy, and the band pass filters defining the spectral channels also differed in regard to their width and their positions relative to the Raman band. In this section we compare the prospects for predicting water temperature using blue and green excitation, and we also evaluate the potential benefits that blue excitation might have when combined with LIDAR depth-resolved measurements. Table 4 summarises the key characteristics of the blue and green excitation lasers used here and in [19] respectively, along with the corresponding channel width, centre positions and wavelength bands, as well as the key findings for temperature prediction in Milli-Q water and in natural waters.

Table 4. Technical overview of two multichannel LIDAR-compatible RS integrated to 473 nm (blue) and 532 nm (green) excitation lasers. Data in brackets is based on the analysis of 4 datasets; data without brackets is based on the “average markers” dataset. Refer to section 2.2 for details.

	Blue multichannel RS	Green multichannel RS [19]
Excitation wavelength (nm)	473	532
Laser energy ( $\mu\text{J}/\text{pulse}$ )	5	25
Pulse duration at FWHM (ns)	1.5	0.9
Wavelength of Raman photons (nm)	550 – 575	630 – 660
Spectral channel widths ( $\text{cm}^{-1}$ )	254	315
	136	463
<b>Milli-Q water</b>		
Best sensitivity ( $\%/^{\circ}\text{C}$ ) [marker]	0.92 [depolarisation(A)]	0.68 [depolarisation(A)]
Best RMSTE ( $\pm^{\circ}\text{C}$ ) [marker]	0.5 [Two-colour(II)]	0.4 [Two-colour(II)]
RMSTE (LC)	0.3	0.3
<b>Natural water samples</b>		
Best sensitivity ( $\%/^{\circ}\text{C}$ ) [marker]	0.85 [depolarisation(A)]	0.59 [depolarisation(A)]
Best RMSTE ( $\pm^{\circ}\text{C}$ ) [marker]	0.5 [Two-colour(II)]	0.4 [Two-colour(II)]
RMSTE (LC)	0.2	0.3

We start our comparison by analysing the accuracies achieved by each equipment measuring natural water temperature in the laboratory. Predictions performed by the green multichannel RS exhibited maximum accuracy of  $\pm 0.4^{\circ}\text{C}$ , marginally higher than the RMSTEs achieved by the blue multichannel RS ( $\pm 0.5^{\circ}\text{C}$ ). In both cases, these accuracies were achieved by temperature predictions using two-colour(II) markers. Linear combination methods were effective in predicting temperature more accurately for both setups, with final accuracies of  $\pm 0.2^{\circ}\text{C}$  being found for the blue RS and  $\pm 0.3^{\circ}\text{C}$  for the green RS. These are the maximum accuracies ever reported for LIDAR-compatible Raman spectrometers predicting natural waters temperatures.

The key factors affecting RMSTEs are the intrinsic dependence of Raman spectra on temperature, and the errors and uncertainties associated with its measurement. In Milli-Q water, the measured sensitivities for the various markers reflect this dependence, plus the positions and widths of the spectral channels. According to simulations performed by [17] for ultrapure (Reverse-Osmosis) water, an optimum trade-off between Raman signals strength and RMSTEs would be obtained for acquisition channels with spectral widths of around  $200\text{ cm}^{-1}$ . Optimum spectral positions for such channels were explored using simulations in [25], with the “low shift” channel central position at  $3200\text{ cm}^{-1}$  and the “high shift” channel central position at  $3600\text{ cm}^{-1}$ . The availability of commercial Band Pass filters within these conditions is extremely limited, therefore the differences between spectral widths for channels collecting signals in the blue ( $254\text{ cm}^{-1}$  and  $136\text{ cm}^{-1}$ ) and green ( $315\text{ cm}^{-1}$  and  $463\text{ cm}^{-1}$ ) setups. Higher sensitivities for both setups were found for depolarisation(A) markers calculated from Raman signals scattered by Milli-Q water samples, with sensitivities of  $0.92\%/^{\circ}\text{C}$  found in the blue setup and  $0.59\%/^{\circ}\text{C}$  in the green.



These values found in both setups are in agreement with was proposed by the simulations in [17].

The errors and uncertainties associated with measurements performed on Milli-Q water originate from the SNR for each channel, and here the 5-times higher pulse energy of the green excitation laser, the higher Raman cross-section for blue excitation [24] and the characteristics of the band pass filters all contribute. As can be seen in table 4, despite the significant differences between the blue and green RS, the RMSTEs are remarkably similar for both cases. When it comes to natural waters, we can expect fluorescence signals arising from optically-active constituents such as DOM and photosynthetic pigments compromising the achievable RMSTE to some extent. As discussed earlier, the overlapping between the water Raman peak for this excitation and the chlorophyll-a peak at 680 nm is inevitable, reducing the accuracies that could be achieved by Raman signal analyses. Conversely, Raman photons from blue excitation have green wavelengths (550-575 nm), which exhibit good vertical transmission in water and do not overlap with the Chl-a peak; however, they are susceptible to other interactions with optically active constituents in water, such as DOM and phytoplankton.

The overlapping between the Raman peak for blue excitation and fluorescence from DOM has been previously assessed by other researchers [26,27], who used Artificial Neural Networks (ANN) to solve for DOM fluorescence in water Raman spectra. The authors of [26] created a database of Raman spectra excited by a blue laser (488 nm) acquired from water samples at different temperatures, salinities and DOM concentrations, which was used as reference by the ANN model. In the occasion, accuracies of  $\pm 0.8^\circ\text{C}$  were achieved for water temperature determination, and the model was able to neglect the overlapping between DOM and Raman peaks. Later, the authors of [27] conducted laboratory investigations of natural water samples using the same ANN model, achieving accuracies of up to  $\pm 0.1^\circ\text{C}$ . It is clear that ANN models are capable of minimising the effect of the overlap between DOM fluorescence and Raman peaks acquired with blue excitation; however, this approach requires complex data manipulation and is not compatible with rapid, LIDAR methods. In [18] we proposed a new technique for minimizing spectral baselines arising from fluorescence in natural waters named “correction by temperature markers”. In this method, Raman two-colour markers are calculated for a “standard” water sample (*i.e.* a water sample without optically active constituents interacting with the excitation light) and compared with Raman markers calculated for same temperature from signals scattered by natural waters. The premise of the method is that the differences between the markers values are due to fluorescence from natural water constituents, and accuracies of up to  $\pm 0.2^\circ\text{C}$  were achieved for temperature predictions in natural waters after the correction.

When it comes to considering the best excitation wavelength for combining our RS with LIDAR methods, there are additional facts to take into account. The number of Raman photons generated at a depth  $z$  and reaching the surface,  $N_{\text{Raman}}(z)$ , can be described by equation 9, which is based and adapted from theory presented in [15]. For simplicity, we have overlooked Fresnel reflections into and out of the water and assumed solid angles of collection sufficiently small so that the Raman photons reach the surface at near-normal angles of incidence.

$$N_{\text{Raman}}(z) = N_{\text{laser}}(z) N_{\text{scat}} \sigma_{\text{Raman}} \Delta R \frac{\Omega(z)}{n^2} T_{\lambda_1}(z) T_{\lambda_2}(z) \quad (9)$$

where  $N_{\text{laser}}(z)$  is the number of excitation laser photons at a given depth ( $z$ );  $N_{\text{scat}}$  is the density of water molecules interacting with the excitation light (molecules/m<sup>3</sup>);  $\sigma_{\text{Raman}}$  is the Raman scattering cross-section per molecule per steradian (m<sup>2</sup>/molecule sr);  $\Delta R$  is the minimum vertical range resolution, determined by the laser pulse duration (m);

$\Omega(z)$  is the solid angle of collection, dependent on the diameter of the telescope or other collection optics used (steradians) at a given depth;

$n$  is the refractive index of seawater;

$T_{\lambda 1}(z)$  and  $T_{\lambda 2}(z)$  are, respectively, the vertical transmission values for the excitation and Raman wavelengths in water ( $\text{m}^{-1}$ ). These are functions of  $T_{\lambda} = e^{-K_d z}$ , where  $K_d(\lambda)$  is the diffuse attenuation coefficient for light in water.

Modelling retrieval of Raman photons requires knowledge about the transmitter and receiver geometries and is beyond the scope of this paper. Here our purpose is to explore the relative benefit of using blue excitation, compared to green excitation. It is relatively straightforward to estimate the ratio of the expected Raman returns using blue or green excitation by considering only the terms in equation 9 that are wavelength-dependent. The ratio is calculated assuming same pulse energy and duration for both excitation wavelengths (equation 10).

$$\frac{N_{Raman}^{473}(z)}{N_{Raman}^{532}(z)} = \frac{\lambda^{473} \sigma_{Raman}^{473} e^{-((K_d^{473} + K_d^{568})z)}}{\lambda^{532} \sigma_{Raman}^{532} e^{-((K_d^{532} + K_d^{660})z)}} \quad (10)$$

The top section of table 5 provides typical values for the key LIDAR parameters ( $N_{laser}$ ,  $\Delta R$ ,  $N_{scat}$ ,  $\sigma_{Raman}$ ) and the wavelength-dependent parameters used to calculate equation 10. The bottom section of table 5 gives the calculated 1% extinction depths for blue and green excitation and the correspondent Raman wavelengths. These are calculated for three Jerlov water types. Jerlov water type I represents oceanic clear waters, and coastal waters were represented by types 1C (clear coastal water) and 7C (turbid coastal water). Raman cross-sections  $\sigma_{Raman}$  were calculated according to [24] for collection channels centred at 568 nm (for blue excitation) and 660 nm (for green excitation). These “high shift” channels were chosen because attenuation increases with increasing wavelength.

The transmissions of the excitation laser photons and returning Raman photons in the water column were estimated using the downwelling diffuse attenuation coefficient  $K_d(\lambda)$ . The values of  $K_d(\lambda)$  for Jerlov water types I, 1C and 7C were obtained from [28] and interpolated for the wavelengths of interest in our study.

Table 5. Input parameters for LIDAR modelling and outcomes for blue and green excitation lights in Jerlov water types I, 1C and 7C.

	<b>Blue (473 nm)</b>			<b>Green (532 nm)</b>		
$N_{laser}$ (photons/mJ)	$2.38 \times 10^{15}$			$1.34 \times 10^{16}$		
$\Delta R$ for typical 2 ns pulse (m)	0.5			0.5		
$N_{scat}$ (molecules/m <sup>3</sup> )	$4.32 \times 10^{20}$			$4.32 \times 10^{20}$		
$\sigma_{Raman}$ (m <sup>2</sup> /molecule sr)	$9.62 \times 10^{-30}$			$5.14 \times 10^{-30}$		
n	1.34			1.34		
Raman wavelength (nm)	568			660		
Coefficients of light attenuation in water (m <sup>-1</sup> )	I	1C	7C	I	1C	7C
$K_d$ (excitation)	0.020936	0.141501	0.724552	0.056522	0.125776	0.454200
$K_d$ (Raman)	0.067273	0.126629	0.363474	0.373014	0.481169	0.701930
<b>Model outcomes</b>						
Calculated 1% extinction depth for excitation laser (m)	> 150	49	9.5	122.5	55	15
Calculated 1% extinction depth for Raman photons (m)	68.5	36.5	12.5	12.5	10	6.5

The depths of extinction (1% of incident light) for excitation and Raman photons varied between different Jerlov water types. For excitation light, blue light exhibited better transmission in waters type I (oceanic clear) and 1C (coastal clear); in contrast, green light had better transmission in turbid coastal waters (type 7C) in comparison with blue. For Raman returns the depths of extinction of photons at 568 nm (for blue excitation) were always greater than for 660 nm (for green excitation). Bigger differences were found in type I (factor of 5), lesser differences in type 1C (factor of 3) and small differences in type 7C (factor of 2).

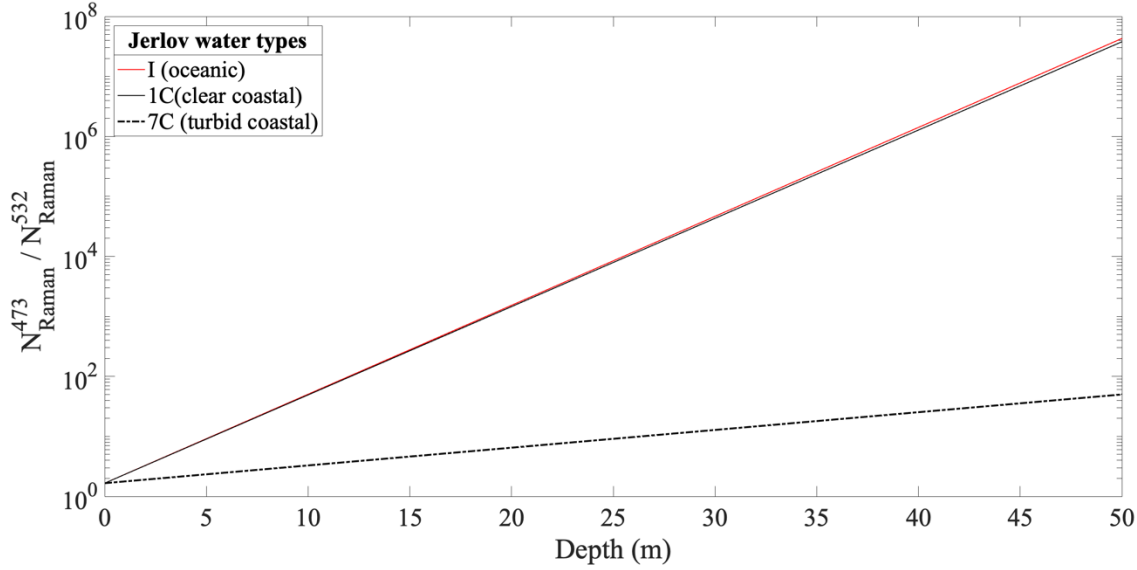


Figure 6. The ratio given in equation 10 is plotted as a function of depth ( $z$ ) for Jerlov water types: oceanic type I, and coastal types 1C and 7C.

Figure 6 shows the ratio of expected Raman returns under blue vs green excitation, as a function of depth. The ratio is always greater than 1, due to the higher Raman cross-section when blue excitation is used (factor approaching two), and the ratio increases exponentially with increasing depth. Large and very similar ratios were calculated for types I and 1C, indicating big benefits to using blue excitation, mainly due to the combination of better excitation/Raman transmissions in water. The use of blue light, however, exhibited somewhat smaller advantages for type 7C, where the much higher transmission of Raman photons (568 nm vs 660 nm) is offset by the higher transmission of green excitation compared to blue. While this model is a rudimentary one, it clearly indicates the benefits of using blue excitation, predicting much greater Raman returns and therefore higher potential to determine subsurface water temperatures with reasonable accuracies. More sophisticated modelling would be required to calculate actual Raman returns and to predict the depth at which subsurface water temperature could be determined.

## 5. CONCLUSION

We have presented the design and performance of a custom-built multichannel Raman spectrometer integrated to a 473 nm pulsed laser, employing commercial optical filters to collect polarised Raman signals at spectral regions of interest for the remote sensing of natural water temperature. Our spectrometer design is LIDAR-compatible and comprised of (1) a pulsed laser source with period  $\leq 2$  ns at the FWHM, to allow for depth resolutions better than 0.5 m; (2) collection of Raman signals at spectral regions highly sensitive to changes in temperature; (3) fast, sensitive detection by photomultipliers.

This was the first time that polarised Raman signals scattered from blue excitation (473 nm) were acquired in spectral channels for samples of natural waters and temperature was determined with accuracies as high as  $\pm 0.5^\circ\text{C}$ . The simultaneous acquisition of Raman signals in four channels at different polarisation states and wavelength ranges allowed for calculation of different types of temperature markers. Two-colour(II) (from parallel-polarised Raman signals) and depolarisation(A) (calculated from signals of different polarisation states) exhibited best performances when predicting water temperature, followed by two-colour( $\perp$ ) and depolarisation(B). When all four markers were incorporated

in the linear combination model, enhanced RMSTEs up to  $\pm 0.2^{\circ}\text{C}$  were achieved. Those RMSTEs were similar to values reported in previous studies for green excitation [19].

Lastly, we have presented a simple model which predicts substantially higher Raman returns when blue excitation is used. The use of blue light is beneficial to our final goal of rapidly profiling the water column temperature by using a LIDAR-compatible system. The advantages over green light, traditionally used in oceanographic studies, include: (1) reduced spectral overlapping between Raman and fluorescence peak from chlorophyll-a at 680 nm; (2) higher Raman returns due to lower attenuation coefficients and higher Raman cross-sections.

## 6. REFERENCES

1. IPCC, *Summary for Policymakers* (2014).
2. T. D. Dickey, "A vision of oceanographic instrumentation and technologies in the early twenty-first century," in *Oceans 2020*, J. G. Field, G. Hempl, and C. P. Summerhayes, eds. (Island Press, 2002), pp. 209–254.
3. W. G. Rees, *Physical Principles of Remote Sensing*, second (Cambridge University Press, 2001).
4. M. Solan, J. D. Germano, D. C. Rhoads, C. Smith, E. Michaud, D. Parry, F. Wenzhöfer, B. Kennedy, C. Henriques, E. Battle, D. Carey, L. Iocco, R. Valente, J. Watson, and R. Rosenberg, "Towards a greater understanding of pattern, scale and process in marine benthic systems: A picture is worth a thousand worms," *J. Exp. Mar. Bio. Ecol.* **285–286**, 313–338 (2003).
5. B. Breschi, G. Cecchi, L. Pantani, V. Raimondi, D. Tirelli, and G. Valmori, "Measurement of Water Column Temperature by Raman Scattering," *EARsel Adv. Remote Sens.* **1**(2), 131–134 (1992).
6. A. Soloviev and R. Lukas, *The Near-Surface Layer of the Ocean*, Atmospheric and Oceanographic Sciences Library (Springer Netherlands, 2014), **48**.
7. R. J. W. Brewin, L. de Mora, O. Billson, T. Jackson, P. Russell, T. G. Brewin, J. D. Shutler, P. I. Miller, B. H. Taylor, T. J. Smyth, and J. R. Fishwick, "Evaluating operational AVHRR sea surface temperature data at the coastline using surfers," *Estuar. Coast. Shelf Sci.* **196**, 276–289 (2017).
8. J. H. Churnside, "Polarization effects on oceanographic lidar.," *Opt. Express* **16**(2), 1196–1207 (2008).
9. H. R. Gordon, "Interpretation of airborne oceanic lidar: effects of multiple scattering.," *Appl. Opt.* **21**(16), 2996–3001 (1982).
10. H. R. Gordon, ed., "Ocean remote sensing using lasers," in (1980).
11. D. M. Carey and G. M. Korenowski, "Measurement of the Raman spectrum of liquid water," *J. Chem. Phys.* **108**(7), 2669–2675 (1998).
12. G. E. Walrafen, M. R. Fisher, M. S. Hokmabadi, and W.-H. Yang, "Temperature dependence of the low- and high-frequency Raman scattering from liquid water," *J. Chem. Phys.* **85**(12), 6970–6982 (1986).
13. D. N. Whiteman, G. E. Walrafen, W. H. Yang, and S. H. Melfi, "Measurement of an isosbestic point in the Raman spectrum of liquid water by use of a backscattering geometry.," *Appl. Opt.* **38**(12), 2614–2615 (1999).
14. C. H. Chang and L. A. Young, *Seawater Temperature Measurement from Raman Spectra* (1972).
15. D. A. Leonard, B. Caputo, and F. E. Hoge, "Remote sensing of subsurface water temperature by Raman scattering," *Appl. Opt.* **18**(11), 1732–45 (1979).
16. D. A. Leonard and B. Caputo, "Raman Remote Sensing Of The Ocean Mixed-Layer Depth," *Opt. Eng.* **22**(3), (1983).

17. C. P. Artlett and H. M. Pask, "Optical remote sensing of water temperature using Raman spectroscopy," *Opt. Express* **23**(25), 31844 (2015).
18. A. de Lima Ribeiro, C. Arlett, P. Ajani, C. Derkenne, and H. Pask, "Manuscript 1. "The impact of fluorescence on Raman remote sensing of temperature in natural water samples"", To be Submitt. to *Opt. Express* (n.d.).
19. A. de Lima Ribeiro, C. Artlett, and H. Pask, "Manuscript 2."A LIDAR-compatible, multichannel Raman spectrometer for remote sensing of water temperature"", To be Submitt. to *Sensors* (n.d.).
20. C. Lin, "Tunable laser induced scattering from coastal water," *IEEE Trans. Geosci. Remote Sens.* **37**(5), 2461–2468 (1999).
21. J. E. James, C. S. Lin, and W. P. Hooper, "Simulation of laser-induced light emissions from water and extraction of Raman signal," *J. Atmos. Ocean. Technol.* **16**(2–3), 394–401 (1999).
22. C. S. Lin, "Characteristics of laser-induced inelastic-scattering signals from coastal waters," *Remote Sens. Environ.* **77**(1), 104–111 (2001).
23. N. G. Jerlov, ed., *Optical Oceanography*, 1st editio (Elsevier, 1968).
24. G. W. Faris and R. A. Copeland, "Wavelength dependence of the Raman cross section for liquid water," *Appl. Opt.* **36**(12), 2686 (1997).
25. C. P. Artlett and H. M. Pask, "New approach to remote sensing of temperature and salinity in natural water samples," *Opt. Express* **25**(3), 2840 (2017).
26. T. Dolenko, S. Burikov, A. Sabirov, and V. Fadeev, "Remote determination of temperature and salinity in presence of dissolved organic matter in natural waters using laser spectroscopy," *EARSeL eProceedings* **10**(2), 159–165 (2011).
27. A. Vervalde, E. Mazurin, and I. Plastinin, "Simultaneous Determination of Temperature and Salinity of Natural Waters By Raman Spectra Using," (1), 28–36 (2015).
28. M. G. Solonenko and C. D. Mobley, "Inherent optical properties of Jerlov water types," *Appl. Opt.* **54**(17), 5392 (2015)

## 5.2. Acquisition overview

Raman signal acquisitions using our multichannel RS (blue, 473 nm excitation) were performed for a Milli-Q water sample. The temperature-dependent signals are shown in figure 5.1.

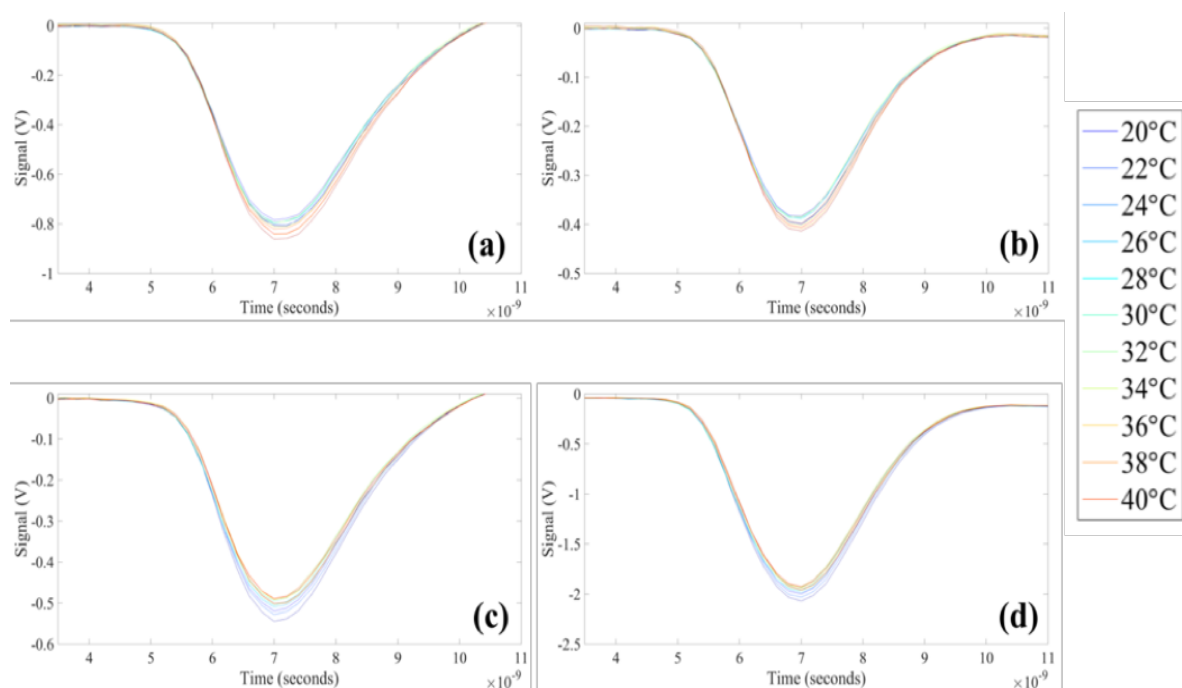


Figure 5.1. Raman signal acquisition by overview for a Milli-Q (473 nm excitation). “High shift” channels: (a) parallel-polarised and (b) perpendicularly-polarised; “low shift” channels: (c) parallel-polarised and (d) perpendicularly-polarised

As previously discussed in section 4.2, it is not possible to compare the signal *intensities* registered in each channel, as the Band Pass filters used in our RS had different bandwidths; nevertheless, it is possible to make a *qualitative* comparison regarding the general response of the Raman signals to changes in temperature. For all water samples analysed in this study, higher signal counts were associated with high temperatures for channels collecting signals at the low Raman shift (figures 5.1a-b); contrariwise, higher signal intensities collected by “high shift” channels were associated with lower temperatures (figures 5.1c-d). This inversion in the general temperature-dependent behaviour of the Raman signal in channels across the isosbestic point was also identified in the Raman spectra [63].

### 5.3. A more comprehensive analysis of temperature markers and their usefulness

In manuscript 3 [115], I showed accuracies (RMSTEs) for averaged temperature markers as a synopsis of my research; nevertheless, results from three other independent acquisitions (datasets) were not included in the final manuscript. This section is dedicated to presenting the RMSTEs found for all datasets collected from ultrapure (Milli-Q) and natural water samples; furthermore, I will expand the discussion and evaluate which of the markers is more suitable for predicting water temperature from Raman signals acquired by my multichannel RS (blue excitation).

As discussed in section 4.3., standard deviations were calculated for RMSTEs found for markers sets 1,2,3 and also calculated using “average markers”, these being an average of the markers values calculated for the datasets abovementioned. Regardless the need of more datasets for a complete and meaningful numerical analysis, the standard deviation is useful for a preliminary assessment of replicability of temperature predictions by the same marker.

RMSTEs and their respective standard deviations for markers calculated from water samples analysed in manuscript 3 [115] are shown in tables 5.1-5.5 and in figures 5.2-5.6. Accuracies smaller or equal to  $\pm 0.5^{\circ}\text{C}$  are indicated in green; accuracies between  $\pm 0.6^{\circ}\text{C}$  and  $\pm 1.0^{\circ}\text{C}$  are shown in blue; from  $\pm 1.1^{\circ}\text{C}$  to  $2.0^{\circ}\text{C}$  are presented in yellow; and RMSTEs bigger than  $\pm 2.0^{\circ}\text{C}$  are indicated in red. This data is presented both graphically and in tabulated form on the following pages.



## Milli-Q water sample

Table 5.1. RMSTEs for two-colour and depolarisation markers calculated for a Milli- Q water sample (multichannel RS, 473 nm excitation).

Temperature Markers	RMSTE using Dataset 1 ( $\pm^{\circ}\text{C}$ )	RMSTE using Dataset 2 ( $\pm^{\circ}\text{C}$ )	RMSTE using Dataset 3 ( $\pm^{\circ}\text{C}$ )	RMSTE using “average markers” ( $\pm^{\circ}\text{C}$ )	RMSTE standard deviation ( $\pm^{\circ}\text{C}$ )
Two-colour( $\parallel$ )	0.6	0.7	0.6	0.5	$\pm 0.08$ ( $<0.1$ )
Two-colour( $\perp$ )	1.6	1.6	1.0	0.7	$\pm 0.45$
Depolarisation(A)	0.5	0.6	0.6	0.5	$\pm 0.10$
Depolarisation(B)	2.5	2.5	3.5	3.2	$\pm 0.50$

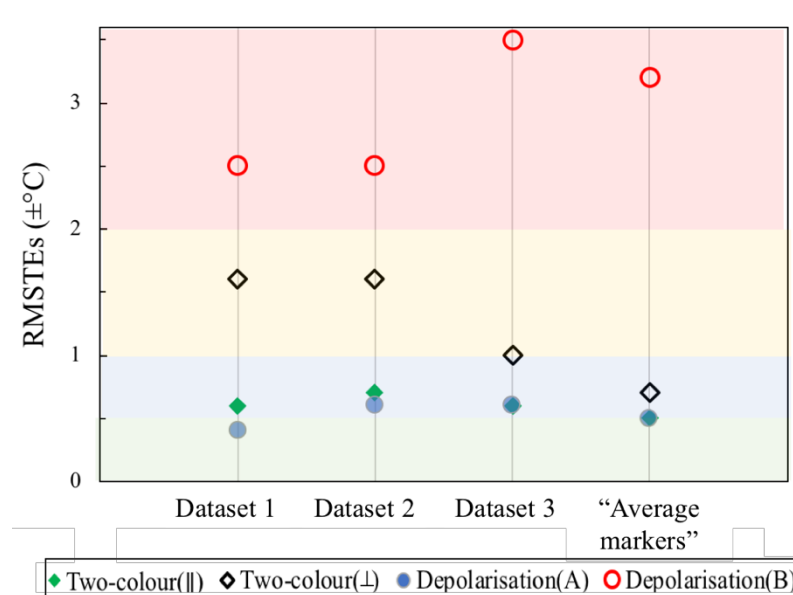


Figure 5.2. Graphical representation of the data in Table 5.1.

## Key observations – Milli Q water sample

- Best RMSTE of  $\pm 0.5^{\circ}\text{C}$  was found for the “average markers” dataset for both two-colour( $\parallel$ ) and depolarisation(A).
- Two-colour( $\perp$ ) markers exhibited RMSTEs  $< \pm 2.0^{\circ}\text{C}$ .
- Depolarisation(B) markers had RMSTE  $\geq 2.5^{\circ}\text{C}$ .
- Standard deviations for two-colour( $\parallel$ ) and depolarisation(A) markers were within  $\pm 0.1^{\circ}\text{C}$ , showing consistency between temperature predictions.
- Standard deviations for Two-colour( $\perp$ ) and depolarisation(B) markers were found to be  $\leq \pm 0.50^{\circ}\text{C}$ .

## Natural water sample 1

Table 5.2. RMSTEs for two-colour and depolarisation markers calculated for natural water sample 1 (multichannel RS, 473 nm excitation).

Temperature markers	RMSTE using Data set 1 ( $\pm^{\circ}\text{C}$ )	RMSTE using Data set 2 ( $\pm^{\circ}\text{C}$ )	RMSTE using Data set 3 ( $\pm^{\circ}\text{C}$ )	RMSTE using the average of 3 markers ( $\pm^{\circ}\text{C}$ )	RMSTE Standard deviation
Two-colour( $\parallel$ )	0.8	0.8	0.8	0.7	$\pm 0.05$ ( $<0.1$ )
Two-colour( $\perp$ )	2.4	2.6	1.9	1.5	$\pm 0.50$
Depolarisation(A)	1.2	1.7	1.4	1.3	$\pm 0.22$
Depolarisation(B)	4.7	5.4	4.8	7.2	$\pm 1.11$

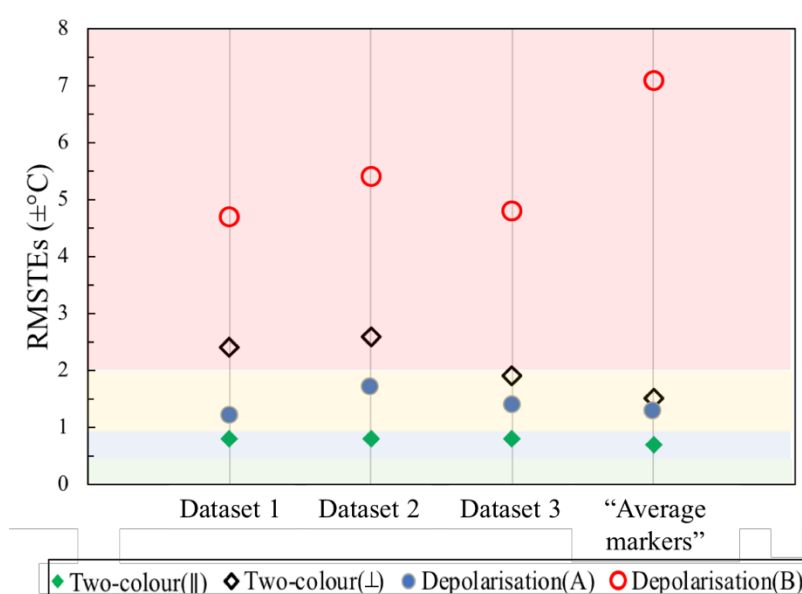


Figure 5.3. Graphical representation of the data in Table 5.2.

## Key observations – Natural water sample 1

- Best RMSTE of  $\pm 0.7^{\circ}\text{C}$  was found for the “average markers” dataset for two-colour( $\parallel$ ) markers. Best consistency between measurements was also found for two-colour( $\parallel$ ) (standard deviation  $< \pm 0.1^{\circ}\text{C}$  among datasets).
- Depolarisation(A) exhibited RMSTEs  $\leq \pm 1.7^{\circ}\text{C}$ .
- Two-colour( $\perp$ ) markers exhibited RMSTEs  $\leq \pm 2.6^{\circ}\text{C}$ .
- Depolarisation(B) markers exhibited poor RMSTEs of  $\leq \pm 7.2^{\circ}\text{C}$  and poor consistency between measurements (standard deviation of  $\pm 1.11^{\circ}\text{C}$  for the given datasets).

## Natural water sample 2

Table 5.3. RMSTEs for two-colour and depolarisation markers calculated for natural water sample 2 (multichannel RS, 473 nm excitation).

Temperature Markers	RMSTE using Dataset 1 ( $\pm^{\circ}\text{C}$ )	RMSTE using Dataset 2 ( $\pm^{\circ}\text{C}$ )	RMSTE using Dataset 3 ( $\pm^{\circ}\text{C}$ )	RMSTE using “average markers” ( $\pm^{\circ}\text{C}$ )	RMSTE standard deviation ( $\pm^{\circ}\text{C}$ )
Two-colour( $\parallel$ )	1.0	0.8	0.8	0.7	$\pm 0.11$
Two-colour( $\perp$ )	1.9	1.8	2.0	1.2	$\pm 0.35$
Depolarisation(A)	1.6	1.1	1.7	1.3	$\pm 0.21$
Depolarisation(B)	5.4	5.5	5.6	2.3	$\pm 1.40$

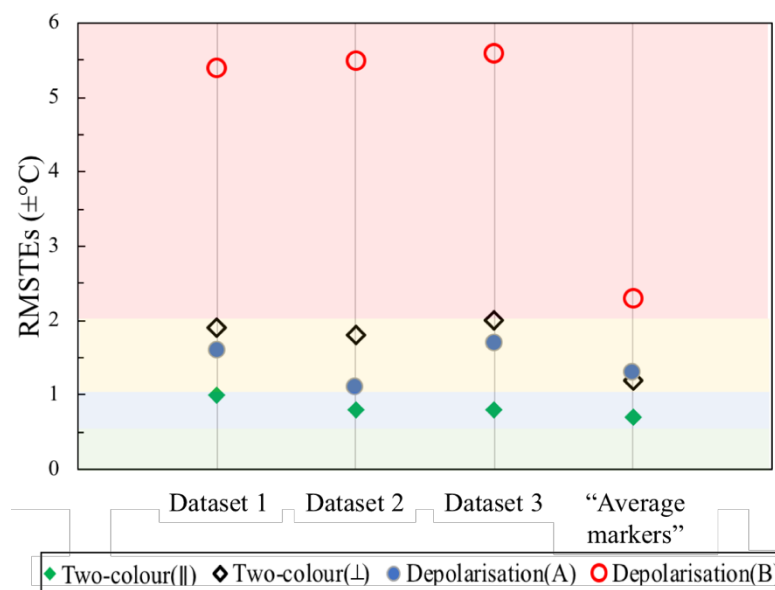


Figure 5.4. Graphical representation of the data in Table 5.3.

## Key observations – Natural water sample 2

- Best RMSTE ( $\pm 0.7^{\circ}\text{C}$ ) was found for the “average markers” dataset for two-colour( $\parallel$ ) markers. Best consistency between measurements was also found for two-colour( $\parallel$ ) (standard deviation  $\pm 0.11^{\circ}\text{C}$  among datasets).
- Two-colour( $\perp$ ) and depolarisation(A) markers exhibited RMSTEs  $\leq \pm 2.0^{\circ}\text{C}$ .
- Depolarisation(B) markers exhibited poor RMSTEs ( $\leq \pm 5.6^{\circ}\text{C}$ ) and poor consistency between measurements (standard deviation of  $\pm 1.40^{\circ}\text{C}$  for the given datasets).

### **Natural water sample 3**

Table 5.4. RMSTEs for two-colour and depolarisation markers calculated for natural water sample 3 (multichannel RS, 473 nm excitation).

Temperature markers	RMSTE using Data set 1 ( $\pm^{\circ}\text{C}$ )	RMSTE using Data set 2 ( $\pm^{\circ}\text{C}$ )	RMSTE using Data set 3 ( $\pm^{\circ}\text{C}$ )	RMSTE using the average of 3 markers ( $\pm^{\circ}\text{C}$ )	RMSTE Standard deviation
Two-colour( $\parallel$ )	0.7	1.1	0.5	0.7	$\pm 0.22$
Two-colour( $\perp$ )	1.5	1.5	1.3	0.9	$\pm 0.25$
Depolarisation(A)	1.0	1.0	0.8	0.8	$\pm 0.10$
Depolarisation(B)	3.7	5.6	4.9	4.9	$\pm 0.68$

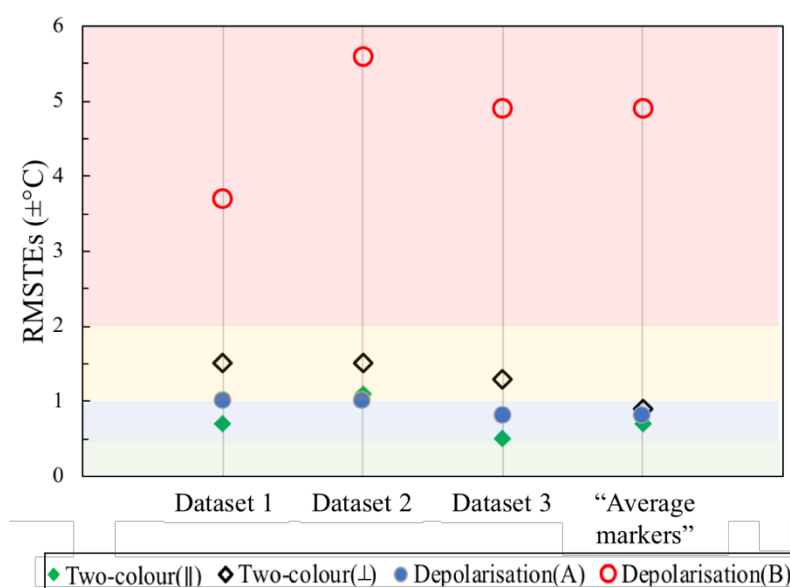


Figure 5.5. Graphical representation of the data in Table 5.4.

### **Key observations – Natural water sample 3**

- Best RMSTE ( $\pm 0.5^{\circ}\text{C}$ ) was found for two-colour( $\parallel$ ) markers, dataset 3.
- Two-colour( $\perp$ ) and depolarisation(A) markers exhibited RMSTEs  $< \pm 1.0^{\circ}\text{C}$ .
- Depolarisation(A) markers exhibited best consistency between datasets, with a standard deviation of  $\pm 0.1^{\circ}\text{C}$ .
- Depolarisation(B) markers exhibited poor RMSTEs ( $\leq \pm 5.6^{\circ}\text{C}$ ) and poor consistency between predictions (standard deviation of  $\pm 0.68^{\circ}\text{C}$  for the given datasets).

## **Natural water sample 4**

Table 5.5. RMSTEs for two-colour and depolarisation markers calculated for natural water sample 4 (multichannel RS, 473 nm excitation).

Temperature markers	RMSTE using Data set 1 ( $\pm^{\circ}\text{C}$ )	RMSTE using Data set 2 ( $\pm^{\circ}\text{C}$ )	RMSTE using Data set 3 ( $\pm^{\circ}\text{C}$ )	RMSTE using the average of 3 markers ( $\pm^{\circ}\text{C}$ )	RMSTE Standard deviation
Two-colour( $\parallel$ )	0.8	0.6	0.7	0.5	$\pm 0.17$
Two-colour( $\perp$ )	1.3	0.9	1.0	0.8	$\pm 0.21$
Depolarisation(A)	1.2	1.1	0.8	0.7	$\pm 0.23$
Depolarisation(B)	1.2	3.7	3.0	2.2	$\pm 1.10$

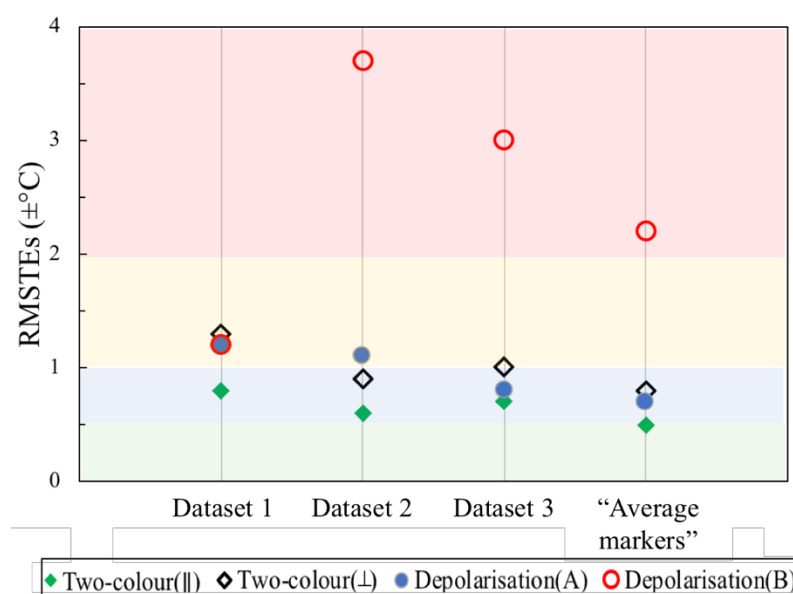


Figure 5.6. Graphical representation of the data in Table 5.5.

## **Key observations – Natural water sample 4**

- Best RMSTE ( $\pm 0.5^{\circ}\text{C}$ ) was found for the “average markers” dataset for two-colour( $\parallel$ ) markers. Two-colour( $\parallel$ ) also exhibited best consistency between measurements (standard deviation of  $\pm 0.17^{\circ}\text{C}$ ).
- Three temperature predictions performed with two-colour( $\perp$ ) exhibited accuracies better than  $\pm 1.0^{\circ}\text{C}$ .
- Depolarisation(A) markers exhibited RMSTEs of up to  $\pm 0.7^{\circ}\text{C}$  for the “average markers” dataset, with standard deviation of  $\pm 0.23^{\circ}\text{C}$  between measurements.
- Depolarisation(B) markers exhibited poor RMSTEs ( $\leq \pm 3.7^{\circ}\text{C}$ ) and poor consistency between predictions (standard deviation of  $\pm 1.1^{\circ}\text{C}$  for the given datasets).

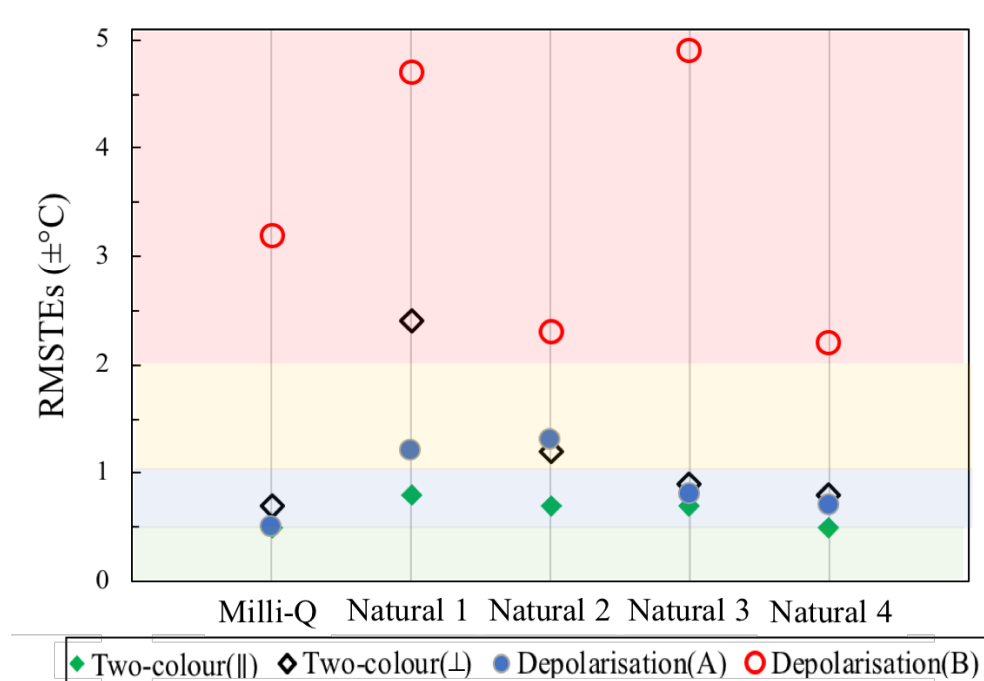


Figure 5.7. RMSTEs calculated from the “average markers” dataset for each of the water samples analysed.

An overview of RMSTEs acquired for the “average markers” dataset is represented in figure 5.7. Considering all temperature predictions for both Milli-Q and natural water samples, the effectiveness of each maker can be listed as it follows:

- i) Two-colour(∥)
- ii) Depolarisation(A)
- iii) Two-colour(⊥)
- iv) Depolarisation(B)

## **Discussion**

Temperature predictions performed with 64 Raman markers were presented in the previous tables and figures, allowing for an overview of all accuracies achieved by my experiments conducted with the blue multichannel RS. I start the discussion by summarising the main findings of the abovementioned tables and figures:

Considering all water samples, best accuracies were always achieved by two-colour( $\parallel$ ) predictions. This is in agreement with the findings reported in [114] for our green multichannel RS and indicate the marker as a logical choice to be used in future investigations.

For Milli-Q water, both two-colour( $\parallel$ ) and depolarisation(A) markers exhibited minimum RMSTEs of  $\pm 0.5^\circ\text{C}$ . Our measurements can be directly compared with the findings reported in [114] and Chapter 4, which explored the performance of our green multichannel RS. We start our comparison by analysing two-colour( $\parallel$ ) markers, which achieved accuracies of  $\pm 0.4^\circ\text{C}$  for experiments conducted with the green multichannel RS and  $\pm 0.5^\circ\text{C}$  for the blue multichannel RS analysis. This indicates marginally better accuracies for the green setup, which can be attributed to technical differences between instruments such as higher laser power, less beam divergence for the green laser, etc. Regarding depolarisation(A) markers, however, the accuracy of  $\pm 0.5^\circ\text{C}$  found for the blue multichannel RS prediction was superior to the findings achieved by using the green multichannel RS ( $\pm 0.8^\circ\text{C}$ ). This was the first time accuracies as high as  $\pm 0.5^\circ\text{C}$  were achieved by depolarisation markers calculated from Raman signals collected in spectral channels. Two-colour( $\perp$ ) exhibited optimum accuracy of  $\pm 0.7^\circ\text{C}$  for the “average markers” dataset, better to the  $\pm 1.5^\circ\text{C}$  achieved by our green multichannel RS reported in [114]. Generally, considering two-colour( $\parallel$ ), two-colour( $\perp$ ) and depolarisation(A) measurements, water temperature predictions for the Milli-Q sample resulted in accuracies better or equal to  $\pm 1.6^\circ\text{C}$ .

Temperature predictions in natural water samples by two-colour( $\parallel$ ) markers exhibited consistently more accurate results than any other marker, as also found for measurements made with our green multichannel RS [114]. The best consistency/repeatability of measurements was also found for two-colour( $\parallel$ ) measurements, closely followed by depolarisation(A) markers.

The poor accuracies (generally  $> \pm 2.0^{\circ}\text{C}$ ) obtained from depolarisation(B) measurements in all water samples are indicative that the marker is not efficiently extracting temperature information from the Raman signals. The marker also exhibited poor repeatability of measurements, which can clearly be seen by the high standard deviation values found in all measurements ( $> \pm 0.5^{\circ}\text{C}$ ).

The findings from RMSTE analyses led to the conclusion that two temperature markers stood out as potential methods for water temperature prediction: two-colour(II) and depolarisation(A). However, Linear Combination (LC) models can be used for enhancing accuracies of temperature predictions from Raman markers and exhibit optimum performance when using the 4 markers, as discussed in section 4.4. Furthermore, the current 4-channel configuration of our blue multichannel Raman spectrometer enables the calculation of these 4 temperature markers, regardless their use in LC models or not. In the future, we hope to evaluate if adding more channels to the RS (and, consequently, allowing for calculation of a bigger number of temperature markers) compensates the lower SNRs for each channel due to further division of Raman signals.



## 5.4. Markers sensitivities in natural water samples

Temperature sensitivities for the Milli-Q water sample were calculated for the “average markers” dataset and presented in manuscript 3 [115], indicating the percentage change in the temperature markers per °C (%/°C). A maximum sensitivity of 0.98%/°C was found for the mean-scaled depolarisation(A) marker, whilst minimum sensitivity of 0.38%/°C was calculated for mean-scaled depolarisation(B) marker.

As previously discussed in section 4.5., sensitivities calculated for ultrapure water are assumed to be associated with changes in temperature *only*, whilst sensitivities estimated for Raman markers in natural waters are further influenced by the presence of signals arising from interactions between the excitation/emission photons and other optically active constituents. This section is dedicated to exploring the temperature sensitivities associated with mean-scaled Raman markers calculated for different natural water samples, collected on different occasions from Sydney Harbour. A linear relationship between temperature and the mean-scaled “average markers” dataset was calculated, and sensitivities were extracted from the slope of this linear model, as described in Chapter 2. Sensitivity results for all four natural waters analysed in this study are shown in figures 5.8-5.11.

Two-colour(II) markers exhibited the best temperature predictions in this study (RMSTEs), as seen in section 5.4. Sensitivity information for mean-scaled two-colour(II) markers was calculated for all water samples (figure 5.8), with values varying from 0.60%/°C (natural sample 4) to 0.71%/°C (natural sample 3); for the Milli-Q water sample, sensitivity values were calculated to be 0.68%/°C, marginally smaller than maximum found for natural sample 3 and natural water sample 1, but larger than or comparable to values for all other water samples.

Natural water sample 4 exhibited the lowest sensitivity found for the two-colour(II) analysis (0.60%/°C), and also a relatively high percentage error; however, high accuracies of  $\pm 0.5^{\circ}\text{C}$  were achieved for temperature predictions using the “average markers” for this sample. In this instance, it is possible to list a series of factors which might have had contributed to this scenario, such as: (1) fluctuations in the laser power; (2) presence of scatterers in the sample (Mie scattering) diverting Raman photons away from the detectors; (3) the averaging of markers had a higher impact on RMSTEs for this sample, when compared to others.

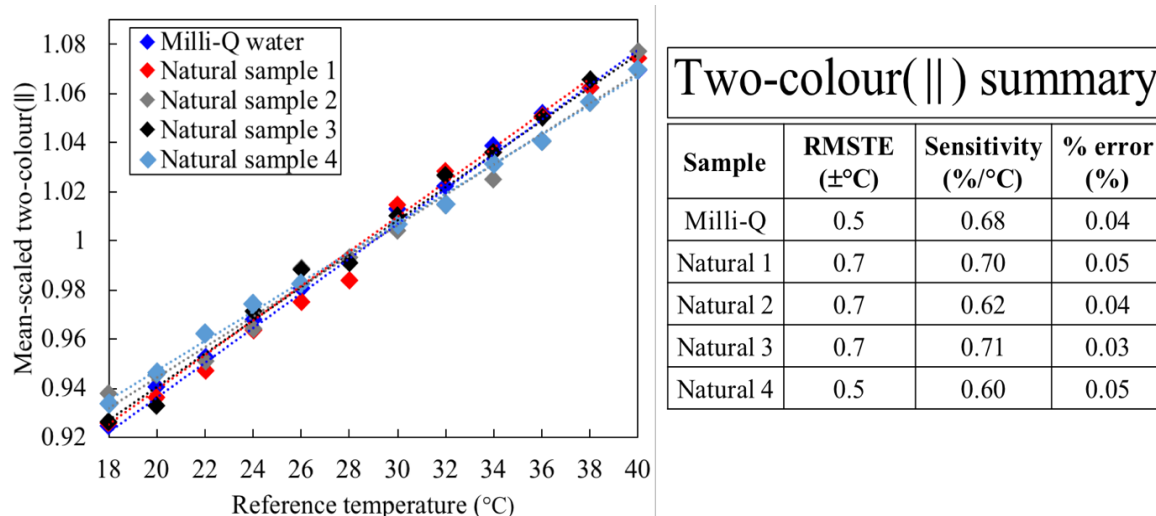


Figure 5.8. Mean-scaled temperature sensitivity data for the two-colour(II) marker. All water samples.

Using the two-colour( $\perp$ ) marker, best RMSTEs were associated with maximum sensitivities for Milli-Q water sample, respectively  $\pm 0.7^{\circ}\text{C}$  and  $0.62\%/^{\circ}\text{C}$  (figure 5.9). For natural waters, maximum accuracies and sensitivities of  $\pm 0.8^{\circ}\text{C}$  and  $0.60\%/^{\circ}\text{C}$  were achieved for sample 4.

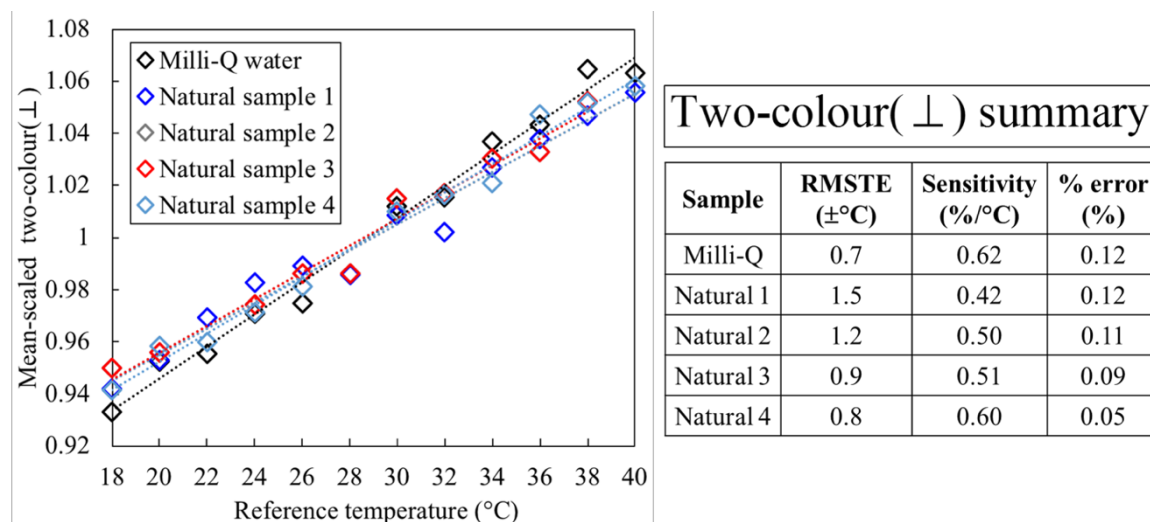


Figure 5.9. Mean-scaled temperature sensitivity data for the two-colour( $\perp$ ) marker. All water samples.

Depolarisation(A) was the marker which achieved highest sensitivity values among the four temperature markers estimated for each water sample (figure 5.10). For Milli-Q water sample, a sensitivity of  $0.92\%/^{\circ}\text{C}$  was found to be associated with RMSTE of  $\pm 0.5^{\circ}\text{C}$ , whilst the best sensitivities and accuracies among natural waters were found in sample 4 ( $0.70\%/^{\circ}\text{C}$  and  $\pm 0.7^{\circ}\text{C}$ , respectively).

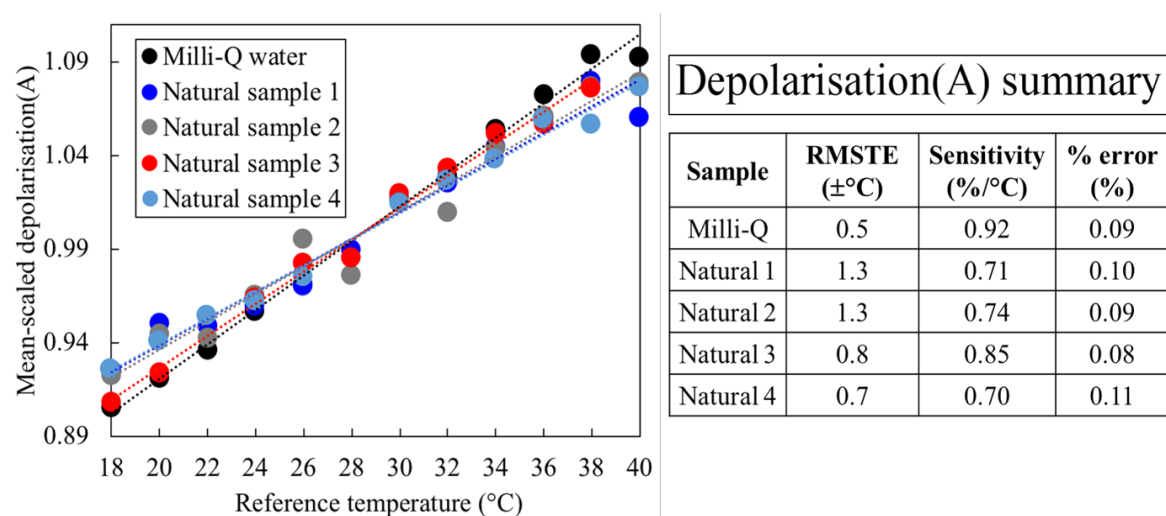


Figure 5.10. Mean-scaled temperature sensitivity data for the depolarisation(A) marker. All water samples.

Finally, sensitivity analysis for depolarisation(B) markers revealed poor sensitivities (smaller than  $0.5\%/^{\circ}\text{C}$ ) and indicate, along with the RMSTE values, that the marker was the least effective when extracting temperature from both natural and ultrapure water samples (figure 5.11).

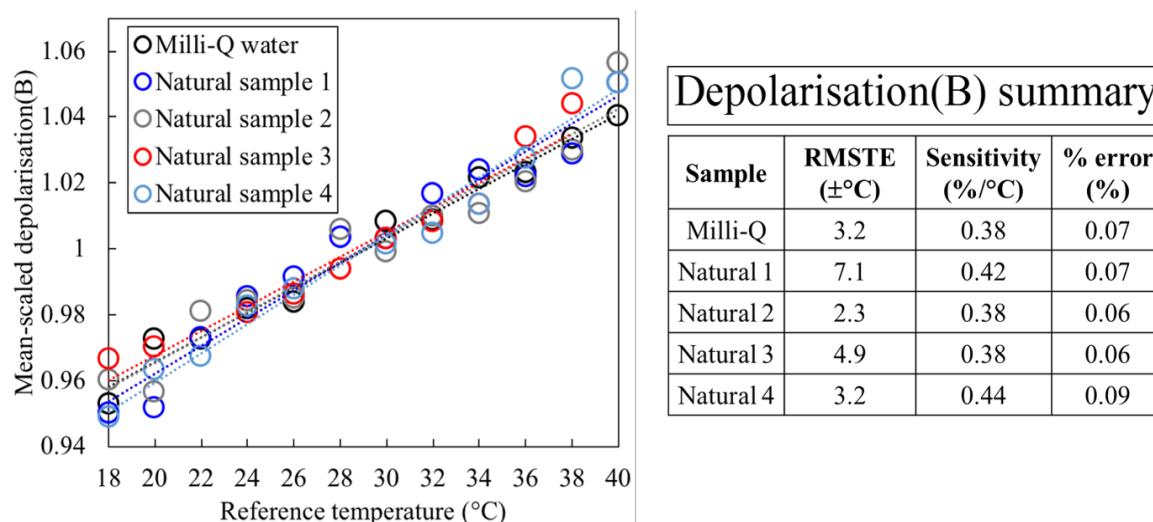


Figure 5.11. Mean-scaled temperature sensitivity data for the depolarisation(B) marker. All water samples.

As discussed in section 4.5, final accuracies (RMTEs) for temperature predictions by Raman markers are associated with a trade-off between markers sensitivities and % errors derived from SNRs. For these particular water sample analyses, depolarisation(B) markers exhibited poor performance for both RMSTEs and sensitivities, which would also impact this trade-off (between % errors and sensitivities). In order to explore this proposition for blue excitation, ratios between % errors and sensitivities were calculated with and without depolarisation(B) markers and are shown in figures 5.12a and 5.12b, respectively.

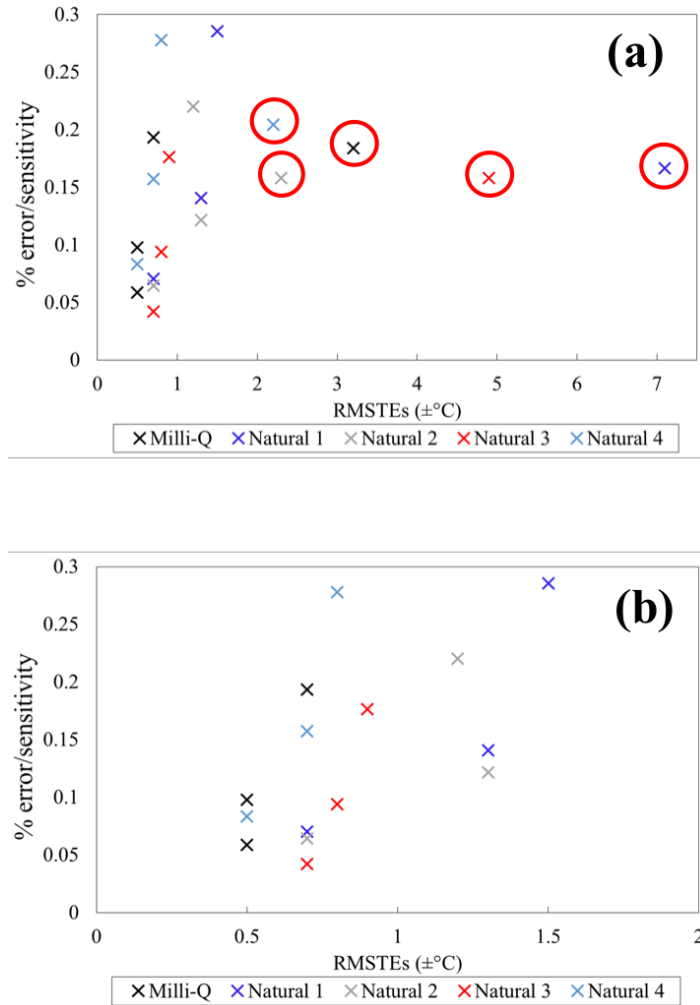


Figure 5.12. Ratios of % error to sensitivity vs RMSTEs for natural and ultrapure water sample including (a) all four markers calculated for each sample; (b) all markers calculated for each sample, except depolarisation(B). Possible outliers are circled in red.

It can be seen in figure 5.12a that the ratios of % errors to marker sensitivities exhibited a clustering which suggests a roughly linear relationship with RMSTEs. However, five data points (circled in red) clearly deviate from this tendency. They all correspond to depolarisation(B) markers for each water sample under analysis, endorsing the proposition that this marker is not extracting meaningful temperature information from Raman signals, as it has been previously discussed in section 5.4. In order to better visualize the data distribution without influence of depolarisation(B), a new plot without depolarisation(B) data is shown in figure 5.12b. The data is scattered and indicates a tendency consistent with the trade-off proposition. Ultimately, increased signal counts lead to higher SNRs and lower % errors in temperature markers and tend to result in more accurate temperature predictions. In the future, we hope to explore more systematically how the presence of other signals – specially DOM fluorescence in natural waters – impact the sensitivities and SNRs of Raman markers acquired from natural waters.

## **Discussion**

Temperature markers calculated from Raman signals collected by our blue multichannel RS exhibited higher sensitivities than temperature markers calculated from acquisitions performed by our green RS [114], and this was true for both Milli-Q and natural water samples analysed in both studies. We attribute the higher temperature sensitivities to the use of narrower filters for selecting Raman photons in our blue multichannel RS, when compared with the bandwidth of filters used in our green setup. Temperature sensitivities for ultrapure water were in agreement with the proposed values of [63], considering the spectral channels widths employed in our blue multichannel RS were  $234\text{ cm}^{-1}$  and  $137\text{ cm}^{-1}$  for low and high shift channels, respectively.

Raman signals in natural water are prone to be overlapped by fluorescence signals; when working with excitation in the blue light range, the most common source of environmental noise is fluorescence from DOM [86,87,104]. The final signals acquired by our detectors for natural waters experiments were not purely temperature-dependent Raman photons, as they also included fluorescence signals from optically active constituents [113]. Consequently, the majority of the markers sensitivities were found to be lower for natural water samples when compared to Milli-Q water. Exceptions occurred in the two-colour(II) marker, with natural sample 1 ( $0.70\%/^{\circ}\text{C}$ ) and natural water sample 3 ( $0.71\%/^{\circ}\text{C}$ ) exhibited marginally higher sensitivities when compared to Milli-Q water ( $0.68\%/^{\circ}\text{C}$ ).

Depolarisation(B) sensitivities exhibited the lowest sensitivities (average of  $0.4\%/^{\circ}\text{C}$  among all samples under analysis), indicating that the marker was not able to extract highly accurate temperature information from Raman signals. This is endorsed by the evaluation of trade-offs between % errors/sensitivities and their impact on the accuracy of temperature predictions by the markers. From all four temperature markers, depolarisation(B) exhibited an outlier behaviour for all water samples, deviating from the clustering of data points. In the future, we hope to evaluate if the performance of depolarisation(B) predictions can be improved without compromising the results achieved other markers.

When figures 5.8 to 5.11 are compared to figures 4.7 to 4.10, the sensitivities determined using a particular marker for all water samples are far more similar for blue excitation. For green excitation, sensitivities varied to a much greater extent across water samples

## 5.5. Considerations for LIDAR implementation

In this final section of Chapter 5 I present LIDAR calculations aimed at comparing the effectiveness between blue and green excitation in generating Raman photons at certain depths, which then propagate to the surface for collection and detection. These calculations were performed in the very final stage of my PhD, are very exciting and there are opportunities to extend them in the future. I begin this section with some background information related to oceanographic LIDAR investigations, before proceeding to my comparison between blue/green excitation.

### 5.5.1. Background and approach

LIDAR methods for oceanographic and hydrological application have been developed since the 1960's, with successful programs developed by Australian and American government agencies and military forces. These entrepreneurs focused on using lasers in the blue-green and infrared ranges for exploring topographic features for oceanic and coastal areas, a technique known as Airborne Laser Bathymetry (ALB). In ALB a pulsed light signal emitted by a laser is directed into the water, undergoing partial reflection by the water surface. The remaining photons propagate (transmit) through the water column until reach the bottom, where they are partly reflected back to the surface and detected by the receiver sensors. Depths are calculated based on the time delay between the detection of photons reflected by the surface and the seafloor. The main factor limiting ALB (and LIDAR systems) operations is water turbidity, as it interferes with the propagation of both excitation (laser) and emission photons, as discussed in Chapter 1.

ALB systems are commonly comprised of four main modules operating simultaneously: the LIDAR transmitter/receiver (transceiver), GPS tools for determining highly accurate horizontal coordinates and heights, data acquisition control and ground processing. Both multichannel RS presented in Chapters 4 and 5 are similar in function to the transceiver module of an ALB system.

The SHOALS system operate with a 200 Hz, frequency-doubled Nd:YAG pulsed laser emitting green light at 532 nm (5 mJ, pulse duration of 5-6 ns at FWHM) and infrared signals at 1064 nm (>5 mJ, pulse duration of 7-9 ns at FWHM). It differs from other LIDAR equipment by collecting signals scattered from water at two green channels, one infrared channel and one channel centred at 650 nm collecting Raman photons. Both infrared and

Raman channels collect signals which can be used for cross-validation and detection of scattering layers (such as air/sea interface) when signals collected by the green channels are compromised by events such as land reflection [116,117]. Operating with this configuration in clear waters, SHOALS systems are able to detect signals emitted from up to 40 m depth, with vertical accuracy on depth determination of  $\pm 15$  cm and a horizontal accuracy of  $\pm 1.5$  m. When compared to reference measurements, depths measured by Raman signals exhibited standard deviation of 40.3 cm and mean errors of 3.1 cm [117]. Considering that the ultimate goal of my research group is retrieving depth-resolved temperature information with vertical resolution of  $\pm 0.5$  m, a LIDAR configuration similar to SHOALS will be considered in the next paragraphs.

A summary comparing the main configurations from the SHOALS transceiver with both green and blue custom-built multichannel RS is shown in table 5.6.

Table 5.6. Technical specifications for SHOALS transceiver and custom-built multichannel Raman spectrometers (532 nm and 473 nm excitation).

<b>LIDAR systems specifications</b>	<b>SHOALS</b>	<b>Green excitation multichannel RS</b>	<b>Blue excitation multichannel RS</b>
<b>Excitation wavelength</b>	532 nm	532 nm	473 nm
<b>Laser power</b>	5 mJ	25 $\mu$ J	5 $\mu$ J
<b>Laser frequency of operation</b>	400 Hz	4.5 kHz	5.0 kHz
<b>Pulse duration (FWHM)</b>	5 ns	0.9 ns	1.5 ns
<b>Optical channels of collection</b>	Green (1, PMT)	640 nm ( $\parallel$ )	561 nm ( $\parallel$ )
	Green (2, ADP)	640 nm ( $\perp$ )	561 nm ( $\perp$ )
	Infrared	660 nm ( $\parallel$ )	568 nm ( $\parallel$ )
	Raman (650 nm)	660 nm ( $\perp$ )	568 nm ( $\perp$ )

We start the comparison addressing the similarities between the three systems, which include: (1) operation integrated to pulsed light sources in the visible range (green or blue); (2) present the same number of optical channels (four) collecting backscattered signals from water; (3) at least one of the channels in each system is dedicated to collecting exclusively Raman photons scattered from water. Despite these similarities, SHOALS systems employ lasers which are 200 times more powerful than the laser used in my green multichannel RS and 1000 times more powerful than the laser integrated to the blue multichannel RS. In order to analyse the feasibility of my system working in the field, I will simulate the performance of both my multichannel Raman spectrometers when collecting Raman signals whilst



integrated to an excitation source with same power used in SHOALS systems. I will also discuss the impacts of light attenuation for propagation excitation and Raman photons in the water column for each of my custom-built system and implications for two-colour markers temperature calculation.

The number of Raman photons generated at a depth ( $z$ ) and reaching the surface,  $N_{Raman\_return}(z)$ , can be described by the equation 5.1, which is based and adapted from theory presented in [71]. It enables comparison between both multichannel systems and the contribution of all processes involved in the final Raman signal collection at the surface can be understood. For simplicity, we have overlooked Fresnel reflections into and out of the water.

$$N_{Raman\_return}(z) = N_{laser} N_{scat} \sigma_{Raman} \Delta R \frac{\Omega(z)}{n^2} T_{\lambda 1} T_{\lambda 2} \quad (5.1)$$

where  $N_{laser}$  is the number of excitation laser photons at a given depth ( $z$ );

$N_{scat}$  is the density of water molecules interacting with the excitation light (molecules/m<sup>3</sup>);

$\sigma_{Raman}$  is the Raman scattering cross-section per molecule per steradian (cm<sup>2</sup>/molecule sr);

$\Delta R$  is the minimum vertical range resolution, determined by the laser pulse duration (m);

$\Omega$  is the solid angle of collection, dependent on the diameter of the telescope or other collection optics used (steradians) at a given depth;

$n$  is the refractive index of seawater;

$T_{\lambda 1}$  and  $T_{\lambda 2}$  are, respectively, the vertical transmission values for the excitation and Raman wavelengths in water (m<sup>-1</sup>).

The abovementioned equation is valid for sufficiently small solid angles of collection so that Raman photons reach the surface at near-normal angles of incidence. It can be decomposed into four main processes: (1) propagation (transmission) of excitation photons; (2) generation of Raman photons; (3) transmission of Raman photons; and (4) collection of Raman photons at the surface.

### 5.5.2. Propagation (transmission) of excitation photons

The vertical transmission of light in water is dependent on the wavelength emitted by the light source, which will be absorbed and scattered by water molecules and other optical constituents in natural waters as seen in **Chapter 1**. For coherent light sources, such as lasers, we can estimate the intensity of light reaching a given depth ( $N_{laser}(z)$ ) by the following relationship (equation 5.2): For the purpose of this study, we neglect any spreading of the excitation beam as it propagates through water and accordingly, we can write

$$N_{laser}(Z) = N_0 e^{(-K_d z)} \quad (5.2)$$

where  $N_0$  represents the intensity of the laser source at  $z=0$  m, and  $K_d(\lambda)$  is the wavelength-dependent coefficient of downwelling attenuation for a certain natural water type.

As discussed in Chapter 1, the downwelling diffuse attenuation coefficients  $K_d(\lambda)$  are expressed in  $m^{-1}$  and quantify the total downwelling light absorption and scattering processes in water, here related to the laser (excitation) light. The choice of using the coefficient of attenuation  $K_d(\lambda)$  instead of coefficients of transmission, as proposed in [71], is beneficial for the comparisons proposed in this study. Updated values of  $K_d(\lambda)$  for different Jerlov water types are available in [100], allowing for readily comparison between performances of each Raman spectrometer in different water types.

Reference values for  $K_d(\lambda)$  in Jerlov water types I (oceanic), 1C (clear coastal) and 7C (coastal exhibiting high turbidity) were obtained from [100] in intervals stepping every 25 nm, being too broad for the intention of this study. In order to estimate  $K_d(\lambda)$  values for smaller wavelength intervals, a low-pass interpolation was performed in Matlab (R2017b), generating a new set of  $K_d(\lambda)$  coefficients with intervals of 1 nm. A summary with interpolated  $K_d(\lambda)$  values for 473 nm and 532 nm excitation light ( $K_d^{473}$  and  $K_d^{532}$ , respectively) for Jerlov water types I, 1C and 7C is shown in table 5.7.

Table 5.7. Coefficients of downwelling diffuse attenuation ( $K_d$ ) calculated for wavelengths 473 nm and 532 nm in Jerlov water types I, 1C and 7C. Original values from [100].

Jerlov water type	$K_d^{473}(m^{-1})$	$K_d^{532}(m^{-1})$
I (clear oceanic)	0.020936627	0.056522943
1C (clear coastal)	0.141501972	0.125776081
7C (turbid coastal)	0.724552790	0.454200219

Assuming a laser with power of 5 mJ per pulse, as used in SHOALSs systems, the initial number of photons  $I_0$  emitted by a light source at 473 nm was estimated to be  $1.19 \times 10^{16}$  photons per pulse, and for a light source at 532 nm it was estimated to be  $1.34 \times 10^{16}$  photons per pulse. Vertical resolutions  $\Delta R$  were set to be 0.5 m, which corresponds to the length of the light pulse in the water and is similar to the depth resolution of the SHOALS system. By applying the respective values of  $N_0$  and  $K_d$  (from table 5.7) in equation 5.2 is possible to simulate the propagation of both blue and green light sources in Jerlov water types I, 1C and 7C. Results obtained for the blue light (473 nm) are shown in figure 5.13a, and for the green light (532 nm) are shown in figure 5.13b.

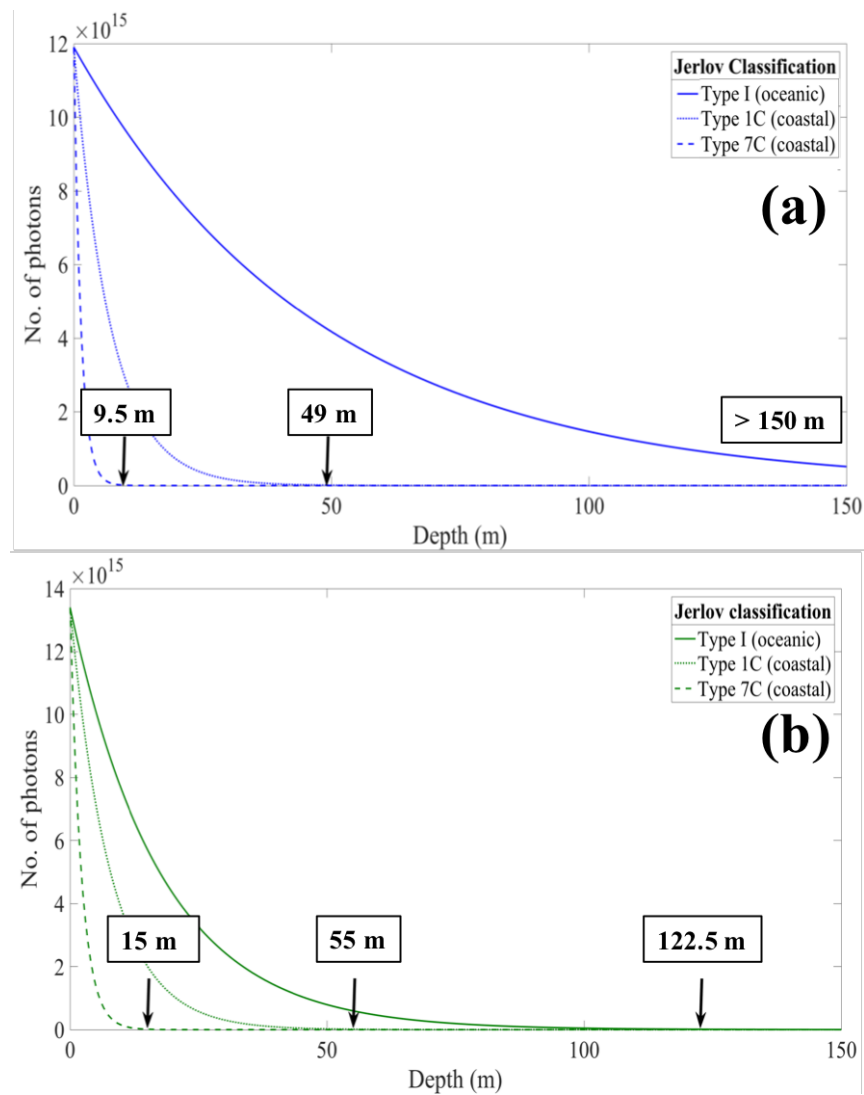


Figure 5.13. Number of excitation photons vertically transmitted in water, to depth  $Z$ , in Jerlov water types I, 1C and 7C for (a) 473 nm excitation and (b) 532 nm excitation. Depths delimiting the euphotic zone (1% transmission) are indicated for each water type.

I start the discussion by addressing light transmission in oceanic clear waters type I. The expression “maximum depth” will be hereafter used to refer to the limit of the euphotic zone, *i.e.*, the depth at which the light intensity is 1% of the initial intensity at the surface [118]. It is important to note that these values will be used solely for comparing the performance between our spectrometers, and that there is no certainty that photons scattered at these depths would be detected at the surface. Both blue and green light exhibited better transmission in oceanic water type I, compared to the transmission in coastal water types. For oceanic waters type I, it is possible to affirm that the blue excitation at 473 nm was less attenuated and reached greater depths ( $> 150$  m) in comparison to the green excitation at 532 nm for which maximum depth was 122.5 m (figures 5.13a and 5.13b, respectively).

Two Jerlov types representative of coastal waters were considered for this simulation: coastal waters in clear conditions (type 1C) and turbid coastal water (type 7C). In both cases, the green excitation was less attenuated (and, consequently, more photons were reached greater depths) than when using blue excitation at 473 nm. For waters type 1C, the maximum depth of reach for the green light was 55 m, whilst for blue excitation this was 49 m; for waters type 7C, green excitation light reached up to 15 m whilst blue excitation light reached 9.5 m (figure 5.13).

Ultimately, the use of blue excitation at 473 nm as excitation would allow for a higher depth penetration in LIDAR systems operating in oceanic water type I, and, conversely, the use of green light at 532 nm would allow for high depth penetration in coastal waters type 1C and 7C. Knowing the number of excitation photons in water at any depth for 473 nm and 532 nm light sources of same pulsed energy, I now proceed to evaluate the depth-resolved generation of Raman photons in water for each excitation wavelength.

### 5.5.3. Generation of Raman photons

The number of Raman photons generated at some depth  $Z$  by an excitation beam depends on three factors: (1) the number of excitation photons reaching each depth; (2) the number of scatterers  $N_{scat}$  interacting with the excitation photons, here represented by the number of water molecules; (3) and the Raman cross-section calculated for water molecules. We consider here the generation of unpolarised Raman signals, *i.e.*, all Raman photons regardless their polarisation state.

The number of excitation photons reaching depth  $Z$  was calculated in the previous section for Jerlov water types I, 1C and 7C for both blue and green excitation lasers, assuming equal laser pulse energy. We assume that both blue and green excitation beams are interacting with the same number of scatterers  $N_{scat}$ . It is also assumed that the laser beams do not undergo divergence and are interacting with cylindrical elements of finite extent whose height dimension corresponds to  $\Delta R = 0.5$  m. For seawater densities of  $1035 \text{ g/m}^3$ ,  $N_{scat}$  is estimated to be  $4.32 \times 10^{24}$  water molecules per element.

Raman cross-sections ( $\sigma_{Raman}$ ) were estimated according to equation 1.2 [49] considering the central wavelengths of 561 nm and 568 nm for the blue RS and 640 nm and 660 nm for the green RS. Unpolarised signals collected from these channels would allow for two-colour markers calculations for temperature predictions. Estimations are shown in table 5.8.

Table 5.8. Raman cross-section estimations for spectral channels collecting Raman signals for the blue multichannel RS (473 nm excitation) and for the green multichannel RS (532 nm excitation)

	Blue multichannel RS		Green multichannel RS	
Stokes-Raman channels (nm)	561	568	640	660
Raman cross-section (cm <sup>2</sup> /molecule sr)	$1.01 \times 10^{-29}$	$9.62 \times 10^{-30}$	$5.82 \times 10^{-30}$	$5.14 \times 10^{-30}$

The depth-resolved generation of Raman photons ( $N_{Raman}^{generated}$ ) was then calculated for water types I, 1C and 7C considering the wavelengths of Raman collection channels according to equation 5.3, and results are shown in figure 5.14.

$$N_{Raman}^{generated}(z) = N_{laser}(z)N_{scat}\sigma_{Raman} \quad (5.3)$$

where  $N_{laser}(z)$  indicates the number of excitation photons at depth  $z$ ,  $N_{scat}$  is the number of scatters interacting with the excitation light and  $\sigma_{Raman}$  is the Raman cross-section calculated for the central wavelength of each signal collection channel.

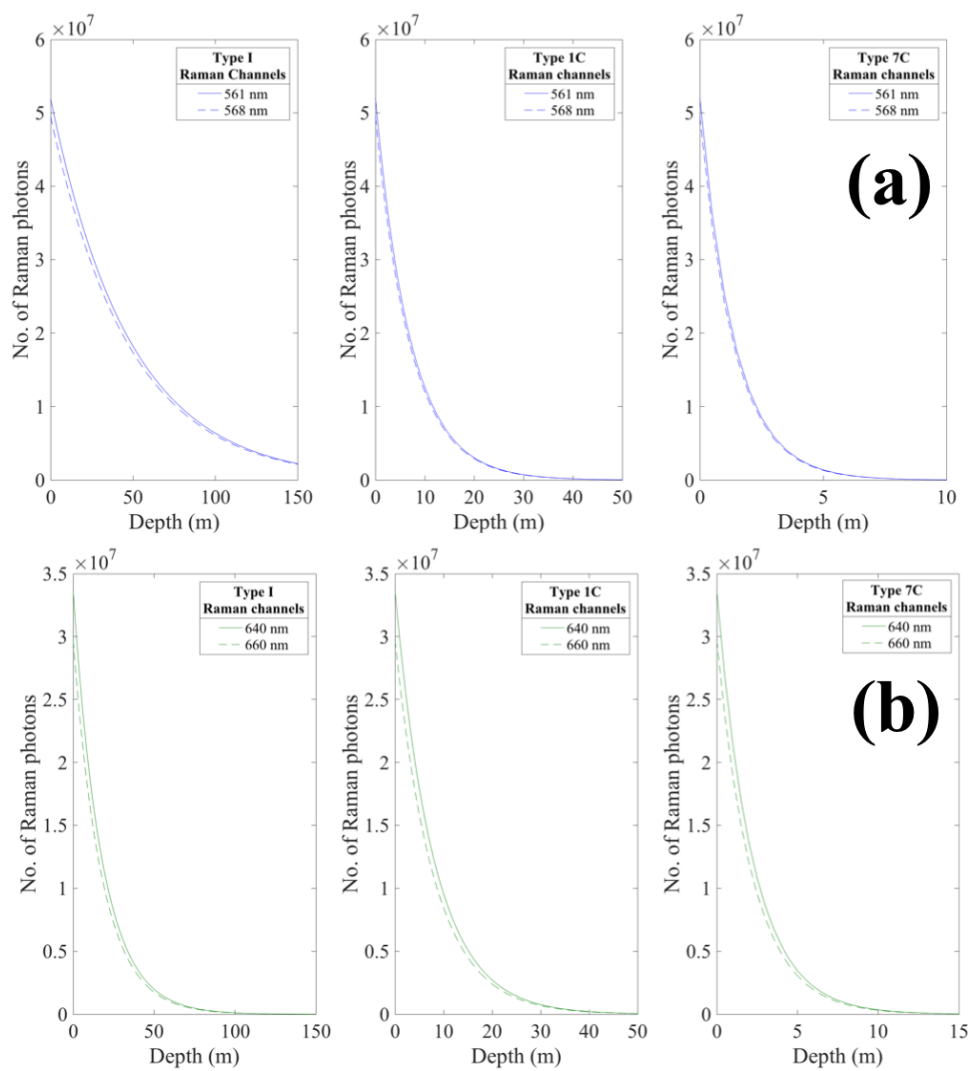


Figure 5.14. Number of Raman photons scattered per depth (m) for Jerlov water types I, 1C and 7C from (a) 473 nm excitation (blue) and (b) 532 nm excitation (green) laser with 5 mJ pulse energy.

Raman photons generation was  $\sim 9$  orders of magnitude smaller than the number of excitation photons, evidencing the importance of using powerful lasers in Raman LIDAR measurements. For all environmental conditions modelled in figure 5.14, higher counts of Raman photons were always found for the “low shift” channel than scattered towards wavelengths correspondent to the “high shift channel” (higher wavelengths). This behaviour was expected due to wavelength-dependence of the Raman cross-section, indicated in table 5.8 and implies that signals collected at different spectral channels will experience different attenuation in water, leading to losses in temperature sensitivity when calculating the markers [97].

When comparing Raman signal generation at same depths, blue excitation generated more Stokes-shifted photons than green excitation for water types I and 1C. For water type 7C, the strong attenuation of the blue excitation light with depth (as seen in figure 5.13a) resulted in less Raman photons generated when compared with green excitation.

#### 5.5.4. Transmission of Raman photons

The fact that Raman signals were generated at certain depths doesn't guarantee them reaching the surface, as firstly they need to be transmitted upwards in the water column, undergoing further attenuation. Raman photons are assumed to be scattered in all directions ( $4\pi$  sr) and only a fraction of these will be collected by the detection apparatus. For the purpose of this study we assume the solid angle of collection (which depends on depth) to be the same for the cases of blue and green excitation, sufficiently small so that the Stokes photons reach the surface at near-normal angle of incidence.

In this simulation, upward signal refers to Raman photons of wavelengths 568 nm (for blue excitation) and 660 nm (for green excitation). Estimations of  $K_d(Raman)$  for the wavelengths abovementioned in water types I, 1C and 7C are shown in table 5.9 (from [100]).

Table 5.9. Coefficients of downwelling diffuse attenuation  $K_d(Raman)$  calculated for spectral channels collecting Raman signals excited by blue (473 nm) and green (532 nm) lasers in Jerlov water types I, 1C and 7C. Original values from [100]

	Blue multichannel RS	Green multichannel RS
Jerlov water type	$K_d^{568}$ ( $m^{-1}$ )	$K_d^{660}$ ( $m^{-1}$ )
I (clear oceanic)	0.067273	0.373014
1C (clear coastal)	0.126629	0.481169
7C (turbid coastal)	0.363473	0.701930

Tracking all photons packets originated at a certain depth  $Z$  is a complex task, usually performed with the use of Monte Carlo algorithms. The technique is broadly used in LIDAR investigations, allowing for correlations between the origin of the scattered Raman photon and its detection at surface. This approach, however, is not within the scope of this thesis. It is possible to estimate the transmission of Raman photons ( $T_{\lambda_2}(Z)$ ) in the water column according to equation 5.4:

$$T_{\lambda_2}(z) = N_{Raman}^{generated}(z)e^{(-K_d z)} \quad (5.4)$$

where  $N_{Raman}^{generated}$  is the number of Raman photons generated at a given depth  $z$ , and  $K_d$  is the coefficient of diffuse attenuation. This calculation allows for determining the percentage of the Raman photons originated at depth  $Z$  reached the surface after undergoing attenuation. Here, the “maximum depths” refers to the depths from which at least 1% of the Raman photons generated can reach the surface. Estimations for Raman channels used in our multichannel Raman spectrometers are shown in figure 5.15.



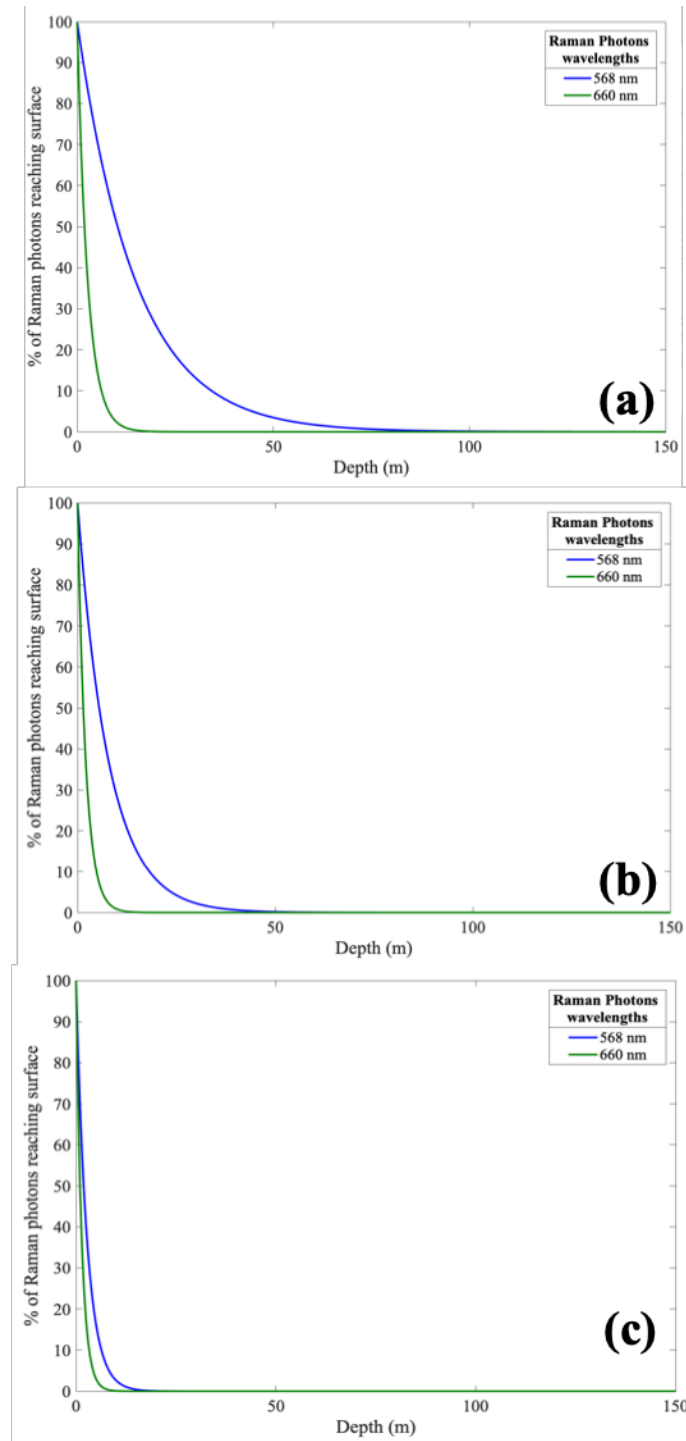


Figure 5.15. Transmission of Raman photons as a function of vertical propagation distance for Jerlov water types (a) I-oceanic, (b) 1C-coastal, (c) 7C-coastal.

Raman photons scattered from blue excitation underwent smaller attenuations in all water types under analyses and, as a consequence, Raman-shifted photons from higher depths achieved the surface when compared with the case for green excitation. The approximate maximum depths of generation for a meaningful acquisition of Raman photons at the surface were extracted from figure 5.15 and are summarised in table 5.10.

Table 5.11. Maximum depths from which Raman signals could be retrieved.

	Blue multichannel RS	Green multichannel RS
<b>I (clear oceanic)</b>	68.5 m	12.5 m
<b>1C (clear coastal)</b>	36.5 m	10.0 m
<b>7C (turbid coastal)</b>	12.5 m	6.5 m

From figure 5.15 and table 5.10 it becomes clear that the use of blue excitation would allow for higher vertical range (*i.e.* collection of Raman photons from greater depths) for all water types analysed.

### 5.5.5. Comparing the Raman returns for blue and green excitation

Finally, we compare the relative number of Raman photons that were generated at a given depth  $Z$  and subsequently reached the surface for the cases of excitation by a 5 mJ laser source at 473 nm and a 5 mJ laser at 532 nm. Equation 5.1 can be re-written to group terms that do not depend on wavelength into a single constant (equation 5.5):

$$C(z) = \frac{N_{scat} \Delta R \Omega(z)}{n^2} \quad (5.5)$$

Thus, the number of Raman photons reaching the detector at the surface of the water for excitation light at 473 nm and 532 nm can be expressed by equations 5.6 and 5.7, respectively.

$$N_{Raman}^{473}(z) = C(z) N_0^{473} \sigma_{Raman}^{473} e^{(-K_d^{473} z)} e^{(-K_d^{561/568} z)} \quad (5.6)$$

$$N_{Raman}^{532}(z) = C(z) N_0^{532} \sigma_{Raman}^{532} e^{(-K_d^{532} z)} e^{(-K_d^{640/660} z)} \quad (5.7)$$

where, as stated before, we have disregarded the Fresnel reflection at the surface.

In order to determine which excitation wavelength is most effective in terms of higher number of Raman photons reaching the surface, we calculated the ratio of  $N_{Raman}^{473}$  to  $N_{Raman}^{532}$ , as in equation 5.8.

$$\frac{N_{Raman}^{473}(z)}{N_{Raman}^{532}(z)} = \frac{N_0^{473}}{N_0^{532}} \frac{\sigma_{Raman}^{473}}{\sigma_{Raman}^{532}} \frac{e^{-((K_d^{473} + K_d^{561/568})z)}}{e^{-((K_d^{532} + K_d^{640/660})z)}} \quad (5.8)$$

where:

$N_0^\lambda$  refers to the initial number of excitation photons being emitted by the laser source of wavelength  $\lambda$ ;

$\sigma_{Raman}^\lambda$  is the Raman scattering cross-section per molecule per steradian for excitation light of a given wavelength  $\lambda$  (cm<sup>2</sup>/molecule sr);

$K_d^\lambda$  refers to the coefficient of downwelling attenuation of excitation light of wavelength  $\lambda$ ;

The ratio proposed in equation 5.8 was calculated for Jerlov water types I, 1C and 7C for both channels collecting Raman signals scattered by water when interacting with each laser source (table 5.6). Here I consider only the Raman photons scattered into the “high” collection channels of both spectrometers (568 nm for the blue excitation and 660 nm for green excitation, respectively). Figure 5.16 shows the ratio for all depths between 0 to 60 m (log-linear graph).

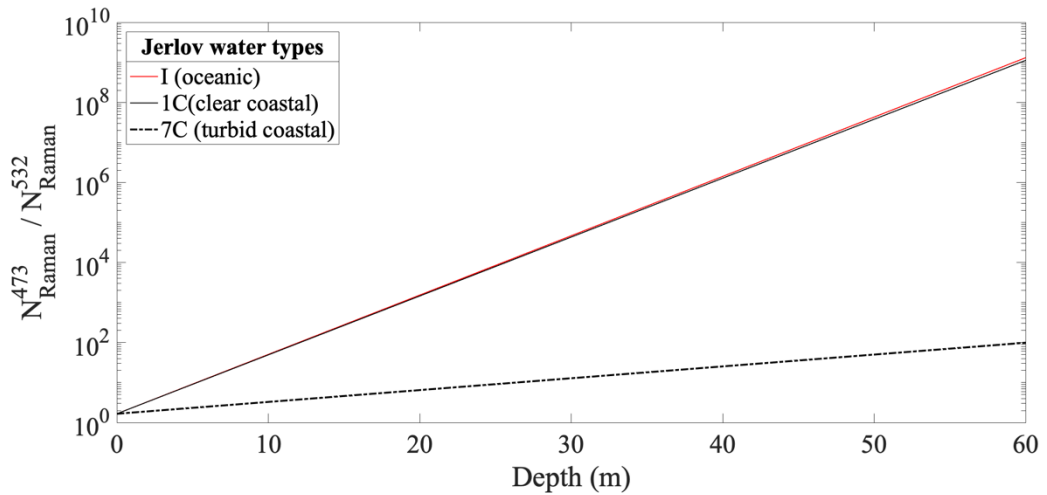


Figure 5.16. The ratio given in equation 5.8 is plotted as a function of depth (Z) for water types: oceanic type I, and coastal types 1C and 7C. All depths between 0 and 60 m are considered.

The following observations were made for all water types investigated in this study:

- 100 times more Raman photons scattered at a depth of  $\sim 12$  m reached the surface when blue excitation was used in the case of oceanic water type I. For coastal waters, this value was also reached at  $\sim 12$  m for type 1C and at  $\sim 60$  m for type 7C.
- Ratios of  $N_{Raman}^{473}$  to  $N_{Raman}^{532}$  were always larger than 1, indicating that a larger number of Raman photons scattered at a given depth  $z$  will reach the surface when excited by blue light than when excited by green light. This was especially true for greater depths (up to 50 m), where the ratio assumed values up to 7 orders of magnitude (figure 5.16).

## 5.6. Summary and conclusion

In this Chapter, I reported the main findings obtained for temperature predictions performed by the custom-built, LIDAR-compatible, blue multichannel Raman spectrometer. The spectrometer was integrated to a 473 nm pulsed laser, and Raman signals were collected in four spectral channels selected by two band pass filters. Band Pass filters had bandwidths of  $234\text{ cm}^{-1}$  (for signals collected in the “low shift” region) and  $137\text{ cm}^{-1}$  (for signals collected in the “high shift: region), respectively. Raman signals were collected by fast-response, sensitive photomultipliers and registered by a multichannel oscilloscope. Four independent temperature markers were calculated from the Raman signals scattered by different water samples, these being two-colour( $\parallel$ ) and two-colour( $\perp$ ) (for Raman signals collected in channels at same polarisation state) and depolarisation(A) and depolarisation(B) (for Raman signals collected in channels at different polarisation states). Accuracies as high as  $\pm 0.5^\circ\text{C}$  were achieved in temperature predictions performed by two-colour( $\parallel$ ) in both Milli-Q and natural water samples, delivering the best RMSTEs among the four markers under investigation. The performance of depolarisation(A) markers was also significant, achieving the second best RMSTEs when predicting temperature ( $\pm 0.5^\circ\text{C}$  for Milli-Q and  $\pm 0.7^\circ\text{C}$  for natural water); furthermore, depolarisation(A) markers exhibited the highest sensitivities in all water samples analysed in this study. By combining temperature information from all four markers in a multiple linear regression model, accuracies as high as  $\pm 0.2^\circ\text{C}$  were achieved for temperature predictions in natural waters.

One of the benefits of using blue lasers in Raman remote sensing of temperature in natural waters is the fact that the Raman peak for this excitation wavelength ( $\sim 560\text{ nm}$ ) lays in a spectral region away from the peak for chlorophyll-a fluorescence ( $\sim 680\text{ nm}$ ). Despite of being effective in avoiding this overlapping, the water Raman peak for blue excitation is prone to be overlap with fluorescence from other optically active components, mostly Dissolved Organic Matter (DOM) and other photosynthetic pigments. The design of our experiment was such that this benefit could not really be tested effectively and did not allow for direct comparison with the results from the green multichannel RS (Chapter 4). This is mainly because of the following reasons: (1) different natural water samples were used, (2) the blue and green lasers had different pulse energies, and (3) the spectral channels positions and widths were also different between spectrometers. Future work could explore the benefit of blue excitation over green more thoroughly in a wider range of water samples.

LIDAR simulations evaluating the operation of blue and green multichannel Raman spectrometers were performed by adapting an equation from [71]. Number of photons emitted by laser sources at 473 nm and 532 nm, 5 mJ laser power were considered for simulations in clear oceanic and turbid coastal waters. For all cases, blue excitation was superior to green due to the following factors: (1) larger Raman cross-section for Stokes-Raman photons scattered from blue excitation; (2) better upward vertical transmission for Raman-shifted photons scattered from blue excitation.

Ultimately, the use of blue laser excitation for Raman remote sensing of water temperature in laboratory resulted in predictions with accuracies up to  $\pm 0.2^{\circ}\text{C}$ , similar to the RMSTEs obtained by natural waters temperature measurements by our green multichannel RS shown in Chapter 4. In terms of field implementation, however, LIDAR simulations suggest a huge benefit to using blue rather than green lasers in terms of the number of Raman photons retrieved at the surface.

## CHAPTER 6

# CONCLUSIONS AND FUTURE OUTLOOK

This thesis has addressed issues regarding LIDAR-compatibility of Raman spectroscopic methods for the remote sensing of temperatures using natural waters samples. It has included laboratory experiments and numerical analyses exploring the temperature-dependent laser-induced Raman scattering in both ultrapure (Milli-Q) and natural water samples, aiming to provide new LIDAR-compatible technologies allowing for depth-resolved remote sensing of water temperature.

In order to transition from traditional commercial Raman spectrometers to custom-built designs, investigations in natural waters were conducted in order to determine the possible origins of baseline signals overlapping with the water Raman peak for 532 nm (green light) excitation. Multivariate Principal Component Analysis (PCA) identified the spectral regions giving rise to variance between natural water samples, which should be avoided for achieving higher accuracy of temperature predictions from Raman markers. Two methods of baseline correction were evaluated, the traditional tilted baseline correction and the new “correction by temperature markers” and both were effective on increasing the accuracy of temperature predictions in natural waters.

The new LIDAR-compatible approach differs from most of the studies in the field by not requiring acquisition of the full Raman spectra; instead, the custom-designed, multichannel, LIDAR-compatible Raman spectrometers presented in this thesis allow for simultaneous collection of Raman signals in spectral channels located at positions of interest for water temperature remote sensing. Two-colour and depolarisation temperature markers were calculated by integrating the Raman signals collected in spectral channels, not requiring spectral decomposition or any further processing. Furthermore, the multichannel configuration enabled the construction of linear combination models with multiple markers for increased robustness and accuracies of temperature predictions.

The relative merits of using blue (473 nm) and green (532 nm) excitation for LIDAR-compatible Raman temperature predictions in natural waters were investigated in detail for Raman signals acquired in laboratory-controlled experiments. Accuracies of temperature predictions (RMSTEs), markers sensitivities, and percentage errors associated with temperature markers were estimated for each excitation wavelength. LIDAR simulations were performed in order to identify which wavelength (blue or green) would be most effective for retrieving Raman signals from various depths in oceanic and coastal environments.



## 6.1. Research outcomes

These investigations have summarised the requirements for Raman remote sensing of temperature in natural waters. The PCA exploration of Raman spectra in Chapter 3 suggested that Raman spectra from various natural water samples exhibited considerable variance, not associated with temperature, that were consistent with literature reports of fluorescence from Dissolved Organic Matter (DOM), chlorophyll-a and other photosynthetic pigments. When overlapping with the Raman peak, these fluorescence signals impacted the values calculated for Raman temperature markers and compromised the accuracies of temperature predictions. The traditional tilted baseline correction was performed, resulting in accuracies up to  $\pm 0.2^{\circ}\text{C}$  (typically  $\pm 0.2^{\circ}\text{C}$  to  $\pm 0.7^{\circ}\text{C}$ ) for two-colour unpolarised temperature predictions in natural waters. A new method for correcting baseline, named “correction by temperature markers” was proposed based on the difference between the two-colour markers values calculated for a “standard” seawater (filtered and UV treated) and for the natural water samples. Accuracies as high as  $\pm 0.2^{\circ}\text{C}$  (typically  $\pm 0.2^{\circ}\text{C}$  to  $\pm 0.4^{\circ}\text{C}$ ) were achieved for the new “correction by temperature markers” method.

The multichannel, LIDAR-compatible Raman spectrometer design and built integrated to a 532 nm (green) excitation effectively acquired Raman signals, and two-colour and depolarisation ratios were calculated for both Milli-Q and natural water samples. The best performance by temperature markers was achieved by two-colour(II), predicting temperatures in natural (Milli-Q) water samples with accuracy as high as  $\pm 0.5^{\circ}\text{C}$  ( $\pm 0.4^{\circ}\text{C}$ ). The use of depolarisation markers for predicting temperature in laboratory was also evaluated, with best results achieved by depolarisation(A) markers, with best accuracies of  $\pm 0.8^{\circ}\text{C}$  found for both Milli-Q and natural water temperature predictions. For the first time, multiple linear regression models were constructed using multiple Raman markers, resulting in improved accuracies for temperature predictions up to  $\pm 0.3^{\circ}\text{C}$  in natural waters. This was only possible due to the multichannel nature of the custom-built RS, which allowed for simultaneous acquisition of parallel and perpendicularly-polarised Raman signals at different spectral channels. The markers sensitivities to temperature were negatively impacted (in our apparatus) by the widths of the spectral channels collecting Raman signals. The spectral widths, which were constrained by the range of available filters, were wider than the optimal values proposed by the authors of [63] and compromised the temperature sensitivity of markers. For the majority of the analyses, higher signal counts were

encountered for natural water samples; however, marker sensitivities for natural samples were lower than the reported for Milli-Q water. This was attributed to overlapping between fluorescence signals with the Raman peak for 532 nm excitation, especially chlorophyll-a, which did not carry temperature information. We hope in the future to work with customised optical filters with the desired bandwidths of  $200\text{ cm}^{-1}$  to improve the markers sensitivities, nevertheless the overlapping between chlorophyll-a fluorescence and the Raman peak for green excitation at 532 nm cannot be avoided. Besides applying the baseline correction techniques proposed in Chapter 3, the use of shorter wavelengths for excitation could be effective to minimise potential overlapping with chlorophyll-a fluorescence in natural waters.

The use of blue excitation Raman spectroscopy was also evaluated for temperature predictions in Milli-Q and natural water samples in the laboratory. The custom-built, multichannel, LIDAR-compatible Raman Spectrometer integrated to a 473 nm pulsed laser source was assembled in a manner which enabled both-orthogonally polarised components of Raman signals scattered from the water samples to be collected simultaneously. In terms of accuracies, two-colour(II) and depolarisation(A) exhibited the best RMSTE value of  $\pm 0.5^{\circ}\text{C}$  for temperature predictions in Milli-Q water. For natural water samples, best accuracies achieved by the two-colour(II) was  $\pm 0.5^{\circ}\text{C}$  and, for depolarisation(A) markers,  $\pm 0.7^{\circ}\text{C}$ . These accuracies for temperature prediction in natural waters were improved up to  $\pm 0.2^{\circ}\text{C}$  by linear combination models constructed by using all four Raman markers. The highest markers sensitivities in were found for the depolarisation(A) marker, with values up to  $0.92\%/^{\circ}\text{C}$  in comparison with  $0.68\%/^{\circ}\text{C}$  for two-colour(II) markers for Milli-Q water analysis. These values are in agreement with the proposed for the bandwidths of Raman collection channels adopted in this RS, which were around  $200\text{ cm}^{-1}$ . One of the biggest motivations for using blue excitation was avoid overlapping of the Raman peak with chlorophyll-a fluorescence; however, the Raman peak for blue (473 nm) does overlap with fluorescence from other optically active constituents found in natural waters, such as DOM and photosynthetic pigments. Preliminary LIDAR modelling shows a huge benefit of using blue excitation at 473 nm instead of green light at 532 nm in both oceanic and coastal waters, allowing for detection of a higher number of Raman photons at the surface and also collection of Raman photons originate at greater depths.

During the three years of my PhD I carried out a series of investigations which were not included in this thesis. First, I explored the use of the method of correction by

temperature markers, proposed in Chapter 3, as a tool for self-predicted measurements in field acquisitions. The results for such analysis for two-colour(II) markers calculated for both blue and green Raman spectrometers are presented in Appendix A.

Second, I designed and assembled two-channel LIDAR-compatible Raman spectrometer integrated to a 473 nm laser for excitation using optical filters of broad bandpass ( $> 40$  nm). In the occasion, unpolarised Raman signals were collected in spectral channels and  $R^2$  of 0.8858 were found for linear models predicting temperature. The main experimental features and results related to these experiments are shown in Appendix C (*“Water temperature measurement using blue excitation and two-channel Raman spectrometer”*).

The achievements presented in this thesis are extremely valuable for implementation of Raman spectroscopic methods for measuring depth-resolved temperature in oceanic and coastal environments. Accuracies for temperature predictions by single marker analysis exhibited values equal or better than  $\pm 0.5^\circ\text{C}$  in all samples analysed, and this performance by enhanced by linear combination and baseline correction techniques. The fact that LIDAR-compatible, Raman-based methods achieved such results in laboratory-based studies demonstrate the potential of the technique to be used for rapid vertical assessment of the water column temperature in oceanic, coastal and underwater remote sensing investigations.

Following a visit and suggestion by Dr. Simin Feng of ONRG (Office of Naval Research Global), my PhD supervisor and I have prepared a white paper (request for funding) to conduct a study to implement this work in the field. The proposal, which is included in Appendix D, involves a collaboration with Prof. Andy Jessup and A.Prof. Chris Chickadel at University of Washington, who I met at a conference and a subsequently visit to their lab (Applied Physics Laboratory). The proposal was submitted in March of 2018, but at this time we have not received any response.

## 6.2. Future outlook

The outcomes of this research provided constructed insights for improving the current design of our Raman spectrometer and adapt them for field implementation. Improvements in the design include the use of custom-built Band Pass filters, allowing for collection of Raman signals at spectral regions with maximum sensitivity to changes in temperature.

Future designs might include accessory channels for collecting fluorescence signals potentially overlapping with the “low” and “high” shift sides of the isosbestic point, which could be used for implementing baseline correction methods. The simultaneous collection of Raman and specific fluorescence signals (such as chlorophyll-a fluorescence) might also be very useful for management of aquaculture farms and algal blooms at coastal areas. The monitoring of the fluorescence particles in water, such as microplastics, might also be explored in the future.

Blue light excitation appeared to be the most promising for Raman remote sensing of water temperature in regards to LIDAR simulations; however, the use of green excitation light should not be completely forwent. As many oceanographic LIDAR systems already operate with pulsed 532 nm (green light) excitation, the implementation of the green multichannel RS should be more simplistic than the blue multichannel RS. Furthermore, the use of dual excitation (*i.e.*, simultaneous use of blue and green lasers) is an interesting strategy for accounting for fluorescences from both Chl-a and DOM in natural waters.

Further LIDAR implementation should be conducted, which include studying the vertical propagation of Raman photons in a stratified water column and also accounting for salinity effects in the OH stretching band shape. By using appropriate filters, both depth-resolved temperature and salinity information could be determined simultaneously, allowing for rapid identification of water masses, pycnoclines and upwelling regions with fishery potential from ship and airborne-based systems.

Laboratory-based analyses have demonstrated a promising potential for using Raman temperature markers for water temperature prediction; however, further investigations are necessary in order to evaluate the feasibility of using these methods for determining subsurface water temperature in the field. The first steps of field implementation involve conducting experiments in a 9 m high water cell at Macquarie University in order to investigate the vertical propagation of Raman photons in a stratified water column, followed by field trials in research vessels.

# BIBLIOGRAPHY

1. T. D. Dickey, "A vision of oceanographic instrumentation and technologies in the early twenty-first century," in *Oceans 2020*, J. G. Field, G. Hempl, and C. P. Summerhayes, eds. (Island Press, 2002), pp. 209–254.
2. W. G. Rees, *Physical Principles of Remote Sensing*, second (Cambridge University Press, 2001).
3. S. M. Davis, D. A. Landgrebe, T. L. Phillips, P. H. Swain, R. M. Hoffer, J. C. Lindenlaub, and L. F. Silva, *Remote Sensing: The Quantitative Approach* (McGraw-Hill International Book Co., 1978).
4. M. Solan, J. D. Germano, D. C. Rhoads, C. Smith, E. Michaud, D. Parry, F. Wenzhöfer, B. Kennedy, C. Henriques, E. Battle, D. Carey, L. Iocco, R. Valente, J. Watson, and R. Rosenberg, "Towards a greater understanding of pattern, scale and process in marine benthic systems: A picture is worth a thousand worms," *J. Exp. Mar. Bio. Ecol.* **285–286**, 313–338 (2003).
5. W. Munk, "Achievements in Physical Oceanography," in *0 Years of Ocean Discovery: National Science Foundation 1950–2000*, National Research Council (US) Ocean Studies Board., ed. (National Academy Press, 2000), p. 276.
6. H. U. Sverdrup, "Wind-Driven Currents in a Baroclinic Ocean; with Application to the Equatorial Currents of the Eastern Pacific," *Proc. Natl. Acad. Sci.* **33**(11), 318 LP-326 (1947).
7. H. Stommel, "The westward intensification of wind-driven ocean currents," *Trans. Am. Geophys. Union* **29**(2), 202 (1948).
8. R. Buss de Souza, ed., *Oceanografia Por Satélites*, 2nd ed. (2009).
9. R. Rajeesh and G. S. Dwarakish, "Satellite Oceanography– A review," *Aquat. Procedia* **4**(Icwrcoe), 165–172 (2015).
10. J. A. Strong and M. Elliott, "The value of remote sensing techniques in supporting

- effective extrapolation across multiple marine spatial scales," *Mar. Pollut. Bull.* **116**(1–2), 405–419 (2017).
11. C. W. Fairall, E. F. Bradley, J. S. Godfrey, G. A. Wick, J. B. Edson, and G. S. Young, "Cool-skin and warm-layer effects on sea surface temperature," *J. Geophys. Res. Ocean.* **101**(C1), 1295–1308 (1996).
  12. D. Tanre, B. N. Holben, and Y. J. Kaufman, "Atmospheric correction against algorithm for NOAA-AVHRR products: theory and application," *IEEE Trans. Geosci. Remote Sens.* **30**(2), 231–248 (1992).
  13. R. J. W. Brewin, L. de Mora, O. Billson, T. Jackson, P. Russell, T. G. Brewin, J. D. Shutler, P. I. Miller, B. H. Taylor, T. J. Smyth, and J. R. Fishwick, "Evaluating operational AVHRR sea surface temperature data at the coastline using surfers," *Estuar. Coast. Shelf Sci.* **196**, 276–289 (2017).
  14. J. P. Abraham and M. Baringer, "A review of global ocean temperature observations: Implications for ocean heat content estimates and climate change," *Rev. Geophys.* **51**, 450–483 (2013).
  15. L. Lippsett, "Climate in flux," *Sci. Am.* 76–83 (2000).
  16. O. Möller Jr and M. P. Abe, "Oceanografia física," in *Estudos Oceanográficos: Do Instrumental Ao Prático*, D. Calazans, ed., 1st ed. (Editora de textos, 2011), p. 462.
  17. "Sippican Expendable Bathythermographic (XBT) Temperature Probe," .
  18. J. H. Churnside, "Polarization effects on oceanographic lidar.," *Opt. Express* **16**(2), 1196–1207 (2008).
  19. H. R. Gordon, "Interpretation of airborne oceanic lidar: effects of multiple scattering.," *Appl. Opt.* **21**(16), 2996–3001 (1982).
  20. M. F. Penny, R. H. Abbot, D. M. Phillips, B. Billard, D. Rees, D. W. Faulkner, D. G. Cartwright, B. Woodcock, G. J. Perry, P. J. Wilsen, T. R. Adams, and J. Richards, "Airborne laser hydrography in Australia," *Appl. Opt.* **25**(13), 2046–2058 (1986).
  21. J. H. Lee, J. H. Churnside, R. D. Marchbanks, P. L. Donaghay, and J. M. Sullivan,

- 
- "Oceanographic lidar profiles compared with estimates from in situ optical measurements," *Appl. Opt.* **52**(4), 786 (2013).
22. D. Bright, *The Use of Laser for Hydrographic Studies*, (1975).
  23. D. M. Philips, R. H. Abbot, and M. F. Penny, "Remote sensing of sea water turbidity with an airborne laser system," *J. Phys. D. Appl. Phys.* **17**(8), 1749–1758 (1984).
  24. H. R. Gordon, ed., "Ocean remote sensing using lasers," in (1980).
  25. E. F. Hoge, W. C. Wright, B. W. Krabill, R. R. Buntzen, D. G. Gilbert, N. R. Swift, K. J. Yungel, and E. R. Berry, "Airborne lidar detection of subsurface oceanic scattering layers," *Appl. Opt.* **27**(19), 3969–3977 (1988).
  26. B. Billard, R. H. Abbot, and M. F. Penny, "Airborne Estimation of Sea Turbidity Parameters from the Wrelads Laser Airborne Depth Sounder," *Appl. Opt.* **25**(13), 2080–2088 (1986).
  27. T. Dickey, M. Lewis, and G. Chang, "Optical oceanography: recent advances and future directions using global remote sensing and in situ observations," *Rev. Geophys.* **44**(2003), 1–39 (2006).
  28. C. D. Mobley, *Ligth and Water : Radiative Transfer in Natural Waters* (1994).
  29. W. S. Pegau, D. Gray, and J. R. V Zaneveld, "Absorption and attenuation of visible and near-infrared light in water: dependence on temperature and salinity," *Appl. Opt.* **36**(24), 6035–6046 (1997).
  30. J. G. Bayly, V. B. Kartha, and W. H. Stevens, "The absorption spectra of liquid phase H<sub>2</sub>O, HDO and D<sub>2</sub>O from 0.7  $\mu$ m to 10  $\mu$ m," *Infrared Phys.* **3**(4), 211–222 (1963).
  31. R. M. Pope and E. S. Fry, "Absorption spectrum (380–700 nm) of pure water II Integrating cavity measurements," *Appl. Opt.* **36**(33), 8710 (1997).
  32. X. Zhang and L. Hu, "Estimating scattering of pure water from density fluctuation of the refractive index," **17**(3), 3485–3489 (2009).
  33. X. Zhang, L. Hu, and M. He, "Scattering by pure seawater : Effect of salinity," **17**(7), 5698–5710 (2009).

34. G. N. I. Clark, C. D. Cappa, J. D. Smith, R. J. Saykally, and T. Head-Gordon, "The structure of ambient water," *Mol. Phys.* **108**(11), 1415–1433 (2010).
35. H. Xu, H. A. Stern, and B. J. Berne, "Can Water Polarizability Be Ignored in Hydrogen Bond Kinetics?," *J. Phys. Chem. B* **106**(8), 2054–2060 (2002).
36. A. Morel, "Optical properties of pure and seawater," in *Optical Aspects of Oceanography*, J. N.G. and E. Steenmann Nielsen, eds. (Academic Press London and New York, 1974).
37. O. Conde, J. Teixeira, O. Conde, and J. T. Hydrogen, "Hydrogen bond dynamics in water studied by depolarized Rayleigh scattering To cite this version : HAL Id : jpa-00209627 by depolarized Rayleigh scattering," (1983).
38. C. J. Montrose, J. A. Bucarot, and T. A. Utovitz, "Depolarized Rayleigh scattering and hydrogen bonding in liquid water \*," **60**(12), 5025–5029 (1974).
39. R. L. Schwiesow and L. Lading, "Temperature profiling by Rayleigh-scattering lidar," *Appl. Opt.* **20**(11), 1972 (1981).
40. R. Xiu-Yun, T. Zhao-Shuo, M. Yang, S. Lan-Jun, and F. Shi-You, "Theoretical study on measuring underwater temperature based on coherent Rayleigh scattering," *Acta Phys. Sin.* **63**(8), 83302 (2014).
41. J. G. Hirschberg, J. D. Byrne, A. W. Wouters, and G. C. Boynton, "Speed of sound and temperature in the ocean by Brillouin scattering," *Appl. Opt.* **23**(15), 2624 (1984).
42. J. L. Guagliardo and H. L. Dufilho, "Range-resolved Brillouin scattering using a pulsed laser," *Rev. Sci. Instrum.* **51**(1), 79–81 (1980).
43. K. Schorstein, A. Popescu, M. Göbel, and T. Walther, "Remote Water Temperature Measurements Based on Brillouin Scattering with a Frequency Doubled Pulsed Yb:doped Fiber Amplifier," *Sensors* **8**(9), 5820–5831 (2008).
44. K. Schorstein, E. S. Fry, and T. Walther, "Depth-resolved temperature measurements of water using the Brillouin lidar technique," *Appl. Phys. B* **97**(4), 931–934 (2009).
45. J. Graul and T. Lilly, "Coherent Rayleigh-Brillouin scattering measurement of



- 
- atmospheric atomic and molecular gas temperature," *Opt. Express* **22**(17), 20117 (2014).
46. K. Liang, J. Xu, P. Zhang, Y. Wang, Q. Niu, L. Peng, and B. Zhou, "Temperature Dependence of the Rayleigh Brillouin Spectrum Linewidth in Air and Nitrogen," *Sensors* **17**(7), 1503 (2017).
  47. J. Ferraro and K. Nakamoto, *Introductory Raman Spectroscopy* (Elsevier, 2003).
  48. D. M. Carey and G. M. Korenowski, "Measurement of the Raman spectrum of liquid water," *J. Chem. Phys.* **108**(7), 2669 (1998).
  49. G. W. Faris and R. A. Copeland, "Wavelength dependence of the Raman cross section for liquid water," *Appl. Opt.* **36**(12), 2686 (1997).
  50. T. Plakhotnik and J. Reichardt, "Accurate absolute measurements of the Raman backscattering differential cross-section of water and ice and its dependence on the temperature and excitation wavelength," *J. Quant. Spectrosc. Radiat. Transf.* **194**, 58–64 (2017).
  51. W. K. Bischel, G. Black, Test, C. S. Allman, C. S. Allman, M. Smith, D. Saltzberg, and T. Troscher, "Wavelength dependence of raman scattering cross sections from 200-600 nm," in *AIP Conference Proceedings* (AIP, 1983), **100**, pp. 181–187.
  52. C. P. Artlett, "Remote sensing of water temperature using Raman spectroscopy," Sydney, Australia : Macquarie University (2015).
  53. G. E. Walrafen, "Raman Spectral Studies of the Effects of Temperature on Water Structure," *J. Chem. Phys.* **47**(1), 114 (1967).
  54. W. B. Monosmith and G. E. Walrafen, "Temperature dependence of the Raman OH-stretching overtone from liquid water," *J. Chem. Phys.* **81**(2), 669–674 (1984).
  55. Q. Sun, "Raman spectroscopic study of the effects of dissolved NaCl on water structure," *Vib. Spectrosc.* **62**, 110–114 (2012).
  56. C. P. Artlett and H. M. Pask, "New approach to remote sensing of temperature and salinity in natural water samples," *Opt. Express* **25**(3), 2840 (2017).

57. G. E. Walrafen, M. R. Fisher, M. S. Hokmabadi, and W.-H. Yang, "Temperature dependence of the low- and high-frequency Raman scattering from liquid water," *J. Chem. Phys.* **85**(12), 6970–6982 (1986).
58. E. Ségre, "No Title," *Rend. Lincei* **13**(929), (1931).
59. G. Bolla, "No Title," *Nuovo Cim.* **9**(290), (1932).
60. a. V. Kargovsky, "On temperature dependence of the valence band in the Raman spectrum of liquid water," *Laser Phys. Lett.* **3**(12), 567–572 (2006).
61. C. H. Chang and L. A. Young, *Seawater Temperature Measurement from Raman Spectra* (1972).
62. D. a Leonard, B. Caputo, and F. E. Hoge, "Remote sensing of subsurface water temperature by Raman scattering.," *Appl. Opt.* **18**(11), 1732–45 (1979).
63. C. P. Artlett and H. M. Pask, "Optical remote sensing of water temperature using Raman spectroscopy," *Opt. Express* **23**(25), 31844 (2015).
64. D. N. Whiteman, G. E. Walrafen, W. H. Yang, and S. H. Melfi, "Measurement of an isosbestic point in the Raman spectrum of liquid water by use of a backscattering geometry.," *Appl. Opt.* **38**(12), 2614–2615 (1999).
65. G. E. Walrafen, M. S. Hokmabadi, and W.-H. Yang, "Raman isosbestic points from liquid water," *J. Chem. Phys.* **85**(12), 6964 (1986).
66. J. D. Eaves, J. J. Loparo, C. J. Fecko, S. T. Roberts, A. Tokmakoff, and P. L. Geissler, "Hydrogen bonds in liquid water are broken only fleetingly.," *Proc. Natl. Acad. Sci. U. S. A.* **102**(37), 13019–22 (2005).
67. J. D. Smith, C. D. Cappa, K. R. Wilson, R. C. Cohen, P. L. Geissler, and R. J. Saykally, "Unified description of temperature-dependent hydrogen-bond rearrangements in liquid water," *Proc. Natl. Acad. Sci.* **102**(40), 14171–14174 (2005).
68. C. H. Chang and L. A. Young, *Seawater Temperature Measurement from Raman Spectra* (1972).
69. D. A. Leonard, B. Caputo, and R. L. Johnson, "Experimental remote sensing of

- subsurface temperature in natural ocean water," *Geophys. Res. Lett.* **4**(7), 279–281 (1977).
70. R. SCHWIESOW, "Raman scattering studies of pollutant systems," in *Joint Conference on Sensing of Environmental Pollutants* (American Institute of Aeronautics and Astronautics, 1971).
  71. D. A. Leonard, B. Caputo, and F. E. Hoge, "Remote sensing of subsurface water temperature by Raman scattering," *Appl. Opt.* **18**(11), 1732–45 (1979).
  72. B. Breschi, G. Cecchi, L. Pantani, V. Raimondi, D. Tirelli, and G. Valmori, "Measurement of Water Column Temperature by Raman Scattering," *EARsel Adv. Remote Sens.* **1**(2), 131–134 (1992).
  73. Z. Liu, J. Zhang, and W. Chen, "Remote sending of subsurface water temperature using Raman Lidar," *SPIE* **1633**(Laser Radar VII), 321–329 (1992).
  74. G. Cecchi and V. Raimondi, "Remote Raman spectra for the monitoring of water column temperature," in *1995 International Geoscience and Remote Sensing Symposium, IGARSS '95. Quantitative Remote Sensing for Science and Applications* (IEEE, n.d.), **3**, pp. 1741–1743.
  75. M. . Becucci, S. . Cavalieri, R. . Eramo, L. . Fini, and M. . Materazzi, "Accuracy of remote sensing of water temperature by Raman spectroscopy," *Appl. Opt.* **38**(6), 928–931 (1999).
  76. D. Risović and K. Furić, "Comparison of Raman spectroscopic methods for the determination of supercooled and liquid water temperature," *J. Raman Spectrosc.* **36**(8), 771–776 (2005).
  77. T. Dolenko, S. Burikov, A. Sabirov, and V. Fadeev, "Remote determination of temperature and salinity in presence of dissolved organic matter in natural waters using laser spectroscopy," *EARSeL eProceedings* **10**(2), 159–165 (2011).
  78. S. A. Burikov, T. A. Dolenko, P. A. Velikotny, A. V Sugonyaev, and V. V Fadeev, "The Effect of Hydration of Ions of Inorganic Salts on the Shape of the Raman Stretching Band of Water," *Opt. Spectrosc.* **98**(2), 235–279 (2005).

79. C. H. Chang and L. A. Young, "Remote measurement of ocean temperature from depolarization in Raman scattering," in *The Use of Lasers for Hydrographic Studies* (1975), pp. 105–112.
80. D. A. Leonard and B. Caputo, "Raman Remote Sensing Of The Ocean Mixed-Layer Depth," *Opt. Eng.* **22**(3), (1983).
81. C. S. Reynolds, *The Ecology of Phytoplankton* (Cambridge University Press, 2006).
82. B. Greg Mitchell and D. A. Kiefer, "Chlorophyll  $\alpha$  specific absorption and fluorescence excitation spectra for light-limited phytoplankton," *Deep Sea Res. Part A, Oceanogr. Res. Pap.* (1988).
83. J. W. Hofstraat, K. Rubelowsky, and S. Slutter, "Corrected fluorescence excitation and emission spectra of phytoplankton: Toward a more uniform approach to fluorescence measurements," *J. Plankton Res.* **14**(5), 625–636 (1992).
84. F. Zhang, R. Su, J. He, M. Cai, W. Luo, and X. Wang, "Identifying phytoplankton in seawater based on discrete excitation-emission fluorescence spectra," *J. Phycol.* **46**(2), 403–411 (2010).
85. C. W. Proctor and C. S. Roesler, "New insights on obtaining phytoplankton concentration and composition from in situ multispectral Chlorophyll fluorescence," *Limnol. Oceanogr. Methods* **8**(Dickey 1991), 695–708 (2010).
86. J. E. James, C. S. Lin, and W. P. Hooper, "Simulation of laser-induced light emissions from water and extraction of Raman signal," *J. Atmos. Ocean. Technol.* **16**(2–3), 394–401 (1999).
87. C. S. Lin, "Characteristics of laser-induced inelastic-scattering signals from coastal waters," *Remote Sens. Environ.* **77**(1), 104–111 (2001).
88. P. Chen, D. Pan, and Z. Mao, "Fluorescence measured using a field-portable laser fluorometer as a proxy for CDOM absorption," *Estuar. Coast. Shelf Sci.* **146**, 33–41 (2014).
89. P. G. Coble, "Marine Optical Biogeochemistry: The Chemistry of Ocean Color," *Chem. Rev.* **107**(2), 402–418 (2007).

- 
90. S. Patsayeva and R. Reuter, "Spectroscopic study of major components of dissolved organic matter naturally occurring in water," 10 (1995).
  91. K. Kalle, "The problem of the gelbstoff in the sea," *Ocean. Mar. Biol. Ann. Rev.* **4**, (1966).
  92. A. Vervald, E. Mazurin, and I. Plastinin, "Simultaneous Determination of Temperature and Salinity of Natural Waters By Raman Spectra Using," (1), 28–36 (2015).
  93. G. C. Chang and T. D. Dickey, "Correction to "Optical and physical variability on timescales from minutes to the seasonal cycle on the New England shelf: July 1996 to June 1997" by G. C. Chang and T. D. Dickey," *J. Geophys. Res.* **106**(June 1997), 19997 (2001).
  94. X. Zhang, M. Lewis, and B. Johnson, "Influence of bubbles on scattering of light in the ocean," *Appl. Opt.* **37**(27), 6525 (1998).
  95. D. Stramski and S. B. Woźniak, "On the role of colloidal particles in light scattering in the ocean," *Limnol. Oceanogr.* **50**(5), 1581–1591 (2005).
  96. A. L. Whitmire, W. S. Pegau, L. Karp-Boss, E. Boss, and T. J. Cowles, "Spectral backscattering properties of marine phytoplankton cultures," *Opt. Express* **18**(14), 15073–15093 (2010).
  97. D. A. Leonard and B. Caputo, "Raman Remote Sensing Of The Ocean Mixed-Layer Depth," *Opt. Eng.* **22**(3), (1983).
  98. F. A. Bunkin, K. V. Klinkov, N. V. Lednev, L. D. Lushnikov, V. A. Marchenko, G. E. Morozov, M. S. Pershin, N. R. Yulmetov, A. F. Bunkin, V. K. Klinkov, V. N. Lednev, D. L. Lushnikov, A. V. Marchenko, E. G. Morozov, S. M. Pershin, and R. N. Yulmetov, "Remote sensing of seawater and drifting ice in Svalbard fjords by compact Raman lidar," *Appl. Opt.* **51**(22), 5477–5485 (2012).
  99. R. C. Smith and K. S. Baker, "Optical properties of the clearest natural waters (200–800 nm)," *Appl. Opt.* **20**(2), 177 (1981).
  100. M. G. Solonenko and C. D. Mobley, "Inherent optical properties of Jerlov water

- types," *Appl. Opt.* **54**(17), 5392 (2015).
101. N. G. Jerlov, ed., *Optical Oceanography*, 1st editio (Elsevier, 1968).
102. C. D. Mobley, "Overview of Optical Oceanography," [http://www.oceanopticsbook.info/view/overview\\_of\\_optical\\_oceanography/classification\\_schemes](http://www.oceanopticsbook.info/view/overview_of_optical_oceanography/classification_schemes).
103. J. T. O. Kirk, "The upwelling light stream in natural waters," *Limnol. Oceanogr.* **34**(8), 1410–1425 (1989).
104. C. Lin, "Tunable laser induced scattering from coastal water," *IEEE Trans. Geosci. Remote Sens.* **37**(5), 2461–2468 (1999).
105. M. Oh, H. Kang, N. E. Yu, B. H. Kim, J. Kim, J. Lee, and G. W. Hyung, "Ultimate sensing resolution of water temperature by remote Raman spectroscopy," *Appl. Opt.* **54**(10), 2639–2646 (2015).
106. K. H. Esbensen, D. Guyot, F. Westad, and L. P. Houmøller, *Multivariate Data Analysis: In Practice: An Introduction to Multivariate Data Analysis and Experimental Design*, 5th ed. (CAMO Process AS, 2002).
107. J. Shlens, "A Tutorial on Principal Component Analysis," (2014).
108. H. Abdi and L. J. Williams, "Principal component analysis," *Wiley Interdiscip. Rev. Comput. Stat.* **2**(4), 433–459 (2010).
109. H. E. Nystad, "Comparison of Principal Component Analysis and Spectral Angle Mapping for Identification of Materials in Terahertz Transmission Measurements," (2015).
110. Hamamatsu Photonics K.K. All Rights Reserved., "Photosensor module Hamamatsu," <https://www.hamamatsu.com/jp/en/product/type/H10721-110/index.html>.
111. K. Cunningham and P. A. Lyons, "Depolarization ratio studies on liquid water," *J. Chem. Phys.* **59**(4), 2132–2139 (1973).

- 
112. R. M. Measures, *Laser Remote Sensing: Fundamentals and Applications* (John Wiley & Sons Inc, 1984).
  113. A. de Lima Ribeiro, C. Arlett, P. Ajani, C. Derkenne, and H. Pask, "Manuscript 1. "The impact of fluorescence on Raman remote sensing of temperature in natural water samples"", To be Submitt. to Opt. Express (n.d.).
  114. A. de Lima Ribeiro, C. Artlett, and H. Pask, "Manuscript 2."A LIDAR-compatible, multichannel Raman spectrometer for remote sensing of water temperature"", To be Submitt. to Sensors (n.d.).
  115. A. de lima Ribeiro and H. Pask, "Manuscript 3. "Remote sensing of temperature in natural water samples using a multichannel, lidar-compatible Raman spectrometer and blue excitation (473 nm)"" To be Submitt. to Front. Mar. Sci. (n.d.).
  116. J. Wozencraft and D. Millar, "Airborne Lidar and Integrated Technologies for Coastal Mapping and Nautical Charting," Mar. Technol. Soc. J. **39**(3), 27–35 (2005).
  117. T. Allouis, J. S. Bailly, Y. Pastol, and C. Le Roux, "Comparison of LiDAR waveform processing methods for very shallow water bathymetry using Raman, near-infrared and green signals," Earth Surf. Process. Landforms **35**(6), 640–650 (2010).
  118. J. H. Ryther, "in the Ocean as a Function Photosynthesis of Light," Soc. Am. **1**(1), 61–70 (2013).

# APPENDIX A

## APPLYING “CORRECTION BY MARKERS”

As a complementary investigation, I explored the use of the method of correction by temperature markers, proposed in Chapter 3, as a tool for self-predicted measurements in field acquisitions.

### A.1. Green multichannel Raman spectrometer markers

Our multichannel Raman spectrometer exhibited high performance measuring water temperatures in laboratory, achieving accuracies as high as  $\pm 0.4^{\circ}\text{C}$  (without LC analysis) in comparison with reference temperature values measured by a probe. When performing field trials, however, reference temperatures are not available for correlating with every temperature marker. In Chapter 3, I presented an innovative baseline correction technique based on temperature marker values for two-colour unpolarised signals; in this section, I discuss how this technique could support self-predicted measurements by using only one reference temperature measurement.

The correction method by temperature marker values is based on the premise that, in the absence of other signal sources, Raman marker values should have the same values for any water sample of given temperature. In Chapter 3, “standard” marker values were attributed to Rose Bay water, which underwent UV treatment and mechanical filtration. In those simulations (which were based in real data), temperature markers were calculated for unpolarised channels of  $200\text{ cm}^{-1}$  width and collected by a commercial Raman spectrometer integrated to a CW-532 nm Nd:YAG laser. For the work reported in this Chapter, Rose Bay water was not available to us, and accordingly, the best “standard” marker values are the ones calculated from by Milli-Q water signals acquired by our multichannel RS.

Differences between “standard” and natural waters temperature marker values are believed to be caused by overlapping between the Raman peak and other signals from optically active constituents, such as fluorescence from DOM and photosynthetic pigments. Differences in salinity are a second factor impacting our predictions. Differences in salinity



is a second factor. These differences are estimated by two parameters,  $\Delta R$  and  $C$ , which are explained in detail in **manuscript 1**.  $\Delta R$  is calculated by subtracting “standard” temperature-dependent marker values from markers calculated for a natural water sample, whilst  $C$  corresponds to the ratio between markers from natural and “standard” waters. This correction method requires one measurement performed *in situ* by the spectrometer to be associated with a known temperature. As detailed in Chapter 3, this calibration in the field could be performed by collecting a sample of water, using an *in situ* temperature sampler (e.g. a buoy) or potentially data from a satellite. Here we will assume such a measurement has been made so we know the temperature associated with a given ratio collected *in situ*,  $\Delta R$  and  $C$  could be estimated between the *in situ* marker and the “standard” marker for the known temperature. “Standard” linear models of temperature prediction could then be applied to corrected ratios from natural waters.

In order to evaluate if the approach described above is feasible,  $\Delta R$  and  $C$  parameters were calculated for every set of measurements for the natural water samples presented in this study by using Milli-Q water markers as “standards”. Average values for both  $\Delta R$  and  $C$  were independently used to correct the temperature markers for the natural water samples. After correction, predictive linear models determined for Milli-Q “standard” water were applied to the new, corrected natural water ratios and RMSTEs were estimated. The goal for this analysis is exploring if one (or more) global prediction models based on marker ratios could determine temperatures in the field. RMSTEs estimations for calibrated temperature markers are shown in table A.1. Temperature accuracies better or equal to  $\pm 1.0^\circ\text{C}$  are indicated in green; from  $\pm 1.1^\circ\text{C}$  to  $\pm 2.0^\circ\text{C}$  are signalled in yellow; and RMSTEs higher than  $\pm 2.0^\circ\text{C}$  are indicated in red.

Table A.1. RMSTEs for natural water samples calibrated by Milli-Q  $\Delta R$  and  $C$  estimations

Temperature markers	Natural sample 1		Natural sample 2		Natural sample 3	
	RMSTE for $\Delta R$ calibration ( $\pm^\circ\text{C}$ )	RMSTE for $C$ calibration ( $\pm^\circ\text{C}$ )	RMSTE for $\Delta R$ calibration ( $\pm^\circ\text{C}$ )	RMSTE for $C$ calibration ( $\pm^\circ\text{C}$ )	RMSTE for $\Delta R$ calibration ( $\pm^\circ\text{C}$ )	RMSTE for $C$ calibration ( $\pm^\circ\text{C}$ )
Two-colour( $\parallel$ )	1.3	1.1	0.4	0.5	0.7	0.8
Two-colour( $\perp$ )	3.8	4.0	1.3	1.3	1.1	1.5
Depolarisation(A)	2.0	2.3	1.5	1.4	4.9	5.0
Depolarisation(B)	3.0	3.5	1.7	1.6	6.9	4.6

Temperature predictions performed by two-colour( $\parallel$ ) applied to “standard” models showed best accuracies among markers, ranging from  $\pm 0.4^\circ\text{C}$  to  $\pm 1.3^\circ\text{C}$ . Considering recent estimations indicate errors from  $\pm 1.0^\circ\text{C}$  to  $\pm 2.0^\circ\text{C}$  for sea surface temperature measurements made by satellite images at coastal zones, the accuracies found in this analysis are of interest for remote sensing measurements. Prediction by “standard” models applied to two-colour( $\perp$ ), depolarisation(A) and depolarisation(B) exhibited considerably less accurate results.

In due course, improvements could be made in this calibration process by having “standard” marker values in a range of temperatures and salinities for different Jerlov water types and this calibration process could be further used in combination with LC methods.

## A.2. Blue multichannel Raman spectrometer markers

In this section, I aim to evaluate the theoretical performance of our blue multichannel RS as a self-calibrated system using the “correction by temperature markers” method proposed in manuscript 1 [113]. The methods employed in this section are described in detail in section A.1, and consider the premise that the marker values for a natural water sample deviate from the values calculated for a “standard” water sample due to the presence of optically active components in water overlapping with the water Raman peak. *Here, the “standard” water sample markers values were calculated for a Milli-Q water sample and were used for calibration of markers obtained from natural waters.* RMSTEs for the calibrated temperature markers are shown in table A.2. Temperature accuracies lower than  $\pm 1.0$  are indicated in green; from

Table A.2. RMSTEs for natural water samples calibrated by Milli-Q  $\Delta R$  and C estimations.

Temperature markers	Natural sample 1		Natural sample 2		Natural sample 3		Natural sample 4	
	RMSTE for $\Delta R$ calibration ( $\pm^\circ\text{C}$ )	RMSTE for C calibration ( $\pm^\circ\text{C}$ )	RMSTE for $\Delta R$ calibration ( $\pm^\circ\text{C}$ )	RMSTE for C calibration ( $\pm^\circ\text{C}$ )	RMSTE for $\Delta R$ calibration ( $\pm^\circ\text{C}$ )	RMSTE for C calibration ( $\pm^\circ\text{C}$ )	RMSTE for $\Delta R$ calibration ( $\pm^\circ\text{C}$ )	RMSTE for C calibration ( $\pm^\circ\text{C}$ )
Two-colour( $\parallel$ )	1.3	0.7	1.4	0.9	1.3	0.8	1.8	0.9
Two-colour( $\perp$ )	2.2	2.4	1.7	1.6	1.2	1.1	1.0	1.0
Depolarisation(A)	1.5	2.0	1.5	1.7	0.9	0.9	1.6	1.8
Depolarisation(B)	3.9	3.9	3.9	3.8	3.9	3.5	4.6	4.1

25% of the temperature predictions performed by the calibrated temperature markers exhibited accuracies better than  $\pm 1.0^\circ\text{C}$ . Two-colour( $\parallel$ ) were responsible for half of these highly accurate measurements, whilst two-colour( $\perp$ ) and depolarisation(A) each contributed to 25% of these measurements. Accuracies between  $\pm 1.1^\circ\text{C}$  and  $\pm 2.0^\circ\text{C}$  were achieved in 37.5% of the measurements for the abovementioned calibrated temperature markers. Calibrated depolarisation(B) markers exhibited the poorest accuracies, varying from  $\pm 3.5^\circ\text{C}$  and  $\pm 4.6^\circ\text{C}$ .

For the natural water samples analysed in our study, two-colour( $\parallel$ ), two-colour( $\perp$ ) and depolarisation(B) calibrated Raman markers excited from blue light have shown the potential for achieving accuracies similar to measurements performed by traditional remote sensing methods, such as infrared satellite imagery, in coastal areas. We expect to increase these predictions in the future by calculating “standard” markers for water samples with different salinities and optically active constituents. In the future, we also expect to increase the accuracies of self-prediction measurements by associating them to LC methods

# APPENDIX B

## OPTICAL FILTERS SPECIFICATIONS

A series of optical filters were used in my multichannel Raman spectrometers, as shown in chapters 4 and 5. This appendix includes technical specifications and detailed description of each of these filters.

### B.1. Optical filters – green multichannel RS (532 nm excitation)

#### Long Pass filter for 532 nm excitation – Semrock BLP01-532 R

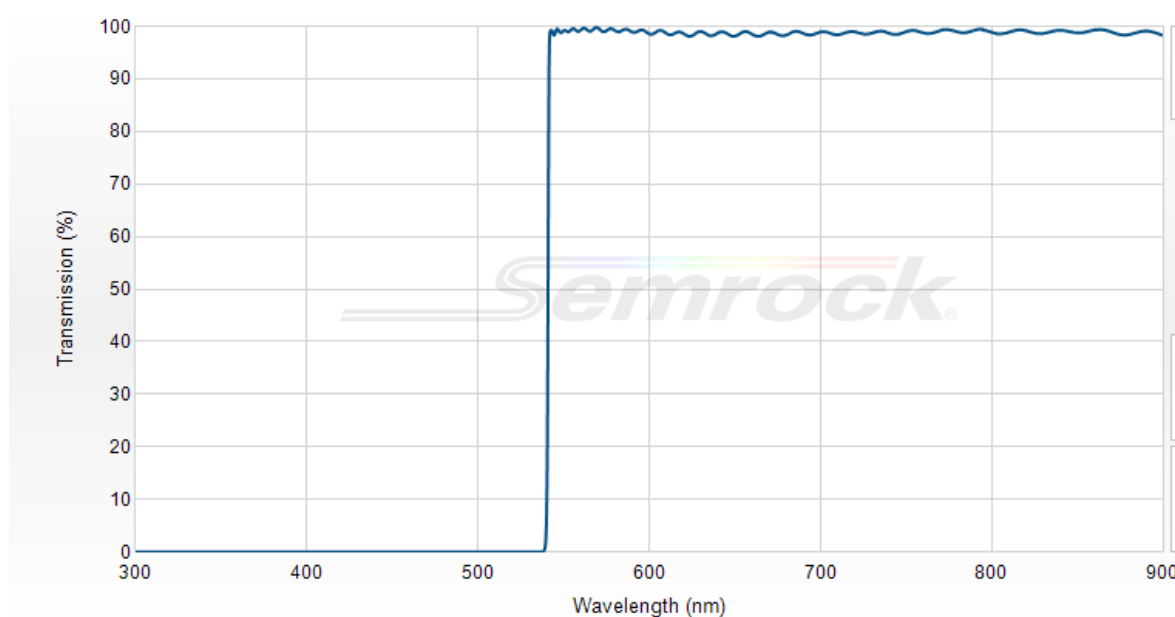


Figure B.1. Wavelength-dependent transmission (%) for Long Pass filter Semrock BLP01522-R

Table B.1. Technical specifications for Long Pass filter Semrock BLP01522-R

Specification	Value
Transmission Band 1	$T_{\text{avg}} > 93\%$ 532-900 nm
Blocking Band 1	$OD_{\text{avg}} > 5$ 270-435.6 nm
Blocking Band 2	$OD_{\text{abs}} > 6$ 425.6-532 nm

### **Band Pass filter for “low channel” (green RS) – Semrock LD01-640/8**

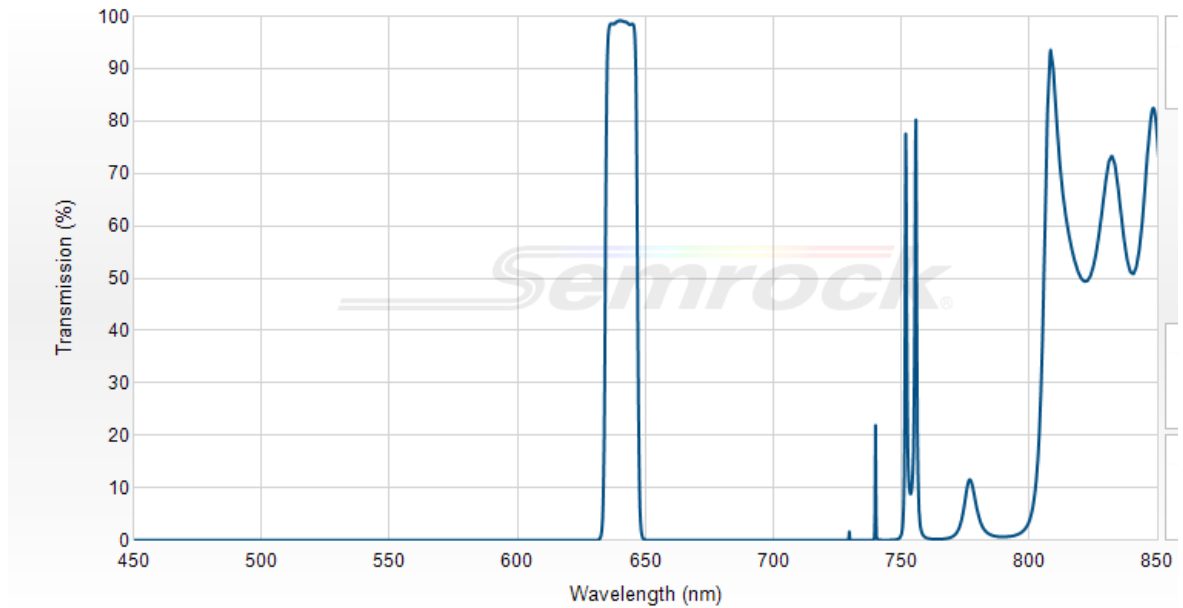


Figure B.2. Wavelength-dependent transmission (%) for Band Pass filter Semrock LD01-640/8.

Table B.2. Technical specifications for Long Pass filter Semrock BLP01522-R

<b>Specification</b>	<b>Value</b>
Transmission Band 1	$T_{\text{avg}} > 90\%$ 636.3-644.3 nm
Center Wavelength	640 nm
Blocking Band 1	$OD_{\text{avg}} > 5$ 270-435.6 nm
FWHM Bandwidth 1 (nominal)	12.9 nm
Blocking Band 1	$OD_{\text{avg}} > 3$ 400-625 nm
Blocking Band 2	$OD_{\text{avg}} > 5$ 580-622 nm
Blocking Band. 3	$OD_{\text{avg}} > 5$ 658-717 nm
Blocking Band 4	$OD_{\text{avg}} > 3$ 655-720 nm

**Band Pass filter for “high channel” (green RS) – Semrock FF01-660/13**

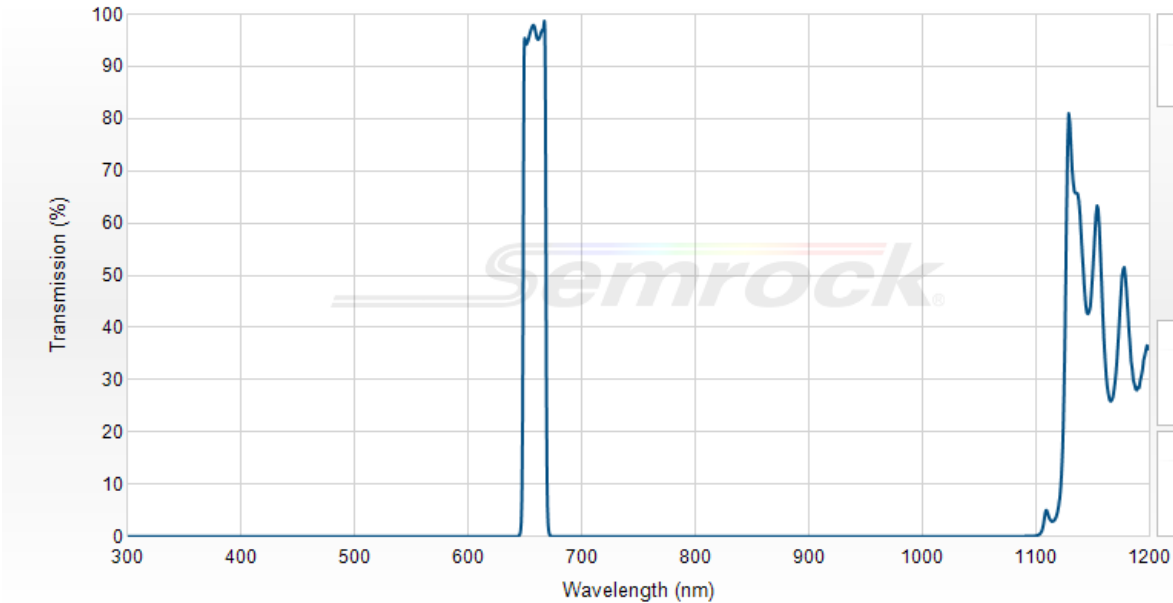


Figure B.3. Wavelength-dependent transmission (%) for Band Pass filter Semrock FF01-660/8.

Table B.3. Technical specifications for Long Pass filter Semrock FF01-660/8..

Specification	Value
Transmission Band 1	$T_{avg} > 93\%$ 653.5-666.5 nm
Center Wavelength	660 nm
FWHM Bandwidth 1 (nominal)	20.2 nm

## B.2. Optical filters – blue multichannel RS (473 nm excitation)

### Long Pass filter for 473 nm excitation – Semrock BLP01-473R

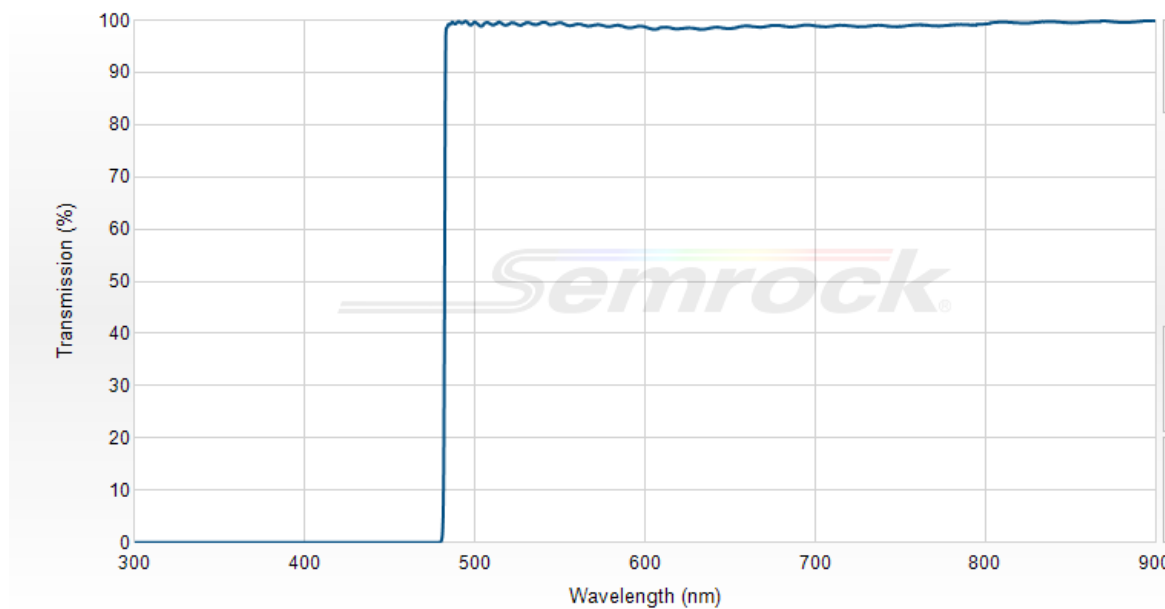


Figure B.4. Wavelength-dependent transmission (%) for Long Pass filter Semrock BLP01-473-R

Table B.4. Technical specifications for Long Pass filter Semrock BLP01522-R

Specification	Value
Transmission Band 1	$T_{\text{avg}} > 93\%$ 473-900 nm
Blocking Band 1	$OD_{\text{avg}} > 5$ 200-378.4.6 nm
Blocking Band 2	$OD_{\text{abs}} > 6$ 378.4.6-473 nm

**Band Pass filter for “low channel” (blue RS) – Semrock FF001-568**

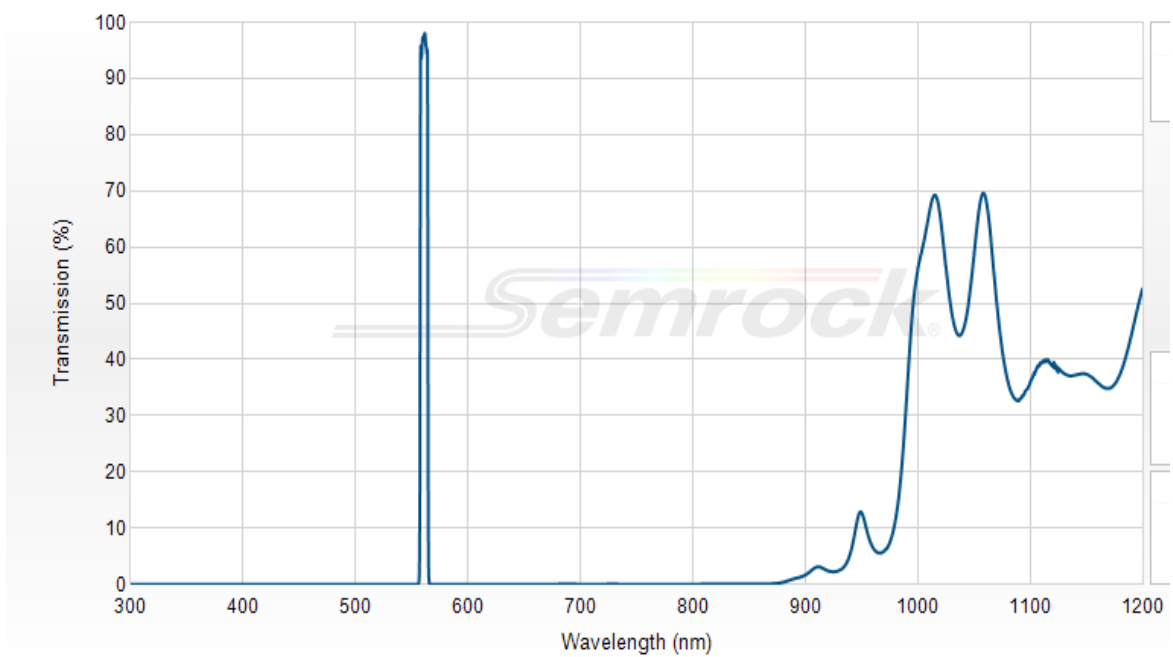


Figure B.5. Wavelength-dependent transmission (%) for Band Pass filter Semrock LD01-640/8.

Table B.5. Technical specifications for Long Pass filter Semrock BLP01522-R

Specification	Value
Transmission Band 1	T <sub>avg</sub> > 93% 559-563 nm
Center Wavelength	561 nm
FWHM Bandwidth 1 (nominal)	7.2 nm



### **Band Pass filter for “high channel” (bue RS) – Semrock LL01-568**

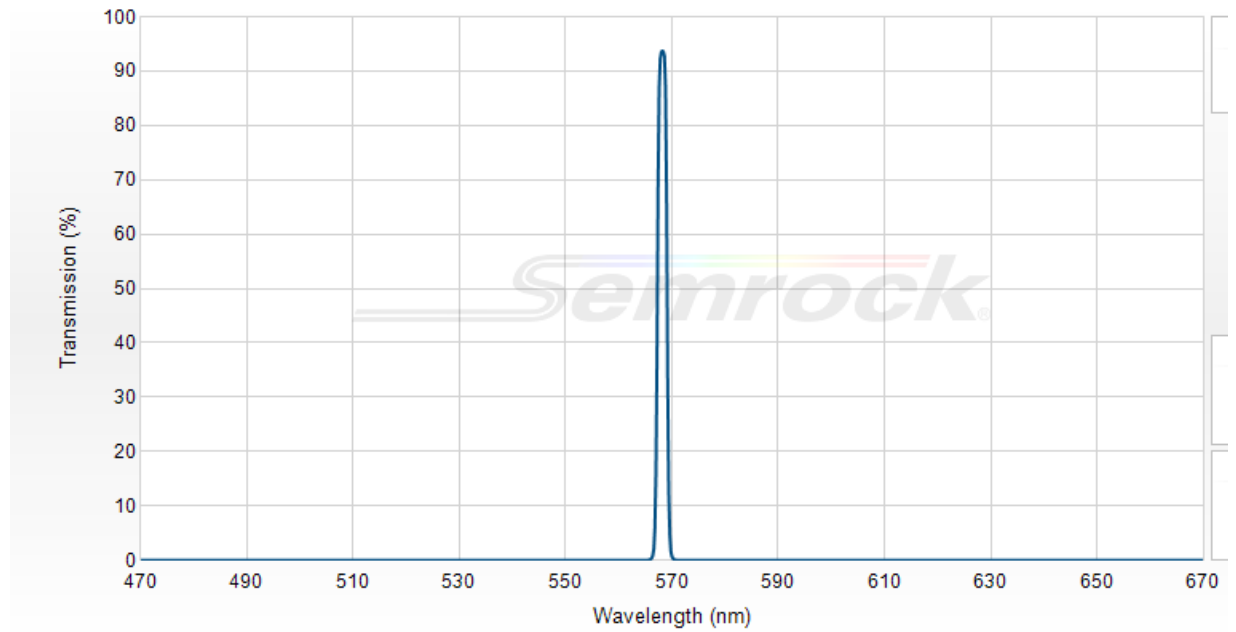


Figure B.6. Wavelength-dependent transmission (%) for Band Pass filter Semrock FF01-660/8.

Table B.6. Technical specifications for Long Pass filter Semrock FF01-660/8..

<b>Specification</b>	<b>Value</b>
Transmission Band 1	$T_{\text{avg}} > 90\%$ 568.2 nm
Center Wavelength	568.2 nm
FWHM Bandwidth 1 (nominal)	2.2 nm (typical); 4 nm (maximum)

# APPENDIX C

## CONFERENCE PRESENTATIONS

- A. de Lima Ribeiro, C. Artlett and H. Pask, “Active remote sensing of water temperature using a LIDAR-compatible Raman Spectrometer and different excitation lasers”, Poster presentation, Ocean Sciences Meeting, Portland, USA (2018).
- A. de Lima Ribeiro and H. Pask. “Four-channel Raman Spectrometer and linear combination methods: increasing the accuracy for remote water temperature measurement”, Poster presentation, Ocean Sciences meeting, Portland, USA (2018).
- C. Artlett, A. de Lima Ribeiro and H. Pask, “Impact of baseline correction on the accuracy of water temperature measurement with Raman spectroscopy”, Poster presentation, Joint 25th AMOS National Conference and 12th International Conference for Southern Hemisphere Meteorology and Oceanography, Sydney, Australia (2018).
- A. de Lima Ribeiro, P. Ajani, C. Derkenne, C. Artlett and H. Pask. “Fluorescence impact on Raman remote sensing of water temperature”. Oral presentation, Joint 25th AMOS National Conference and 12th International Conference for Southern Hemisphere Meteorology and Oceanography, Sydney, Australia (2018).
- A. de Lima Ribeiro, C. Artlett and H. Pask. “Methods for temperature sensing in natural waters based on Raman spectroscopy and blue excitation”, Oral presentation, 3<sup>rd</sup> Australia New Zealand Conference on Optics and Photonics, Queenstown, New Zealand (2017).
- A. de Lima Ribeiro, C. Artlett and H. Pask. “Water temperature measurement using blue excitation and two-channel Raman spectrometer”, Poster presentation, Joint 13<sup>th</sup> Asia Pacific Physics Conference and 22<sup>nd</sup> Australian Institute of Physics Congress, Brisbane, Australia (2016).

### ACTIVE REMOTE SENSING OF WATER TEMPERATURE USING A LIDAR-COMPATIBLE RAMAN SPECTROMETER AND DIFFERENT LASER SOURCES (BLUE AND GREEN)

Andréa de Lima Ribeiro<sup>1</sup>, Christopher Artlett<sup>1,2</sup> and Helen Pask<sup>1</sup>

<sup>1</sup>*Macquarie University, Physics and Astronomy, Sydney, Australia,*

<sup>2</sup>*Defence, Science and Technology Group, Australia*

The Raman signal (RS) of water exhibits significant variation with temperature, hence Raman spectroscopy is a technique that associated with LIDAR methods has the potential to provide depth-resolved temperature data. We propose a LIDAR compatible, custom-built Raman spectrometer to determine water temperature and compare the accuracy of blue (473 nm) and green (532 nm) active excitation lights. Both lasers were short pulsed ( $\leq 2$  ns), characteristics that along with time-resolved detectors (photomultipliers) enabled us to retrieve RS from 6 m depth on preliminary field studies. We aimed to collect RS on regions of the spectra before and after the isosbestic point highly correlated to temperature, therefore we acquired Raman spectra using a commercial spectrometer and generated Root Mean Square Temperature Error (RMSTE) maps. Based on these maps, we selected band pass filters centred on areas with smallest RMSTE and coupled them to our system in two independent collecting channels. Unpolarised RS of natural water were acquired in laboratory by using either of the laser sources. Each signal was integrated around the peak and a prediction marker was calculated (“two-colour” ratio). Linear models correlated the prediction ratios and known temperature. The RMSTEs for samples excited with green (blue) light ranged from  $\pm 0.5^{\circ}\text{C}$  to  $\pm 0.8^{\circ}\text{C}$  ( $\pm 0.6^{\circ}\text{C}$  to  $\pm 1.2^{\circ}\text{C}$ ). To evaluate how the system would work on the field, we built a model of generation of Raman signal dependent on excitation wavelength (475 nm and 532 nm, same number of incident photons). The diffuse attenuation coefficients for Jerlov water type 1 (coastal) were used to identify the maximum depth achieved by the excitation source ( $< 1\%$  of incident light) and potential for RS detection. The maximum depth for green (blue) excitation was 30 m (27 m), with RS potential collection of up to 8 m (15 m). This shows that both lasers are suitable to our LIDAR-based Raman spectrometer, working on different optimal depths.

# FOUR-CHANNEL RAMAN SPECTROMETER AND LINEAR COMBINATION METHODS: INCREASING THE ACCURACY FOR REMOTE WATER TEMPERATURE MEASUREMENT

Andréa de Lima Ribeiro<sup>1</sup> and Helen Pask<sup>1</sup>

<sup>1</sup>*Macquarie University, Physics and Astronomy, Sydney, Australia*

Raman scattering is the inelastic scattering of a photon by a molecule and, in water, its characteristics depend on temperature. We built a four-channel spectrometer using 532 nm laser excitation, to simultaneously collect polarised Raman signals (RS) at two spectral bands across the OH stretching band. From these, different temperature markers can be calculated: the “two-colour” ratios relate to intensities of signals having a common polarisation, and the “depolarisation” ratios relate to the perpendicular and parallel polarised RS within a defined spectral band. Narrow bandpass filters were chosen to optimise the sensitivity of the above ratios to changes in temperature. Natural water samples were placed in a temperature-controlled (to  $\pm 0.2^\circ\text{C}$ ) cell and the temperature was varied from  $18^\circ\text{C}$  to  $40^\circ\text{C}$ . The four Raman signals scattered by the sample were detected simultaneously by four fast photomultipliers and registered using a multichannel oscilloscope. Four different prediction ratios were calculated based on this setup and linear models of ratio versus temperature were evaluated individually, with RMSTE (Root Mean Square Temperature Error) varying among the samples from  $\pm 0.4^\circ\text{C}$  to  $\pm 2.34^\circ$  (two-colour) and from  $\pm 0.8^\circ\text{C}$  to  $\pm 2.55^\circ$  (depolarisation) ratios. Aiming to increase the accuracy and repeatability of our analyses we then built linear combination models for each sample, attributing a coefficient of maximum cross correlation for every ratio. Linear combination RMSTEs ranged from  $\pm 0.3^\circ\text{C}$  to  $\pm 0.5^\circ\text{C}$ , representing a substantial average improvement of 20% with respect to the best individual ratios. The multichannel design has enabled the depolarisation ratio to be harnessed and for the innovative use of linear combination method, which leads to better temperature accuracy in predicting water temperature. This design is compatible with LIDAR methods and has the potential to acquire spatially resolved, surface and subsurface temperature data.

## IMPACT OF BASELINE CORRECTION ON THE ACCURACY OF WATER TEMPERATURE MEASUREMENT WITH RAMAN SPECTROSCOPY

Artlett, Christopher<sup>1,2</sup>, **de Lima Ribeiro, Andréa**<sup>1</sup>, Pask, Helen<sup>1</sup>

<sup>1</sup> *Macquarie University, NSW, Australia*

<sup>2</sup> *Defence Science and Technology Group, NSW, Australia.*

Numerical modelling is an efficient tool to understand the hydrodynamics in any environment emulating the water column structure, geostrophic flow and air-sea interactions. To this end, models need water temperature validation data, not always available on the spatial and temporal scale needed. Here we present here a method based on Raman Spectroscopy (RS) and evaluate the accuracy with which the temperature of natural water samples can be determined.

RS is based on the inelastic scattering of light by the water molecule and spectral content of the retrieved signal is correlated to its temperature. The Raman spectra for 10 sites around Sydney were measured using an Enwave EZRaman-I dispersive spectrometer (8 cm<sup>-1</sup> spectral resolution, 30 mW excitation laser, 532 nm). A ratio was calculated using two channels of 200 cm<sup>-1</sup> width on either side of the isosbestic point (“two-colour ratio”), and a linear regression performed against temperature. The RMS temperature error (RMSTE) typically varied from  $\pm 0.2^{\circ}\text{C}$  to  $\pm 0.5^{\circ}\text{C}$ , and for some samples was strongly affected by the centre position of the two channels.

Most spectra exhibited a “baseline” which has been attributed to fluorescence from dissolved organic matter and Chlorophyll-a. To minimize the impact of this, a tilted linear baseline correction was applied to all measured Raman spectra, and was effective in improving the temperature accuracy to  $\pm 0.1^{\circ}\text{C}$  to  $\pm 0.3^{\circ}\text{C}$ . Moreover the precise positions of the two channels became less important.

Our findings show that baseline correction helps to achieve a high accuracy on natural water temperature determination using RS. Based on these results, we have demonstrated a multi-channel Raman spectrometer compatible with LIDAR methods. We are also commencing experiments to provide depth-resolved temperature data so, in the future, the technique can be used for data validation.

## FLUORESCENCE IMPACT ON RAMAN REMOTE SENSING OF WATER TEMPERATURE

de Lima Ribeiro, Andréa<sup>1</sup>, Ajani, Penelope<sup>2</sup>, Derkenne, Caro<sup>1</sup>, Artlett, Christopher<sup>1,3</sup>, Pask, Helen<sup>1</sup>

<sup>1</sup> *Macquarie University, NSW, Australia*

<sup>2</sup> *University of Technology Sydney, NSW, Australia.*

<sup>3</sup> *Defence Science and Technology Group, NSW, Australia.*

Raman spectroscopy (RS) is based on the inelastic scattering of photons. In water, the scattering depends systematically on water temperature, and accordingly the Raman signal can be analysed to predict temperature with accuracy as high as  $\pm 0.1^\circ\text{C}$  in pure (milli-Q) samples. In combination with LIDAR methods, RS offers a means of determining subsurface water temperature, extremely valuable in oceanographic studies. However, implementing such methods is challenging due to local variations in salinity, dissolved organic matter (DOM), phytoplankton density and particulate matter. The Raman spectra of 10 sites around Sydney were measured (Enwave EZRaman-I dispersive spectrometer, spectral resolution of  $8\text{cm}^{-1}$ , 30mW excitation laser, 532 nm) and RMS temperature accuracies ranged from  $\pm 0.1^\circ\text{C}$  to  $\pm 0.5^\circ\text{C}$ . A Principal Component Analysis of the normalised spectra revealed that signals peaking around 580 nm and 680 nm accounted for a significant amount of variance between the locations, and can be associated with fluorescence from DOM and chlorophyll-a (Chl-a), the latter of which is present in all phytoplankton species. To explore the extent to which fluorescence from Chl-a might mask the water Raman signal, therefore, we carried out a controlled experiment in which we grew three species of phytoplankton and calculated the cell densities that produced fluorescence comparable to the Raman signal. These were found to include: *Nannochloropsis sp.* ( $9.14 \times 10^3 \text{ cells.mL}^{-1}$ ); *Synechococcus* Green ( $7.78 \times 10^4 \text{ cells.mL}^{-1}$ ); *Synechococcus* Red ( $1.23 \times 10^5 \text{ cells.mL}^{-1}$ ). These concentrations are found in the natural environment, indicating that the presence of Chl-a fluorescence may compromise the accuracy of our method of water temperature prediction. Our findings will help us to develop methods that are less susceptible to the presence of fluorescing matter, such as using an excitation wavelength where there is reduced overlap between Raman and fluorescence signals and baseline correction models.

# Methods for Temperature Sensing in Natural Waters Based on Raman Spectroscopy and Blue Excitation

Andréa de Lima Ribeiro<sup>1</sup>, Christopher Artlett<sup>1,2</sup>, Helen Pask<sup>1</sup>

*MQ Photonics Research Centre, Department of Physics and Astronomy, Macquarie University, Sydney, NSW 2109  
Defence Science and Technology Group, Sydney, NSW, Australia  
andrea.delimaribeiro@mq.edu.au*

**Abstract:** Polarised and unpolarised Raman signals were used to predict water temperature. Both methods had similar accuracies for Milli-Q and natural waters (RMSTE  $\pm 0.6^\circ\text{C}$ ), but polarised signal ratios were more sensitive (% change per  $^\circ\text{C}$ ).

**OCIS codes:** (300.6450) Spectroscopy, Raman; (280.6780) Temperature; (010.7340) Water

## 1. Introduction

Water temperature is a primordial parameter to be measured in any aquatic study, as it determines heat exchange with atmosphere, water column stratification and geostrophic flow. The majority of water temperature data from the oceans is acquired remotely by satellite sensors, with depth limitations, sparse spatial/temporal resolution and dependent on the presence of clouds and other meteorological systems affecting the detection of infrared signal [1]. Raman Spectroscopy (RS), in combination with LIDAR method, has exciting potential to provide depth-resolved water temperature data for local and regional studies. First proposed several decades ago [2,3], advances in lasers, detector sensitivity and numerical methods have enabled the temperature of laboratory water to be predicted with an accuracy of  $\pm 0.1^\circ\text{C}$ , using a 30mW continuous-wave laser at 532 nm for excitation [4].

Extending the work reported in [4], depth-resolved temperature measurement requires consideration of several factors. A pulsed laser of  $\leq 2\text{ns}$  full-width at half maximum (FWHM) is desirable to achieve a depth resolution better than 0.5m, a multi-channel Raman spectrometer is required with spectral channels appropriately selected to give accurate temperature determination, and the use of fast, sensitive detection is also needed to achieve sufficiently-high signal to noise ratio and depth-resolution.

In this paper we report the use of two custom-designed 2-channel Raman spectrometers based on blue laser excitation. The use of blue excitation, compared to the green excitation used in [4], was driven by 3 key factors: larger Raman scattering cross-section at the shorter wavelength, the opportunity to avoid overlapping with between the Raman signal (around 550-575 nm) with fluorescence of chlorophyll-a around 680 nm that can occur in natural waters, and the lower transmission losses for returned Raman signal photons traversing the water column around 560 nm (for blue excitation) compared to around 650 nm (for green excitation). The focus of the work reported here is on measuring water temperature in a laboratory setting, i.e. using water samples in a temperature-controlled apparatus.

## 2. Experimental details

An experimental setup for a 2-channel Raman spectrometer is shown on Figure 1a, designed based on findings in [4,5]. Ultrapure (Milli-Q) and natural water samples were placed inside a temperature controlled probe (QNW Qpod2e, accuracy of  $\pm 0.2^\circ\text{C}$ ), and their temperature was varied from  $20^\circ\text{C}$  to  $40^\circ\text{C}$ , stepping every  $2^\circ\text{C}$ . A linearly-polarised 473 nm pulsed laser (2 ns at FWHM) was used on all measurements and its light was coupled into the sample by a Dichroic Mirror (DM). Two methods were chosen to analyze the water Raman signal in order to predict temperature, one using unpolarised Raman signals (“two-colour” ratio) and the other using polarised Raman signals (depolarisation ratio). For both methods, a ratio is calculated with the integrated signal retrieved from channels positioned on either side of the isosbestic point. Our experimental setup allows us to collect both types of signal by using a non-polarizing Beam Splitter Cube (BSC) for the “two-colour” analysis and replacing it by a Polarizing Beam Splitter Cube (PBSC) for the “depolarisation” analysis (Figure 1a).

The Raman signal scattered by the water sample passed through a Long Pass filter (LP) to eliminate Rayleigh scattering and was divided by a splitter cube depending on the analysis. Two commercially-available Band Pass filters (BP) were selected which would allow portions of the water Raman spectra on either side of the isosbestic point to be collected, as indicated in Figure 1b. BP1 (Semrock FF01-561/14-25) had a center wavelength of 561 nm and band-pass FWHM of 20.1 nm; BP2 (Semrock LL01-568/12.5) had a center wavelength of 568.2 nm and a typical transmittance at FWHM of 2.2 nm. All signals were collected by Photomultipliers (PMTs) Hamamatsu/H10721-20 and recorded with a multi-channel Tektronix DPO4104B oscilloscope, averaging over 532 pulses. The ratio of the collected signals has a linear dependence on temperature.

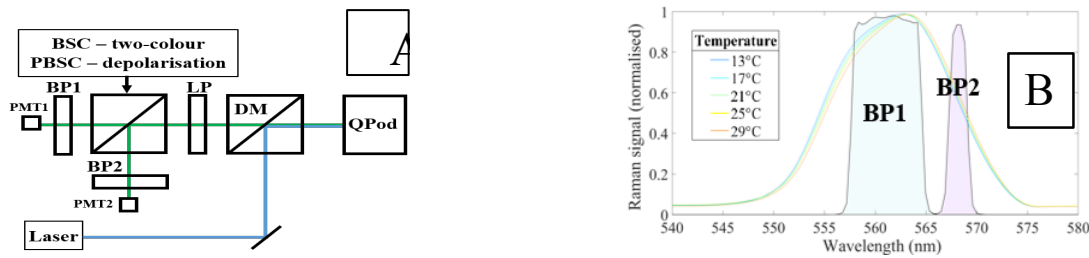


Figure 1. (a) Experimental setup for collection of unpolarised and polarised temperature-dependent Raman spectra of water. (b) Band Pass filter positions in relation to water Raman spectra.

The retrieved Raman signal was integrated over an interval of 3 ns around its peak and the prediction ratios were calculated for each temperature. A linear regression model of predicted vs measured (probe) temperature was performed, and the Root Mean Square Error on temperature prediction (RMSTE) was calculated.

### 3. Results

A summary of our findings is presented on table 1. For ultrapure water samples, the accuracy on temperature measurement achieved by the 2-colour method varied from  $\pm 0.6^\circ\text{C}$  to  $\pm 1.1^\circ\text{C}$ ; for the depolarisation ratio ranged from  $\pm 0.6^\circ\text{C}$  to  $\pm 1.2^\circ\text{C}$ . Considering the accuracy ( $\pm 0.2^\circ\text{C}$ ) with which the reference temperature was measured and the fact both analyses were performed on the same samples, it's possible to say both methods had similar performance. When predicting natural water temperature, both methods presented a higher range of accuracies, justified by different environmental conditions at different sampling days.

Table 1. Maxima and minima accuracies on temperature prediction for ultrapure and natural water samples

Sample	Two-colour	Depolarisation ratio
Milli-Q	$\pm 0.6^\circ\text{C}$ - $\pm 1.1^\circ\text{C}$	$\pm 0.6^\circ\text{C}$ - $\pm 1.2^\circ\text{C}$
Natural	$\pm 0.6^\circ\text{C}$ - $\pm 1.2^\circ\text{C}$	$\pm 0.8^\circ\text{C}$ - $\pm 1.7^\circ\text{C}$

The sensitivity for both analysis methods, represented by the percentage change in the ratios per  $^\circ\text{C}$ , is shown in figures 2a (Milli-Q water) and 2b (natural water sample). The depolarisation ratio exhibited a higher sensitivity to temperature for both types of water (0.84% per  $^\circ\text{C}$  for Milli-Q and 0.75% per  $^\circ\text{C}$  for natural sample) compared to the two colour ratio (0.60% per  $^\circ\text{C}$  for Milli-Q and 0.54% per  $^\circ\text{C}$  for natural sample). Higher sensitivities between Raman signal and temperature are advantageous, particularly when working on natural waters where another signals (e.g. fluorescence) may overlap with the Raman spectra; hence depolarisation ratio has the potential to complement the more widely-used two-colour method. Its usefulness here has been enabled by the 2-channel Raman spectrometer design which enables simultaneous acquisition of two orthogonally-polarised Raman signals.

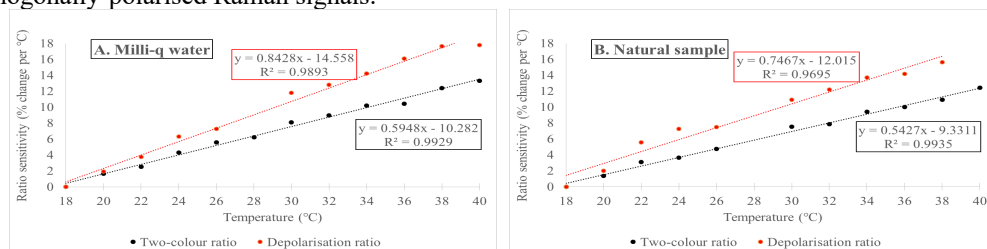


Figure 2. (A) Ratios sensitivity (% change per  $^\circ\text{C}$ ) for Milli-Q water. (B) Ratios sensitivity (% change per  $^\circ\text{C}$ ) for natural waters.

Our findings have helped us to evaluate the potential of RS for predicting temperature from different water types using either the two-colour or depolarisation method, and we have demonstrated very simple instrumentation that enables water temperature to be predicted with reasonable accuracy. Our next step will be to build a 4-channel Raman spectrometer, where both polarised and unpolarised components of the Raman signal can be retrieved at the same time and build linear combination models based on both ratios, aiming to achieve higher accuracies on water temperature determination.

### 4. Acknowledgments

Ms. Andréa de Lima Ribeiro would like to acknowledge Macquarie University for the iMQRES PhD. scholarship.

### 5. References

- [1] E. Bauer, "The Scattering of Infrared Radiation from Clouds," *Applied Optics* **3**, 197-202 (1964).
- [2] D. Leonard, B. Caputo, F. Hoge, "Remote sensing of subsurface water temperature by Raman scattering", *Applied Optics* **18** (11), 1732-1745 (1979).
- [3] C. H. Chang, L. A. Young, "Seawater temperature measurement from Raman spectra," in contract N62269-73-C-0073, sponsored by Advanced Research Projects Agency, ARPA Order 2194 (1972).
- [4] C. Artlett, H. Pask, "Optical remote sensing of water temperature using Raman spectroscopy", *Optics Express* **23**(25), 31844-31856 (2015).
- [5] C. Artlett, H. Pask, "New approach to remote sensing of temperature and salinity in natural water samples", *Optics Express* **25**(3), 2840-2851 (2017).



## Water temperature measurement using blue excitation and two-channel Raman spectrometer

Andréa Ribeiro<sup>a</sup>, Christopher Artlett<sup>a,b</sup>, Helen Pask<sup>a</sup>

<sup>a</sup>Department of Physics and Astronomy, Macquarie University, Sydney, Australia

<sup>b</sup>Lastek PTY Ltd.

Raman spectroscopy (RS) is a technique with potential to solve several problems in oceanographic remote sensing, including being able to provide reliable data about subsurface water properties (e.g. temperature, salinity).

Several studies established a relationship between water Raman spectra and temperature that could be used in remote sensing equipment [1,2]. Recently, experiments conducted using RS and a 532nm (green) excitation laser found an accuracy of  $\pm 0.1^\circ\text{C}$  for pure water temperature measurements [2]. However, when this technique was applied to natural waters, it was found that fluorescence from Chlorophyll at 680nm overlapped the Raman signal and adversely affected the accuracy with which temperature could be determined.

Aiming to avoid the impact of fluorescence, we conducted experiments to retrieve temperature-dependent polarised Raman spectra of Milli-Q water with a pulsed (2 ns duration) 473nm (blue) laser as excitation source. The use of blue light can also be a benefit for *in situ* measurements, as blue light has near optimal penetration in the water column.

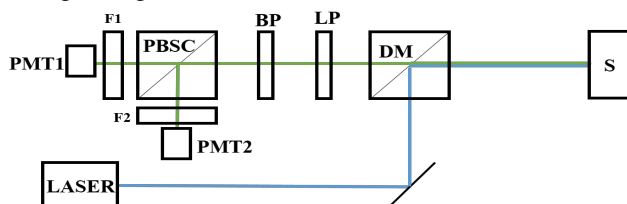


**Figure 1: Experimental setup for collection of polarized temperature-dependent Raman spectra of Milli-Q water.**

Our experiment setup is shown in Figure 1. A Milli-Q water sample (S) was placed inside a temperature-controlled cuvette holder and its temperature was varied from  $20^\circ\text{C}$  to  $40^\circ\text{C}$ , stepping every  $2^\circ\text{C}$ . The Raman signal scattered by the sample passed through a dichroic mirror (DM) and through a Long Pass filter (LP) to eliminate Rayleigh scattered photons. The Raman signal was then split into two components – perpendicular and parallel – to the polarisation of the excitation laser using a Polarising Beam Splitter Cube (PBSC). Each component was detected by a Photomultiplier (PMT): PMT1 retrieved signal from the parallel component with a 590nm Band Pass filter (F1), and PMT2 from the perpendicular component with a 545nm Band Pass filter (F2). The signal from each PMT was collected by a multi-channel oscilloscope, with averaging over 532 pulses.

The band pass filters F1 and F2 were used to select parts of the spectra positioned before and after the isosbestic point and were chosen on the basis of polarised Raman spectra presented in [2]. Higher signal intensities were found for the perpendicular component (see Fig 2.A) than the perpendicular

(see Fig. 2.B); this is due to the tetrahedral structure of water molecule and its vibrational modes [3].

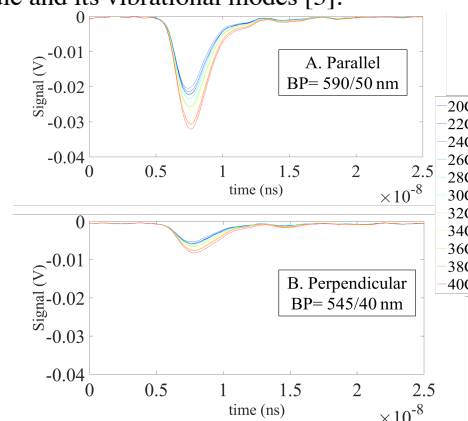


**Figure 2: Parallel (A) and Perpendicular (B) polarised Raman pulses for Milli-Q water (temperatures of  $20^\circ\text{C}$  to  $40^\circ\text{C}$ ).**

In the liquid state, water molecules bond in clusters and the number of bonds is dependent on temperature; as temperature rises these bonds break and change the molecules vibrational frequency [4]. This behaviour was detected in both components (Fig. 2).

As was also found in [5], there is a linear relationship between decreasing temperature and the depolarisation ratio, i.e., the ratio between the intensities in the perpendicular and parallel components. Our results are shown in Figure 3, where the average change in ratio over this temperature was close to 1% and the  $R=0.8858$ .

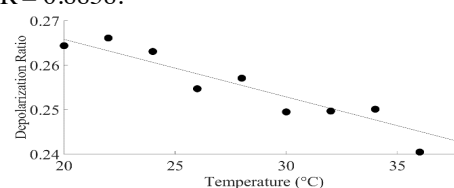


**Figure 3: Depolarisation ratio as a function of temperature.**

To our knowledge, this is the first time that RS has been applied to determine temperature using the depolarisation ratio and blue excitation at 473nm. Most significantly, this has been achieved using a two-channel Raman spectrometer and without retrieving the full Raman spectra. Our ongoing work will be focused on natural water samples and on combining with LIDAR methods for depth-resolved measurements.

### References

- [1] Walrafen *et al.*, *The journal of Chemical Physics*, 1985
- [2] Artlett & Pask, *Optics express* 23 (25), 2015
- [3] Tominaga *et al.*, *Fluid phase equilibria* 144 (1-2), 1998
- [4] Carey *et al.*, *The journal of Chemical Physics* 12, 1998
- [5] Leonard *et al.*, *Applied Optics* 1

# APPENDIX D

## White Paper for ONRG

### Depth-resolved Remote sensing of water temperature using Raman spectroscopy

Prof Helen Pask and Ms Andrea Ribeiro

Department of Physics and Astronomy, MQ Photonics, Macquarie University, NSW 2109,  
Australia

Email: [helen.pask@mq.edu.au](mailto:helen.pask@mq.edu.au)

Sent on 6th April, 2018 to:

Dr. Simin Feng (ONRG Tokyo office): [Simin.Feng.civ@mail.mil](mailto:Simin.Feng.civ@mail.mil)

Dr. Jeff Simmen (ONRG Singapore Office): [simmenj@onr.navy.mil](mailto:simmenj@onr.navy.mil)



## Abstract

This proposal seeks research funding to develop early-stage research into the remote sensing of subsurface water temperature profiles. Information about subsurface water temperature is of value to defence, oceanography and biology/environmental science sectors, with particular applications relating to the validation of hydrologic models, underwater sound propagation, and predicting algal bloom events. Our laboratory studies are well advanced and a funded research project would focus on the field implementation of our research findings.



## Background to the Project and the Team

This project was initiated when I attended a workshop organised by the Australian defence company Tenix (subsequently acquired by BAE systems), aimed at identifying means by which their system for bathymetry (LADS) could be evolved to provide additional information about the water column. I became interested in the prospects for measuring water temperature using Raman spectroscopy, and was successful in getting modest funding from the NSW Environment Trust and Australian Research Council to support the project from 2011-2016. The project has not been funded since then.

Two PhD students have worked on the project. The first was awarded his PhD in 2015 and is now working at DSTG (Defence Science and technology Group), Maritime division, Sydney. The second student has just returned from a US conference and lab visits where her work was well received and will submit her thesis in August this year.

My credentials for carrying out this project include the following metrics: author of >70 well cited journal papers, 3601 citations and h index = 28 according to Google Scholar, invited review papers, inventor on 10 patents. I have an excellent track record for working with industry partners, achieving project outcomes and goals. Examples include the licensed commercialisation of yellow lasers for retinal surgery, and collaborations with several laser manufacturers.

My colleague and PhD student Andrea Ribeiro is a highly capable, skilled and enthusiastic researcher and oceanographer. I anticipate she would play a key role in the project.

### *A new collaboration*

We propose to collaborate with Prof. Andrew Jessup, A.Prof Chris Chickadel and colleagues at the Applied Physics Laboratory, University of Washington, Seattle, USA. This would be a new and mutually-beneficial collaboration, building on a recent visit by Andrea. The group at APL will assist the Macquarie team to do some field testing on their research vessel alongside profiling CTDs and radiometer measurements of surface temperature.

Successful research outcomes will provide the group at APL with a new technology that they can deploy to measure subsurface water temperature and salinity in coastal regions. Collecting near-real time data would be extremely valuable for the project **Inner Shelf Dynamics**, already being conducted by Dr. Chris Chickadel (APL – ONR grant n° N000141512389). Our technique has the potential to bring light to cross-shelf processes, vertical structure and dynamics of the mixing layer (e.g. Langmuir circulation) and to validate other remote sensing and LIDAR data collected on field trials.

## Background and key research achievements

- We understand where our work fits in the context of the previous work. We note our methods build on early work by others [1,2], including at NASA and US Defence labs.
- We have identified the spectral features most sensitive to temperature and developed models to optimise the design parameters and performance of a LIDAR-compatible, multi-channel Raman spectrometer to determine water temperature [3]

- We have developed multivariate analysis methods to demonstrate the potential for simultaneously extracting temperature and salinity information [4]
- We understand the origin of background (non-Raman) signals, and have evaluated methods to correct for these. Such methods are critical to accurately determine temperature in natural waters. [paper in preparation]
- We have constructed of 2 and 4-channel Raman spectrometers capable of determining temperature of natural and lab water samples with accuracies better than  $\pm 0.5^{\circ}\text{C}$  for both natural and pure lab waters.
- We have tested novel analysis methods that harness both depolarisation and spectral dependence of Raman spectra on temperature [paper in preparation], thereby improving accuracy up to  $\pm 0.2^{\circ}\text{C}$  for natural water samples. This analysis is particularly useful when studying different Jerlov water types with diverse optical constituents.
- We have investigated blue and green laser excitation for determining temperature in natural water samples, with a view to minimising the effects of fluorescence and increasing Raman signal returns. Blue excitation also enables a separate channel at 680nm for monitoring Chl-a fluorescence. [paper in preparation]
- We have undertaken preliminary field studies in which Raman signals were obtained from depths of 6-8m. Raman signals considerably exceeded ambient daytime light levels, and the maximum depth from which signals were acquired was limited by the PMT dynamic range.

### **Key Distinguishing features of our research**

Most other researchers have used spectral decomposition (superimposing several Gaussians to fit the full Raman spectra), and some have used neural networks. Our approach is unique 1) because it is LIDAR-compatible and 2) because there is no requirement to collect a full Raman spectra, the detection apparatus is compact and affordable comprising optical filters and PMTs. In principle, the excitation laser could be the same one used for bathymetry.

### **Research proposal**

The focus of this proposal will be on implementing our methods in the field. This will be accomplished through a combination of experimental studies and numerical simulations. Laboratory-based work will be carried out where needed to address particular issues such as the refining of analytical methods and collecting full Raman spectra or fluorescence spectra. Field-based trials and evaluation will be carried out in various settings which include: a 9m high water cell at Macquarie, a small punt on Sydney Harbour, and a research vessel accessed via collaboration with Andy Jessup, Chris Chikadel and colleagues at University of Washington, USA.

Target specifications will be  $\pm 0.5^{\circ}\text{C}$  temperature accuracy, and 0.5m depth resolution. We will steer the research towards the following questions:

- What is the maximum depth from which Raman signals can be obtained, in various natural waters, and what factors limit this depth?
- What is the maximum depth at which temperature can be predicted with reasonable accuracy (say  $\pm 0.5^{\circ}\text{C}$ )?
- To what extent does the choice of excitation wavelength influence the temperature accuracy and depth that can be profiled?
- In what Jerlov water types can we demonstrate effective depth-profiling of water temperature?

- Can we extend our temperature profiling to extract additional information on salinity and chlorophyll-a concentration?
- Can temperature profiling be accomplished in near-real time?
- How well do our methods for depth-profiling water temperature compare to the information measured using instruments such as CTDs and radiometers?
- How effectively can temperature profiles be acquired using surface-based, land-based, underwater and air-based platforms? Here we will seek to bring together experimental and numerical studies to evaluate the future “practicality and usefulness” of our methods.

## References

1. C. H. Chang, and L. A. Young, “Seawater temperature measurement from Raman spectra,” (contract N62269–73-C-0073, sponsored by Advanced Research Projects Agency, ARPA Order 2194, 1972).
2. D. A. Leonard, B. Caputo, and F. E. Hoge, “Remote sensing of subsurface water temperature by Raman scattering,” *Appl. Opt.* **18**(11), 1732–1745 (1979).
3. C. P. Artlett and H. M. Pask, "Optical remote sensing of water temperature using Raman spectroscopy," *Opt. Express* **23**, 31844-31856 (2015)
4. C. P. Artlett and H. M. Pask, "New approach to remote sensing of temperature and salinity in natural water samples," *Opt. Express* **25**, 2840-2851 (2017)

